A Multiscale Analysis of Frictional Interaction between Human Skin and Nonwoven Fabrics

A dissertation submitted to
University College London
for the degree of
Doctor of Philosophy (Ph.D)

David John Cottenden

Continence and Skin Technology Group
Department of Medical Physics and Bioengineering
University College London

This thesis has been set in Adobe Garamond Pro using XeLaTeX with the author's djcthesis class, which is in turn derived from Andy Buckley's hepthesis LaTeX class.

Abstract

Various hygiene products, notably incontinence pads, bring nonwoven "topsheet" fabrics into contact with individuals' skin. This contact can damage the skin in various ways, including abrading it by friction, a mechanism enhanced by the presence of moisture. In recent years skin-nonwoven friction has been the subject of significant experimental study in the Continence and Skin Technology Group, UCL, in the course of which methods have been developed which can detect differences in friction between a chosen nonwoven and equivalent skin sites on different individuals under fixed conditions. The reasons for these differences are unknown; their elucidation is one focus of this work. The other is to establish the influence of coarse geometry on the dynamics of a tense nonwoven sheet sliding over a substrate and interacting with it by friction.

The first part of this work ("microfriction") is primarily experimental in nature, and involves two separate experiments. The first involves using a microscope with a shallow depth of field to determine the length of nonwoven fibre in contact with a facing surface as a function of pressure; the second consists of measuring friction between chosen nonwovens and a skin surrogate at a variety of pressures and speeds whilst simultaneously observing the behaviour of the interface down a microscope. Both techniques were extensively validated, and the data from the two experiments were then compared. It had originally been intended to conduct the friction experiment on skin (the other experiment does not require it), and though all equipment was developed with this in mind and all relevant permission was sought and obtained, it was not eventually possible. Instead, a skin friction surrogate (Lorica Soft) established in the literature was used. Data from this show that Amontons' law (with respect to load) is obeyed to high precision ($R^2 > 0.999$ in all cases), though there is the suggestion of sublinearity at low loads. Detailed consideration of the friction traces suggests that two different friction mechanisms are important, and comparison with the contact data suggests tentatively that they may correspond to adhesion between two different populations of contacts, one "rough" and one "smooth".

Further work applying these techniques to skin is necessary.

The second aspect of the work is "geometric friction"; that is, the relationship between the geometry of a surface (on the centimetre scale and upwards) and the friction experienced by a compliant sheet (such as nonwoven topsheet) laid over it in tension. A general equation of motion for slippage between sheet and surface has been derived which in principle allows for both objects to deform and interact according to any plausible friction law. This has then been solved in integral form for

Amontons' law and a low density strip exhibiting no Poisson contraction sliding over any surface with zero Gaussian curvature; closed form solutions for the specific cases of a prism and a circular cone have then been derived and compared. Experimental verification has been provided by a colleague, which shows very good agreement between theory and experiment. It has also been shown that, taking a naïve approach, the classic model for a rigid cylinder can be applied even to a quite extreme cone with experimentally negligible error.

NB All prior copyrighted material (diagrams in all cases) has been removed from this edition to facilitate electronic distribution. They have been replaced with boxes of the same size, so pagination is identical with the complete version.

Declaration

I, David John Cottenden, confirm that the work presented in this thesis is my own. Where information has been derived from other sources, I confirm that this has been indicated in the thesis.

David John Cottenden
December 9, 2010

Acknowledgements

In the course of the work presented herein I have received assistance and helpful criticism from many quarters. Most obviously, my UCL supervisors Jem Hebden and Alan Cottenden have put a great deal of time into advising me, and have made themselves available with little or no notice, which in light of their busy schedules is due still further thanks. Thanks also go to my primary SCA supervisor Carolyn Berland, who has been very helpful in providing feedback, suggestions, and in placing considerable resources and expertise at my disposal, and to Per Bergström, Anne Farbrot, and Kerstin Johansson, her fellow SCA supervisors, as well as Anna Nihlstrand for hunting up and supplying me with various very useful additional data sets.

Many people with no formal affiliation with my project have nonetheless been very helpful, and should be acknowledged: Frank Smith for reading my work and bringing his mathematical experience to bear when I have been stuck; Margaret Macaulay for sorting out so many administrative things which might have fallen to me, even though it's not her job; Rebecca Wong for providing me with all sorts of information and guidance based on her experience of researching skin-nonwoven friction; Adam Gibson for helping with Matlab problems; David Atkinson for his helpful suggestions with regards to image enhancement; and especially Vasileios Asimakopoulos for sharing his experimental results on geometric friction with me. Several friends have been very helpful, especially Mike Davison who (both directly and indirectly) has suggested various materials for experiments (and supplied the first inner tube), Matt Jack who helped with various oddments of coding, and Simon Cottrell who brought a fresh pair of eyes to bear and provided a helpful critique of the literature review.

Many people have been lent a hand either literally or figuratively in my efforts to obtain skin to experiment on. In particular I would like to thank Sonia Buckingham for initial advice on procedures; Pratik Sufi for pointing us at likely looking surgeons; Oke Avwenagha and Dave Wilson for their assistance with the IRAS form and associated paperwork; Senga Steel for making the R&D process just *work* at the Whittington end; and in particular James Malone-Lee for letting me trade under his name throughout the whole process. Thanks also go to Lotta Jonsson for facilitating with all her might; and to Sam Bishara, Shozab Khan, and Zahra Mohammadi for offering to prepare the samples. Jay Vaidya and Alan Wilson are acknowledged for agreeing to supply the skin itself.

I acknowledge with thanks SCA Hygiene Products AB and the Engineering and Physical Sciences Research Council for funding my work.

I would also like to thank Raquel Santamarta Vilela with whom I have shared an office for the past three years for remembering to smile in the mornings, and for cheerfully accepting my humming, occasional rants, and conversations with pieces of paper. Finally, I thank my wife Janet for being there when I get home, and being nothing to do with work!

Glossary

Asperity A region (typically nucleated) on a material surface which is raised relative to the average surface height. Contact between surfaces thus occurs at asperities. Asperities typically make up a very small proportion of a surface's area.

Cauchy stress Stress measured relative to deformed space. In two dimensions, force per unit deformed distance; in three dimensions, force per unit deformed area.

Constitutive equation An equation that relates the configuration of a body (not generally limited to mechanical parameters) and its history to the current local stress.

Coverstock The top sheet in a hygiene product. In modern disposable products these are often nonwovens.

Crimp Short wavelength corrugations in a fibre, often introduced to improve nonwoven cohesion.

Decitex A unit used by textile technologists to measure the linear density of fibre, defined as the mass in grams of 10 km of fibre.

Differentiable manifold A generalised mathematical space which, in the neighbourhood of any point, behaves like Euclidean space, but generally does not do so globally. Differentiability ensures that neighbourhoods of different points can be related by smooth mappings.

Dynamic friction The frictional force acting to reduce speed in sliding systems.

Elastic deformation Material deformation which does not result in the dissipation of energy.

Filament Nonwovens terminology meaning a continuous, effectively endless fibre extruded during the production of the nonwoven which it is used to make.

Finishing treatment A stage of nonwoven production. Finishing treatments involve applying some type of surface treatment to the finished nonwoven, often to manipulate the degree of hydrophilicity.

Hysteresis theory Any of a range of theories that derive a frictional force macroscopically by considering that the finite recovery time of a viscoelastic substrate prevents an impressed object from reclaiming all of the energy used to effect the impression.

Instantaneous isotropic interface An interface between two surfaces at which any frictional force acts in the opposite direction to velocity (in the dynamic case) or applied force (in the static case). In practice, this requires surface isotropy and a very limited class of material memory effects.

Kelvin-Voigt model A viscoelastic model consisting of a spring in series with a parallel spring-dashpot pair.

Material frame indifference The principle which states that constitutive equations describing a body which are satisfied by stress and configuration $\{ \mathbf{T}, \chi \}$ should also be satisfied by $\{ \mathbf{T}^*, \chi^* \}$, where stars denote a change in frame of reference.

Metric A second rank tensor which relates changes in co-ordinates to distances. Inner products between the components of tensors must be performed across the metric.

Needlefelt A nonwoven fabric manufactured by repeatedly punching barbed needles through a diffuse web of fibres in order to compact and entangle them. Needlefelts are typically several millimetres thick.

Needling speed The frequency with which the barbed needles used to make needlefelt are punched through a fibre web.

Nonwoven A fabric composed either of short staple fibres or of a continuous fibre (filament) held together by means other than weaving or knitting, commonly entanglement and / or thermal bonding.

Pinning model Any of a class of models that treat frictional interactions between surfaces as arising from local repulsive potentials corresponding to asperities. Such models also include elastic deformation of surfaces, and so make dissipative transits of potentials possible.

Plastic deformation Material deformation which results in permanent change to a body.

Ploughing term A term in Bowden & Tabor's analysis of friction considered to be due to lasting plastic deformation of surfaces caused by asperities on one surface gouging grooves in the other.

Rate theory Any of a range of friction theories that calculate the sliding velocity under an applied force by introducing "pinning sites" on a substrate and allowing transition between them based on thermal excitation over the energy barriers between such sites, modified by the potential due to the applied force.

Reference configuration An arbitrarily selected configuration of a material body, chosen as a means by which to relate particles in the body manifold to spatial positions and distances. In practice, this is often a stress-free configuration.

Rotational technique A category of experimental techniques used in determining the frictional force between two surfaces. All such techniques involve a rotating disc or annulus faced with one material in contact with a plane faced with the other. The complex force fields generated by such methods make measurements hard to interpret.

Shear strength The maximum shear stress (or force, depending on context) that a contact can support before failure. This is a specialisation of the more general meaning of this term.

Shearing term A term of Bowden & Tabor's analysis of friction considered to be due to the shear force required to break bonds formed between asperities on corresponding surfaces. This term was assumed to scale with true contact area.

Simple material A class of materials in which stress depends *only* upon the first derivative of the deformation.

Spunbond A spunbond nonwoven is formed from continuous filament fibre extruded from a spinneret onto a flat surface, which is then passed between patterned or plane hot rollers (*calendered*), softening and bonding the fibres to provide cohesion.

Staple Fibre cut to finite length before processing into a textile.

Static friction The frictional force acting to oppose impressed forces in the absence of relative motion between surfaces.

Stick-slip The regime of inter-surface motion characterised by periods of no motion followed by rapid adjustments; the instantaneous velocity is often far from the mean velocity.

Straight pull technique A category of experimental techniques used in determining the frictional force between two surfaces. All such techniques involve a linear application of force (as opposed to a rotating contact) to one surface whilst the other is held motionless. The category includes techniques using both flat and curved contacts.

Tensor A mathematical object in $\mathfrak{n}$ dimensions with rank $\mathfrak{m}$, and $\mathfrak{n}^{\mathfrak{m}}$ components, which transforms under a fixed set of rules, and multiplies with reference to a metric which specifies the nature of the space it inhabits. The term "tensor" is taken to include *any rank*, thereby encompassing scalars, vectors, and all higher rank objects.

Thermal calendering A nonwoven production technique. The process of passing a nonwoven web between a pair of heated rollers to soften and fuse some of (or some component of some of) the constituent fibres. The rollers can be smooth or patterned; the latter leaves a regular grid embossed into the nonwoven.

Thermal depinning Early transit of an asperity-potential in a pinning model caused by thermal excitations.

Tribology The study of interacting surfaces, often in relative motion. It includes friction, wear, and any lubrication effects present.

Tribosystem A system of two surfaces (and any lubricants or other contaminants) interacting by friction, and generally wearing down in consequence.

Viscoelastic deformation Material deformation in which stress depends upon deformation rate. This class of deformation is dissipative of energy, but is usually taken not to cause permanent deformation.

Voigt element A parallel combination of a spring and a viscous dashpot. Such a combination makes no instant displacement response to a step increase in applied force, rather gradually accommodating to it.

Web bonding A stage of nonwoven production. Web bonding is any process which imparts mechanical integrity to the fibre web by bonding its fibres. This can involve an external material (for example, latex spots) but more commonly involves repeated punching by barbed needles (for thicker felts) or thermal bonding of some type (common for coverstocks).

Web formation A stage of nonwoven production. Web formation is any process which takes fibres and distributes them over a bed in essentially their final configuration.

Yield point / stress The point / stress at which elastic deformation gives way to plastic deformation. Viscoelastic behaviour causes its location to depend on strain rate.

Notation

Symbols are grouped thematically by usage. A symbol with different meanings in different contexts may appear more than once. In the literature review (§2) the symbols used in the work reported are retained (so far as is possible) for ease of comparison with the original work; such symbols are defined at their point of use, and do not appear in this list.

Operators and decorations

$\mathbf{a} := \mathbf{b}$	Definition. $\mathbf{a}$ is defined to be equal to the pre-existing $\mathbf{b}$.
$\mathbf{a} \otimes \mathbf{b}$	The outer product of tensors $\mathbf{a}$ and $\mathbf{b}$. The symbol may be omitted if this does not cause ambiguity.
$\mathbf{a} \cdot \mathbf{b}$	The inner product of tensors $\mathbf{a}$ and $\mathbf{b}$. If $\mathbf{a}$ and $\mathbf{b}$ are of rank higher than one, the last index of the first tensor is contracted with the first index of the second (except for differential operators).
$\mathbf{a} \times \mathbf{b}$	The cross product of tensors $\mathbf{a}$ and $\mathbf{b}$. If the tensors are of rank higher than one then the last index of $\mathbf{a}$ and the first of $\mathbf{b}$ are the only indices affected.
$\mathrm{Tr}\mathbf{A}$	The trace of tensor $\mathbf{A}$. For a second rank tensor there is no ambiguity over the indices to be contracted; traces of higher rank tensors are clarified where used.
$\mathbf{A}^{\mathsf{T}}$	The transpose of tensor $\mathbf{A}$. For a second rank tensor there is no ambiguity over the indices to be transposed; transposes of higher rank tensors are clarified where used.
$\hat{\mathbf{a}}$	Normalisation; $\hat{\mathbf{a}}$ is a unit vector in the direction $\mathbf{a}$.
$\boldsymbol{\nabla}\mathbf{a}$	The gradient of tensor $\mathbf{a}$.
$\boldsymbol{\nabla} \cdot \mathbf{a}$	The divergence of tensor $\mathbf{a}$. For higher rank tensors, the contraction between $\boldsymbol{\nabla}$ and the tensor is on the tensor's *final* index.
$\boldsymbol{\nabla} \times \mathbf{a}$	The curl of tensor $\mathbf{a}$. For higher rank tensors, the alternating tensor contracts with $\boldsymbol{\nabla}$ and $\mathbf{a}$'s *final* index.
$\boldsymbol{\nabla}_{\mathbf{X}}\mathbf{a}$	The gradient of tensor $\mathbf{a}$ with respect to the space described by $\mathbf{X}$. Divergence and curl in this space are defined for consistency.
$\partial_t \mathbf{a}$	Spatial description time derivative of $\mathbf{a}$; that is, considering $\mathbf{a}$ as a function of spatial position and time.

$\dot{\mathbf{a}}$	Material description time derivative of $\mathbf{a}$; that is, considering $\mathbf{a}$ as a function of material co-ordinates and time.

Geometry and co-ordinates

$\mathbb{R}^n$	n dimensional Euclidean space.
$\mathbf{x}$	A location in physical space.
$\boldsymbol{\eta}$	A small displacement in physical space.
(x, y, z)	Cartesian components of $\mathbf{x}$.
(r, θ)	Co-ordinates of a point in plane polars.
$R(\theta)$	Radial plane polar co-ordinate as a function of the azimuthal plane polar co-ordinate in the context of geometric friction on a prism.
(ρ, ϕ, z)	Co-ordinates of a point in cylindrical polars.
$d\check{\mathbf{x}}$	An element of axial distance, defined as the two-dimensional analogue of an axial area vector in three dimensions.
t	Time.
$\mathcal{B}$, $\mathcal{L}$, $\mathcal{S}$, $\mathcal{P}$	Manifolds representing a non-specific body, a deformable substrate, a nonwoven sheet, and the surface particles of $\mathcal{L}$, respectively.
$\{w_\nu\}$, $\{v_\nu\}$, $\{u_\nu\}$	Co-ordinates for material points within $\mathcal{B}$, $\mathcal{L}$, and $\mathcal{S}$, respectively.
$\boldsymbol{\chi}$, $\boldsymbol{\lambda}$, $\boldsymbol{\sigma}$	Mappings from the manifolds $\mathcal{B}$, $\mathcal{L}$, and $\mathcal{S}$, respectively into space. Generally dependent on time.
$\varkappa$, $\boldsymbol{\Lambda}$, $\boldsymbol{\Sigma}$	Reference configurations: specific instances of $\boldsymbol{\chi}$, $\boldsymbol{\lambda}$, and $\boldsymbol{\sigma}$ used to provide a real space reference for points in the manifolds $\mathcal{B}$, $\mathcal{L}$, and $\mathcal{S}$.
$\mathcal{B}$, $\mathcal{L}$, $\mathcal{S}$, $\mathcal{P}$	The images of $\mathcal{B}$, $\mathcal{L}$, $\mathcal{S}$ and $\mathcal{P}$ under the mappings $\boldsymbol{\chi}$, $\boldsymbol{\lambda}$, $\boldsymbol{\sigma}$, and $\boldsymbol{\lambda}$, respectively.
$\mathbf{l}$, $\mathbf{s}$, $\mathbf{p}$	Locations in the real space sets $\mathcal{L}$, $\mathcal{S}$, and $\mathcal{P}$, respectively.
$\mathbf{X}$, $\mathbf{L}$, $\mathbf{S}$, $\mathbf{P}$	Real space reference locations corresponding to the current locations $\mathbf{x}$, $\mathbf{l}$, $\mathbf{s}$, and $\mathbf{p}$, respectively.
$\mathcal{F}_{\mathrm{I}}$, $\mathcal{F}_{\mathrm{II}}$	The first and second fundamental forms of a surface patch, respectively. The first form is a surface metric; the second is a measure of curvature.
$\mathcal{A}$	A simply connected subset of $\mathcal{S}$.
$\hat{\mathbf{N}}$	An outward pointing normal of $\mathcal{S}$.
$\mathbf{C}$	The gradient of $\hat{\mathbf{N}}$, $\mathbf{C} := \boldsymbol{\nabla}\hat{\mathbf{N}}$.
$\mathcal{R}_j$	Regions of $\mathcal{P}$ which coincide with $\mathcal{S}$; that is, regions where the sheet and substrate are in contact.
$\mathcal{C}_{ji}$	Bounding curves to regions of contact, $\mathcal{R}_j$, with $\mathcal{C}_{j0}$ the outermost curve, and other $\mathcal{C}_{ji}$ defining the bounds of any holes in $\mathcal{R}_j$ in the case of multiple connectivity.

Continuum mechanics

$\mathbf{T}$	Cauchy stress.
$\mathbf{f}$	Body force per unit volume.

ρ	Mass density, which is generally a function of deformation.
ν	Poisson's ratio.
E	Young's modulus
E^*	Reduced Young's modulus; the harmonic mean of $E/(1-\nu)$ for two contacting surfaces.
$\mathbf{F}$	Deformation gradient, the gradient of the deformation function $\chi(\mathbf{X})$ with respect to the reference configuration.
$\mathbf{R}$	The orthogonal tensor from a polar decomposition of the deformation gradient.
$\mathbf{U}$	The symmetric tensor from a *right* polar decomposition of the deformation gradient.
$\mathbf{V}$	The symmetric tensor from a *left* polar decomposition of the deformation gradient.
$\mathbf{B}$	The *left* Cauchy-Green strain tensor.
$\mathbf{C}$	The *right* Cauchy-Green strain tensor.
dR	Scalar element of contact force.
L	Half-length for a cylindrical contact.
a	Half-width for a cylindrical contact.
R	Radius of a cylinder in a contact situation.
P	Load on an indenting body.
p_{nom}, p	Nominal pressure at an interface; mean true pressure at the contacts.
Π	Material independent pressure; $\Pi = p_{nom}/E^*$.

Friction

N	Normal reaction force from a surface.
μ, μ_*, μ_s, μ_d	Coefficients of friction. The first form does not refer specifically to either static or dynamic friction; the second form refers non-specifically to either; the third is the static coefficient; and the fourth is the dynamic coefficient.
F	Friction force.
ψ_*, ψ_s, ψ_d	Friction scalars for an isotropic instantaneous interface; suffices follow the convention given for μ.
γ	A loss factor after that introduced by Greenwood & Tabor.
ϕ	Contact fraction for an interface; that is, the proportion of nominal contact area that is in "true" contact, defined at some scale.

Contents

"Le savant n'étudie pas la nature parce que cela est utile; il l'étudie parce qu'il y prend plaisir, et il y prend plaisir parce qu'elle est belle."

— Henri Poincaré, 1854–1912

Chapter 1

Introduction

"The most exciting phrase in science is not 'Eureka', but rather, 'That's funny…'."
— Isaac Asimov, 1920–1992

The work reported in this thesis is concerned with understanding the mechanisms of friction between human skin (§2.2) and thin nonwoven fabrics (§2.3). Despite the broad relevance of this topic it has received little attention to date, with few studies published. However, experimental techniques have recently been developed [1] which are sensitive enough to discern differences in friction between individuals for a given nonwoven and equivalent sites. This is the first time that such differences have been reliably measured, so they naturally raise the question of their origins. In fact, there is no firm evidence of *where* friction between skin and nonwovens comes from (§2.4.2), either in terms of location in the skin or nonwoven or in terms of the principal mechanisms. One of the foci of this work is thus to determine the fundamental origin of friction at the skin-nonwoven interface.

However important, fundamental understanding of where friction between a flat skin-nonwoven interface comes from is limited: on the scale of tens of centimetres people are *not* flat. It is thus also important (both from the perspective of simulation and in order to interpret experimental results) that the relationship between anatomical curvature, fabric tension, and friction is also understood. This constitutes the other focus of the work reported here.

1.1 The nature of friction, and the healthcare context

Everyone is familiar with friction: it keeps people on their feet, makes most sports possible, and enables cars, bicycles, and trains to both accelerate and brake. However, as with many phenomena defined by an observed effect—that force must be applied to initiate motion and to maintain it—it is not the case that all systems where the friction is observed generate it via the same mechanism. Since the study of the origins of friction began in the mid twentieth century, the number of identified effects and mechanisms that have marched under the single banner of "friction" has multiplied massively. The dominant mechanism(s) are now known to depend upon not only the nature of *both* of the materials in contact, but also their surface finishes, the sliding speed or dwell time,

the magnitude and direction of applied force, the presence of any lubricants or contaminants, the temperature, and even the history of sliding long finished (§2.4).

As well as the many useful impacts of friction, it causes considerable problems. As well as the familiar and well-researched areas such as gear wheel (and similar) wear, lubrication, heating, and geophysics (earthquakes are, fundamentally, a result of friction) there are many far less well-known and less researched topics. In healthcare, shear forces caused by friction are known to increase the susceptibility of tissue to decubitus [2]—a significant problem, especially for elderly and immobile patients. Wearers of personal hygiene products such as sanitary towels, baby diapers, and incontinence pads frequently develop skin damage due to the potent combination of increased skin hydration and abrasion [3]. With three million people in the UK incontinent of urine (a number anticipated to increase as the population ages) [4], the incontinence pad sector alone mandates considerable research. An improved understanding of the relationship between skin state, fabric properties, product and patient geometry, and friction would enable products to be designed where friction was low or high (desirable to keep products in place) in the locations where this was important.

1.2 An outline of the project

This thesis is divided into six chapters, including this one. Chapter 2 is a substantial literature review of friction between skin and nonwoven fabrics. It also covers the mechanical properties of both skin and nonwovens, as well as the basics of the continuum mechanics necessary to describe large deformations in compliant media. As well as skin-nonwoven friction, it reviews skin-X[1] friction, nonwoven-X friction, and several other different systems with contextual relevance.

Chapter 3 is a careful consideration of what was found in the literature review. It considers the different mechanisms of friction that may be relevant and the scales and features (both in the skin and nonwoven) that they depend upon. This process mandates a split between fundamental mechanisms of friction and those associated with bulk geometry. Aims and objectives for both branches of the project are then given.

Chapter 4 reports work on the small-scale fundamental mechanisms of friction. Since these mechanisms are not known (the literature review finds at best an indication that *some* mechanisms are *sometimes* important) the work reported in this chapter is principally experimental. It comprises work to measure the nature and size of the contacts between a skin surrogate (which is demonstrated to be equivalent to skin for these purposes) and nonwoven, and to measure friction force and gather qualitative information on what happens to a skin surrogate-nonwoven interface during sliding. Both experiments are conducted at a range of pressures, and the latter at a range of sliding speeds. Unfortunately, it has not been possible to conduct experiments on any real skin; the reasons for this and its implications are discussed. Validation work on the equipment developed and used for the work in this chapter is located in appendices B, C, and D; additional graphs are given in appendix E.

Chapter 5 consists of a theoretical analysis of a flexible, compliant sheet moving over a curved surface under tension with friction coupling the two. The problem is defined carefully for a fairly

[1] Any non-specific material is referred to as "X" (roman face) throughout this work.

general class of frictional interfaces, and conditions for contact and non-contact deduced. An equation of motion is then produced, governing the dynamics of the sheet, and providing boundary conditions for the behaviour of the curved substrate. A general solution in integral form is found for the special case of surfaces with zero Gaussian curvature and sliding strips with zero Poisson's ratio subject to external forces only at their (distant) ends, and closed form solutions are derived for a strip sliding at any angle over a general convex prism and for a circular cone. The solutions are compared, and experimental data from a colleague are shown to validate the model.

A final summary and conclusions are given in chapter 6, along with recommendations for future work, and a list of outputs from the project.

Chapter 2

Literature review

"'Just the place for a Snark!' the Bellman cried…"
— Lewis Carroll, 1832–1898

The scope of this review is defined by the established techniques that have been applied to the modelling of skin-nonwoven friction and related areas, and experimental work on this or related systems. In order to reduce the incidence of forward-reference, work on topics that support the friction review is presented first (§2.1, §2.2, §2.3), followed by the friction review itself (§2.4).

The broad relationship between the sections is as follows. Theoretical work on friction first requires an understanding of how two surfaces conform to each other [5, 6, 7, 8, 9]; that is, continuum mechanics (§2.1). However, the constitutive rules that characterise objects and enable predictions to be made are highly specific to materials or classes of materials, so the mechanical properties of both skin and nonwovens must be reviewed individually and in detail (§2.2, §2.3). Having laid the groundwork, it is then possible to review friction (§2.4), considering first "classic" models (§2.4.1), then work specific to skin, fabric, or both (§2.4.2, §2.4.3, §2.4.4), and finally work specific to neither material but containing useful or applicable ideas (§2.4.5–§2.4.9).

2.1 Continuum mechanics

Truesdell and Noll [10] adroitly observed that matter is commonly found in the form of materials. In consequence of this fact, largely overlooked in "classic" analytical mechanics and "modern" physics, the formalisms used in those two areas have been extensively adapted in order to describe continuous media[1]. This work primarily considers such media, so the aforementioned formalisms must be considered.

2.1.1 Material and spatial descriptions

Before any progress can be made, unambiguous notation must be established. Continuum mechanics is the study of deformation of continua, the constituent particles of which move around in space as a function of time. This introduces an unavoidable question in describing fields: should they

[1] That is, media which cannot for the purpose at hand be considered as an assembly of particles or a single particle.

be described as fields over material particles, or as fields over space? Each has advantages in some circumstances, so it is not sensible to choose one over the other; rather an unambiguous notation must be used to distinguish them. There is not a single universal system, so the notation used in this work is modelled on that used in differential geometry (see Pressley [11] or others), which can be summarised as follows.

- Material particles exist in a space $\mathcal{B}$ and are described by co-ordinates w_ν; Greek suffices are reserved for $\mathcal{B}$ and analogous spaces.
- The spatial position of the particle with co-ordinates $\{w_\nu\}$ is given at time t by a function $\chi(\{w_\nu\}, t)$.
- The material co-ordinates of a particle at position $\mathbf{x}$ at time t are given by the expression ${\chi^{-1}}_\nu(\mathbf{x}, t)$.
- Spatial derivatives are denoted by $\boldsymbol{\nabla}$; derivatives with respect to the material co-ordinates are denoted by ∂_ν.

This basic notation makes it possible to define functions over either space or the material. However, notation for time derivatives is still needed. If the arguments of a function are specified, for example $f(\mathbf{x}, t)$, $g(w_\nu, t)$ then derivatives with respect to time can be taken unambiguously, clearly relating to the derivative evaluated at a spatial location or tracking a material particle, respectively. However this is unwieldy, so it is common [10] to define two different notations for time derivatives depending on whether the associated variable is w_ν or $\mathbf{x}$:

$$a = f(\mathbf{x}, t) = g(w_\nu, t) \qquad , \qquad \partial_t a = \frac{\partial}{\partial t} f(\mathbf{x}, t) \qquad , \qquad \dot{a} = \frac{\partial}{\partial t} g(w_\nu, t).$$

These are related by

$$\dot{a} = \partial_t a + \dot{\chi} \cdot \boldsymbol{\nabla} a. \tag{2.1}$$

The derivative described by equation 2.1 is known as the *material* or *convective derivative* since it follows the particle flow [10, 12].

2.1.2 Finite deformations

Historically, the study of infinitesimal strain[2] continuum mechanics—usually characterised by linear relationships between stress and strain—has received far more attention than theories of larger strains or nonlinear stress-strain relationships, with whole books covering a wide variety of situations scarcely mentioning finite strains [13, 14]. Whilst it is true that in many situations strains *are* very small, these theories by no means describe all physical systems that may be encountered [10]. Finite-strain continuum mechanics seeks to provide a more general framework which can encompass almost any material and situation, and be specialised to describe individual situations.

A key feature of finite-strain continuum mechanics is that a raft of different theories collapse to a single infinitesimal strain theory [10]. This is mostly due to an ambiguity that is not important for

[2] That is, strains which are sufficiently small that essentially all quantities of importance can be estimated linearly, as would be perfectly correct if the strains in fact *were* limitingly small.

small strains: should reference be made to the *deformed* or *undeformed* space? Clearly, choices must be made (and made consistently) for a theory of finite deformations.

In their notable treatise of 1965 [10], Truesdell and Noll gave a superbly detailed and coherent presentation of the theory of continuum mechanics for finite deformations. In essence, they described a body and its deformations using a variant of the notation described in §2.1.1, additionally defining a specific instance of χ as a *reference configuration* $\varkappa(\mathcal{W}_\nu)$, and a *deformation function*, also denoted χ and defined as $\chi(\mathbf{X}, t) := \chi(\varkappa^{-1}(\mathbf{X}), t)$. The deformation function maps a particle's Euclidean space position in the reference configuration to the corresponding position in a different configuration, and is the fundamental strain quantity in finite strain continuum mechanics.

2.1.3 Stress and equations of motion

For finite deformations there are several possible generalisations of the the stress used in infinitesimal strain mechanics, corresponding to the possible choices of body configuration in which force and area could be measured. The stress measure most relevant to the work reported in this thesis is the *Cauchy stress*, $\mathbf{T}$, which measures both force and area relative to the *current* configuration. This means that stress relates to forces and areas in the current configuration in an intuitive fashion.

Using the Cauchy stress, Newton's second law can easily be transformed into a form more useful in the context of continuum mechanics, *Cauchy's law of motion* [10]:

$$\boldsymbol{\nabla} \cdot \mathbf{T} + \mathbf{f} = \rho \ddot{\chi} \qquad , \qquad \mathbf{T} = \mathbf{T}^{\mathsf{T}}, \tag{2.2}$$

where $\mathbf{f}$ is a body force per unit volume, and ρ is local density, which is generally a functional[3] of deformation. The latter equation is required to avoid infinite angular accelerations; it is not a statement of any type of equilibrium.

2.1.4 Constitutive relations and material frame indifference

The most general constitutive equation that could be posed would allow the Cauchy stress to depend on the complete history of deformation up to the present over the entire body, $\mathcal{B}$ [10]:

$$\mathbf{T}(\mathbf{X}, t) = \mathbf{D}_t[\chi],$$

where $\mathbf{D}_t[\chi]$ is a functional that can depend on the values of χ up to time t. However, some constraints are imposed on the possible forms that $\mathbf{D}_t$ can take by the requirement that it transforms between frames of reference consistently. This requirement is known as the principle of material-frame indifference.

Definition — "Material frame indifference" If a constitutive equation is satisfied for a pair $\{\chi, \mathbf{T}\}$ then it must be satisfied for a pair $\{\chi^*, \mathbf{T}^*\}$, where the starred variables have been transformed to a new frame of reference by translations in space and time, and rigid rotations [10].

[3] A functional can be thought of as depending on a function in the same way that a function depends on a variable. An example would be $F_t[f] = \int_{-\infty}^{t} \kappa f(t')^2 dt'$.

A *simple material* is one for which all dependence on χ is in terms of its first derivative, the deformation gradient $\mathbf{F} := \nabla_X \chi$. By the polar decomposition theorem ([15] or others) $\mathbf{F}$ can be decomposed into the product of a unitary tensor ($\mathbf{U}$, $\mathbf{V}$) representing strain without rotation, and an orthogonal tensor ($\mathbf{R}$) as either of $\mathbf{V} \cdot \mathbf{R} := \mathbf{F} =: \mathbf{R} \cdot \mathbf{U}$. Using this decomposition, the constitutive equation can be given [10] in an automatically frame-indifferent form as

$$\mathbf{T}(t) = \mathbf{R}(t) \cdot \mathbf{E}[\mathbf{U}(t-\tau)] \cdot \mathbf{R}(t)^T,$$

where $\mathbf{E}$ is any tensor-valued functional[4] and $\tau > 0$.

2.1.5 Compatibility

Several strain measures are commonly used in finite strain continuum mechanics, all derived from the deformation gradient in different ways:

- $\mathbf{F}$, the deformation gradient, which can be decomposed into $\mathbf{V} \cdot \mathbf{R}$ or $\mathbf{R} \cdot \mathbf{U}$ as noted in §2.1.4.
- $\mathbf{C} := \mathbf{U}^2 = \mathbf{F}^T\mathbf{F}$, the right Cauchy-Green tensor.
- $\mathbf{B} := \mathbf{V}^2 = \mathbf{F}\mathbf{F}^T$, the left Cauchy-Green tensor.

However, not all second rank tensor fields are valid as strain measures, as eloquently explained by Acharya [16]. For example, $\mathbf{F}$ must by definition be a gradient and so obey $\nabla \times \mathbf{F} = 0$. In order to establish what the *compatibility conditions* are for other strain measures, it can be helpful to consider an analogy with Riemannian geometry[5]. This analogy involves considering the deformation as a change in co-ordinates in a metric space, and the strain measure as the new metric [16]. For example, transforming from co-ordinates X^i, to y^α,

$$dy^\alpha = F^\alpha{}_j dX^j,$$

so

$$dy^\alpha dy_\alpha = dX^i\, F^T{}_i{}^\alpha F_{\alpha j}\, dX^j = dX^i\, (\mathbf{F}^T \cdot \mathbf{F})_{ij}\, dX^j = dX^i\, C_{ij}\, dX^j.$$

The covariant components of the right Cauchy-Green tensor can thus be interpreted as the covariant components of the metric of X^i in the deformed space. Results like this enable a large number of results from Riemannian geometry to be applied.

The compatibility conditions for the Cauchy-Green tensors, $\mathbf{R}$ and $\mathbf{U}$ are:

Right Cauchy-Green tensor, $\mathbf{C}$. By considering $\mathbf{C}$ as the metric tensor for the reference co-ordinates in the deformed space i.e. $\|d\mathbf{y}\|^2 = dX^i C_{ij} dX^j$, Blume [17] (and others) showed that the Riemann curvature tensor based on the metric $\mathbf{C}$ is zero:

$$\tfrac{1}{2}(C_{jk,il} + C_{il,jk} - C_{jl,ik} - C_{ik,jl}) + C^{-1}{}_{pq}(\Gamma_{jkp}\Gamma_{ilq} - \Gamma_{jlp}\Gamma_{ikq}) = 0,$$

[4] The notation $E[U(t-\tau)]$ denotes that the functional E can depend upon the function U over the region of the latter's domain where $\tau > 0$. This ensured causality.

[5] Roughly, the geometry of spaces which have a smooth metric which is neither generally flat nor constant throughout the manifold.

where the Christoffel symbols are derived from $\mathbf{C}$ as $\Gamma_{ijk} = \frac{1}{2}(C_{jk,i} + C_{ik,j} - C_{ij,k})$. Note that since this is an equation *of* the metric the repeated indices in the second term should be contracted across the identity.

Left Cauchy-Green tensor, $\mathbf{B}$. By considering the left Cauchy-Green tensor as the metric of the deformed co-ordinates in the reference space, Acharya [16] derived a compatibility condition for $\mathbf{B}$ in the case of a twice differentiable deformation,

$$\frac{\partial F^{i}{}_{\alpha}}{\partial X^{\beta}} = -\frac{B^{im}}{2}\left[\frac{\partial B_{rm}}{\partial X^{\beta}}F^{r}{}_{\alpha} + \frac{\partial B_{sm}}{\partial X^{\alpha}}F^{s}{}_{\beta} - \frac{\partial B_{rs}}{\partial X^{\rho}}(F^{-1})^{\rho}{}_{m}F^{r}{}_{\alpha}F^{s}{}_{\beta}\right].$$

This condition is clearly less neat than the corresponding condition on the right Cauchy-Green tensor, in that it is not expressed purely in terms of $\mathbf{B}$.

Rotation tensor and right stretch tensor, $\mathbf{R}$ *and* $\mathbf{U}$. An elegant paper by Shield [18] pointed out that since $\mathbf{C} = \mathbf{U}^2$, a compatibility condition for $\mathbf{U}$ follows immediately from the condition for $\mathbf{C}$. He also showed that by substituting the polar decomposition of $\mathbf{F}$ into $\Gamma_{ijk} = F_{mi,k}F_{mr}$ (derived from the fundamental definition of a Christoffel symbol) a differential equation for $\mathbf{R}$ in terms of $\mathbf{U}$ could be obtained:

$$R_{ij,k} = R_{il}A_{ljk}(\mathbf{U}),$$

where A_{ljk} is a prescribed function of $\mathbf{U}$. Again, the repeated indices should be contracted across the identity.

These conditions are of central importance in solving any differential equations in terms of their respective strain measures.

2.1.6 Contact mechanics

Contact mechanics is the study of the deformation that occurs when two surfaces are brought into contact. This is a specific subset of continuum mechanics, and has received substantial attention.

The first treatment of the contact between two deformable bodies was made in 1882 by Hertz [19], who considered contact between two ellipsoids (figure 2.1). His treatment made a series of assumptions (summarised by Johnson [14]) about the geometry of the situation and the elastic behaviour of the bodies in question:

- To determine the contact region, the initial separation was assumed to be a paraboloid and deformation to occur as shown in figure 2.1.
- To determine the deformation, both surfaces were assumed to be elastic half spaces with plane surfaces. For small indents the contradiction between this and the previous assumption is gentle.
- The characteristic length of the contact region a was very small compared to the radii of the contacting ellipsoids (R', R''), and the true thickness of the block of material.
- The material obeyed the equation of isotropic linear elasticity, $\mathbf{T} = \alpha\boldsymbol{\epsilon} + \beta \mathrm{Tr}(\boldsymbol{\epsilon})\mathbf{I}$, where $\boldsymbol{\epsilon}$ is engineering strain, Tr signifies the tensor trace, $\mathbf{1}$ is the second rank identity tensor, and α and β are constants.

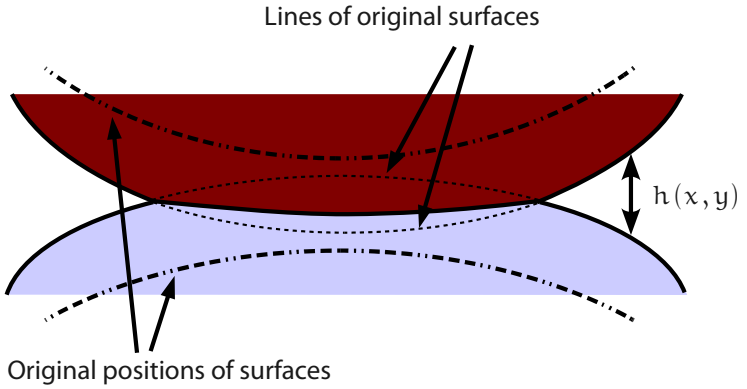

Figure 2.1: The contact first modelled by Hertz [19]. The current separation is a function $h(x,y)$ over the "plane" of contact, and the undeformed separation at the point of first contact is a 2d parabola described by curvatures R' and R''.

- The only forces present were normal to the plane. This means that friction was not and cannot be included in the basic Hertz analysis.

Hertz solved the equilibrium equation for the stress:

$$\nabla \cdot \mathbf{T} = -\mathbf{f},$$

subject to the compatibility conditions for engineering strain. The boundary conditions dictated that surface stress was matched on either side of the contact within the area of contact, zero outside it, and that the stress fell to zero at infinity. This produced a characteristic pressure distribution, which for a circular contact was given by $p \propto \sqrt{1 - r^2/a^2}$, where r is distance from the centre.

Hertz's theory was extended by Cerruti, Bousinesq, and Love (reported by Johnson [14]) to provide solutions for more general surface forces, including shear tractions. They obtained solutions (in the form of integrals) to this more general problem. However, their solutions are deeply dependent on the linearity and specific form of classic elastic theory in that they were based on integration over Green's functions (or similar potential methods) [14], and used the specific form of the constitutive equation to relate the strain compatibility equations to the conditions on stress [13].

In addition to these pure linear elastic models there has also been considerable work done since the 1950s on the problem of how adhesion between the contacting surfaces alters their behaviour. The first coherent model to be published was that of Johnson, Kendall, & Roberts (*JKR*) in 1971 [20] which assumed that adhesion was a zero-range force; that is, it ceased to act as soon as contact was lost. Using an energy balance argument to add this effect into the known Hertzian contact behaviour (a hemisphere was assumed for simplicity), JKR produced a modified contact formula for contact area against pressure which included adhesion, and experimental evidence of its accuracy. A different approach was taken by Derjaguin, Muller & Toporov (*DMT*) [21] who calculated the impact of long range adhesive forces, having assumed that they would simply lead to the same Hertzian contact shapes being accessed sooner than they would be by applied force alone. Subject to this assumption

they found (again using an energy balance argument) that the adhesive force was constant for all deformations, and thus that the only impact of the adhesion was to add an additional constant force to the applied force in the Hertzian equations. It is far from clear that DMT's unlikely assumption of elastically determined shapes was not the principal cause of this result.

These theories co-existed for almost twenty years before Maugis [22] unified them into a single model with a single free adhesion parameter (essentially equivalent to the Tabor parameter [23]): as the parameter slid from one extreme to the other the solution changed smoothly from JKR to DMT. Maugis' model is in a sense very crude (considering the adhesive pressure distribution to be a boxcar function, for example), and it has been equally criticised and praised for its flexibility; that is, its ability to accommodate a wide variety of results due to its many parameters.

Many of these ideas have historically been applied to the deformation of skin and subcutaneous tissues for a variety of investigations, including nervous reaction [24] and digital spatial acuity [25], as well as friction [26, 27]. They have been used widely in studying elastomer friction and adhesion [5, 7, 20, 28, 9].

2.2 Mechanics of skin and subcutaneous tissue

In order to model the mechanical behaviour of the skin, and moreover to understand any differences between individuals' skins, it is important to be able to link structure with mechanical properties. This section of the review will thus first consider the structures that make up the skin and immediately subcutaneous tissue, before looking at their properties and models which have been used to describe them.

2.2.1 Mechanical structure of the skin and subcutaneous tissue

The skin is a multilayered structure, with mechanical properties varying considerably between the different layers. At the simplest level, the skin can be regarded as two layers, the dermis (lower, 1 mm–4 mm thick) and epidermis (upper, 0.06 mm–1 mm thick), separated by the collagen "basement membrane" [29]. These layers can then be further subdivided according to their changing character with depth.

Dermis It is usually claimed in the literature that the dermis dominates the mechanical properties of the skin under normal conditions [29]. It is divided, though not very sharply, into the reticular layer (lower) and the papillary layer (upper, typically twice the thickness of the epidermis). From a mechanical point of view, the reticular layer is characterised by large, interwoven, tortuous collagen fibres, and elastic fibres, whereas the papillary layer contains smaller, less organised collagen and immature elastic fibres (figure 2.2).

Epidermis The majority of the epidermis is mechanically relatively compliant and is usually claimed to contribute less than the dermis to the mechanical properties of the skin as a whole. It is divided into four sublayers at most anatomical sites, the basal, spiny, granular, and horny layers, from deep to superficial. The horny layer is more commonly known by its Latin name, the *stratum corneum*, and is very much stiffer than the rest of the epidermis. The chief change that occurs through the

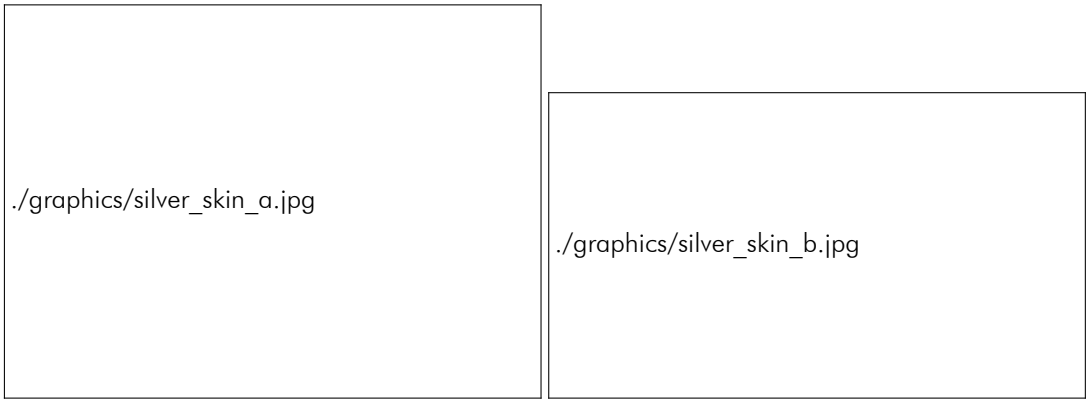

Figure 2.2: Diagrams of the skin from Silver *et al.* [29]. (a) The skin is shown in cross-section, illustrating the composition at different layers, and the possible forces. (b) The structure of the dermis and epidermis in more detail.

layers of the epidermis is the progressive keratinisation (filling with keratin, a horny protein) of cells from the lower layers to the upper ones. It is important to note that the epidermal cells are in mechanical contact with each other, and their keratin structures (*cytoskeletons*) are connected and capable of bearing limited loads [29].

These two layers are mechanically connected across the basement membrane by collagen "pegs" that penetrate the membrane and fix into the structures on either side.

The whole of the skin is in tension under normal "relaxed" *in vivo* conditions, with one of the principal axes of stress aligned roughly with the "Langer lines" (lines with a typical width scale around 200 µm [30]) on the skin. The tensile stress is commonly reported to be primarily borne by the dermis, but is also transmitted to the epidermis by the collagen pegs that penetrate the basement membrane.

Subcutaneous tissue In its most literal sense, subcutaneous tissue simply refers to tissue below the skin, and as such exactly what is referred to depends on the location on the body, though in most cases it is a combination of fat and muscle down to the bone.

These structures provide a variety of mechanisms for bearing applied stresses. They are divided by Silver *et al.* [29] into "passive" and "active" mechanisms depending on whether they are consequences of intrinsic material properties or active biological responses.

The "passive" mechanisms are stretching of cytoskeletal connections in the epidermis, stretching of elastic fibres in the dermis, and stretching of the collagen fibres in the dermis. These are all linked together in parallel by the pegging through the basement membrane. One of the key properties of the skin, the sigmoid stress-strain curve (figure 2.3) arises from the fact that the stiff collagen fibres do not initially contribute to the total stress response by virtue of their significant tortuosity in the relaxed dermis: they are not in tension until a strain of about 30 % is imposed [29]. For this reason,

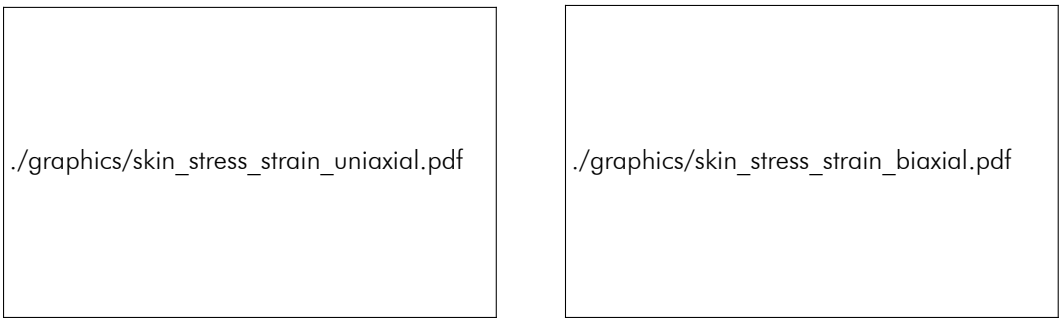

Figure 2.3: Diagrams of the stress-strain curve for excised skin, adapted from Silver *et al.* [29]. (a) shows the curve for uniaxial tension. (b) shows the curve for biaxial tension. As the skin is excised, it is to be presumed that *in vivo* skin would not exhibit the portion of the curve below the Langer stress (reported as $\approx$ 1 MPa by Silver *et al.* [29]).

the stress-strain response of skin below ~30 % is often reckoned to be dominated by the relatively low modulus dermal elastic fibres and epidermal cytoskeletons, switching over to higher modulus behaviour above this. It is interesting to note that collagen fibres reorient themselves to the direction of a uniaxial applied force. A biaxial stress can thus precipitate failure at a much lower strain since not all collagen fibres are contributing to the load bearing [29].

The "active" stress bearing mechanisms are based on contraction of objects called fibrils that are attached to collagen fibres in the dermis. These can supply an additional or replacement stress, and are important in wound healing. Unfortunately data on the time scale of the active response from fibrils (as distinct from their passive viscoelastic behaviour) have not been found in the literature.

2.2.2 Methods for measuring skin mechanical properties

The key consequences of the aforementioned structure is that the skin is not isotropic or linear, and is viscoelastic. Unfortunately, assessment of its mechanical properties is complicated: *in vivo* the skin is intimately connected with underlying tissues with broadly similar mechanical properties so is hard to isolate; and *ex vivo* it rapidly begins to die and dehydrate, and moreover the pre-stress present *in vivo* has been removed and must be approximately replaced. In respect of *ex vivo* measurements, chemical and freezing preservation techniques that are routine when preserving a sample for biological measurement are very likely to alter its physical nature, so measurements on samples treated in these ways should be viewed with considerable scepticism. In spite of these difficulties many attempts have been made to measure some (sometimes composite) characteristic of skin's mechanical properties.

Considering first *in vivo* measurements, a review of methods has been given by Marks [31]; using his categories mechanical properties have been measured using suction, indentation, rotation, tangential traction, and sound wave methods. Each of these methods has its own strengths and

weaknesses.

Suction Suction techniques are perhaps the most commonly used of all techniques for measuring skin mechanical properties, in large measure due to the wide availability and ease of use of the Courage & Khazaka Cutometer[6] [32]. This device itself has been used widely [33, 34, 35, 36, 37] and other devices operating on the same partial vacuum principle have also been used [38, 39, 40, 33]. The raw results from the Cutometer (and similar devices) are in the form of maximum deflection as a function of time, with the device software using this to produce some numbers intended to characterise the degree of "pure" elastic deformation, "viscous" deformation, response time, etc. Unfortunately each of these numbers is a composite of many different fundamental mechanical quantities, so whilst increased deformation (all other parameters remaining constant) implies reduced modulus it is certainly not valid to assume a linear relationship other than, perhaps, for very small deformations. Modulus values *were* computed in an early paper by some of the developers of the Cutometer [32], but they appear to have been based upon a tangent to a graph of applied pressure against deflection[7]: if this produces a reasonable value it should be viewed as serendipity.

For this reason it is fairly common to mix suction device measurements with computational finite element models (*FEM*) of the skin and underlying tissue, adjusting the values of the mechanical parameters to match the stress-displacement experimental data [38, 39, 40, 34]. The chief complexity in this approach has been how to model the skin-subcutaneous tissue system: Hendriks *et al.* tried one-layer [38, 39] and two-layer [40] hyperelastic models; and Delalleau *et al.* [34] used a single layer; neither group acknowledged subcutaneous tissue. However, the fact that even the more imitative two-layer model of Hendriks *et al.* [40] was unable to make accurate predictions for experiments using suction chamber apertures of ⌀ 1 mm, ⌀ 2 mm, and ⌀ 6 mm on the basis of a single set of constitutive parameters suggests that FEM-interpreted suction experiments should be treated with considerable caution. Additionally, since Hendriks *et al.* in all cases used a coupling gel or liquid it is likely that the skin was substantially softened at the time of measurement.

Indentation Indentation testing is particularly relevant to this work as it is very similar to a commonly used friction measurement technique. Relatively few studies of this type of have been done explicitly for the purpose of measuring skin mechanical properties. Pailler-Mattéi *et al.* used a steel conical indentor with 45° half angle [41] and a hemispherical steel indentor of diameter 12.7 mm [42], Jachowicz *et al.* [43] used stainless steel spheres with diameters 7.9 mm, 15.9 mm, and 31.8 mm, whilst Kwiatkowska *et al.* [37] used smooth steel balls of diameters 2 mm and 5 mm. Jachowicz *et al.* and Kwiatkowska *et al.* used a simple Hertzian analysis to extract Young's moduli from the forearm (both) and face (Jachowicz *et al.*), though considering the complicated composite structure comprising different layers with different elastic properties it is unclear what this single number might mean. In their 2007 paper Pailler-Mattéi *et al.* used a model in which muscle, hypodermis, and dermis were considered as three series springs to produce an overall stiffness, which was then used in a Bousinesq-type model. This is clearly an approximation, but is an interesting method for

[6]The Cutometer consists of a small chamber that can be partially evacuated, inducing a bulge in the skin. The maximum deflection is then measured optically.

[7]The method for computing a strain from this deflection is not given; normalising by the aperture diameter seems plausible.

extracting dermal stiffness if the other layers' moduli are known; unfortunately they are no more precisely known than dermal modulus is, so although Pailler-Mattéi *et al.* obtained a good fit their modulus value should be treated with caution. In their later paper [42], some of the same authors interpreted their results using a single layer model in conjuction with the same Bousinesq-type contact solution.

Rotation Few papers have reported the use of rotation devices to measure skin stiffness, probably due to the complexity of analysing a mixture of graded shears and compressions. Agache *et al.* [44] is one of the few. They used a ⌀25 mm disc attached to (shaved and tape-stripped) forearm skin and surrounded by a "guard ring" with an internal diameter of 35 mm (described in [45]) to cause a 2°–6° rotation of the skin under the influence of a single prescribed torque. The data obtained in this way were interpreted by assuming that the skin was a linear elastic sheet floating over the body, an assumption that apparently bears little resemblance to the known anatomy or indeed to everyday experience. Again, the modulus values obtained should be viewed with extreme caution.

Tangential force Three devices that implement and measure the consequences of tangential forces *in vivo* have been found, due to Christensen *et al.* [46], Khatyr *et al.* [47], and Evans & Holt [48]. Christensen's equipment involved a small plastic pad bonded to the skin with cyanoacrylate and pulled tangentially with a wire; Khatyr *et al.* attached two clamps to the skin (method unspecified) and separated them to a known distance; Evans & Holt fixed a single fine wire to the skin surface with adhesive tape and pulled while the surface was monitored using digital image correlation (*DIC*). All groups of authors appear to have ignored the presence of underlying tissue when analysing their data: Khatyr *et al.* made the assumption silently; and Evans & Holt on the basis of unpublished "preliminary tests"; while Christensen *et al.* did not try to extract fundamental parameters, content with force against displacement graphs. This assertion seems plausible for small displacements, though further, published evidence is needed. However, with maximum displacements of 16 mm and around 8 mm reported by Khatyr *et al.* and Evans & Holt respectively, it could reasonably be argued that these displacements are *not* small compared to the other scales. Evans & Holt's report of skin wrinkling increases uncertainty on this point.

Khatyr *et al.* [47] interpreted their results with an *ad hoc* viscoelastic model composed of a one dimensional chain of Voigt elements (described in §2.4.5), and then separately used experiments run in four different directions to attempt to validate an orthotropic[8] model of skin stiffness. Unfortunately as the orthotropic model used had four parameters and Khatyr *et al.* gathered only four data points their "validation" is no such thing; the idea remains interesting, but is not validated. Many experimental details are missing from their paper, so it is hard to judge the validity of their results. Evans & Holt [48] used a simple Ogden strain energy function with two parameters in an FEM to fit their experimental data. They used only three, very closely spaced tangential forces (0.7 N–1.25 N) and found errors on the order of 10 % in the FEM fit to data; a much wider range of forces would be needed to validate the model convincingly, though the agreement is fair based on the data presented.

[8]The orthotropic model is perhaps the simplest anisotropic elastic model. It attributes distinct elastic properties in each orthogonal direction and considers directions between these to experience a weighted mixture of the "pure" directional properties.

Sound waves Two slightly different approaches to measuring skin properties with sound waves have been identified, due to Dawes-Higgs *et al.* [49] and Gennisson *et al.* [50]. Dawes-Higgs *et al.* devised a device that applied a 20 Hz sinusoidal oscillation to the skin surface and measured the response with strain gauges. The data were Fourier transformed and stiffness (*not* modulus) extracted from the data by undisclosed means. The authors took considerable care to ensure that the readings were repeatable and correlated well with shear modulus as determined from a poorly specified indentor experiment. Gennisson *et al.* [50] used a ring-shaped oscillator at 300 Hz "tuned" to focus on the focal point of an ultrasound transducer, and completed a series of simulations to help them interpret their results skin-layer-by-skin-layer. They used these data to obtain a shear modulus for the dermis and hypodermis; the epidermis is too thin to be reliably observed.

Both of these methods have been carefully validated and in the case of Gennisson *et al.* offer convincing separation of layers. However, each is only as good as the linear elastic approximation by which the results are interpreted.

Tests on excised skin or skin layers require much less interpretation than those on *in vivo* skin as there are no other layers attached: the only allowance that must be made in mechanical terms is for testing geometry. The difficulty in these cases is in preparation of the samples. Most *ex vivo* methods have involved extension tests on full thickness or a particular layer of excised skin [51, 52, 53, 54], though the work of Christensen *et al.* [46] involved a tangential force that was applied to a circle of skin (full thickness, without stratum corneum, or without any epidermal layers) secured at the periphery, and Pailler-Mattéi *et al.* [41] performed indentation tests on excised stratum corneum. Christensen *et al.* made no attempt to extract fundamental characteristics, so their work will not be considered further; Pailler-Mattéi *et al. did* extract a modulus, but their report that it *dropped by an order of magnitude* between its relaxed state and about 30 % strain is so unexpected that in the absence of independent corroboration it cannot be relied upon.

The extension tests were all of a similar form: after some form of preparation the samples were clamped into the jaws of a tensometer and stretched. Details of the pull rate and reciprocity differed, though Park & Baddiel [51], Dunn & Silver [52], and Silver *et al.* [54] all used strain rates in the region of 0.1 min^{-1}; Oxlund *et al.* [53] did not specify the strain rate used. The aspect ratios of the samples between grips were somewhat more variable: as width × height they were 2 mm × 10 mm–20 mm [51]; 10 mm–15 mm × more than 20 mm [52][9]; 4 mm × 5 mm [53]; and 40 mm × < 500 mm[10] [54]. These dimensions imply that most tests were almost purely uniaxial [51, 52, 54] and one somewhere between uniaxial and biaxial [53].

Skin samples for the various experiments were of varied provenance and had been subjected to various preparation routines before testing began. Park & Baddiel [51] used skin removed from pigs' ears (it is not specified whether they were living or dead), incubated it overnight at 37 °C with the dermis side in contact with trypsin, and then teased the stratum corneum away in a water bath. The

[9] Dunn & Silver only specified that the gauge length of the sample was 20 mm; the sample length was clearly greater than this, but is not specified.

[10] Silver *et al.* specified the dimensions of the sample, so the length between grips will perhaps have been 10 mm less than this. Additionally, the dimensions they did specify were extremely large, raising the question of whether they perhaps published the wrong units.

sample was then dried, punched to size, and exposed to a range of humidities during testing. Dunn & Silver [52] obtained skin from the thorax and abdomen of cadavers during autopsy. Treatment *before* autopsy was not specified, but once harvested samples were immersed in a phosphate-buffer saline solution with an antimicrobial agent and stored at 4 °C for at most seven days. Oxlund *et al.* [53] used rat skin: they anaesthetised the rat, shaved it, tattooed a grid to obtain an *in vivo* scale, then killed the rat with an overdose and cut the skin free. The sample was then placed on cardboard, damped with Ringer's solution, wrapped in plastic, frozen, then subsequently thawed in a 22 °C Ringer's solution, whereafter some were treated with elastase. Pailler-Mattéi *et al.* [41] gave no details of their sample preparation methods. Finally, Silver *et al.* procured skin samples from a tissue bank (where they had been cryopreserved), thawed them, treated them with chemicals to remove the epidermis and cellular materials, virally inactivated them, and washed, froze, and freeze dried them before hydrating them in a room temperature phosphate buffer solution before testing.

Clearly, considering the variety of ways in which skin has been prepared (in some cases including several freezing / thawing cycles) it is by no means *a priori* apparent that mechanical properties measured using them are strongly related to the equivalent *in vivo* properties.

2.2.3 Mechanical properties of the skin

Not all of the papers reviewed in §2.2.2 provided fundamental mechanical properties: in some cases the measurement was not the principal aim of the paper, and in others no attempt was made to extract them from the raw experimental data. Those in which such properties *were* extracted did not all use the same model, which makes comparison difficult. However, for the purposes of this work the principal interest is in the low strain regime in which linear elasticity is a fair approximation to most generalised models, so (where it could be extracted) Young's modulus is perhaps more useful than the results presented by the original authors. Objections of the type voiced by Wu & Cutlip [55] (that approximating nonlinear systems with linear ones is misguided) are noted, but at low strain are considered to be unhelpfully purist: the *approximation* is indeed approximate, but as variation between individuals is frequently several hundred percent this is not the greatest source of inaccuracy.

A summary of all "low strain" modulus values that could be determined from the cited literature is given in table 2.1; results that merit additional comment are described in more detail here.

The results of Hendriks *et al.* [38, 39, 40] in their three papers using an FEM based on the extended Mooney model[11] are rich in detail. They are summarised in table 2.2. The authors found that using a one-layer model the skin appeared to become *more* compliant when moving from a ⌀ 6 mm hole to a ⌀ 1 mm hole. For their two-layer model they found that they could predict the behaviour at 1 mm and 6 mm well (using a simplified model where C_{11} was always zero, thus reducing it to the incompressible neo-Hookean model) if $C_{10,\,\text{upper}} = 0.11$ kPa, $C_{10,\,\text{lower}} = 160$ kPa, but that this model was stiffer than experiment dictated at ⌀ 2 mm.

[11] The extended Mooney model is a hyperelastic model based on the strain energy $W = C_{10}(I_1 - 3) + C_{11}(I_1 - 3)(I_2 - 3)$, where C_{10} and C_{11} are constants and I_i is the ith invariant of the Left Cauchy-Green strain tensor (§2.1.5, otherwise known as the Finger strain tensor).

Author	Method	Equivalent Young's modulus at low strain / kPa				Notes
		Hypodermis	Dermis	Epidermis†	SC	
Delalleau *et al.* 2008 [34]	Suction (Cutometer), ⌀ 2 mm(?), volar forearm	100–200				It is not clear which of several proposed models was finally used.
Hendriks *et al.* 2003 [38]	Suction, ⌀6 mm, volar forearm, water present	28.8–107				—
Hendriks *et al.* 2004 [39]	Suction, ⌀1 mm–6 mm, volar forearm	66–180				Variation represents variation between aperture sizes, not between subjects.
Hendriks *et al.* 2006 [40]	Suction, ⌀1 mm–6 mm, volar forearm	132–366				Single-layer model.
		960		0.66		Two layer model. Shown division is an approximation to the authors' comments.
Pailler-Mattéi *et al.* 2007 [41]	45° Steel conical indentor, volar forearm	7–8				The reported values with and without SC are the same.
Pailler-Mattéi *et al.* 2008 [42]	⌀12.7 mm spherical steel indentor, volar forearm	2	35			Also, modulus for muscle is given as 80 kPa.
Jachowicz *et al.* 2007 [43]	Steel spherical indentors, ⌀7.9 mm–31.8 mm, face & forearm	4–33				Lower limit calculated as harmonic mean of springs.
Kwiatkowska *et al.* 2009 [37]	Steel spherical indentors, ⌀2 mm & 5 mm	30–120				Lower values go with lower forces and larger diameters.
Agache *et al.* 1980 [44]	Rotation, ⌀25 mm disc, 35 mm ID guard ring, forearm	420–850				—

Table 2.1: A summary of approximate Young's modulus values for all cited papers. Details of the methodologies are given in the main text. SC is short for stratum corneum. †The epidermis here does not include the SC. *Continues…*

Author	Method	Equivalent Young's modulus at low strain / kPa				Notes
		Hypodermis	Dermis	Epidermis	SC	
Khatyr *et al.* 2004 [47]	Tangential stretch of forearm skin, 12 mm–28 mm between grips	100–500				Overall moduli calculated as harmonic means of series springs.
Evans & Holt 2009 [48]	Tangential pull from bonded fibre, volar forearm	0.26				—
Gennisson *et al.* 2004 [50]	Sonic method interpreted using linear elasticity, forearm	9.7	1980			—
Park & Baddiel 1972 [51]	Uniaxial extension of excised SC at various humidities				6×10^3–2×10^6	Lowest value corresponds to about 100 % RH; highest to about 30 % RH.
Dunn & Silver 1983 [52]	Uniaxial extension tests of excised full thickness skin		$\lessapprox$180			Layers conjectured; modulus for <40 % strain; uncertainty due to small graph scale.
Oxlund *et al.* 1988 [53]	"Sesquiaxial"‡ extension on full thickness excised skin		~500			Harmonic mean of series springs.
	"Sesquiaxial"‡ extension on skin with no elastin		~1000			Harmonic mean of series springs.
Silver *et al.* 2002 [54]	Uniaxial extension tests on processed dermis		600–4600			Huge variation due to different strains, and young and old skin.
Pailler-Mattéi *et al.* 2007 [41]	45° Steel conical indentor, excised SC				10^5–10^6	Highest at 20 nm compression; lowest at 6 µm.

Table 2.1: *…Continued* RH stands for relative humidity. ‡The term "sesquiaxial" refers to the fact that the aspect ratio of the sample places it neither clearly in the uniaxial nor the biaxial regime. Explained further in the text.

Year of paper	Parameter	Parameter values / kPa		
		⌀1 mm	⌀2 mm	⌀6 mm
2003 [38]	C_{10}	—	—	4.7–17.8
	C_{11}	—	—	23–231
2004 [39]	C_{10}	11 ± 10	12 ± 9	30 ± 21
	C_{11}	9 ± 8	18 ± 13	500 ± 600
2006 [40]	C_{10}	22	24	61
	C_{11}	0.5	4	1400

Table 2.2: A summary of the extended Mooney parameters derived by Hendriks *et al.* in three papers [38, 39, 40]. In the first paper only a ⌀6 mm aperture was used; the values reported for the third paper refer to the single-layer model proposed there, not the two-layer version. The variation of the parameters across the range of aperture diameters is concerning.

Pailler-Matéi *et al.* [41] conducted a number of tests, but only the results on excised stratum corneum require comment. Those authors found that at 20 %–30 % relative humidity isolated stratum cornuem dropped in stiffness from 1 GPa to 100 MPa as compressive strain increased from about 0.1 % to about 40 %. This would represent strain softening on an unprecedented scale, so in the absence of independent corroboration it would be unwise to accept the result uncritically.

Kwiatkowska *et al.* [37] obtained four different moduli corresponding to two different loads (0.19 N and 0.5 N) and two different diameters of spherical indentor (2 mm and 5 mm):

$$E_{0.19\,\mathrm{N},2\,\mathrm{mm}} = 85\,\mathrm{kPa} \quad , \quad E_{0.5\,\mathrm{N},2\,\mathrm{mm}} = 120\,\mathrm{kPa}$$
$$E_{0.19\,\mathrm{N},5\,\mathrm{mm}} = 30\,\mathrm{kPa} \quad , \quad E_{0.5\,\mathrm{N},5\,\mathrm{mm}} = 76\,\mathrm{kPa}.$$

This accords with the idea that larger diameter probes are influenced by deeper layers, and so results gathered with them reflect in greater measure the more compliant subcutaneous tissue.

Jachowicz *et al.* [43] used two different models to interpret their data. In addition to a simple Hertzian analysis on the forearm (a "600 N" load gave a modulus of 7 kPa–33 kPa, and "1000 N" lead to 7 kPa–29 kPa) and face (a "600 N" load gave a modulus of 8 kPa–16 kPa), they also used a Kelvin-Voigt model (spring g_1 in series with a parallel spring-dashpot pair g_2 and η, respectively). It is clear that the loads reported in the Hertzian analysis are incorrect: in particular 100 kg over (in one case) a ⌀7.9 mm circle would have been equivalent to a heavily-built man in stilettos standing on the subjects' forearms and faces; the mistake is, perhaps, at least common, and the ratio of forces truly was 6 : 10. In the latter analysis $g_1 = 5\,\mathrm{kPa}$–$17\,\mathrm{kPa}$, $g_2 = 22\,\mathrm{kPa}$–$141\,\mathrm{kPa}$, and $\eta = 3.7\,\mathrm{Pa}\cdot\mathrm{s}$–$27.7\,\mathrm{Pa}\cdot\mathrm{s}$. This result implies that Jachowicz *et al.* found that the difference between instantaneous and final strain was a fairly small proportion of the final value.

Khatyr *et al.* [47] made measurements at four different angles to the axis of the arm (two were equivalent, so only three are referred to henceforth) and interpreted their results using a complicated model of springs and dashpots; here, the system is simplified to a Kelvin-Voigt model of a spring

in series with a parallel dashpot and spring pair. Essentially, the springs remained in proportion to each other as they varied from their stiffest (parallel to the arm axis) around to their most compliant (perpendicular to the arm axis). The time constant of the spring / dashpot pair remained essentially constant (about 1 s) at all angles.

Dunn & Silver [52] found that the elastic response of skin was extremely nonlinear, remaining quite compliant (with modulus reported in table 2.1) to about 40 % nominal strain before stiffening very considerably to about 8 MPa.

Finally, Silver *et al.* [54] gave details of the effective moduli at high and low strains, high and low strain rates, on young and old dermis, and corresponding to instantaneous response ("elastic") and delayed response ("viscoelastic"). However, in view of the questionable validity of computing Young's modulus for the viscous component of a system the details are omitted.

The range of full-thickness Young's modulus values in table 2.1 is vast, stretching from Evans & Holt's [48] full-thickness value of 0.26 kPa up to the result of Agache *et al.* [44] who reported 850 kPa, more than three orders of magnitude higher. This variation is vastly bigger than can plausibly be attributed to natural variation, and the lower end of the range is not credible: the latex rubber used in medical gloves has a modulus in the order of a few hundreds of kilopascals (§C.2), so the assertion that skin is one thousand times more compliant is absurd. Clearly other factors figure in the reported spread.

The key to understanding this spread lies in the manner in which the different skin strata act together. If they are pulled parallel to the plane of the skin then a near-uniform *tensile strain* is imposed across all strata, and the overall modulus that is observed is approximately the *arithmetic* mean of the individual tensile moduli, weighted by stratum thickness. If conversely a test involves *compression* normal to the skin surface then each layer will experience the same *stress*, resulting in an overall modulus approximately equal to the *harmonic* mean of the moduli, again weighted by the strata thicknesses. If the strata are of very different moduli then the results of these two means can be dramatically different: in the first case a very stiff but thin layer dominates; in the second case it makes little difference.

An insight can be gained by considering the stratum corneum. No estimate of the stratum corneum's stiffness put it below 6 MPa under any circumstances, with a value around 100 MPa under typical humidity conditions. In an extension test (where strains in each layer are equal) this places a surprisingly strong constraint on measured full thickness modulus. As the stratum corneum is typically around 10 µm–20 µm thick [56] it is around 0.5 % of the total skin thickness (excluding hypodermis), and as such the modulus of full thickness skin *cannot* be less than 0.5 % of the stratum corneum's modulus. Making the conservative argument that when stratum corneum remains attached to the rest of the skin it is on average 90 % hydrated the work of Park & Baddiel [51] implies its modulus would be about 20 MPa, requiring that full thickness skin has a mean modulus no less than 100 kPa.

Even this very generous estimate of the lower limit to full thickness modulus is useful. Encouragingly both *ex vivo* extension tests and *in vivo* suction tests with apertures of ⌀2 mm and smaller comply with this requirement, as does the rotational experiment of Agache *et al.* [44]. Both imply that the stratum corneum is a very significant contributor to tensile stiffness at low strains, and in some

cases the principal contributor. However, indentation results (with one exception [37]) fall substantially below this level [41, 42, 43, 37]. It is interesting that for spherical indentors the reported modulus increases as the probe diameter decreases, which suggests the aforementioned physiologically plausible explanation that larger indentors are principally "sampling" the (more compliant) subcutaneous tissues rather than the (stiffer) skin itself.

It is important to consider carefully how the results of indentation tests can so little reflect the presence of the stratum corneum. Given its stiffness and thinness it is clear that it makes little contribution by direct compression, but there are two further ways in which the stratum corneum could contribute to the indentation resistance of the skin: by direct resistance to deformation (as an elastic plate) and by acting as a stiff, tense "hammock" and supporting some load. For a uniform plate of thickness h and modulus E the deformation w and applied normal force density q are related by

$$q(x) = \tfrac{1}{12} E^* h^3 \nabla^2 \nabla^2 w(x),$$

where the differential operators are two-dimensional [57]. By scaling analysis

$$Q \sim \frac{10^{-1} E H^3 W}{L^4},$$

where the variables are replaced by corresponding scales. Substituting values corresponding to the ⌀2 mm spherical indentor of Kwiatkowska *et al.* [37] (the smallest indentor known) and erring on the side of overestimating stiffness, take $E = 10^8$ Pa, $H = 2 \times 10^{-5}$ m, $W = 5 \times 10^{-4}$ m, and $L = 10^{-3}$ m. These values lead to $Q \sim 40$ Pa, or a total force of 120 µN. By comparison with the applied loads of 0.19 N and 0.5 N this is insignificant.

Considering the "hammocking" effect, the normal force density due to this on a sphere is given by the product of the plane stress in the sheet and the curvature (§5.3.3). Considering the same experiments by Kwiatkowska *et al.* [37], curvature is 10^3 m^{-1}. Plane stress is more difficult to calculate since there is no clear fixed boundary. Noting that the modulus value used in the previous calculation was deliberately set to the higher end of likely *in vivo* average moduli, a guess at strain of 1 % is made, leading to a stress of 1 MPa. This corresponds to a plane stress of $20\,\mathrm{N \cdot m^{-1}}$, and so to a force density of 2×10^4 Pa and a total force of about 0.06 N. Since the chosen modulus is probably up to a factor of 5 too high, the strain could be up to perhaps 5 % before this limit would be exceeded. Assuming it is accurate, stratum corneum "hammocking" would account for about one-third of the load in the experiment.

The ⌀2 mm Kwiatkowska *et al.* experiment is an extreme case for indentation experiments: indentor diameters have typically been five times the linear dimensions of theirs or more. The plate deformation effect remains unimportant for all indentors, and as the "hammocking" effect scales roughly inversely with indentor diameter (whereas applied loads are typically larger for larger indentors) it will have little impact on most experiments. This explains how the stratum corneum can both dominate extension tests and tangential tests and yet have little impact on indentation tests.

Considering all of the arguments put forward, it is possible to estimate that the non-stratum corneum layers of the skin have a mean modulus in the region of 50 kPa, principally using the results of Kwiatkowska *et al.* [37] and the "hammocking" analysis above. This is clearly an approximate

figure that will vary substantially between people.

Having accounted for the difference between the results of extension and indentation tests, the only cited work that does *not* fit roughly within the proposed framework is that of Evans & Holt [48]. However, in their discussion they noted that a very similar model to theirs based on tensile test data had found a modulus about 4000 times greater than they did. Given this degree of disagreement using a similar technique it can reasonably be considered unreliable.

In summary, it must be concluded that at low strains and normal relative humidities the stratum corneum is substantially the stiffest layer of the skin, having a modulus around three orders of magnitude higher than the other layers. Due to this, at small strain it dominates extension tests but (except in the presence of tight curvatures) it is all but invisible in compression tests, which characterise some combination of the lower skin strata and the subcutaneous tissue. Suction tests that cause reasonably large surface strains are essentially extension tests of the stratum corneum. This account breaks down above about 40 % strain where the work of Dunn & Silver [52] and Silver *et al.* [54] suggests that the dermis becomes much stiffer, so (considering its substantially greater thickness) it begins to dominate extension testing. However, since the proposed reason for this stiffening is the straightening of collagen fibres (which would not occur in compression) the consequences for indentation experiments are unclear. In addition to this, skin is known to strain-rate stiffen, and appears to be adequately modelled as incompressible or quasi-incompressible. There is no clear consensus on any hyperelastic or viscoelastic model that models skin well, and no presented models have been successful across the entirety of even a modest range of forces or scales.

2.2.4 Skin surrogates

A surrogate is an object used instead of or to replace another. As such, any material co-opted as a surrogate skin must be equivalent to skin in the capacity in which it is being used. The overwhelming majority of surrogate skins have been designed to be used to imitate the biological or histological properties of skin with little or no regard for their mechanical or textural similarity. They are designed to be stable for biological testing, but are not suitable for mechanical experiments [58]. If there have been few mechanical surrogates, there have been fewer friction surrogates.

In their 2007 paper Gerhardt *et al.* [59] stated that there was not at that time a sufficiently validated skin surrogate for friction against fabrics. In that work they referred to work undertaken by some of their group and published at a similar time [60] which compared friction between skin and a standard woollen fabric with that between a selection of proposed synthetic skin surrogates and the same fabric. This work (by Derler *et al.* [60]) gathered friction data for real skin by having subjects stroke a biaxial force plate faced with the test fabric, exerting varied normal forces; whereas most work on skin surrogates (using a reciprocating, faced circular punch) was at a single load. Comparison between the data for all of the skin surrogates and the skin itself showed that a synthetic leather composed of polyamide fleece with a polyurethane coating, Lorica Soft (Lorica Sud Srl, Milan, Italy), was the closest match. They demonstrated that the coefficient of friction against the test fabric was similar to that of skin against the same fabric for normal loads from almost nothing to about 10 N. Additionally, Gerhardt *et al.* [59] noted that the mean absolute deviation from the

surface mean plane and a measure of the difference between the highest "peaks" and lowest "valleys" were similar for Lorica Soft and for young, dry, hairless skin.

Gerhardt *et al.* [36] also did some work on preparing an artificial sebum mixture to apply to Lorica Soft but they did not make substantial direct comparisons with skin, so their success is hard to assess.

Separately, two different sets of mechanical (*not* friction) skin surrogates have been found in the literature. The first set were published by Silver *et al.* [61], the second by Jachowicz *et al.* [43]. Silver's surrogates were all biological samples based on collagen; the extension test results published show good agreement between the models and the excised skin. However substituting skin and the complications and irregularities that go with it for similarly variable and awkward biological surrogates is of questionable value. Jachowicz *et al.* [43] used rubber surrogates, but the agreement between them and skin was not very close in most respects. Additionally, the *in vivo* indentation tests used by those authors conveyed little information about the skin itself (§2.2.3).

2.3 Nonwoven fabrics

The European Disposables And Nonwovens Association (EDANA) defines a nonwoven as "a sheet of fibres, continuous filaments, or chopped yarns of any nature or origin, that have been formed into a web by any means, and bonded together by any means, with the exception of weaving or knitting…" [62], subject to a few exclusions. Curiously, nonwovens are thus (as the name implies) defined by what they are *not*, leading to the inclusion of a great diversity of fabrics in the category. Only the limited class of nonwovens that are used as the top, skin-contacting layer in hygiene products (*coverstocks*) are considered here.

Having considered the methods of manufacture of nonwovens of this type and their general properties (§2.3.1), mechanical models relating the microscopic characteristics of nonwovens to macroscopic properties such as Young's modulus and Poisson ratio are reviewed. These fall into two key groups: mechanistic models (§2.3.2) and semi-computational models (§2.3.3).

2.3.1 Manufacture, and general characteristics

Manufacture of nonwovens falls into three stages [63]: *web formation*, in which pre-cut lengths of fibre (*staple*) or continuously produced fibres (*filament*) are arranged into the desired three dimensional form; *web bonding*, in which the constituent fibres are somehow entangled or fused to imbue mechanical resilience; and *finishing treatments*, in which any desired surface treatments can be applied to the nonwoven to fit it to a specific application. At each stage many different technologies exist, but the vast majority of nonwoven coverstocks are *spunbond* nonwovens; that is, nonwovens where the web is formed by the spunlaid method and bonded by thermal means [64].

Although the details of the spunlaid and thermal bonding processes are beyond the remit of this review, an outline of the processes and a brief summary of the parameters that can be adjusted will be helpful. The spunlaid process [65] starts with thermoplastic polymer chips as a material input, melts them, and extrudes fine fibres from spinnerets. These fibres are then cooled and stretched before being laid down semi-randomly on a bed. The principal parameters here are the choice of polymer (polypropylene and polyester are the most common), the diameter of the eventual fibre,

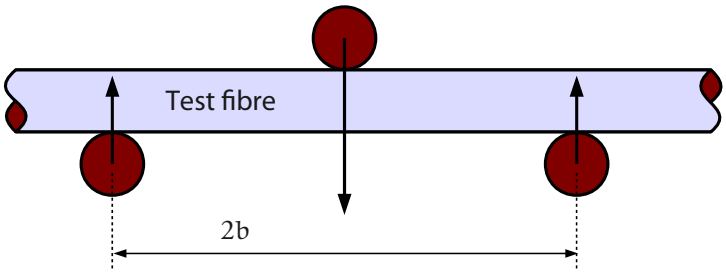

Figure 2.4: van Wyck considered contacts between fibres to be arranged as shown. The distance b is the average inter-contact distance.

and the area density with which fibre is laid down on the bed. Thermal bonding [66] simply involves passing the nonwoven web between heated rollers (either patterned or plane) which cause the thermoplastic fibres of the web to soften and bond, thereby imparting mechanical strength to (*stabilising*) it. The key variable in this process is the pattern (or absence of pattern) on the rollers: in the case of patterning, the size of the bonding points and their spatial frequency can be adjusted.

Nonwovens made using these techniques can in principle have very widely varying properties. Filament diameter can vary from 11 µm to 80 µm (with 15 µm to 50 µm most common), and area density from $10^{-2}\,\mathrm{kg}\cdot\mathrm{m}^{-2}$ to $0.8\,\mathrm{kg}\cdot\mathrm{m}^{-2}$, with the range $1.7\times10^{-2}\,\mathrm{kg}\cdot\mathrm{m}^{-2}$ to $0.18\,\mathrm{kg}\cdot\mathrm{m}^{-2}$ most common [67]. Typical tensile moduli for spunlaid and thermally bonded nonwovens used as hygiene product coverstocks are in the range 4 MPa–10 MPa [68].

2.3.2 "Mechanistic" models of nonwoven deformation

The theoretical study of the continuum mechanics of fibre beds in terms of the statistical and material properties of their constituent fibres was initiated in 1946 by van Wyck [69]. In this first paper van Wyck considered the effect of compressing an isotropically oriented bed of straight, cylindrical fibres by estimating the average distance between two successive contacts on a "test" fibre and then applying a simple "beam" formula to the deformation of this test fibre (figure 2.4). Using this approach he related compression of the fibre mass to the pressure applied, deriving the expression

$$p = K\left[\frac{1}{V^3} - \frac{1}{V_0^3}\right], \tag{2.3}$$

where p is pressure, K is an experimentally determined constant, V is the current nonwoven volume, and V_0 is the nonwoven volume when no pressure is exerted. This proved a quite remarkable fit to data [69].

Unfortunately, the model's many shortcomings meant that relating the microscopic properties of the nonwoven to the constants in equation 2.3 is essentially impossible. Examples of the grosser problems with the theory include the treatment of force as a scalar which can be shared amongst all fibre intersections in each "layer" of fibres equally irrespective of their orientation; the assumption

of perfect regularity of fibre arrangements; and the treatment of fibre intersections as though they are bonded.

After two flurries of activity in the 1970s [70, 71, 72] and another in the late 1980s and 1990s [73, 74, 75, 76, 77, 78, 79, 80, 81] the state of modelling was very much improved. Following Komori & Makishima's 1977 paper [71] all work was based on the orientation distribution of fibre segments, and following Lee & Lee's work in 1986 [73] forces were treated as vectors. Development of the probabilistic approach suffered significantly from premature averaging of quantities [73, 74] and at least one fundamental mathematical mistake [78] (described by Komori & Itoh [80]), but has been further developed so as to disallow one type of interpenetration of fibres.

Despite this substantial progress, several important issues remain outstanding.

Lack of experimental verification. After van Wyck [69] only Lee & Lee [73], Carnaby & Pan [74] and Toll [81] have both proposed a model *and* provided any corresponding experimental work. Lee & Lee's results showed their Poisson's ratio model to be very inaccurate, and their Young's modulus model to be fair for uniaxially orientated fibres, and of the right form but wrong scale for isotropically oriented fibres. Carnaby & Pan found that their similar model[12] predicted approximately the observed form for compression as a function of load, but did not include the initially more compliant behaviour that experiment showed. Toll's experimental results are not for nonwoven fabrics (his interests were in fibre reinforcement) but were fit well over a wide range by his formulae. The most recent experimental evidence on nonwovens to accompany theory was thus published in 1989 [75].

Poor tensor algebra and violation of material frame indifference. Komori & Itoh's 1991 papers [76, 77] contained a bold attempt to take models of this type and write down a strain-energy relation; from this it would be possible in principle to obtain predictions for any mechanical quantity. Unfortunately, they based their energy expression on stress and strain measures that were not energy conjugates and thus the resulting expression could not obey the principle of material frame indifference (§2.1.4). Additionally, they made many mistakes in their tensor algebra [77] including missing indices and indices appearing more than twice.

Method of calculating intersection probability flawed. In all papers found (following Komori & Makishima [71]), the method for calculating intersection density was based upon conceptually assembling the fibre bed fibre by fibre. The probability of fibre intersections has in all cases been based upon the probability of intersection of two fibres: if the model says that they would intersect, they are deemed to be crossing. Only Toll [81] and Stearn [70] were explicit about this, but all cited papers assumed it. It is clear why this has been assumed: an alternative is not immediately apparent; but it is nonetheless certainly not valid. A method more akin to the relevant method of manufacture may be more informative; that is, in the case of thin coverstocks, considering filament being extruded and falling onto the fibre already present.

Double-counting of fibre exclusion effects. Pan [78] and then Komori & Itoh [80] suggested improvements to the simple model of Komori & Makishima [71] for the probability of intersection

[12] Carnaby & Pan assumed that the "beams" by which they represented fibres were free to orient themselves as they wished, whereas Lee & Lee fixed not only the positions of the fibre "ends" but also their orientations, resulting in much stiffer behaviour.

between fibres to allow for the reduced space remaining in the nominal nonwoven volume as fibres are "added" (see previous item). Both approaches involve prohibiting the placement of a "new" fibre in particular places with respect to the existing fibres, one by determining a "forbidden length", the other by considering a "forbidden volume" within which the centre of mass of new fibres cannot be placed. These two requirements are in principle identical, but in at least one paper [80] *both* were implemented, resulting in an incorrect modification to the probabilities.

No adequate treatment of fibre slippage or non-uniform binding. Two papers [74, 75] attempted to allow for slippage at fibre contacts by assuming no slip until the tangential component of load exceeded the product of a coefficient of friction and the normal load. This approach is sensible, but the implementation is erroneous, attempting to write an inequality for vectors, mixing scalar and vector terms in a single expression, and assuming that no significant force is transmitted in any direction at slipping contacts. None of the cited papers have considered the impact of binding points such as those caused by thermal calendering or needlepunching.

Unsatisfactory treatment of curved fibres. All of the treatments cited have essentially assumed straight line fibres. The only papers to address this at all seriously were those of Komori & Itoh [80] and Toll [79]. The former defined a type of autocorrelation function and noted that if this fell to "virtually zero" at distances much larger than the intercontact distance then the fibre could be considered straight for the purposes of the analysis. Toll generated an expression for contact density that could be applied to any shape fibres, but only applied it himself to cylinders.

Stretching or straightening due to tension are ignored. The only mechanism whereby a fibre is allowed to give a force response is by bending perpendicular to its local tangent. It is reasonably argued that fibres are much less stiff in this mode than in extension, but if fibres are not straight (which they generally are not) then a tensile force will act to straighten them out, removing crimps and bends. This mechanism has been wholly overlooked in this type of model, though in the context of another class of model Kabla & Mahadevan [82] addressed it comprehensively.

A slightly different approach from that described above was mooted by Stearn in 1971 [70]. He suggested that the probability density function for the orientation of fibres ought to be transformed by making an affine approximation; that is, to scale all points in the fibre mass linearly in the direction of compression, changing a co-ordinate z to αz while leaving the other directions unchanged. He then proceeded in the "traditional" manner, but two papers by Komori and Itoh [76, 77] used the affine mapping and calculated the curvature introduced by it if the fibre lengths were to be conserved. This curvature incurred an energy cost, corresponding to the fibre mass' resistance to compression. The mathematical details were erroneous, but the approach is interesting.

2.3.3 Semi-computational model of nonwoven deformation

A different class of models has been developed more recently dealing more explicitly with the fibre mass as a network and less explicitly with the mechanical details of the interfaces. The most conservative work of this type was by Kabla & Mahadevan [82], who determined the behaviour of a single, initially tortuous fibre and then constructed what they considered to be the minimum network that

might exhibit the behaviour characteristic of the fibre mass. Chandran & Barocas took a similar but less measured approach, immediately attempting to construct a representative network and ascribing simple mechanical properties to the fibres and nodes. Head *et al.* [83] and Storm *et al.* [84] were the most network-oriented: they set up a network of fibres or polymer chains and intersection nodes based on observation of their target system, ascribed it a Hamiltonian, and then evaluated the Hamiltonian under various simulated deformations, thus enabling mechanical properties to be extracted.

This more network-oriented approach enabled Head *et al.* [83] to establish that unconstrained deformation was not affine, though the fidelity of the affine approximation depended somewhat on the scale observed. This is perhaps unsurprising in retrospect as the affine approximation essentially imposes a larger number of additional constraints on the fibre system: relaxing the constraints could not result in the system moving to a *higher* energy state, and only a very regular system might be expected to have attained the lowest energy state already. This result was corroborated by Chandran & Barocas [85] using a slightly different set of assumptions about force and torques at nodes, and other details[13], which implies that affinity is absent from irregular networks in general rather than being absent subject to the details of the fibres and nodes.

The key variable features of these types of model are the mechanical properties of the constituent fibres and nodes (encoded in the Hamiltonian, or evaluated directly), the distribution of these properties through the components of the network in the case of non-uniformity, and any constraints placed upon the network. The details of all of these vary from paper to paper depending on the specific focus, but in general the constituent fibres are penalised for stretching and bending using a linear force response (quadratic Hamiltonian term), and nodes transmit forces but not torques. The main exceptions to this were that Chandran & Barocas [85] prohibited bending and ascribed different compression and extension moduli; that Kabla & Mahadevan [82] augmented their simple arrangement with a rule intended to represent recruitment of further fibres; and that Storm *et al.* [84] claimed to disallow stretching, replacing that term with an apparently erroneous one of the same form but with extension modulus replaced by external force.

These models have been used for uniaxial extension [83, 85, 82] and shear [83, 84], but no papers have been identified which have used this type of model for compression. This contrasts with the models reported in §2.3.2 which were used almost exclusively to model compression.

By their nature none of these models provide a simple relationship between the network behaviour and the microscopic details of network layout or of the constituent fibre properties; such details could only be found by a series of simulations.

2.4 Friction

As noted in §1.1, "friction" is an umbrella term for a large number of different effects of different origins and magnitudes. Different mechanisms are dominant for different material interfaces,

[13] Chandran & Barocas stated their result in the form that enforcing affine deformation resulted in a stiffer fibre mass; by energy minimisation this is equivalent to stating that unconstrained deformation is not affine.

so historically as theories have become more descriptive of mechanisms they have split into many different families.

This section of the review starts with the earliest friction models and early theories that were proposed to explain them (§2.4.1). The specific skin-nonwoven tribosystem will then be considered (§2.4.2). Since the literature is limited in this area, the scope will then be progressively widened, first to situations involving only one of those materials (§2.4.3, §2.4.4), then to systems, models, and results that provide some insight without actually involving either material (§2.4.5–§2.4.9).

2.4.1 "Classic" friction models

Although he was certainly not the first to consider the problem, history attributes the basic law of friction to Guillaume Amontons who published in 1699 [86]. This paper is inaccessible, but Bhushan [87] reports that Amontons gave two key experimental results:

Friction is proportional to normal force. $F = \mu_* N$. Amontons apparently concluded that μ_* was always ⅓ [88], though this was soon abandoned.

Friction is independent of contact area. It is important to remember that Amontons referred to *nominal* contact area. He was presumably operating in a normal force range in which no bulk deformation of his samples was apparent.

Additionally, it was discovered in the 18th century (possibly by Coulomb) that static and dynamic friction coefficients (μ_s and μ_d, respectively) were generally different, and that the latter was roughly invariant with velocity [87]. Very little further work seems to have been done on friction in the next century.

It appears that no clear statement about the *direction* of frictional forces was made, or has been made since in relation to Amontons' law: no mention is made in a variety of good texts [89, 90, 87, 91]. It is therefore presumed that in the case of a block in motion friction acts in the opposite direction to its *velocity*, and for a static block that friction opposes the net applied *force*.

Shortly after World War Two, two models were developed that attempted to explain Amontons' law in terms of surface and material properties. Both built upon the experimentally established fact that, for metals, the true contact area between surfaces was a very small fraction of the nominal contact area [6], and assumed that frictional force was the product of contact shear strength σ and true contact area A,

$$F = \sigma A. \tag{2.4}$$

The difference between the approaches of Bowden & Tabor [89] and of Archard [92] was that the former pair invoked plastic deformation of contacts, whilst Archard assumed elasticity.

"Plastic friction". Bowden & Tabor [6, 89] asserted that friction was due to "cold welding" between *asperities* (individual microscopic outcrops from a surface which collectively constitute roughness) that had deformed plastically under the applied load. They argued that since the true contact area between metals was typically so small, almost all contacts substantially exceeded their yield stress, and spread freely by plastic flow until the contact area had increased such that local stress had reduced

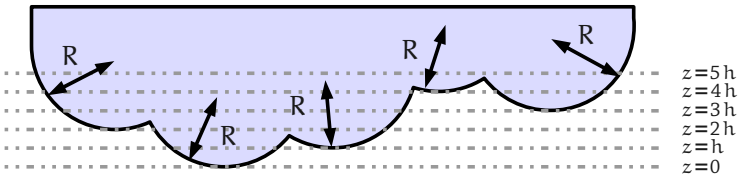

Figure 2.5: Archard's original multi contact model of 1953 (adapted from [94]). All asperities are hemispherical with radius R, and the peaks are arranged at integer multiples of a constant, h.

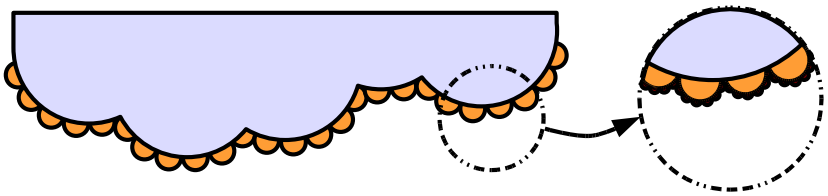

Figure 2.6: Archard's "decorated" multi contact model of 1957 (adapted from [92]). It is derived from the model shown in figure 2.5 by attaching much smaller spherical contacts to those already present, and then repeating this process indefinitely. Only the first two layers of decoration are shown.

to the yield point. This gave proportionality between normal force and contact area, which along with their model of asperity cold welding produced Amontons' law. This model gave rise to an equation for the coefficient of friction between two metals,

$$\mu = \frac{\text{shear strength of softer metal}}{\text{yield pressure of softer metal}}$$

[89] in the absence of significant work hardening. However, this did not apply well to all metals, and its applicability to other materials was very unclear. Additionally, there was no evidence of the supposed "cold welds" persisting so that they could be measured directly [93].

"Elastic friction". Archard advanced a different mechanism, partially motivated by a desire to emphasise that Amontons' law did not *necessarily* imply plastic deformation [92]. Archard demonstrated that whilst the contact area under a single spherical contact, A, varied with applied load, W, as $A \propto W^{\frac{2}{3}}$ (§2.1.6), more intricate contacts behaved differently. In an earlier paper [94] he had suggested a multi contact model (figure 2.5) which obeyed $A \propto W^{\frac{4}{5}}$, which he modified by "decorating" each asperity with smaller "sub-asperities", and then those in turn with "sub-sub-asperities", etc (figure 2.6). In the limit of infinite fine decoration, he showed that $A \propto W^{1}$.

Whilst this model was rather contrived, it demonstrated that elastic deformation could result in Amontons' law. However, the model has no quantitative predictive power as presented by Archard, as he made no attempt to relate contact area to frictional force, other than asserting a proportionality.

Both models were developed further, notably by Greenwood & Williamson [95] and Whitehouse & Archard [96]. The former authors generalised Archard's 1957 model [92] and considered a surface

as a large number of identical, independent, spherical asperities with peak heights obeying a general probability distribution. Contacts were considered to be made when a virtual "contacting surface" reached a given asperity's peak height. Asperities were assumed to deform elastically initially, and then to become plastic above a certain pressure; the transition between the two was characterised by a *plasticity index*; for common height distributions this was found by calculation to be the principal deciding factor of how an interface behaved, more important indeed than pressure. This theory brought the elastic and plastic models together quite neatly, but contains several unlikely approximations (including that the asperities are spherical, identical, and independent), and at least one omission that matters at high pressures (asperities that have "turned plastic" are still counted in the elastic sums).

Whitehouse and Archard [96] contributed a new and powerful way of considering a surface by relating it to a random signal characterised by an overall surface height distribution (*not* just for asperities) and autocorrelation function. They demonstrated that asperities could be identified and an asperity height distribution found, and that a curvature distribution could be likewise extracted. Additionally, they produced a yield criterion and a plasticity index, which they demonstrated under commonly applicable circumstances was similar to Greenwood & Williamson's [95]. However, the authors took the perplexing approach of identifying asperities by taking a three point sample *and ensuring that the three points were too far apart to be correlated*. If the samples were essentially uncorrelated then the discovery that the middle was the highest of the three merely implied that an asperity was to be found in the interval; it did *not* imply that the three points defined the asperity's shape; there may even have been *many* asperities in the interval. Indeed, the whole idea of the so-called three-point asperity (which was introduced by Greenwood & Williamson [95]) was systematically discredited by Greenwood himself in collaboration with Wu [97]. In consequence, the precise mathematical forms generated by Whitehouse & Archard [96] are flawed, though the idea behind them remains potent.

Both approaches are interesting and have been developed further in the literature (and notably both plasticity indices were derived by Tabor [98] using a beautifully simple approximate model), but since substantial development involves specialisation to a material, nothing further is of help in considering the skin-nonwoven tribosystem.

2.4.2 The skin-fabric tribosystem

The skin-fabric tribosystem has received very little attention in the literature: a recent review by Wong [99] identified only four papers which have studied friction at such interfaces. All of these (and five more recent papers by Gwosdow *et al.* [100], Derler *et al.* [60], Cottenden *et al.* [1], and Gerhardt *et al.* [35, 36]) are primarily experimental in nature and have studied various aspects of skin-fabric friction, including the effects of hydration; applicability of Amontons' law in terms of independence of μ of normal force and velocity; the effect of ageing and gender; and the relationship between surface properties and friction.

Five of these nine papers used an "experimenter-controlled linear pull" technique, in which a linear force is applied to cause one surface to slide over the other. Kenins [101] and Cottenden *et al.* [1] employed a "curved pull" variant of this technique, using automated tensometer devices to pull

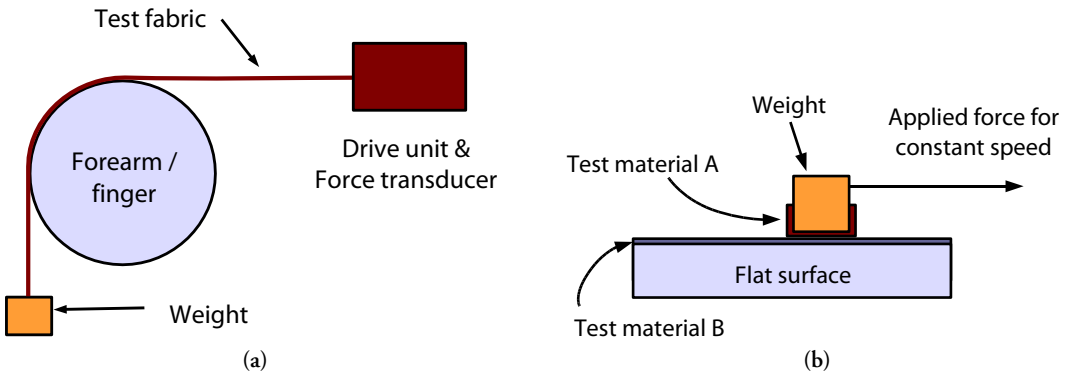

Figure 2.7: Variations of the "straight pull" method used by skin-fabric investigators. (a) Kenins [101] and Cottenden *et al.* [1] used mechanical devices to pull a test fabric around an appendage and measure the force. (b) Hong *et al.* [102] and Comaish & Bottoms [103] pulled over a flat surface. Hong measured force with a load cell in the flat surface, whilst Comaish & Bottoms used the known value of deadweights.

strips of fabric with weights on one end around the forearm (Kenins, Cottenden *et al.*) or index finger (Kenins) at a constant rate, and measured the force required to do so (figure 2.7a). Gwosdow *et al.* [100] also used the curved pull technique, but with a hand-held spring balance rather than a tensometer. Hong *et al.* [102] and Comaish & Bottoms [103] used a "flat pull" variant, pulling a weighted sled across the flat (figure 2.7b): Hong faced his sled with sheepskin and the flat surface with various nonwovens; Comaish & Bottoms used excised skin or living skin as the flat surface and faced their slider with knitted fabrics or polymer sheet. In addition to their "curved" experiments, Cottenden *et al.* [1] also used a variant of this "flat pull", using a PTFE disc and weights to load a region of a nonwoven strip as it was dragged over the forearm.

Derler *et al.* [60] and the two papers of Gerhardt *et al.* [35, 36] used a "subject-controlled linear pull" in which a test subject drew a finger (Derler *et al.*) or a volar forearm (Gerhardt *et al.*) across a force plate faced with the counter surface of interest. The force plate measured both normal and tangential components of force, enabling instantaneous effective friction coefficients to be extracted. However, neither the normal force nor the stroke length could be controlled using this method.

In contrast to other work, Zhang & Mak [104] used a flat *rotating* disc faced with fabric and applied directly to skin. The complex stress fields and buckling caused by this technique make the results difficult to interpret.

The three authors who made use of a curved pull could not extract coefficients of friction so easily as those who used a flat pull, as the normal force varied around the contact. Kenins [101] recognised this and did not attempt to extract coefficients of friction, while Gwosdow *et al.* [100] and Cottenden *et al.* [1] used a well-known equation [105] to extract μ from their force data assuming Amontons' law and that the arm was a rigid cylinder:

$$\mu = \frac{1}{\Theta} \log \left[\frac{F}{mg} \right], \tag{2.5}$$

where F was the force applied during or at slip, mg was the applied load, and Θ was the total arc of contact. This equation is valid for rigid cylinders provided Amontons' law holds. Howell [106] produced a generalised solution applicable to any interface that obeyed a power-law-based friction relationship, but this has not been used in the skin-nonwoven friction literature. Separately, it was shown by Cottenden *et al.* [107] that, assuming Amontons' law, equation 2.5 is valid for any convex prism[14], thus explaining why their previous paper [1] had found such close numerical agreement between coefficients of friction calculated with equation 2.5 and those derived from their flat pull measurements.

With regards to Amontons' law, a close inspection of these papers reveals that none of them presented compelling evidence that μ varied with either normal load *or* velocity for skin-fabric systems. Comaish & Bottoms [103] only presented load results for polyethythene sheet against the skin; Zhang & Mak [104] reported load and velocity data for all of their test materials, but did not say which was which; and Cottenden *et al.* [1] found no disagreement with Amontons' law in terms of load in their curved pull experiment, but the experiment was very insensitive to variation of μ at the low end of their 0.36 kPa–2.23 kPa pressure range. The flat pull experiments of Cottenden *et al.* provided fair corroboration of Amontons' law, though the normal load was varied by less than a factor of ten and only took four values. Derler *et al.* provided a graph of coefficient of friction against normal load for both "dry" and "wet" skin; by virtue of their subject-controlled, *in vivo* technique their data suffered from very substantial scatter, but suggested that μ was constant for "dry" skin and increased at low loads for "wet" skin. However, it appears that the principal justification for fitting the chosen "wet" skin curve was a large number of data points at essentially zero normal force, which ought to be treated with extreme caution given the sensitivity of coefficients of friction in this region to error in normal force measurements. As a body, these papers *suggest* that Amontons' law may break down for the skin-fabric system at low pressure (especially for wet skin), but the matter is far from proven.

A number of relationships between skin condition and properties and friction have been noted. All investigators who studied it reported that the coefficient of friction between skin and their fabrics increased with hydration, though since they all used different methods to achieve and measure different levels of hydration little more can be said on this. Gerhardt *et al.* [36] found that the friction coefficient for a given fabric against equivalent skin regions on different individuals was essentially independent of age and gender[15], in spite of the very substantial differences to the mechanical properties of skin that age wrought. Kenins [101] commented that the "hairiness" of fabrics made little difference to their coefficients of friction by comparison with changes due to humidity; other researchers made no comment on the effect of surface properties on μ.

Reported relationships between mechanical properties and friction are especially significant. Gerhardt *et al.* [35] reported from their results that there was no correlation between any measured vis-

[14]This conclusion is subject to an appropriate choice of co-ordinate centre. However, such a choice is a fairly natural one, and that which had serendipitously been made in their earlier work.

[15]These authors found that the proportional increase in coefficients of friction between "normal" skin and fully hydrated skin was greater in women than in men, but although it was claimed to be "significant", it is not apparent that this significance extends beyond the formal, statistical sense of the word.

coelastic skin property and friction coefficient (though the "properties" were somewhat impure[16] Courage & Khazaka Corneometer results), and thus concluded that adhesion was the principal friction mechanism, an argument that carries some conviction within the parameter ranges they explored. However, some of the same authors [36] later modified this conclusion on the basis of a somewhat more qualitative argument, suggesting that for older people deformation losses become important. The assertion of the dominance of adhesion in skin-fabric friction is repeated in several other cited papers, but without adding evidence, and (where citations are given) by reference to friction between skin and another material, or indeed without reference to skin at all.

2.4.3 Other tribosystems involving the skin

Given the paucity of work on the exact tribosystem of interest, related systems must be considered. If the scope is widened to include work on skin-X systems, then a little more work presents itself. However, it is not universally appreciated that frictional forces depend upon *both* of the surfaces in contact, and so some authors claim wider applicability for their or others' work than is valid. Nonetheless, several useful results and ideas can be gleaned from the literature in this area.

Considerable work has been done to establish whether various skin-X tribosystems obey Amontons' law with respect to velocity and normal loading. The non-skin surfaces, experimental approaches, and friction types considered are summarised in table 2.3. Many authors found static [103, 109, 112, 114] and dynamic [109, 108, 110, 111, 112, 113, 114] friction coefficients to increase at low loading or in general as load reduced, but this was not always found in all circumstances: Johnson *et al.* [108] found this result for wet skin and not for dry skin, a result corroborated by many of the same authors [114] using a very similar technique; Tang *et al.* [115] found the coefficient of dynamic friction *increased* as normal force increased. A fascinating meta-analysis by Tomlinson *et al.* [117] collated some results cited here and some others into a single graph of friction against normal force[17]. This showed that a best-fit line through a log-log graph of all the data over five orders of magnitude in normal force had a gradient of 1.05; that is, they were fit by Amontons' law to remarkable fidelity. It should be noted that this conclusion was not shared by the majority of the authors from whom the data were taken.

It is frequently claimed that adhesion is a major cause of friction against skin [26, 41, 60, 114, 35, 116]; indeed, some authors claim it is the *only* significant contributor. The former assertion finds strong support in experimental evidence from the literature; in most circumstances and for most facing surfaces, the latter does not. The most direct evidence found for the importance of adhesion for at least some skin-X friction is the work of Pailler-Mattéi *et al.* [41] in which the stratum corneum was progressively tape-stripped, and adhesion and friction (measured independently) against a smooth steel sphere with ⌀12.5 mm were found to follow the same highly nonlinear pattern. It is important to note that this work involved the application of a very small force (15 mN) to a reasonably large, spherical indentor, presumably leading to very little deformation.

[16] In common with many Courage & Khazaka instruments, the Corneometer—a capacitive tool for measuring skin hydration—reports its results in arbitrary units that may not be linear in the nominally measured quantity.

[17] Clearly the aggregation of data gathered using different techniques and in different circumstances is open to considerable criticism, but allowing that the results remain interesting.

Author	Probe	Motion type	Load / N	Speed / $mm \cdot s^{-1}$	Conclusion	Notes
Comaish [103]	Various polymer sheets and textiles fixed to a round-edged flat (~⌀ 28 mm–35 mm)	Linear pull	0.03–10	—	μ_s increases for $P \lessapprox 2$ N for skin-polythene.	—
Johnson [108]	Glass sphere segment (⌀ 16 mm)	Linear, reciprocating action	0.05–1	0.25–50	$\mu_d \propto\sim P^{-0.06}, V^{0.05}$ when dry; $\mu_d \propto\sim P^{-0.15}, V^{-0.29}$ when wet.	Water and other lubricants used, as well as dry skin.
El-Shimi [109]	Stainless steel hemisphere (⌀ 12 mm)	Rotating head	~0.2–2?	0.06 Hz–9.7 Hz[†]	$\mu \propto P^a$, where a is between -0.33 and -0.04, and independent of speed.	The method of extracting friction *forces* is questionable.
Nakajima [110]	Gold plated aluminium hemicylinder (⌀ 20 mm, 20 mm long)	Linear pull?	3×10^{-2}–0.11?	3.5?	μ increases for $P < 5 \times 10^{-2}$ N. NB F-P graph would not intersect origin.	The experimental method is unclear.
Bobjer [111]	Textured polycarbonate surface	Interactive	1–20	45–55	Difference in textures has no significant effect on μ_d	"Subject controlled linear pull" (§2.4.2).
Koudine [112]	Glass sphere segment (⌀ unspecified)	Linear pull?	2×10^{-2}–0.8	0.125	$\mu_s \propto P^{-0.55}$, $\mu_d \propto P^{-0.28}$, the latter suggesting dominant adhesion.	—
Sivamani [113]	Stainless steel sphere (⌀ 10 mm)	Linear	5×10^{-2}–0.45	0.083	$\mu_d \propto P^{-0.32}$ suggests Hertzian contact and mainly adhesive friction.	Skin was hydrated in various ways, but none were adequately described.

Table 2.3: A summary of the methods used to investigate the applicability of Amontons' law to the skin-X tribosystem. In this table F is friction force, P applied normal load, V velocity, and SC stands for stratum corneum. Most authors measured dynamic friction; Comaish & Bottoms [103] measured *only* static friction; El-Shimi [109], Koudine *et al.* [112], Adams *et al.* [114], and Pailler-Mattéi *et al.* [41] measured both static and dynamic fiction. [†]As the probe had contact from the centre of rotation to the periphery no meaningful linear velocity can be given. *Continues…*

Author	Probe	Motion type	Force / N	Speed / $mm \cdot s^{-1}$	Conclusion	Notes
Adams [114]	Glass sphere segments (⌀15.6 mm, 41.4 mm), polypropylene hemisphere (⌀40.4 mm)	Linear, reciprocating action	10^{-2}–4	8	$\mu_d \propto (P + \alpha)^{0.02}$ when dry; $\mu_d \propto (P - \alpha)^{-0.15}$ when wet‡.	Method of hydration is insufficient to produce deep hydration of the SC.
Pailler-Mattéi [41]	Diamond sphere (⌀ 15.6 µm); smooth steel sphere (⌀12.5 mm)	Linear?; ?	10^{-5}–10^{-3}; 0.015	10^{-3}; 0.4	Friction and adhesion followed similar curves as SC was stripped	The first test was on excised SC, the second on volar forearm.
Tang [115]	Polypropylene sphere (⌀ 10 mm)	Linear	0.1–0.9	0.5–4	μ_d *increased* from 0.38 to 0.50 as load (and indentation) increased, implicating deformation friction	Indentation was so large that the hypodermis principally determined mechanical properties.
Kwiatkowska [37]	Smooth steel spheres (⌀ 2 mm, 5 mm)	Linear, reciprocating action	0.19 and 0.5	16	Deformation does not make a significant contribution	The throw of the experiment was less than twice the distance skin deformed before slipping.
Hendriks [116]	Variously finished metallic and polymeric annuli	Rotating head	0.625	100 (at periphery)	Between 0.1 µm and 10 µm friction decreased with roughness, suggesting adhesion.	Humidity and skin wetness were varied; results inconclusive.

Table 2.3: …*Continued* ‡These results are for the polypropylene hemisphere; those for the glass sliders are similar.

Another reasonably direct argument for the importance of adhesion is the influence of surface roughness. Both of the "classic" theories of adhesion (JKR and DMT—§2.1.6) assume very short[18] or zero range adhesive forces: it is universally accepted that adhesion requires intimate contact between surfaces, so adhesion between two candidate surfaces must be strongly dependent upon their surface roughnesses. El-Shimi [109] made a somewhat parenthetic comment on the difference in frictional torque between a "polished" indentor and one which had been roughened with emery paper, noting that the friction associated with the polished probe was significantly larger. Unfortunately no quantitative data on the differences between the indentors or the friction torques associated with them are given. The results of Bobjer *et al.* [111] are more difficult to interpret. They found the same as El-Shimi for "normal" skin, the reverse for "greasy" skin, and still differently for "sweaty" skin, and also that the details of the texture of a polycarbonate sample only affected the coefficient of dynamic friction if the skin was "greasy" or "wet". Nakajima & Narasaka [110] reported that coefficients of friction were inversely proportional to the number of "domains" (bounded by fine lines or wrinkles) on the skin; that is, friction was directly proportional to the area of uninterrupted smooth skin. Both El-Shimi's [109] and Nakajima & Narasaka's [110] results provide circumstantial evidence of the importance of adhesion in friction of rigid sliders against skin.

Hendriks & Franklin [116] made the effect of surface roughness the sole subject of their work, and produced substantial quantitative data. Whilst the rotating annulus equipment that they used gives rise to complicated force fields and their model for extracting the coefficient of friction is certainly over-simplified, the quantity which they designate μ is almost certainly at least strongly correlated with the true coefficient of friction. Their chosen counter materials were a selection of aluminium alloys and polymers with surface roughnesses[19] varying from 90 nm up to 11.5 µm, all of which (other than PTFE and polyphenyleneoxide) had surface energies between $32\,\mathrm{mN \cdot m^{-1}}$ and $36.5\,\mathrm{mN \cdot m^{-1}}$. They found that friction coefficient was a strong, reducing function of surface roughness on (relatively smooth) forearm skin, but that the relationship was much less certain on cheek skin, a fact that Hendriks & Franklin attributed to the confounding presence of beard hairs (nine out of ten of the subjects were men). Both the strong correlation with roughness on the forearm and the weaker correlation on the cheek are consistent with adhesion dominating friction in these circumstances. Further, the only surface which did not follow the expected trend based purely upon its surface roughness—that is, which showed behaviour peculiar to the material from which it was made—was PTFE, a material notably difficult to bond to anything. This also suggests that surface energy was important, but that features such as Young's modulus or shear strength (which vary widely between aluminium alloys and the polymers used) were not, and thus that adhesion was dominant. Though the experiment was designed to eliminate viscoelastic dissipation so far as possible (thus emphasising other mechanisms) this result remains strongly supportive of the relevance of adhesion in skin-X friction.

A more common and abstracted argument for the importance of adhesion revolves around the proportionality of friction and measured nominal contact area [26, 112, 113]. The usual presen-

[18] Describing the range of the adhesion forces invoked by DMT as "short" may appear inconsistent with their description in §2.1.6 as "long" range. However, which word is appropriate depends on the scale to which they are being compared: in the former case zero-range forces; here potentially substantial surface roughness.

[19] Roughness is defined as the arithmetic mean of the absolute deviation of a surface from its mean plane.

tation involves asserting that the true contact area at the skin-X interface is proportional to the nominal contact area; predicting the variation of the nominal contact area with applied force using a linear elastic model (often Hertz's for a sphere); and comparing the resultant power law with a power law fit to the data. Wolfram [26] presented this argument influentially in a review article in 1983, essentially in the above form; Johnson *et al.* [108] presented a more nuanced version in which they observed that Archard's work [94, 92] had shown that pure geometry could result in true contact area varying with applied force raised to any index between ⅔ and 1. Wolfram interpreted El-Shimi's results [109] to support adhesion using this argument; Koudine *et al.* [112] observed the similarity between their results and this argument but did not explicitly claim it as proof of adhesive dominance; and Sivamani *et al.* [113] referred to Wolfram's theory, noted it fit their results well, and failed to draw any conclusion at all.

A variant of this adhesion argument has been proposed by Johnson *et al.* [108], Adams *et al.* [114], and Hendriks & Franklin [116] in which the adhesive shear strength per unit area is not taken to be constant, but rather to vary linearly with pressure. Johnson *et al.* [108] defended this with an unlikely association of stratum corneum with glassy polymers; Adams *et al.* [114] and Hendriks & Franklin [116] used a more defensible appeal to experimental results relating to counter surfaces covered in a thin organic film. Irrespective of the justification, the result of the ansatz is the addition of a constant to the load-varying expression for coefficient of friction. Adams *et al.* [114] showed the resultant equation to fit their data very well.

The latter arguments provide justification for ascribing essentially any sublinear dependence of friction on normal load to adhesion, but this is so imprecise a prediction that conclusions reached on the basis of it cannot be relied upon. However, the work on roughness and the work of Pailler-Mattéi *et al.* [41] *are* compelling evidence that adhesion in very important or indeed dominant against rigid, smooth surfaces for small deformations.

Of the two terms that Bowden & Tabor [89] initially recognised as contributors to friction, their "shearing term" corresponds to the adhesion discussed above. Several authors have searched for evidence of their "ploughing" term (corresponding to permanent plastic deformation of one surface by asperities in the other) in the skin-X class of tribosystems. El-Shimi [109] and Nakajima & Narasaka [110] both looked for evidence of ploughing in the tribosystems that they investigated (table 2.3), El-Shimi with a scanning electron microscope, and Nakajima & Narasaka by undisclosed methods. Neither found any evidence of ploughing, which ruled out large scale plastic deformation as a source of friction in these systems. However, neither paper specified the length of time for which the skin relaxed between friction testing and scanning, so "viscoelastic ploughing" cannot be ruled out on the basis of these results.

Viscoelastic dissipation has been considered by a number of authors who have reached various conclusions as to its relevance. Various theories of viscoelastic dissipation or hystertic friction are considered in detail in §2.4.5; only their application to skin is considered here. All of Johnson *et al.* [108], Zahouani *et al.* [27], Adams *et al.* [114], and Kwiatkowska *et al.* [37] reproduced a calculation of Greenwood & Tabor [7] for a simple model of friction. Zahouani *et al.* [27] did little with the result, but each of Johnson *et al.* [108], Adams *et al.* [114], and Kwiatkowska *et al.* [37] used the model to estimate the contribution of viscous dissipation to the overall coefficient

of friction: the first authors predicted a contribution of 0.05 at a load of 0.2 N (the contribution increases with load); the second obtained 0.04; and the last found results from 0.04–0.06 from their various experiments. In all cases this calculated viscoelastic contribution was much smaller than the measured total friction. All were nominally similar experiments involving essentially rigid spheres: Johnson *et al.* [108] and Adams *et al.* [114] used spheres with diameters in the tens of millimetres with substantial run lengths; Kwiatkowska *et al.* [37] used spheres five to ten times smaller and a very short run length. The short run length is a serious weakness of that work in this context: since there was no sliding for the first two thirds of the throw the data have little to say on dynamic friction.

All of these models are open to all of the criticisms levelled at the original Greenwood & Tabor model, as reported in §2.4.5.

A similar but very crude model based on (apparently unobserved) plastic ploughing has been advanced by Tang *et al.* [115] in an attempt to explain their result[20] that $\mu \propto P^{0.11}$. Whilst the model is unlikely, their data are the only ones reported in all the work cited here for which an index greater than zero was found.

It is possible to bring all of these results into a single, qualitative picture by considering the structure of the skin, and in particular the relative stiffnesses of the stratum corneum and the lower layers (§2.2.3). It has been established that the stratum corneum is much the stiffest layer of the skin in essentially all circumstances, but that as it is very thin its impact on gross deformation under compression is in most cases negligible. However, as it constitutes the outermost layer of the skin it is responsible for intimate contact. Considering the stratum corneum as a stiff, rough surface, it is possible to explain obedience to Amontons' law at high forces and proportionality to nominal contact area at low ones. At low forces the stratum corneum roughness is essentially rigid but the lower skin and subcutaneous layers are not: the applied load can be more easily supported by increasing the nominal contact area than by deforming the stratum corneum roughness, so intimate contact per unit nominal area remains constant as the nominal area increases. At high loads the stratum corneum deforms just as any other rough surface would, restoring Amontons' law. Increased hydration is known to reduce the stiffness of the stratum corneum by orders of magnitude (§2.2.3), but although this might naïvely be expected to lower the pressure required for transition from nominal contact dependence to Amontons' law, if the softening proceeds so far as to enable stratum corneum texture to be almost entirely flattened by very moderate pressures the result may in fact be the converse: friction would essentially *always* be found to depend on nominal contact area.

This proposed model has both the benefit and drawback that essentially all of the results reported and many others could be accommodated in principle, and the additional data that would be required to prove or disprove it (for example, contact pressure for each friction result, profilometry of the skin, measurement of nominal and true contact area, etc.) are in no cases provided.

Various other observations have been made by different authors. Johnson *et al.* [108] found that μ_d for wet skin (though not dry skin) in contact with a glass lens increased sharply as velocity decreased; El-Shimi [109] concurred for dry skin and made no measurements for wet skin. It has been widely reported (as for the skin-fabric system) that both coefficients of friction increased when the

[20] Tang *et al.* in fact fit a third order polynomial to their data. Their reasons for the use of such an apparently unlikely function are not clear, but a power law fit to their reported cubic is close ($R^2 = 0.99$) and has the reported index.

Author	Materials	μ_d or μ_s	Pressure / Pa	Velocity / mm · min^{-1}
Wilson [118]	w/w	μ_d	19.6–29000	~1500
Carr [119]	w/w	Both	345–34500	?
Ajayi [120, 121]	w/w	Both	63	50–5000
Hosseini-Ravandi [122]	Perspex/w	μ_d	924	20
Virto [123]	Steel/w	μ_d	2000–14000	20–100
Jeddi [124]	?/w	Both	95	50
Ramkumar [126]	Steel/nw	Both	200–450	?
Ramkumar [125]	?/w	μ_d	177–422	100–1000
Ramkumar [127]	Steel/nw	Both	195–440	100–1000
Hermann [129]	w/w?	μ_d	194–439	250–1000
Wang [128]	Al/nw	Both	280–24700	? - known to vary

Table 2.4: A summary of the methods used to investigate friction in the fabric-X tribosystem. In this table, "w" stands for a woven fabric, and "nw" for a nonwoven.

skin was hydrated [26, 108, 27, 113, 114], and thus often attributed to softening and a subsequent increase in contact area.

2.4.4 Other tribosystems involving fabrics

Having considered the tribology of the skin-X interface, fabrics in contact with other materials are now reviewed. Most work has related to woven fabrics [118, 119, 120, 121, 122, 123, 124, 125], with much less on nonwovens [126, 127, 128]. A variety of surfaces, pressure ranges, and velocity ranges have been used (summarised in table 2.4), but all except Wilson[21] [118] used a straight pull flat bed experimental design (figure 2.7b).

The main themes of fabric-X interface friction research have been the testing and modification of Amontons' law; studying the relationship between structure and friction (mostly for woven fabrics); and an attempt to derive a friction model from first principles. These are detailed below.

In 1963, Wilson [118] carried out an impressive set of experiments on the friction between similar and dissimilar woven fabrics. The results (corresponding to normal pressures varying over three orders of magnitude—table 2.4) were fit quite poorly by Amontons' law, which led Wilson to propose an alternative empirical friction law:

$$F = \exp(C)p^n \qquad \Leftrightarrow \qquad \log(F) = C + n\log(p), \tag{2.6}$$

where F is the frictional force, p is applied pressure, and C and n are constants characteristic of the interface. This model has been found to fit both fabric-fabric and fabric-metal static and dynamic

[21] Wilson's experiment involved a rotating armature with a small flat pad on the end. Though not a linear experiment, the large radius of the armature relative to the pad size suggests that there would be little discrepancy between Wilson's results and corresponding ones obtained with a linear experiment.

friction data very well by a number of authors [118, 119, 120, 125, 127, 128], though none have attempted to apply it over such a wide pressure range as Wilson himself did. Though more commonly applied to woven fabrics, both Ramkumar *et al.* [125, 127] and Wang [128] have applied Wilson's model to nonwovens. However, data from neither of Ramkumar's papers deviate from Amontons' law by more than experimental error in the very small pressure range used, so only Wang's work [128] can truly be said to support Wilson's model for nonwovens.

It should be noted that there has been some considerable confusion with regards to the friction characteristics C and n. Wilson [118] and Carr [119] both found that C and n (as defined in equation 2.6) were approximately inversely related, which prompted Ramkumar [126] to attempt to unify them into one single constant. However, whether intentionally or not, he defined a constant $C_R := \exp(C)$ but *continued to call it* C. This has caused confusion in at least one paper [128]. Ramkumar's subsequent definition [126] of $R := C_R/n$ as a single friction measure is apparently without foundation.

The results of five authors who measured friction at a variety of velocities are inconclusive. One did not report results [125]; one found a peak for all test fabrics at $\sim 500\,\mathrm{mm \cdot min^{-1}}$ (though few velocities were tested in this region) [127]; one found a peak at $\sim 400\,\mathrm{mm \cdot min^{-1}}$ for the single fabric tested (the results presented for static friction at various speeds are of unclear significance) [129]; one found that friction reduced with velocity (though on *very* limited data) [123]; and the last found an inverse relationship between friction and velocity for *most* fabrics, but not all [120]. No clear conclusions can be reached on this point.

Work has been done both on relating observed structures in woven fabrics to friction [121, 122, 124], and on the more abstract relationship between nonwoven machine parameters and the nonwovens' consequent frictional properties [126, 128].

For the former, the first connection noted was positive correlation between friction and the spatial frequency of fibres [121]. Further work confirmed some connection between weave pattern and frictional force by establishing that some spikes in power-frequency spectra obtained by Fourier transform of friction-time data coincided with the spatial frequencies of features of the weave [122]. However, many peaks in the spectra, including the largest, did not correspond to any known feature. In the most ambitious attempt to date to relate structure and friction, Jeddi *et al.* [124] found a fair correlation (on very limited sample data) between the difference between static and dynamic friction force and a quantity that they termed "fabric-structural-asperity index" (FSAI), which was calculated from the weave structure. However, they presented no compelling argument in favour of their method of calculating it, and no experimental data that showed its universality.

The experiments relating machine parameters to friction for nonwovens are sparse, and somewhat mixed. The experiment of Ramkumar & Roedel [126] which investigated the effect of needling speed on friction properties was rather impure: they varied needling speed, but did not say whether they kept the time of needling or the total number of strokes constant. The analysis was bizarre, and their conclusions lacked strong support from their data. Wang *et al.* [128] made a careful study of the impact of air speed and thermal bonding temperature and time on the frictional properties of a through-air thermal bonded nonwoven. They found that air speed was unimportant, but that both static and dynamic friction increased with bonding time and temperature, though the effects were

relatively small. No explanation was offered.

Virto & Naik [123] attempted to derive an expression for μ_d in fabrics by considering ploughing and asperity shear. However, they presented no evidence that either process occurred in such materials. Several parts of their analysis seem unlikely, for instance attributing asperity shear strength to molecular van der Waals forces rather than, for example, mechanical interlocking. Whilst interesting, and the only known example of a first principles friction expression derived for fabrics, it seems unlikely that Virto & Naik's approach will succeed.

2.4.5 Hysteresis theories

Hysteresis theories of friction were originally developed to describe rubber-[rigid material] interfaces. All such theories are fundamentally based on the fact that, by definition, viscoelastic materials dissipate energy when strained at finite speeds [130]. The first such theory was developed by Greenwood & Tabor [7] to explain experimental results for a well-lubricated system, and consisted of the application of Hertz's deformation model and the generalisations of it (§2.1.6) to steel sliders of various shapes dragged across a rubber surface at several metres per second. Greenwood & Tabor's approach was to calculate the pressure under the slider, and thus the work done by the "front" half to move forwards a little. Having assumed that a fraction α of this work was never recovered at the rear, the frictional work done and thus the force were easily determined.

This model has been criticised by Moore & Geyer [131] as self-contradictory: using Hertz's model or any of its descendants implies acceptance of linear elastic properties, and so it is incompatible with any viscosity. For instance, the degree of deformation will generally depend on velocity for a viscoelastic material, which was not reflected in Greenwood & Tabor's [7] model. Additionally, the model invokes Hertzian deformation in the presence of friction, which is not valid (§2.1.6).

An alternative approach pursued by several authors was to assume that viscoelastic materials consist of an array of individual, unconnected linear Voigt elements (figure 2.8) and then consider the passage of the viscoelastic material over a rigid counterpart [132, 133, 131]. Flom & Bueche [132] considered a rigid sphere rolling (or non-adhesively sliding) over a viscoelastic plane; Norman [133] considered a similar situation involving a cylinder; Reiger [134] (German language, reviewed by Moore & Geyer [131]) considered a viscoelastic plane passing over a one-dimensional, sinusoidal, rigid substrate.

All of these authors considered the asymmetry introduced by a moving rigid object across a viscoelastic material (figure 2.9), calculating the loss of contact on either side by considering where the intersurface pressure was zero. Since this asymmetry effect varies with velocity, ignoring it qualitatively changes the friction force obtained [131].

However, all of these models suffer from two significant shortcomings. The first is that there is no reason to assume a Voigt model of viscoelasticity. The second, more serious problem is that they all assume that the forces and displacements at different locations in the viscoelastic material are independent: they take no account of shear forces. Since this is the case, they systematically overestimate the deformation caused by a given imposed force, and the pressure distribution does not reduce to the Hertzian one (or equivalent) in the static case, as it should. The disagreement is

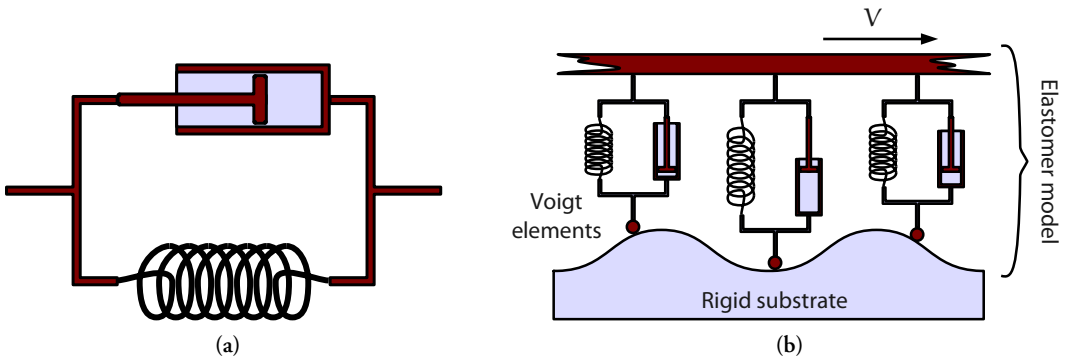

Figure 2.8: A common model of viscoelasticity. (a) The basic Voigt viscoelastic unit consists of a dashpot of viscosity η (obeying $F = \eta\dot{x}$) and a spring with constant k in parallel, producing a force $F = kx + \eta\dot{x}$ for a displacement x. (b) An example of the model adopted by several authors. In this case, the viscoelastic model is moving over a sinusoidal, rigid substrate, as considered by Reiger [134]. Essentially the same model was adopted by others, with differently shaped rigid surfaces.

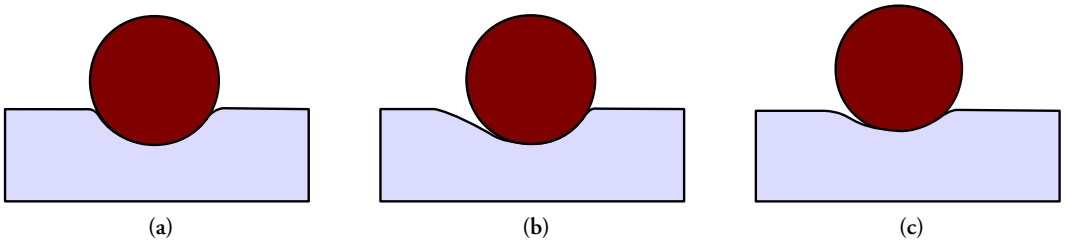

Figure 2.9: Asymmetry induced in a contact by motion. (a) When the cylinder is stationary the contact is symmetric. (b) At low speeds the contact becomes slightly asymmetric. (c) At very high speeds the asymmetry reduces again as the deformation reduces [131].

slight in the case of small deformations (as noted by Norman [133]), but invalidates the models for larger deformations.

A much more recent model due to Persson [135] addressed the second problem comprehensively: a complete small-deformation solution for contact in a linear elastic half-space which exhibits rate-dependent stiffness (according to the Maxwell-Voigt viscoelastic model) was given. This was used to compute the energy dissipated by sliding against a fairly general surface, subject to the assumption that only normal forces made any significant contribution. Persson also dealt neatly with non-perfect contact due to the finite response time of viscous systems. This work has been developed further along similar lines by others, notably Müser [136]. However, as these solutions became very intricate whilst continuing to ignore horizontal forces (the sole consideration of which—by Greenwood & Tabor [7]—gave rise to good agreement with experiment) it is questionable whether, for all their mathematical elegance, they correspond to the mechanisms which truly dominate.

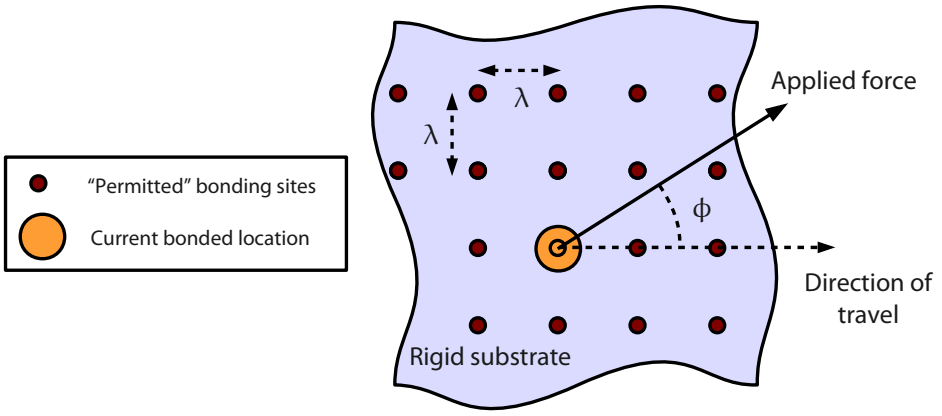

Figure 2.10: The physical model assumed in the basic rate theories of Schallamach [138] and Bartenev (see [137]).

2.4.6 Rate theories

The term "rate theories" was used by Moore & Geyer [137] to describe a class of theories in which motion arose by means of thermal excitation overcoming an asymmetric, often periodic potential. In the basic model (due to Schallamach [138] and Bartenev (inaccessible, reported by Moore & Geyer [137])) it was assumed that certain sites on an interface are possible bonding points, and that these are separated by energy barriers of height E (figure 2.10). This surface potential was then modified by an applied linear potential (corresponding to a uniform force) so that the energy barrier between two sites i and j became

$$E - \delta E = E - \lambda \mathbf{F} \cdot \widehat{(\mathbf{x}_j - \mathbf{x}_i)},$$

where $\mathbf{F}$ is the applied force, λ is the intersite distance, and $\widehat{(\mathbf{x}_j - \mathbf{x}_i)}$ is a unit vector in the direction of travel. Consideration of a Boltzmann factor led both authors to propose that

$$V = V_0 \exp\left[-\frac{E - \lambda \mathbf{F} \cdot \widehat{(\mathbf{x}_j - \mathbf{x}_i)}}{k_B T}\right],$$

where V is velocity, V_0 some reference velocity, k_B Boltzmann's constant, and T the absolute temperature. Whilst clearly expressing something of a potential mechanism, this equation has several flaws. The most serious is evident in the situation of low or no applied force: the sliding speed remains non-zero, which would be sound for an individual particle but cannot apply to a large system of coupled sites. Related to this, it is clear that this model cannot support any static friction.

In a later development, Schallamach [139] modified the model so that both bond-making and bond-breaking were thermally activated processes with characteristic energy costs. The energy barrier to bond breaking was modified by the progress of sliding with time, so that $E_{break} = E_{break\,0} -$

λMVt, where M is the bond stiffness and t is bond age. Schallamach then argued that the frictional force was proportional to the number of instantaneous contacts and the mean bond force, and used his bond-making and -breaking conditions to calculate the former. This resulted in a model with the characteristic peak in velocity that experimental results required, but resulted in no friction at both low and high velocities.

A much later rate theory devised by Heslot *et al.* [140] in an attempt to explain their experimental results (described in §2.4.9) took the original model of Schallamach [138] and Bartenev (see [137]) and applied a much more careful statistical mechanics treatment. They assumed a periodic potential with a much wider harmonic "driving" potential (due to a spring) overlaid, a stochastic delta-correlated noise force, and the corresponding damping term prescribed by the fluctuation-dissipation theorem. This gave rise to an equation of motion, which they proceeded to analyse. It is worth noting that Heslot's model assumed a dwell-strengthening potential, described by the Ruina geometric aging model (§2.4.8). However, the model fails due to scaling problems: the scale of the forces produced by it are many orders of magnitude too small, a fact which was overlooked in the authors' own scaling analysis by erroneously attributing only one degree of freedom to a cellulose molecule rather than the manifold degrees that it in fact possesses.

2.4.7 Phenomenological "pinning" models

The common feature of pinning models is that they represent interactions between the two surfaces at an interface with a potential (which can conceptually be attached to one surface) within which "test points" (which can be thought of as contacts from the other surface) move. There is also an elastic response force from the surface, and thermal excitations are sometimes invoked in order to enable transitions to occur before a threshold force has been reached.

Single asperity models consider the pinning potential in one surface, and independently moving test points in the other surface which are always in equilibrium under the pinning force and elastic forces which seek to maintain test points in their undeformed positions relative to the second surface (figure 2.11) [141, 142, 137]. Friction arises due to energy becoming multivalued with respect to the undistorted positions of test points. For a single one-dimensional asperity energy is given by

$$U_{tot} = \Phi(x + \chi) + \tfrac{1}{2}\lambda\chi^2,$$

(adapted from Caroli & Velicky [141]), where Φ is a potential function, x is the equilibrium position of a test point, χ is its displacement from equilibrium, and λ is an elastic constant. For local equilibrium, $-\Phi'(x+\chi) = \lambda\chi$, so the progress of the equilibrium point x across the potential Φ can be tracked, as in figure 2.11. As shown in figure 2.12 for the example of an approximately Gaussian potential function, for an adequately soft elastic response (relative to the potential), multistability gives rise to dissipation [141, 142].

Despite generating a frictional force elegantly from conservative force fields, the model has a few shortcomings. First, it is assumed that the asperity interaction can be described in terms of a fixed potential, denying the possibility of the potential itself undergoing change as a result of the interaction (though Caroli & Velicky [141] made a purely dwell-time dependent modification

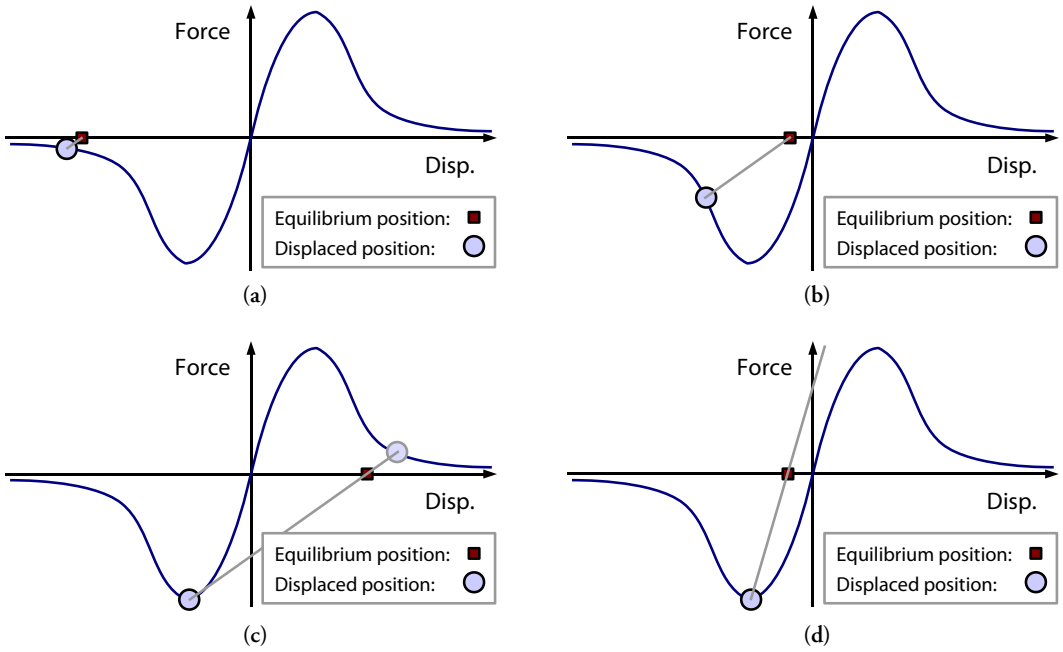

Figure 2.11: The mechanism of energy dissipation in elastic material pinning models. (a) Test points are always in equilibrium with the pinning potential; that is, the location of the test point is where the straight force-displacement trace meets the curve Φ'. (b) As the undeformed position moves, new equilibria are adopted. (c) At the lowest point of the force curve the test particle will move to another equilibrium without the undeformed co-ordinate changing. The new position has a lower energy, so dissipation has occurred. (d) This can only happen if the elastic force curve is shallow enough for a second equilibrium point to exist.

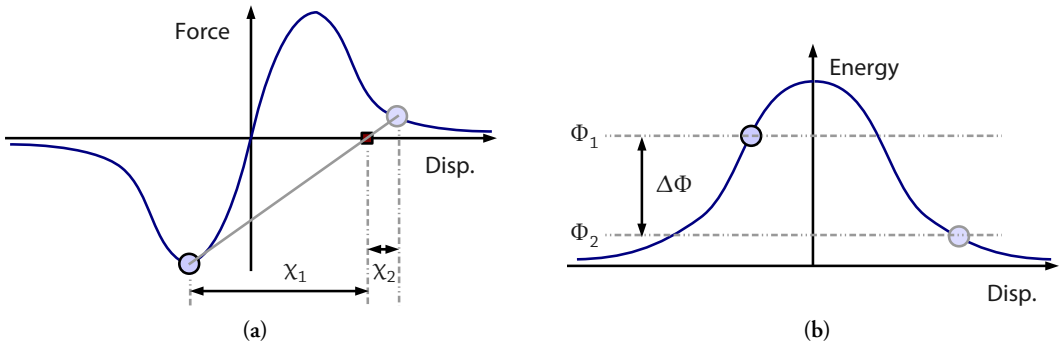

Figure 2.12: Energy dissipation in elastic material pinning models. (a) Elastic energy is lost, since elastic energy is proportional to χ^2. (b) Pinning potential energy is lost since the new equilibrium point is further down the potential energy slope.

(§2.4.8)). Second, dissipation is essentially attained by neglect of kinetic energy and momentum: if these were included and the equilibrium point allowed to respond to them then energy would be conserved, unless an explicitly dissipative constitutive relation was used. Last, an important point is that the *details* of the model are deeply intertwined with its *framework*. This makes fundamental improvements essentially impossible within the theory as presented, though the ideas can, of course, be used.

Caroli & Nozières [142] presented an analysis of the behaviour of a single asperity pinning system under steady sliding, no sliding, and various oscillatory scenarios. To do this, they considered a large ensemble of "pinning centres" on a surface, and from this defined a "density of states" ν, where

$$\nu := \frac{dn}{dx};$$

that is, the number of states per unit length, where a state's position was defined as its equilibrium position.

Assuming uniform distribution of asperities over a surface, the dynamic case has a uniform state density (figure 2.13a) [142]. If the driving force is suddenly removed then the distribution of states must shift so that the net force exerted by them is zero,

$$\int \nu(x)F(x)dx = 0, \tag{2.7}$$

where $F(x)$ is the force corresponding to the *undeformed* position x (as distinct from the force acting on the particles which have been carried to x by deformation of the body). Baumberger *et al.* [143] stated this formula with a summation corresponding to the different populated regions of their x axis, which is omitted here as unnecessary. If this "recoil" is rigid (a matter discussed by Caroli & Nozières [142]) then the states assume the distribution shown in figure 2.13b. If sliding were to resume, since no transitions (and thus no friction) can occur until the first states reach the maximum force, this theory predicts that a small amount of sliding in either direction will occur without *any* friction.

However, the population shown in figure 2.13b is by no means the only force-free configuration: any configuration obeying equation 2.7 is a valid static state. Since the force at which bulk sliding begins depends on this configuration, Caroli & Nozières [142] concluded that static friction is *not* an intrinsic property of a junction, but rather a function of its history.

In spite of the interesting static / dynamic features of the basic pinning model, it predicts a frictional force that is invariant with velocity. In the context of Amontons' law this is in its favour, but many materials are known to exhibit velocity-dependent friction [144], so various authors [137, 145] have extended this model to introduce velocity dependence. In essence, the extension acknowledges that the transitions between equilibrium states take place at finite temperature, and thus a degree of oscillation around the stable displaced position is always present. This presents the possibility of a particular test point absorbing energy from the environment greater than or equal to the remaining energy barrier, and so undergoing premature transition.

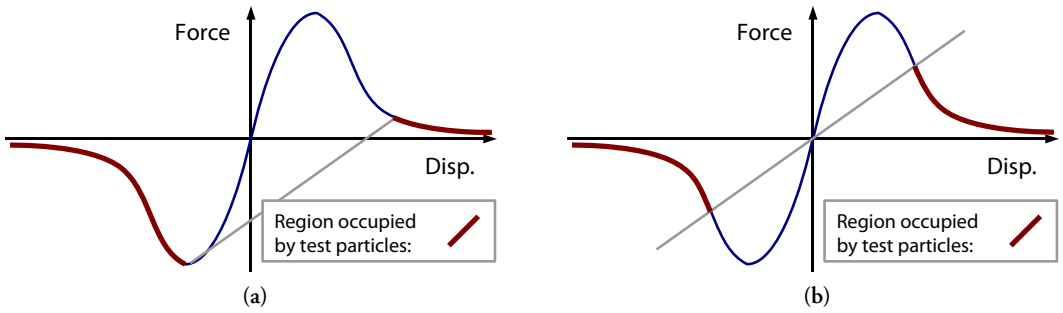

Figure 2.13: Non dynamic frictional behaviour for the pinning model is very different from the dynamic case. (a) For steady sliding the state density is uniform within the stable regions. NB There is no gap in occupation measured in the undeformed co-ordinates; rather there is a discontinuity in $F(x)$. (b) A rigid recoil causes a symmetric arrangement of states.

Baumberger *et al.* [145] noted that the frequency with which this occurs is governed by

$$f(x) \propto \exp\left[-\frac{\Delta E}{k_B T}\right],$$

where ΔE is the energy barrier, k_B is Boltzmann's constant, and T is absolute temperature. Since the premature transition rate is very sensitive to the remaining energy barrier, it is implicitly sensitive to the density of states ν around the transition point. The density of states itself obeys an advection-transition differential equation,

$$\frac{\partial \nu}{\partial t} = -V\frac{\partial \nu}{\partial x} - f(x)\nu$$
$$\frac{\partial \nu}{\partial t} = 0 \quad \Rightarrow \quad \nu(x,V) = \nu_0 \exp\left[-\int_0^x \frac{1}{V} f(x')dx'\right],$$

where V is the sliding velocity [145, 143]. This reduction of state density with increasing velocity reflects the increased premature transport, which in turn leads to a frictional force that likewise increases with velocity. An approximate solution to this system is of the form

$$F \propto 1 + a \log\left[\frac{V}{V^*}\right], \tag{2.8}$$

where a is a constant depending on the system, and V^* is a constant determined by surface properties.

So far asperities have been considered in isolation, effectively elastically isolated from each other. This is clearly not so, and though apparently overlooked by authors up to 1972 [137] it *has* been recognised by several more recent authors [141, 146, 142, 147, 148]. Various approaches have been tried to deal with these interactions, from investigating limits where they are unimportant [141] to attempts at a fairly general solution. However, Baumberger & Caroli's 2006 review [143] still

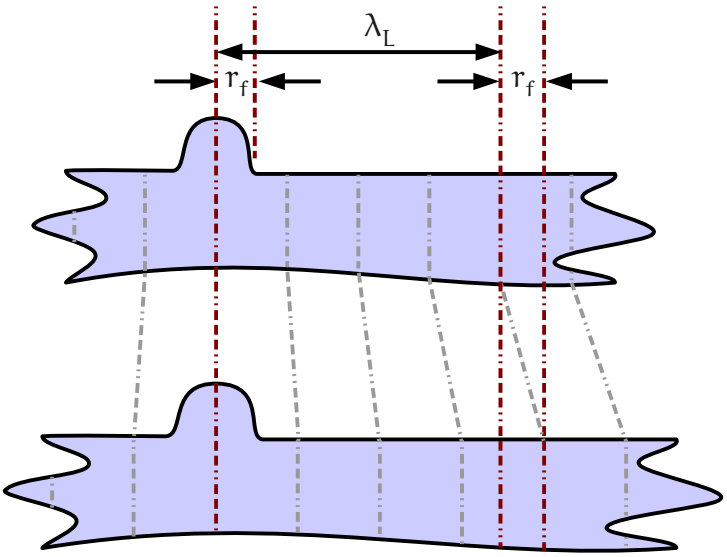

Figure 2.14: The Larkin length is the distance at which elastic deformation is equal in magnitude to the dimensions of a pinning centre. If the distance between pinning centres is less than λ_L then the deformation will not influence the alignment of the pinning centres, and they thus behave independently; if otherwise, the pinning centres will be realigned, and they will behave as an ensemble.

considered the problem fundamentally unsolved.

Before attempting a solution, it is wise to determine whether an effect is important. In this field, the relevant condition was formulated by Larkin & Ovchinnikov [149] (in the formally equivalent context of type II superconductors). Assuming that a pinning site had a force with a characteristic range r_f, they defined the *Larkin length* $\lambda_L := \|\mathbf{R}\|$, where

$$\langle [\chi(\mathbf{R}) - \chi(\mathbf{0})]^2 \rangle = {r_f}^2,$$

where χ is the deformation in response to the pinning forces applied within a sphere of radius λ_L, and the angled brackets denote an ensemble average. In essence, the Larkin length is the distance in an elastic material above which deformations due to a pinning force are large enough to cause shifts at another pinning centre of comparable size to the centre itself (figure 2.14). It is thus often taken that if the interasperity distance is greater (less) than the Larkin length then the asperities elastically interact (do not interact).

Unfortunately, the Larkin length is very sensitive to the size of asperities, and there is disagreement about its magnitude: Caroli & Velicky [141] reported that it was for all practical purposes infinite (apparently considering asperities on the ~10 nm scale); Sokoloff [150] showed by order of magnitude calculations that for multimicron asperities the Larkin length was comparable in size to the asperities themselves. It seems likely that both domains are represented in nature.

Various attempts have been made to solve the interaction problem. Vollmer & Natterman [146], Tanguy *et al.* [147], and Tanguy & Vettorel [148] all chose to write their elastic interactions as nom-

inal separation decaying force laws reminiscent of gravity or electrostatic interactions. These are evidently approximations which will be poor in the large deformation limit, but they were used rigorously and self-consistently, and have the virtue of allowing different types of interaction (for example, surface or bulk) to be represented by variation of the power to which the separation is raised. Vollmer & Natterman [146] took an interesting approach to obtaining approximate solutions in the weak interaction limit, calculating expansions in the elastic interaction coefficient by using propagators by analogy to their use in quantum field theories.

Caroli & Nozières [142] also tried expansions in terms of elastic interactions, but with a different and interesting model. They considered writing the displacement of an asperity from equilibrium in terms of an elastic *compliance* matrix and the asperity forces throughout the interface. Although this remains a complicated system (the asperity forces depend on all of the deformed positions), solutions retaining different numbers of interactions can be obtained. Again, this expansion only converged for weak elastic interactions. The same authors [142] and others [143] looked at the much simpler idea of *dynamic noise*, a stochastic quantity arising from the force coupling between asperities. They considered that it provided a source of noise in parallel with thermal noise.

All of these models have assumed instantaneous linear elasticity.

2.4.8 "Geometric aging"

"Geometric aging" is an elegant concept which can be used to provide a coherent framework to deal with dwell-time strengthening of friction and variation of friction with velocity, both features reported or implied for skin or nonwovens. However, since the most innovative work on friction in the last twenty years appears to have related to geophysics, geometric aging was first suggested in that context. Experimental results gave rise to the idea that instantaneous apparent functions of state were not sufficient to describe dynamic and static friction [151]. In consequence, several researchers, notably Ruina [152], developed a theoretical framework which allowed less apparent "state variables" to have a role in determining instantaneous friction, which in turn obeyed differential equations of a specific form. Of the several theories of this type that were developed, the most successful in describing friction between rocks (of primary interest to geophysicists) was based on the idea (originally proposed by Dieterich [153]) that friction increases logarithmically with the age of an individual interasperity contact. Benefitting from the work of Ruina [152] and others, this was developed into

$$\mu = \mu_0 + a \log\left[\frac{V}{V_0}\right] + b \log\left[\frac{V_0\theta}{D_c}\right] \qquad , \qquad \frac{d\theta}{dt} = 1 - \frac{V\theta}{D_c}, \tag{2.9}$$

where V_0 is a reference velocity, D_c is a critical distance in some sense corresponding to asperity size, and θ is the state variable (termed "geometric age" by Baumberger & Caroli [143]) [151]. This geometric age is a generalisation of "dwell time" (for static friction) and "contact time" (for steady dynamic friction) consistent with the framework laid down by Ruina [152]: if $V = 0$ then $\theta = t$; if θ is a constant then it takes the value $\theta = D_c/V$, consistent with the time taken for an asperity transit.

Theories of this type are empirically derived, but a little progress has been made in setting them on a theoretical footing. Baumberger *et al.* [145] noticed that apart from a product of logarithms (assumed to be small, though possibly not negligible (§2.4.9)), equation 2.9 could be written as

$$\mu = \mu_0 \left[1 + m \log\left(\frac{\theta V_0}{D_c}\right)\right] \left[1 + \alpha \log\left(\frac{V}{V_0}\right)\right], \tag{2.10}$$

where m and α are constants. The significance of this factorisation is that it enabled Bowden & Tabor's "shear strength $\times$ contact area" decomposition (equation 2.4) to be applied. The second bracket was assigned the role of σ as it could be identified with equation 2.8, and the first was interpreted as a dwell-dependent spreading. Interestingly, the same approach was taken by Dieterich [153] when the law was first proposed, but was abandoned during the subsequent refinement.

Geometric aging still lacks theoretical foundation (though Baumberger & Caroli [143] report suggestions that it may be thermally activated), but Baumberger *et al.* [145] provided a clearer indication of its physical origin.

2.4.9 Non-static sliding

Non-static sliding or "stick-slip" behaviour, is "…a phenomenon where the instantaneous sliding speed of an object does not remain close to the average speed." [91] This includes both *global* stick-slip (where a body moves rigidly) and *local* stick-slip (where parts of a body undergo stick-slip at different times). This phenomenon is responsible for much machinery squeaking, the function of a stringed instrument's bow, and geological fault slipping [144].

A fair amount of work has been done looking into the conditions under which stick-slip can occur, and some theoretical models have been proposed which reproduce the behaviour. The groundbreaking work of Rice & Ruina [144] generalised the Rayleigh conditions for stick-slip (that frictional stress is a decreasing function of velocity) by considering systems which retained a fading memory of their history. They considered a velocity perturbation $V \to V + \dot{x}(t)$ from $t = 0$ onwards to cause a stress perturbation

$$\tau_{ss} \to \tau(t) = \tau_{ss} + f\dot{x} - \int_0^t h(t - t')\dot{x}(t')dt',$$

where τ_{ss} is steady state stress at velocity V, f is an instantaneous response to velocity change, and $h(t)$ is a delayed response function. Based on the experimental observation that $f > 0$, Rice and Ruina [144] showed that stick-slip could occur if f and $h(t)$ obeyed

$$\int_0^\infty h(t)dt > f.$$

Both f and $h(t)$ generally depend on the velocity V about which perturbations were made, which implies that stick-slip behaviour can be a feature of some velocity regimes and not others.

More concretely, Ruina [152] considered the problem of stability applied to a specific class of single "state variable" models (§2.4.8) that generalised the Dieterich model (equation 2.9) to any

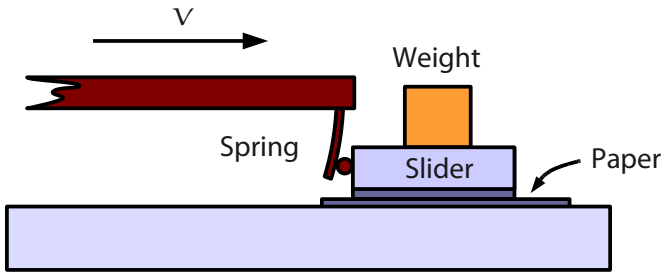

Figure 2.15: Heslot *et al.* [140] built the illustrated equipment after the theoretical model of Ruina [152]. The elastic response of a system is modelled by a spring with constant k, whilst the interacting paper surfaces are attributed no elastic behaviour. Very similar apparatus was used by Baumberger *et al.* [145]. After Heslot *et al.*

system described by

$$\tau = f(\theta, V) \qquad , \qquad \dot{\theta} = g(\theta, V), \tag{2.11}$$

where f and g are general functions. For simplicity he assumed that all the elastic stiffness in the system could be described by a single characteristic stiffness k, and found that if

$$k < -\frac{V}{D_c}\frac{d\tau_{ss}}{dV} \tag{2.12}$$

(where D_c is again a measure of asperity size) the system was unstable in steady sliding, and would develop stick-slip.

Experimental work on such a system was carried out by Heslot *et al.* [140] (with a paper-paper ("Bristol board") sliding interface—figure 2.15) and Baumberger *et al.* [145] (using polystyrene-polystyrene (*PS-PS*) and polymethylmethacrylate-polymethylmethacrylate (*PMMA-PMMA*) interfaces). Both groups found that over their velocity range (Heslot, 0.1 $\mu m \cdot s^{-1}$–100 $\mu m \cdot s^{-1}$; Baumberger, 0.5 $\mu m \cdot s^{-1}$–10 $\mu m \cdot s^{-1}$) μ_d was fit very well by

$$\mu_d(V) = \mu_d(V_{ref}) - \beta_d \log\left[\frac{V}{V_{ref}}\right].$$

Baumberger *et al.* [145] considered the Dieterich model (equation 2.9) for their data, and calculated that Ruina's critical spring constant (equation 2.12) ought to be independent of velocity for their system. Their results (figure 2.16) showed fair agreement with this prediction, though there was a significant reduction in the critical k as velocity increases, especially for PS. Interestingly, the changes in k were of the same order as the extra term introduced by Baumberger's factorisation of Dieterich's equation (§2.4.8, equation 2.10), which the authors suggested might imply that one was explained by the other.

Though Heslot *et al.* [140] found similarly within the velocity range probed by Baumberger *et al.*, their results beyond this region differed markedly from a naïve extrapolation (figure 2.17). Although the authors state otherwise, their k-V phase diagram shows very clearly that their system is *not* of the

Figure 2.16: The phase diagrams from Baumberger *et al.* [145]. (a) k-V phase diagram showing the steady sliding / slip-stick bifurcation for PS at 23 ℃ (solid circles) and 87 ℃ (open circles). (b) k-V phase diagram showing the steady sliding / slip-stick bifurcation for PMMA at 24 ℃ (solid circles) and 72 ℃ (open circles).

single state variable type considered by Ruina, and in the "In" region it is a very poor approximation. This is of interest for the work presented in this thesis, as paper shares qualitative similarities to nonwoven fabrics.

Non-static sliding is known to be important for some rubber-[rigid material] interfaces. In 1971, Schallamach [154] reported having observed "waves of detachment" between a rubber slider and a Perspex (PMMA) track (figure 2.18). These consisted of a buckle forming in the compressed material at the leading edge of the slider, and running backwards towards the trailing edge, in some ways analogous to dislocations facilitating plastic flow in metals. Schallamach showed that for the rubbers where this occurred there was no movement apart from that mediated by these waves.

Various attempts to explain the origin and frictional characteristics of these "Schallamach waves" have been made. Gent [8] constructed a theory in which non-buckling Schallamach waves were caused by the relationship between different stress components, but this was contradicted by the experiments of Barquins & Courtel [28]. Roberts & Jackson [155] constructed a theory based on surface energy that predicted friction mediated by Schallamach waves fairly accurately, though it required various measured functions to be specified first. Finally, Barquins & Roberts [9] showed that in the presence of Schallamach waves friction was independent of velocity, load and temperature. Interestingly, this is in agreement with Roberts & Jackson's [155] theory if the speed of wave propagation is proportional to sliding speed.

2.5 Summary

This review has covered a wide variety of subjects relevant to skin-nonwoven friction. In view of its scope, an extremely condensed summary of the most relevant points is given here, with nuances and subtleties removed. Each subject is summarised in turn.

Figure 2.17: The k-V phase diagram from Heslot *et al.* [140]. Region 1 is the stick-slip regime, and the dashed line represents the change in surface interaction mechanism

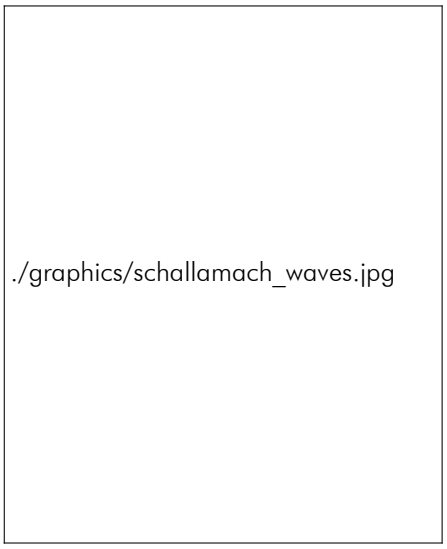

Figure 2.18: An image of Schallamach waves obtained under a low power microscope by two taking two superposed pictures in rapid sequence: the less bright lines correspond to the waves' positions a short while after the brighter ones. From Roberts & Jackson [155].

Mechanical properties of skin. Skin is a layered composite material which is under several kilopascals of tensile stress *in vivo*. The layers have very different moduli (the stratum corneum is much the stiffest at low strains) so the apparent composite stiffness in tangential tension is much higher than in normal compression, an effect exacerbated by the even more compliant subcutaneous tissue below. Because of this, smaller indentors experience a much higher stiffness *in vivo* than larger ones.

Mechanical properties of nonwovens. Despite many interesting approaches and substantial progress, there is still no known expression that relates the mechanical properties of a fibre bed to its microstructure and the mechanical properties of its constituents in a way consistent with experiment. No theory that deals with bonding points has been found at all.

Skin-X friction. For the skin-fabric interface there is no firm evidence for deviation from Amontons' law (though there are suggestions), but it is agreed that hydration increases friction. For many skin-X interfaces (not including fabrics) there is *at least* circumstantial evidence that adhesion is important for friction. Viscoelastic deformation is probably only important for large deformations. An untested model has been proposed in this review which could accommodate the majority of results reported.

Fabric friction. Fabrics against themselves or against hard, smooth surfaces have been found not to obey Amontons' law, but instead for friction to be typically (though not always) sublinear in normal force. There is no consensus on friction's variation with velocity, but there is some evidence for a positive correlation between higher spatial frequency of weave in woven fabrics and friction.

Adhesion. Friction is often attributed to adhesion, though the details of how a normal force produces a tangential force have never been convincingly elucidated. Both plastic and elastic deformation have been shown to be capable of producing Amontons' law if it is assumed that friction is proportional to contact area. For elastic deformation, surface roughness has the effect of increasing the index of the power law between intimate contact and load towards unity.

Hysteresis / Viscoelasticity. Many theories have been proposed to describe viscoelastic friction, but though they have varied widely in mathematical sophistication they have without exception made unjustified (and frequently unjustifiable) physical assumptions; it would thus be hard to mandate the use of the more mathematically complicated theories. They have made a variety of predictions about variation of friction with load and sliding speed; all that is common is that friction *does* vary with sliding speed.

Chapter 3

Initial analysis, and objectives

"Demarcation… We demand rigidly defined areas of doubt and uncertainty!"
— Douglas Adams, 1952–2001

The literature reviewed in §2 has brought to light work on many aspects of friction, but has also shown a marked lack of research into the specific topic area of this thesis. More generally, most work on *mechanisms* of friction has been phenomenological, or motivated more by a desire to produce solvable theories than to reflect theoretically the true mechanisms at play. Since this is the case, the task of gathering reliable experimental data using validated equipment and analysing them to narrow down the range of possible mechanisms remains open, and must be addressed in the course of this work.

3.1 Scope

Friction between skin and nonwovens is an immensely complicated problem, a complete description of which is almost certainly impossible; no matter how keen the model, nuances of material or mechanism will always be overlooked. In order to render the task of describing the system tractable, limits must be imposed on its generality. Conversely, it is possible to retreat too far from this rather lofty vision, to the point where single constants or "fit" functions obscure so much of the underlying physics that no understanding can be gleaned.

The scope of this work is intended to follow a middle way, attempting to identify the physical mechanisms at play and describe them with the simplest theories that take in the most significant features, but deliberately *limiting* focus to those features. The following limitations and requirements are thus applied.

Only "dry" skin and fabric are considered. The literature shows that friction between skin and fabric is dependent on the hydration level of each (§2.4.2). However, the work of Wong [99] and others shows that skin takes at least half an hour to hydrate fully, and frictional behaviour can change entirely when it has done so. In consequence, attention is presently limited to "normal", dry skin and fabric.

Only thin coverstocks are studied. The nonwovens most commonly used as coverstocks in incontinence pads are thin (< 1 mm). Attention is limited to these fabrics as they form a distinct class, and one with clear applications.

Gross geometry is included. In practice, an important situation in which friction arises is where a stressed sheet or strip is pulled over a curved surface. Work related to this has been published (§2.4.2), but it only applies to prisms. The effect of gross geometry is considered in this work, with a view to generalising known results.

Descriptions are based on observables. It is common when investigating complicated systems to fit models to data via a number of parameters. This is undesirable (though sometimes unavoidable) as it robs models of *a priori* predictive power. This work opts for direct dependence on measurable quantities wherever possible in order to increase testability and retain the ability to make predictions.

Additionally, when considering gross geometry an emphasis is placed upon deriving general frameworks to describe mechanisms of friction which, so far as is possible, stand apart from the details of any given materials or interactions. This enables the application of such frameworks beyond the situations in which they were conceived.

3.2 Relevant length scales

The friction problem that lies within the scope outlined in §3.1 remains very broad, and based on the literature review can be expected to depend upon features that vary in scale from ~10 µm (fibre width) up to ~100 mm (gross geometry). In order to consider how this large range of scales might be divided into regimes, it is advisable to consider the structures at each of those scales. These are summarised in figure 3.1, which shows that features divide fairly neatly into two groups, the first covering a range ~10 µm–1 mm, and the other across ~10 mm–100 mm. Additionally, the mechanical mechanisms at play across the scale range are worthy of consideration and are summarised in table 3.1. Again, there is a distinction between the mechanisms in the ranges ~10 µm–1 mm and ~10 mm–100 mm: the former vary widely, but all act directly to oppose an applied shear stress, whereas the latter is a mechanism for producing a *normal* stress from an applied *tangential* stress.

These distinctions suggest the separation of the sub-millimetre from the super-millimetre regime; the regimes are hereafter known as *microfriction* and *geometric friction*, respectively.

3.3 Aims and objectives

The ultimate objective for the study of friction between skin and nonwoven fabrics is to be able to measure some parameters from a subject's skin and anatomical geometry, and from a sample of nonwoven, insert them into a model and produce an accurate, quantitative prediction of the frictional force that they would experience as a function of the applied forces. However, given the relatively undeveloped state of the field at present, this work represents an early step towards this goal, so a more limited and immediate set of objectives are considered.

According to the scale breakdown given in §3.2, objectives are given for microfriction, and then for geometric friction.

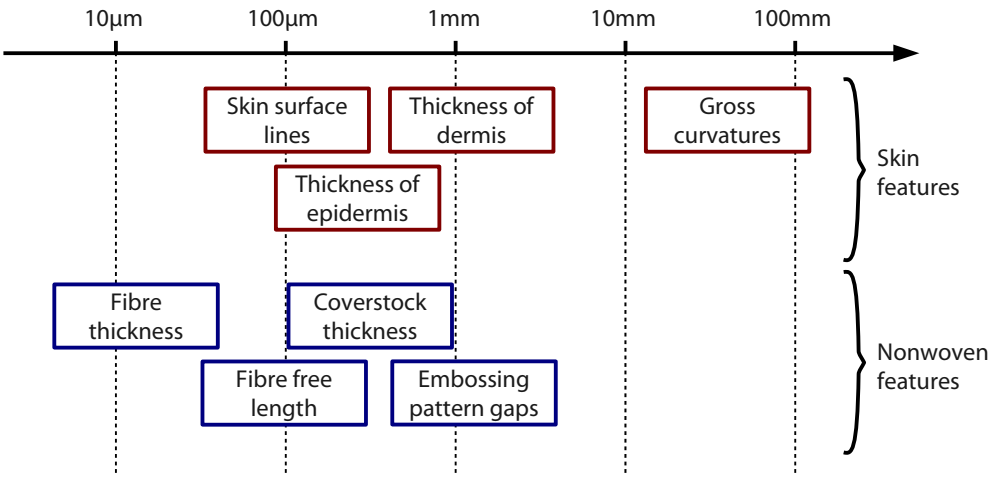

Figure 3.1: A diagram of the different features of skin and nonwoven coverstocks across the scales pertinent to friction. Those pertaining to skin are shown in red; those for fabric are shown in blue. The position of boxes is merely indicative of their typical scale rather than a definite statement of spread. Vertical positions vary purely for visual clarity, and do not correspond to anything.

Approx. scale	Relevant features	Related mechanism
$<10\,\mu m$	Intimate surface contacts.	True molecular adhesion.
$10\,\mu m$–$100\,\mu m$	Fibre thickness, and skin microrelief lines.	Mechanical interlocking, with fibres catching in the depressions.
$100\,\mu m$	Free length of fibres in the nonwoven.	Beam-like bending of fibres.
$100\,\mu m$	Thickness of the epidermis.	Elastic forces perpendicular to interface.
?	?	Elastic forces parallel to interface.
$10\,\mu m$–$100\,\mu m$	Typical anatomical radii of curvature.	Normal forces arising from stress around curves.

Table 3.1: A summary of the different mechanical interaction mechanisms across the range of length scales present at the skin-nonwoven interface. Given the lack of agreed data on the elastic properties of skin and subcutaneous tissue, the scale and relevant features for elastic forces parallel to the interface cannot be given here. Indicated mechanisms are not asserted to be significant; they are merely noted as corresponding to a feature which itself may or may not prove relevant.

3.3.1 Microfriction

A key objective of this work is the characterisation of friction between skin and fabric at a variety of anatomically relevant loads and sliding speeds, along with the nature and dynamics of the interface during sliding. Having gathered such data, they must be analysed to ascertain which friction mechanisms they are compatible with, or used to coin new mechanisms or models. These objectives may be broken down as follows.

To develop and characterise friction and interface apparatus. Equipment that can accurately and reproducibly measure friction force and the nature and dynamics of the interface are a *sine qua non* for robust data. In addition to minimising error, that error which cannot be removed (both random and systematic) must be characterised.

To gather data at various relevant interfaces. The equipment should ideally be used to gather data at a selection of different nonwoven-skin interfaces, as well as any others that might prove useful, perhaps involving skin surrogates. It has not been possible to satisfy this objective entirely, as discussed in §2.2.

To analyse the interface and friction data to identify mechanisms. The relationship between friction force and loading, sliding speed, and various surface, material, and interface parameters will provide substantial information on the relevant mechanisms. Although rigorous proof that a mechanism consistent with the data *is* active will likely be impossible, it should be possible to *disprove* the relevance of various mechanisms.

To relate models of identified mechanisms to material properties and make predictions. Ideally, models should relate only to independently measurable material, surface, and interface properties so that quantitative predictions are possible. At least they must be adequately descriptive to predict correlations between measurable parameters and friction.

3.3.2 Geometric friction

The other key objective of this work is the development of a geometric friction model, which meets the following essential specification.

To describe friction for a simple substrate and sheet. A minimum requirement for a geometric friction model is that simple friction due to stress in a sheet obeying a simple constitutive equation over a fixed convex substrate is accurately described.

To be based on a small number of meaningful parameters. Input parameters must be physically meaningful, and small enough in number to permit interrogation of the model.

To be solvable, at least numerically. Solutions must be obtainable somehow, at least for simple systems.

There are further properties which are desirable.

To permit the use of an accurate constitutive equation for the sheet. This will require the determination of such a relation, and solution methods to be modified.

To permit a range of microfriction laws. If Amontons' law is replaced by another microfriction law, it would be sensible to try to implement it.

To allow for substrate deformation. Human bodies deform noticeably under commonly encountered pressures, so it would be good for a geometric friction model to reflect this.

To allow for concave portions of a surface. This would mean that the permissible surfaces would have been thoroughly generalised.

Chapter 4

Microfriction

"Everything should be made as simple as possible, but not simpler."
— Albert Einstein, 1879–1955

Amontons' law is beautiful in its simplicity, capturing a great deal of the frictional interaction of a wide variety of surfaces in two numbers, the static and dynamic coefficients of friction. However, it has two major shortcomings when applied to the skin-nonwoven tribosystem:

Its accuracy is unproven. Whilst there is no firm published evidence of departures from Amontons' law for the skin-fabric interface (§2.4.2), it is well known that neither skin nor fabrics obey Amontons' law when in contact with other, generally stiffer surfaces (§2.4.4, §2.4.3). Given the dearth of studies on the skin-nonwoven interface and the insensitivity of some to departures from Amontons' law at low pressure, it certainly cannot be said that Amontons' law is well established for this system.

Coefficients of friction are phenomenological. This is as great if not a greater problem than potential inaccuracies. There is no known simple relationship between obvious surface properties and coefficients of friction, despite the exertion of fair experimental effort (§2.4.2). The lack of a theory relating friction to material and surface properties denies guidance to the attempt to engineer materials with specified frictional properties.

If Amontons' law is to be rejected or placed on a firmer footing, much more must be understood about the mechanisms of friction in this instance: not only are the friction mechanisms far from clear, but the very nature of the interface is unknown. The blind application of models developed for common engineering metals to a system so different would be unwise, so experimental establishment of the nature of the skin-nonwoven interface and the key coupling and dissipation mechanisms is imperative.

4.1 Introduction to the microfriction work

Based on the literature, there are a number of *a priori* likely friction (surface coupling or dissipation) mechanisms which consist with known experimental results, and it is worth briefly considering them in order to establish the "signatures" by which their significance would be made apparent.

Plastic dissipation. The hallmark of plastic dissipation is the presence of persistent deformation to the contacting surfaces after sliding. This has been established not to occur for skin [109, 110], but there are no known negative results for nonwovens. Such deformation could in principle be easily detected in nonwovens by taking micrographs of a given region before and after an experiment.

Viscoelastic dissipation. It is very difficult to distinguish instantaneously between plastic and viscoelastic dissipation; the key difference is that viscoelastic deformation relaxes after an experiment, where plastic deformation does not. Viscoelastic deformation must therefore be observed by comparing any deformation *during* an experiment with that observed *afterwards*. Viscoelasticity can further be distinguished from simple non-dissipative elasticity by conducting experiments at different speeds: the former will vary with rate, while the latter will not.

Pinning. Although pinning in combination with pure elasticity does not produce friction (§2.4.7), this mechanism can lead to relatively weak viscoelasticity causing a significant frictional force. This is because, although the dissipative effect of viscoelasticity may be weak at the *mean* sliding velocity, at time of slip the contact points are travelling much faster than this, and so viscous dissipation is substantially increased. The key signature of this mechanism is fibres "pinging"; that is, suddenly freeing themselves from a pinning point and rapidly correcting. Merely observing pinging in an arbitrary system would not, of course, imply that this mechanism is relevant: in the absence of an internal or interfacial dissipative mechanism pinging conserves energy. However, skin is known to be viscoelastic (§2.2.3), and polymers (such as constitute the fibres in common nonwoven coverstocks) are the prototypical viscoelastic materials, so observing pinging may reasonably be assumed to implicate pinning as at least *a* relevant mechanism.

Interfacial adhesion and dissipation. Friction due to true interfacial adhesion and dissipation is very hard to identify unambiguously due to a lack of visible mechanism. In practice, it must be inferred by assessing whether or not the other identified mechanisms account for the measured frictional behaviour.

4.1.1 Data desired

In order to establish which of the aforementioned mechanisms (or indeed those as yet unidentified) are relevant at the nonwoven-skin interface, data on the stress and strain fields throughout both the skin and the nonwoven would ideally be used. However, this is certainly impractical, and probably impossible at this time. A more modest set of data are instead aspired to, which are still capable of providing substantial insight into the processes at and near the nonwoven-skin (surrogate) interface.

Friction against displacement data. Bulk data on frictional force against displacement for the contact are relatively easy to obtain. They are limited in that they are are only representative of any given area to the extent that the area is representative of the whole contact. This condition intrinsically prevents the bulk force data's application to individual fibres and commensurate skin (surrogate) regions. It additionally requires that stresses must be uniform across the contact region for macroscopic force data to be applicable to a chosen mesoscopic region.

Fibre displacement data. By virtue of the relatively sparse nature of the nonwovens used in this work (see figure 4.3), it is possible to see most of the length of most of their constituent fibres under a microscope. It is thus in fact possible in principle to measure their displacements, at least within the plane of the fabric.

Contact data. If the nature, size, and arrangement of the intimate contacts between nonwoven and skin (surrogate) were known then inferences about the coupling mechanisms between the surfaces would be more reliable and easier to draw.

In all cases the data gathered with respect to each of these aspects of interface behaviour are much more powerful if they can be gathered simultaneously, or at least can be readily cross-referenced.

4.1.2 A brief description of microfriction experiments

In pursuit of readily cross-referenced data, it would be ideal to gather all data simultaneously with a single, coherent piece of apparatus. Unfortunately, this has proven impossible (further explanation is given in §4.3.2), but it has been possible to gather all necessary data using only *two* distinct experimental methods and sets of apparatus. These are described only briefly here to relate them to the data they are intended to provide; much more detail is given in §4.3, §4.4, and in appendices B and D.

The first experiment (§4.3) involves using the shallow depth of field of a high magnification microscope to observe the immediate environment of a [rigid material]-nonwoven interface to establish the location and extent of intimate contact: since only features within a small number of micrometers of the interface are in focus, selecting features that retain their "sharp" edges provides a means of identifying where skin and nonwoven touch. This is undertaken at a variety of contact pressures. The technique cannot unfortunately be applied reliably to the skin-nonwoven interface; the reasons for this are laid out in §4.3.2, along with evidence that this almost certainly does not matter.

The second experiment (§4.4) provides simultaneous friction force data and data on the movement of fibres and the skin (surrogate). This is achieved by compressing a slider with a layer of skin (surrogate) on each side between two transparent anvils, each covered with nonwoven and pulling the slider along with a tensometer. This arrangement is placed on the stage of a microscope, the nonwoven fibres and skin (surrogate) surface observed through the anvils at a low magnification, and video footage recorded during sliding. The raw microscopy data can then be used to map the movement of the skin (surrogate) and nonwoven fibres with time.

Before these experiments can be described more fully, the choice and preparation of materials must be described (§4.2); the two aforementioned experiments then follow; and the chapter concludes with an analysis of the data they provide.

4.2 Materials

This project as a whole relates to human skin and nonwoven fabrics. The former is nominally well-defined, but at present the single label covers material from approaching seven billion individuals, each of whom will have marked variation in skin properties across their body. The latter is a *class*

Full code	Short code	Linear density / dtex	Fibre diameter / µm	Fibre density / µm · mm^{-2}
103-237-1	NW1	2.0	16.8 ± 0.2	8.5×10^4
103-237-3	NW3	1.4	14.0 ± 0.3	1.2×10^5
103-237-6	NW6	3.6	22.5 ± 0.2	4.7×10^4

Table 4.1: A summary table for the nonwovens used in this project. The curious "decitex" unit used by textile technologists to measure linear density (*titre*) is defined as the mass in grams of 10 km of fibre. For these fibres this may be converted to a fibre diameter using the circular cross section of the fibres and the density of polypropylene, $\rho_{PP} = (904 \pm 2)\,\mathrm{kg \cdot m^{-3}}$ [156].

of materials, so it is apparent that a small number of examples must be selected. Further, skin is an awkward material to deal with and to obtain, which in addition to the impossibility of obtaining an identical sample upon which to repeat an experiment mandates gathering some example data on a "cleaner", surrogate, material for comparison with data from skin itself, and to ascertain what the techniques are capable of.

4.2.1 Nonwoven fabrics

Nonwovens have been reviewed as a class in §2.3. Although they are in a sense quite simple materials there are many parameters that can be varied, even within the subset of the class that are employed as coverstocks. In what amounts to exploratory work it does not make sense to carry out comprehensive tests of a well-populated multi-dimensional matrix of nonwovens in which all important parameters are varied, but rather to select a small number of nonwovens that are typical of coverstock types but which vary significantly in those parameters that might be guessed as most important to friction.

A set of three fabrics have been selected by nonwovens experts at SCA Hygiene Products (part sponsors of this work) to fulfil these criteria. The chosen nonwovens are all experimental polypropylene fabrics produced by a well-known supplier of nonwovens for the hygiene industry, and all have the same area density (*basis weight* in the language of textiles) of $17\,\mathrm{g \cdot m^{-2}} = 1.7 \times 10^{-2}\,\mathrm{kg \cdot m^{-2}}$. Additionally, all fabrics have the same common surface treatments and the same thermal bonding pattern (*calendering*) both in terms of bonding size and shape and lattice size. The sole variables in which the nonwovens differ are the diameter of the constituent fibres and the fibre length per unit area, which were chosen to represent as wide a range as possible. Details of the fabrics are given in table 4.1.

These fabrics were chosen for several reasons. The principal reason was that the fabrics are identical in all ways other than the mechanical properties of their fibres, which is likely to be the principal factor in determining friction; surface chemistry as determined by the bulk fibre material and surface treatments is thus best kept constant. The selection is therefore optimal from these points of view. It is *not* optimal for the calendering to be identical in all samples: along with the fibres' mechanical properties this might reasonably be expected to be very important in determining the relative importance of mechanical friction mechanisms. However, fabrics in which this parameter varied were not available. Finally, these specific fabrics had previously been the subject of friction work by SCA,

thus motivating further work on fabrics about which substantial data had already been gathered.

All samples of each nonwoven come from the same reel of the same batch; samples of each are thus as nearly equivalent as different samples of nonwoven ever can be.

The method by which nonwovens are produced causes them to be anisotropic: the "upper" surface is different from the "lower" surface, and the "machine direction" is different from the "cross direction". There is no strict convention on which side of nonwoven coverstocks is in contact with skin in use, so the choice of which side to characterise is arbitrary, but must be consistent. The nonwovens used in this work have thus been labelled to identify their orientation; the mark is in all cases copied onto samples cut. It consists simply of a capital "G": this symbol has no reflectional or rotational symmetry, so it can be used to orient a sample unambiguously. The mark orientation has been made consistently across all three nonwovens by observing common distortions in the calendering pattern and the through-thickness position of the bonding points.

4.2.2 Skin

"Skin" is *not* a well-defined material. The skin from, for example, a given site on the volar forearm of a specified individual who has treated it in a particular way *is* well-defined. However, it is not possible to base an experimental series on a single patch of skin, so it is necessary to accept a degree of variation in this material that would usually be carefully avoided in exploratory materials work. A number of factors are thus in tension: the material should be as reproducible as possible, but the potential pool of available donors should not be made too small; the skin from the chosen site and donor should be as simple as possible, but must still be sure to exhibit the same friction mechanisms. An additional complication is that it is impossible to perform accurate microscopy over a protracted period on *in vivo* skin: it must be excised. Since there are no direct benefits to anyone who might donate skin, the skin must be recovered as part of a scheduled medical procedure; a special procedure is not an option, so the choice of sites is further limited.

It could be argued that the choice of demographic and skin site should be dictated by the principal application of this work; that is, the skin should be taken from the diaper region and from elderly individuals in nursing homes. However, there are a number of arguments against this. First and most practically, there are no obvious high-frequency procedures undertaken in this site and demographic group that would yield skin. Second, there are various scientific reasons why this may be a poor choice. When science is undertaken with an application in mind, there is always a tension between pragmatic, "black box" approaches which provide a quicker route to real-world usefulness, and fundamental research which attempts to understand the simplest relevant situation, even at the expense of immediate applicability. This work follows the latter approach, seeking to understand how the simplest "variant" of skin interacts with nonwovens. It is thus important that the skin used is healthy, militating against the use of skin from individuals in nursing homes where Fader *et al.* [157] found that, although mostly transient, skin problems afflicted two-thirds to three-quarters of incontinent residents in any two week period. Further, skin that is "smooth" and hair-free is a better choice than aged, hairy skin as the additional features will doubtless lead to additional complexities. Though these complexities are of course important, given the current limited extent of understanding of how skin-nonwoven friction works it is more sensible to characterise a simple sys-

tem that embodies some of the key features rather than to hope to understand the target system in all its complexity and be confounded by the many interacting mechanisms. Following expert advice [158], breast skin from mastectomy patients has been chosen as fulfilling these requirements.

It was planned that this work would include experiments upon such skin, so all necessary practical and administrative preparations were duly made. In fulfilment of the statutory requirements for the use of human tissue in short-term research an application to the Hammersmith and Queen Charlotte's Research Ethics Committee was made and accepted in which the aims and procedures for this work were laid out as well as they were known at the time. The protocol that was submitted can be found in appendix A. Additionally, research and development permission to carry out research at the Whittington hospital was applied for and obtained.

The protocol will be summarised briefly here for reference. The surgeons were to have provided those of their patients who were suitable with an information sheet about the study; if the patient had consented a skin sample would have been taken from the skin removed during the course of the procedure and transferred to the research facility. Another surgeon would then have prepared the sample by removing subcutaneous fat (leaving only dermis and epidermis) and cutting it to shape and size. The sample would then have been used as any other material. Following use the sample and the slider to which it was bonded would have been disposed of using the clinical waste bins present in the research facility. Following expert advice, samples would not have been kept any longer than 24 hours after excision; freezing alters physical properties, so only refrigeration could have been used to prolong the period for which a sample was usable.

Where the experimental methods described in the protocol and those described in §4.3 and §4.4 differ, the latter are correct: the protocol was written to illustrate the *type* of experiment that would be conducted, fully expecting that the mechanical details would change.

The way in which the sample was prepared might reasonably have been expected to influence the final results of friction testing: if "skin" *in vivo* dissipates a lot of energy in hysteretic loss in the subcutaneous fat then removal of the fat and bonding of the sample to a rigid slider will reduce the energy dissipated per unit distance, thus the "friction". Other scenarios can readily be imagined in which the "friction" is increased instead. The approach was nonetheless to have been used for two principal reasons. First, though the distinction is somewhat artificial it is helpful to divide energy dissipation into that associated with an interface and that associated with the bulk. Both contribute to the force required to maintain motion, so in a crude analysis both would be accounted friction, but there is no reason to assume *a priori* that they are due to the same mechanism; they are thus best dealt with separately, and the interfacial effect is treated here. Second, pragmatically the thickness of the subcutaneous fat is very variable and the thickness that the surgeon leaves on the skin is somewhat hard to control. Both from theoretical and practical considerations it would thus have been preferable to conduct experiments only on the dermis and epidermis, so this procedure was planned to have been used.

A note on the absence of experiments on skin. Due to problems with supply no *experiments* were conducted on skin in the course of this work. However, a very small number of samples *were* obtained and were used to check that various parts of the method that was to have been used worked properly;

the method and procedures are thus validated and ready for use. In consequence, they are described in detail throughout this chapter as they would have been if skin had been available. This is partly to illustrate the work that has been done, but chiefly to expedite follow-up work on skin itself.

4.2.3 Skin surrogates

In view of the difficulties involved in obtaining skin samples, their short lifetimes, the awkwardness of working with them (thorough cleaning following all experiments, etc.), and the impossibility of obtaining a series of truly equivalent samples, there is considerable motivation for identifying an artificial surrogate material that behaves similarly. In particular, it is important that the skin surrogate-nonwoven system exhibits the same friction mechanisms as the skin-nonwoven system. Additionally, in view of the eventual lack of skin to test, surrogates provide an at least broadly similar system with which to demonstrate the data collection and analysis process.

As noted in §2.2.4, though there have been many skin surrogates developed, very few of them have been intended as mechanical surrogates, and even fewer as friction surrogates. In fact, only one has been shown to mimic skin's behaviour reasonably well: Lorica Soft (Lorica Sud Srl, Milan, Italy). However, though it behaves similarly in a variety of macroscopic friction experiments this does not necessarily imply that it will behave similarly in *all* such tests, nor that the mechanisms behind its behaviour are the same as those for skin and the equivalent corresponding surface. It is therefore very necessary that Lorica Soft is validated (or invalidated) in these more stringent tests.

Lorica Soft has therefore been subjected to the same testing regime which had been planned for skin samples with the intention that the resultant data should be compared with analogous data on skin when it is available. Testing on Lorica Soft also demonstrates the analytical techniques developed. Amongst the various colours available, white was arbitrarily selected, and material sourced from Ehrlich Leder Handels GmbH, Biberach, Germany. In all tests (other than validation tests) the pulling direction was along the length of the roll.

4.3 Characterisation of the nonwoven-X interface

As explained in §4.1.1, the ultimate objective of the experiment described in this section was to establish the size and shape of intimate contact between skin (surrogate) and nonwoven, and to do this by using the shallow depth of field (*DoF*) of a high magnification microscope to select only features at the interface in question; the principles behind the technique are explained in §4.3.1. However, for reasons laid out in §4.3.2, this cannot be achieved without some assumptions and compromises. Having established a working compromise, the apparatus is described in §4.3.3, and the method laid out in §4.3.4 and §4.3.5. The experiments done are then described in §4.3.6 and their results are given in §4.3.7, before summary analysis and comments are given in §4.3.8.

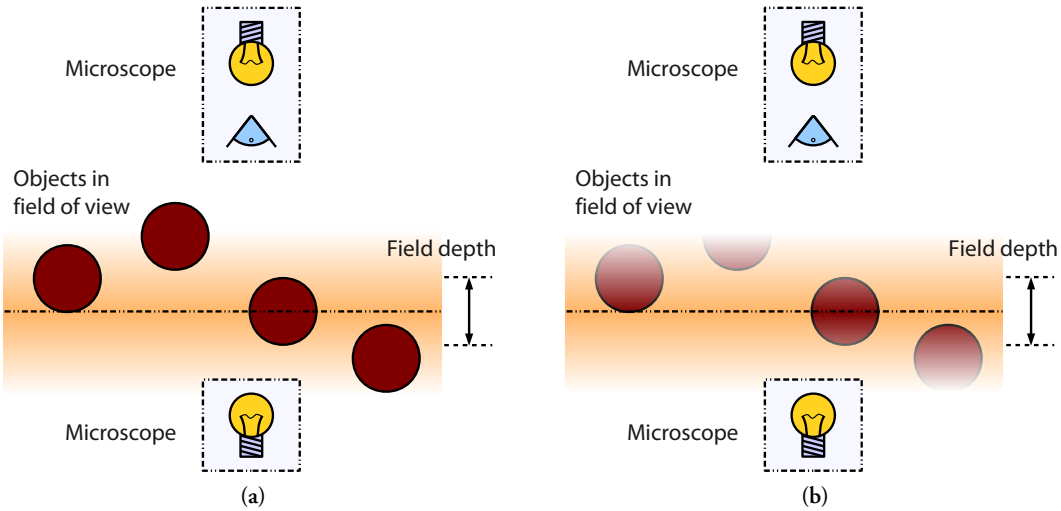

Figure 4.1: Imaging a plane. (a) shows the process of imaging a number of cylinders near the focal plane (dashed line), where the depth of sampling field is represented by orange hatching. (b) shows the cylinders as they are seen by the microscope.

4.3.1 Principles of DoF microscopy

To focus a microscope is to arrange the locations of the lenses so that light rays that diverge from a point in the object plane converge on a point on the image plane, where they are viewed[1]. The nature of geometrical optics means that this focusing is only perfect for points situated exactly on the object plane, but a small displacement from the plane only produces a small amount of defocusing; there is therefore for a given object and set of conditions a characteristic distance from the true focal plane at which an object is first discernibly out of focus (figure 4.1). All other parameters remaining constant, this distance (the *depth of field*) is smaller at high magnifications than at low ones.

This feature of microscopy is the basis of the technique described here. If the plane of focus is placed at the interface between skin (surrogate) and nonwoven then any objects that are not discernibly out of focus must be no further from the focal plane than a single depth of field distance. If the depth of field is shallow enough then this effect can be used to assess whether a fibre is in contact with the skin (surrogate) surface.

Depth of field (or at least its appearance) depends upon many parameters including illumination and magnification, but also the more subjective issue of when a feature is deemed to have become unfocused. This in turn depends upon whether the observation is directly by eye (which is fairly accommodating of poor focus) or indirectly using a microscope camera. In addition to this intrinsic depth of field—which is a property of the observing system—if an object looks essentially the same over a significant depth then as the focal plane is moved through it, the *object* may remain in focus substantially after the *feature* which was originally in focus has become blurred. For a given object

[1]This is, of course, a simplification, but one which includes all the salient features for these purposes.

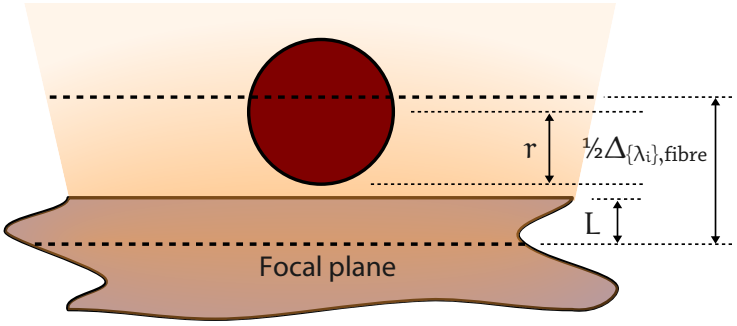

Figure 4.2: Assuming that the fibres cannot interpenetrate with the surface, it is possible to write down an inequality between the three lengths shown.

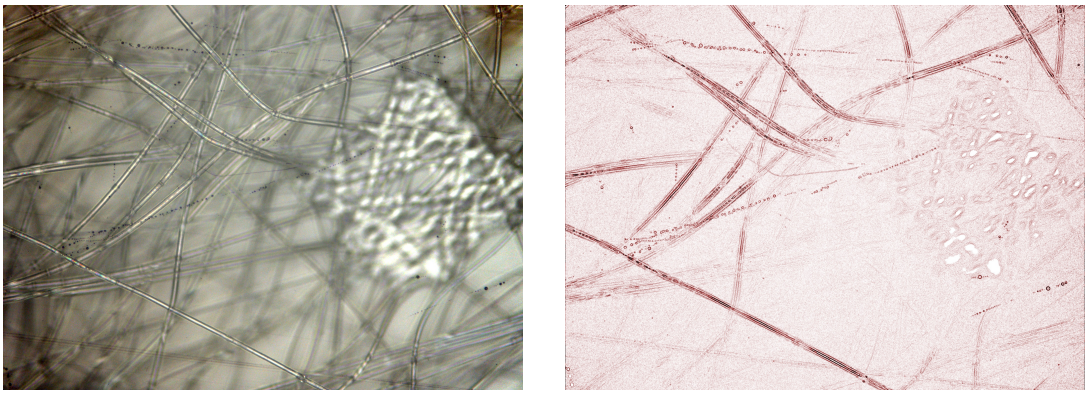

(a) (b)

Figure 4.3: An example of DoF microscopy. (a) is a reflection micrograph of the side of a NW1 sample *closer* to the microscope pressed against glass (an *upper interface*) at 5 kPa using a ×10 lens. It is clear that some fibres are focused and others are not. (b) shows the same image filtered to enhance sharp edges; the focused fibres are now much more apparent.

these effects cannot be readily distinguished, so the *apparent* depth of field for a set of parameters $\{\lambda_i\}$ and an object A will be represented symbolically as $\Delta_{\{\lambda_i\},A}$.

Suppose that for a chosen nonwoven fibre $\Delta_{\{\lambda_i\},\text{fibre}} = l$; that is, the fibre appears in focus as the true focal plane is moved over a distance l. Observing that a fibre cannot interpenetrate the skin (surrogate), consideration of figure 4.2 makes it clear that if the focal plane is a distance L below the skin (surrogate) surface then

$$\tfrac{1}{2}\Delta_{\{\lambda_i\},\text{fibre}} - r \geq L.$$

Considered conversely, if L is initially very large and reduces (the focus is set very low and raised) the point at which the inequality first holds corresponds to fibres resting on the skin (surrogate) surface. An image of NW1 against glass is shown in figure 4.3a to illustrate the images that can be acquired.

Although the distinction between focused and unfocused fibres can be discerned in figure 4.3a it is not very clear. In consequence, it is helpful to enhance the raw images, which is done by considering the green channel of the RGB image and taking the modulus of the gradient. The gradient picks out the sharp changes which are characteristic of focused features and suppresses the blurred features that clutter the raw images; an enhanced version of figure 4.3a is shown in figure 4.3b.

All relevant $\Delta_{\{\lambda_i\},A}$ are reported in appendix D along with the methods used for obtaining them and details of the method for enhancing the images.

4.3.2 Problems and compromises

The ideal way to use this technique would be on the nonwoven-skin (surrogate) interface simultaneously with the collection of force data in the same way as low magnification microscopy data are gathered (§4.4). As previously stated, this is not possible. This is essentially due to a number of problems that prevent the simple DoF principle being effectively employed in the context of the experiments described in §4.4.

Obfuscation of the interface by "higher" fibres. The principal difficulty with applying the simple DoF approach to the nonwoven-skin (surrogate) interface in the experiment described in §4.4 is that—since both skin and Lorica Soft are fairly opaque—micrographs of the interface must necessarily be taken *through* the nonwoven: the interface is on the far side of the nonwoven from the microscope. This means that fibres "above" others at the interface obscure the latter from view. With the nonwovens used in this work this effect is significant enough to make the resultant images very hard to interpret (figure 4.4).

Difficulty in focusing on the skin (surrogate) surface. Skin and materials that seek to imitate it are characterised by an irregular surface, and frequently by a degree of translucency but decided non-transparency. Because of these features, it is frequently difficult to focus on the exact plane of the surface, even if the surface can indeed be reasonably approximated as a plane. Additionally, it is important to note that even if the surface is "grossly" planar, skin and many skin surrogates are covered in fine lines and wrinkles that by definition deviate from the plane: the DoF technique would unavoidably be inaccurate in this respect as it would consider the gross, planar surface not including these details. This latter problem can be overcome if the texturing is known.

Dappled colouration of the skin (surrogate). Clean, transparent materials such as glass are very uniform in appearance under a microscope, and thus the gradient image of a piece of glass is essentially blank (figure 4.3b). Skin and skin surrogates are not transparent, and are frequently quite dappled in colour; the gradient of such an image is certainly *not* blank. Depending upon the degree of dappling, this can significantly obscure the gradient image of the nonwoven fibres.

In view of these limitations it has not been possible to obtain sufficiently good images of the nonwoven-skin (surrogate) interface reliably enough to deploy this technique widely at that interface. However, the technique *does* work well if a transparent medium is used instead of the—at best partially translucent—skin (surrogate). This prompts the question of whether anything of value could be learned from such an experiment.

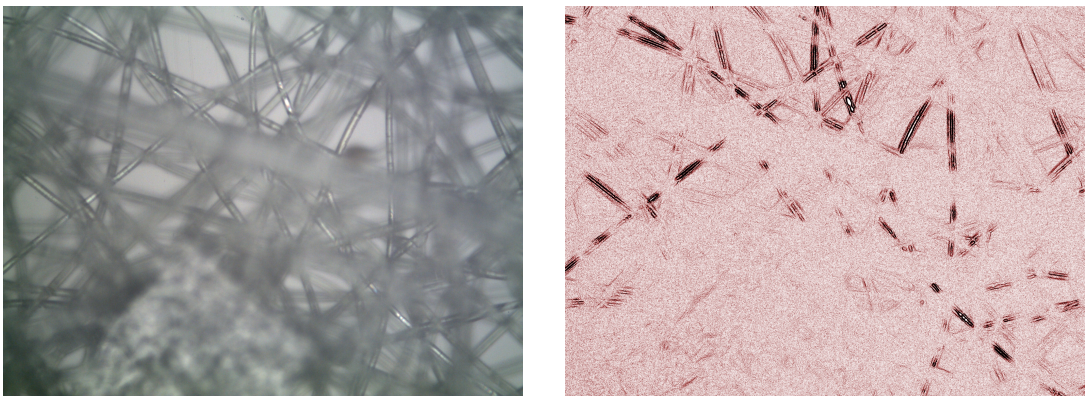

(a) (b)

Figure 4.4: Raw and processed examples of reflection microscopy of a lower NW1-glass interface at 5 kPa using a $\times 10$ lens. The obscuring effect of the higher fibres makes interpretation difficult, especially in the presence of other confounding factors.

In order to assess the extent to and manner in which the substrate[2] is likely to influence the contact behaviour it is necessary to gain some idea of how the surface responds to having a fibre segment impressed upon it. For example, if the result of a series of fibre segments being pressed against any chosen pair of surfaces is that in each case the surface essentially deforms *en bloc*—that is, with little or no "bulging out" between the contacting fibre segments—then the locations, sizes, and shapes of those contact segments can reasonably be expected to be very similar (figure 4.5a). Conversely, if there is substantial bulging in once case and not in the other then where there *is* bulging, additional fibre segments will come into contact with the surface, causing substantial rearrangement to all fibres (figure 4.5b). Similar contact would not, of course, necessarily imply similar friction, but if two surfaces were similar in this sense then the contact data that are the objective of this section could be gathered on either and apply equally well to each[3]. Additionally, a similar contact length would not necessarily imply a similar contact width.

To ascertain whether glass and skin (surrogate) are similar in this way, it is necessary to obtain the characteristic "bulge" height of the surface between fibres as a function of the degree of impression of the fibre contact segments and the typical distance between them. Given the small deformations at hand and the difficulties of measuring such small deformations directly, recourse to linear elasticity theory in a half space is in order. Given the complexity and variety of the fibre contact segments, it is not sensible to attempt to model the details directly; instead, noting that most fibres have a low curvature (§4.3.7) it is more helpful to consider the behaviour of an ensemble of straight fibres of known pitch and dimensions.

[2] That is, the body against which the nonwoven is pressed. The term includes both material and geometry.

[3] It would, of course, still be necessary to take any surface texturing into account separately; DoF methods only apply in their simplest sense to planar surfaces, though for low degrees of texturing a simple geometric correction can be applied.

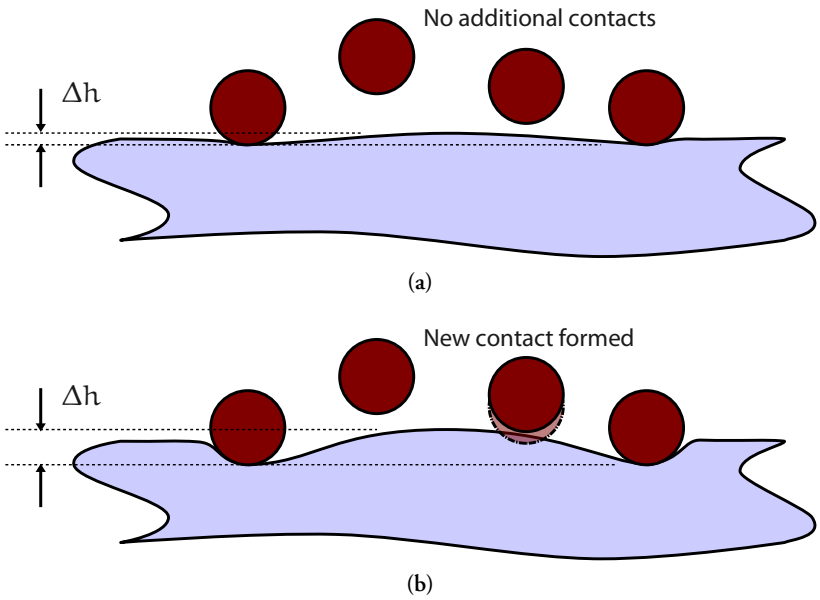

Figure 4.5: The height of the "bulge" between fibre contacts is key is determining whether the contact of a given nonwoven against two different surfaces will be similar. (a) shows the situation where the "bulge height" Δh is substantially less than the fibre diameter, which is a rough scale for the vertical displacement between the contact fibres and the second "tier"; moving to another surface for which Δh is also much less than a fibre diameter will result in little change in the contact. (b) shows a surface where the same arrangement of fibres results in different contact due to the interfibre bulge encountering the second tier of fibres. Though clearly approximate, the characteristic length Δh is useful in predicting this.

Given the linearity of the assumed theory, it is simplest to begin by considering a single fibre. Unfortunately, several apparently promising solutions to line impressions in elastic half spaces are not helpful for a variety of reasons. The first candidate, an infinitely long line force pressed into a surface both diverges logarithmically with distance from the line [159] and has a singularity at the origin, which precludes its use in establishing characteristic distances! It is clear that this logarithmic divergence will emerge whenever the problem is effectively reduced to two dimensions, so only true three-dimensional solutions could be useful. Surface displacements due to a constant line force of finite length $2L$ can easily be calculated from Boussinesq's solution for surface displacements due to a delta function normal force (see Johnson [160]):

$$\bar{u}_z(x,y) = \bar{p}\frac{1-\nu^2}{\pi E}\int_{-L}^{L}\frac{1}{\sqrt{y^2+(x-x')^2}}dx' \tag{4.1}$$

$$= \bar{p}\frac{1-\nu^2}{\pi E}\log\left(\frac{\sqrt{y^2+(x+L)^2}+(x+L)}{\sqrt{y^2+(x-L)^2}+(x-L)}\right), \tag{4.2}$$

where the line force is along $y = 0$ in the x interval $[-L, L]$, is of magnitude $\bar{p}$, and the elastic half space has Young's modulus E and Poisson ratio ν. This expression has a well-defined width, but

displacement diverges[4] at $y = 0$ meaning that it has no z scale: there is no intrinsic indentation depth to which the depression at any position can be compared. Again, it is not hard to see that this is a consequence of the singular loading: in order for a solution to have meaningful width and depression characteristics it must act over a finite area.

It is not entirely clear how this should be done; ideally the lateral pressure distribution should correspond to a cylinder, but (since the approach is only an approximation) the appropriate lengthwise distribution is uncertain. However, the elliptical Hertz distribution (considering the cylinder as an extreme ellipsoid) is very hard to analyse [161]; and though an expression *can* be generated for a lateral Hertz and lengthwise uniform distribution it is prohibitively complicated. In consequence, it is not practical in pursuit of a characteristic length to use the lateral distribution corresponding to a cylinder. It is instead expedient to consider the fibre to exert constant pressure over its area of contact; although this is formally incorrect, the error cannot be expected to be large. An expression for the depression due to a uniform region of force density p of dimensions $2L \times 2a$ can be obtained by integrating $\bar{u}_z(x, y - y')$ (equation 4.2) over the lateral uniform distribution having set $\bar{p}$ to unit magnitude:

$$\begin{aligned} u_z(x,y) &= \int_{-a}^{a} p\bar{u}_z(x, y-y')dy' \\ &= p\frac{1-\nu^2}{\pi E}\int_{-a}^{a} \log\left(\frac{\sqrt{(y-y')^2+(x+L)^2}+(x+L)}{\sqrt{(y-y')^2+(x-L)^2}+(x-L)}\right)dy' \\ &= p\frac{1-\nu^2}{\pi E}\left(\begin{array}{r} f(y+a,x+L,x-L) - f(y-a,x+L,x-L) \\ + f(x+L,y+a,y-a) - f(x-L,y+a,y-a)\end{array}\right), \end{aligned} \tag{4.3}$$

where

$$f(\alpha,\beta,\gamma) \coloneqq \alpha \log\left(\frac{\sqrt{\alpha^2+\beta^2}+\beta}{\sqrt{\alpha^2+\gamma^2}+\gamma}\right).$$

The behaviour of this function as $\sqrt{x^2+y^2} \to \infty$ and when $x = y = 0$ are acceptable. Addressing first the behaviour at large distances from contact, consider $f(\xi+\delta, \zeta+\epsilon, \zeta-\epsilon)$ as $\sqrt{\xi^2+\zeta^2} \to \infty$.

$$\begin{aligned} f(\xi+\delta,\zeta+\epsilon,\zeta-\epsilon) &= (\xi+\delta)\log\left[\frac{1+\dfrac{\epsilon}{\sqrt{(\xi+\delta)^2+(\zeta+\epsilon)^2}+\zeta}}{1-\dfrac{\epsilon}{\sqrt{(\xi+\delta)^2+(\zeta-\epsilon)^2}+\zeta}}\right] \\ &\approx (\xi+\delta)\left[\frac{\epsilon}{\sqrt{(\xi+\delta)^2+(\zeta+\epsilon)^2}+\zeta}+\frac{\epsilon}{\sqrt{(\xi+\delta)^2+(\zeta-\epsilon)^2}+\zeta}\right] \\ &\approx \frac{2\epsilon(\xi+\delta)}{\sqrt{\xi^2+\zeta^2}+x}. \end{aligned} \tag{4.4}$$

[4] Equation 4.2 is computed on the assumption that $y \neq 0$, so care must be taken in evaluating the expression there. It is easier to see that equation 4.1 collapses to $\alpha\int_{-L}^{L}\frac{1}{|x-x'|}dx'$, which diverges since the singularities at $x' = x \pm \epsilon$ have the same sign (due to the modulus in the denominator of the integrand) and thus cannot cancel.

Though the denominator of equation 4.4 tends to infinity, the numerator may also do so in proportion depending on the direction in which the limit is taken. However, the combination of functions in equation 4.3 removes the variables from the numerator leaving only finite constants, so surface displacement does indeed tend to zero at large distance from the fibre contact. Equation 4.3 is trivial to evaluate at $y = x = 0$ (the point of greatest displacement):

$$u_z(0,0) = 2p\frac{1-\nu^2}{\pi E}\left[a\log\left(\frac{\sqrt{a^2+L^2}+L}{\sqrt{a^2+L^2}-L}\right)+L\log\left(\frac{\sqrt{a^2+L^2}+a}{\sqrt{a^2+L^2}-a}\right)\right].$$

Before any characteristics can be obtained, the parameters of the model (a, L, characteristic distance between fibres (λ), and p) must be related to known quantities. For L and λ this is easily done: results in §4.3.7 show that the mean fibre contact length varies very slowly with pressure and is typically about 400 µm, and that if the fibre contacts were laid out in parallel and equally spaced straight lines then they would be separated by about the same distance. Contact pressure can also be dealt with: taking the assumption of uniformity, $p = p_{nom}\lambda/2a$ where p_{nom} is the nominal pressure. Contact width[5] is most convincingly estimated by making use of the two-dimensional Hertz theory for an infinite cylinder pressed into an elastic half space. For this system, the contact width is given by

$$a = \sqrt{\frac{4PR}{\pi E^*}}, \tag{4.5}$$

where P is the linear force density, R is the cylinder radius (set to 10 µm in the following analysis—see table 4.1), and (for a rigid fibre) $E^* = E/(1-\nu^2)$ is the plane modulus [162]. Linear force density is related to mean pressure by $P = 2pa = p_{nom}\lambda$ [162], so

$$a = \sqrt{\frac{4p_{nom}\lambda R}{\pi E^*}} = \sqrt{\frac{4\lambda R}{\pi}\Pi}, \tag{4.6}$$

where $\Pi := p_{nom}(1-\nu^2)/E$ characterises pressure in a material-independent way. Equation 4.3 can thus be written as a function of the parameters Π and L and the variables x and y; a graph of deflection at various x and y locations around a fibre of length 400 µm for $\Pi = 1\times10^{-2}$ is shown in figure 4.6.

The original question of the characteristic "bulge" between fibres can now be addressed by taking multiple instances of this solution centred on locations separated by λ and adding them together. An example of this is shown for reference in figure 4.7; the family of curves represents surface deflection as a function of distance from the central fibre's axis for a variety of values of Π; L is always taken as $\frac{1}{2}\times 400\,\mu m = 200\,\mu m$, and $x = 0$. The maximum "bulge" height for fibre contact segments with the typical parameters used in the graph is tabulated in table 4.2 for a variety of Π values; as noted above, L and λ appear not to change greatly over a wide range of Π

The results presented in figure 4.7 and table 4.2 suggest that—provided $\Pi \lessapprox 5\times10^{-2}$—the bulge is sufficiently small that few "additional" fibre contacts will be formed; that is, moving between two

[5] Recalling the assumptions of the Hertz theory (§2.1.6) there is no distinction between the contact width measured along the curved surface produced by the impressed body and the simple distance.

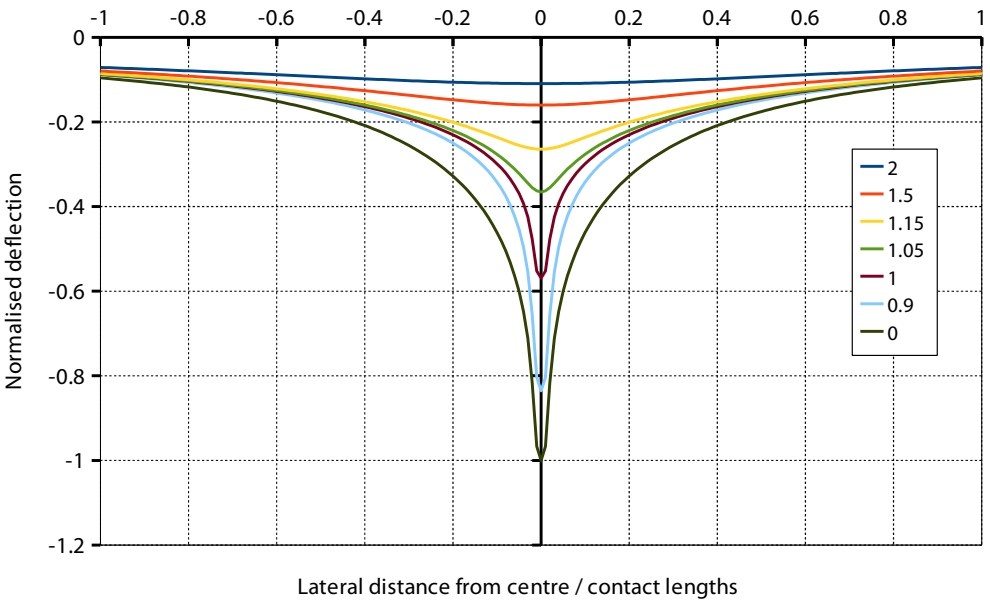

Figure 4.6: A graph of surface deflection due to a single fibre contact of length 400 µm, as calculated on the basis of equation 4.3. The different curves represent deflection in different lateral planes along the fibre's axis (locations are given in multiples of L from the centre of the contact); it is interesting to note the very limited variation within the contact region.

Pressure (Π)	Maximum deflection / µm	Minimum deflection / µm	"Bulge height" / µm
1×10^{-3}	2.2×10^{-2}	7.5×10^{-3}	1.4×10^{-2}
1×10^{-2}	5.9×10^{-1}	2.4×10^{-1}	3.5×10^{-1}
3×10^{-2}	2.8	1.2	1.6
5×10^{-2}	5.8	2.7	3.1
7×10^{-2}	9.3	4.4	4.9
1×10^{-1}	15	7.5	7.8

Table 4.2: Bulge height calculated on the basis of five fibres aligned as described in the text. The "pressure" is in fact $\Pi = p_{nom}(1-\nu^2)/E$ in order to make the table material-independent.

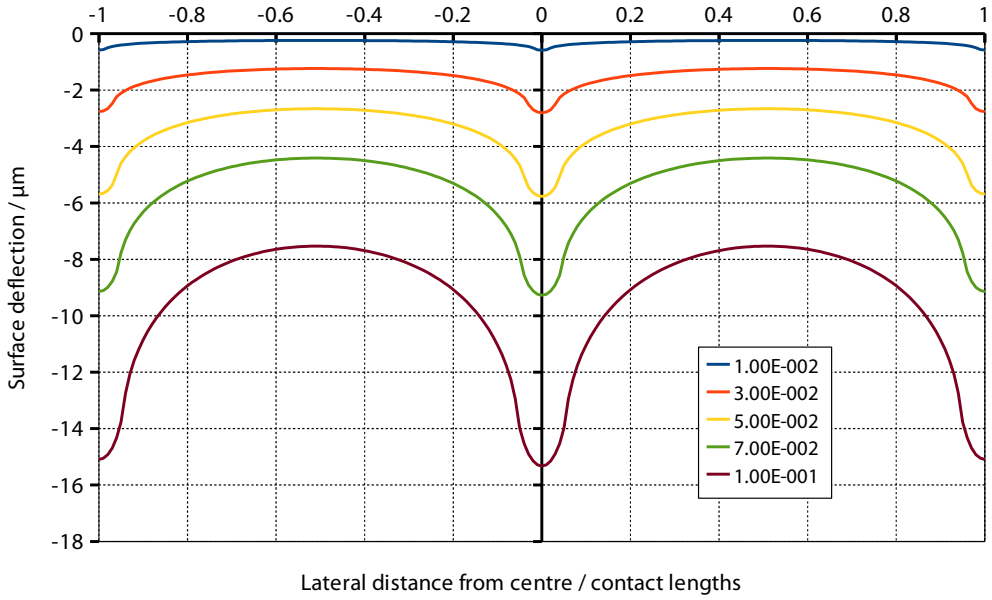

Figure 4.7: Surface deflection due to parallel, aligned fibre segments of length 400 µm each separated by 400 µm. The curves each represent a different pressure (material independent—Π values given in the key). For comparison, the fibre diameter is taken as 20 µm. For simplicity only five fibres were used to create this graph, but as deflections rapidly decay very little error is introduced.

materials for which Π obeys this condition is unlikely to cause any substantial alteration in the fibre contacts.

Since the indentations are on the level of microns, in applying this model to skin the relevant modulus to use in calculations is that of the stratum corneum, representing as it does the outermost 10 µm–20 µm or so of the skin. Though there is significant disagreement about the modulus of the skin as a whole (§2.2.3), it is apparent from the literature review (§2.2) that the stratum corneum is much the stiffest layer. The modulus of stratum corneum varies widely with hydration level, but the lowest value reported in any way by the first major study to measure stratum corneum modulus [51] was 6×10^6 Pa; that is, 120 times the maximum pressure used in these tests. Π is thus always less than 8.3×10^{-3}. At this level, the "bulge height" is 0.3 µm, which is around 1 %–2 % of a fibre diameter. Based on this modulus, contact measurements made on glass (where essentially *no* deformation occurs) can be taken to be accurate surrogates for measurements on skin.

It should be noted that the modulus quoted corresponds to stratum corneum in equilibrium with 100 % relative humidity; at 50 % relative humidity the same study [51] gives the stratum corneum's modulus as about 1 GPa: the modulus used is almost certainly a substantial underestimate of the appropriate value. However, this will merely cause *smaller* bulges, thus improving the applicability of measurements on glass still further.

By virtue of its laminar structure, Lorica Soft exhibits an even more extreme difference between its tangential modulus (~6 MPa up to about 10 % strain, determined by a simple uniaxial stretch) and

its normal modulus (~100 kPa up to about 10 % strain, determined by compression) than skin does. Although the thickness of the polyurethane coating on Lorica Soft could not be exactly determined it was certainly a small fraction of the total thickness of about 1 mm. In consequence by simple proportional reasoning its modulus must be many times the ~6 MPa tangential modulus of the Lorica Soft. By the same reasoning applied to skin it is thus still more valid to apply measurements on glass to Lorica Soft than to skin.

These conclusions, of course, carry caveats: they are only accurate within the assumption of linear elasticity and lack of other surface forces. Since strains are so small, linear elasticity will almost certainly be a reasonable approximation. As an approximation, the modulus value used must be taken over the appropriate strain range, but as Park & Baddiel [51] only used strains up to 1 % in their measurements on skin the range is indeed appropriate; and Lorica Soft has been measured to behave fairly linearly well beyond this range. The impact of significant adhesion (if it is present) would be to cause the surface to "hug" the contact fibres more, leading to a larger bulge. However, adhesion only significantly alters contact in this way for very low surface stiffness or very high surface affinities. The fact that the nonwoven fibres used in this work are made of polypropylene militates against the latter; the former must be allowed, but the degree of compliance required given the expected low surface affinities would seem unlikely.

In summary, although contact measurements cannot be taken on skin and Lorica Soft (as would be ideal), measurements made on glass are excellent surrogates, provided the surface relief of the skin (surrogate) is taken into account.

4.3.3 Apparatus

The apparatus designed to gather DoF data is very simple; it need only apply known pressures within the confined space of the microscope stage, so consists of two perspex plates and an arrangement of springs (figure 4.8). The springs are above the upper plate and serve to apply a compressive force. As the wing nuts are tightened, the force applied increases; the M3 thread on the wing nuts and bolts has a pitch of 0.5 mm so the vertical travel can be controlled very precisely. The rods are identical to those used in the other principal piece of apparatus, and are illustrated in figure B.5. The lower plate is cut from 8 mm perspex sheet; the upper is from 4 mm perspex sheet to minimise the weight.

The springs themselves are high-precision springs obtained from Lee Spring Limited (Wokingham, UK); they are LC 020CD 07S ($l_0 = 15.88\,\mathrm{mm}$, $k = 0.64\,\mathrm{N \cdot mm^{-1}}$) for the higher loads, or LP 016BC 03 ($l_0 = 15.88\,\mathrm{mm}$, $k = 0.141\,\mathrm{N \cdot mm^{-1}}$) for lower loads.

The pressure plates apply their pressure to a piece of nonwoven held between a pair of crossed microscope slides (chosen for transparency and flatness; $24.5 \pm ¼\,\mathrm{mm} \times 76.0 \pm ¼\,\mathrm{mm}$). The high stiffness of glass compared to the applied pressures ($E_{glass} \approx 80\,\mathrm{GPa}$ [156], $p_{max} = 50\,\mathrm{kPa}$) means that no significant deformation of the slides will occur, and thus flat "anvils" can be safely used (§B.1.2).

Due to the difficulty in assessing when the springs first apply pressure to better than about 0.5–1 rotation, the very lowest pressures are achieved using a different method so as not to introduce a substantial error into the applied pressure. The alternative method is pure deadweight loading, using crossed microscope slides to "sandwich" the nonwoven sample, omitting the upper plate and adding a small additional weight with a hole (for microscopy) added on the top. This simple system

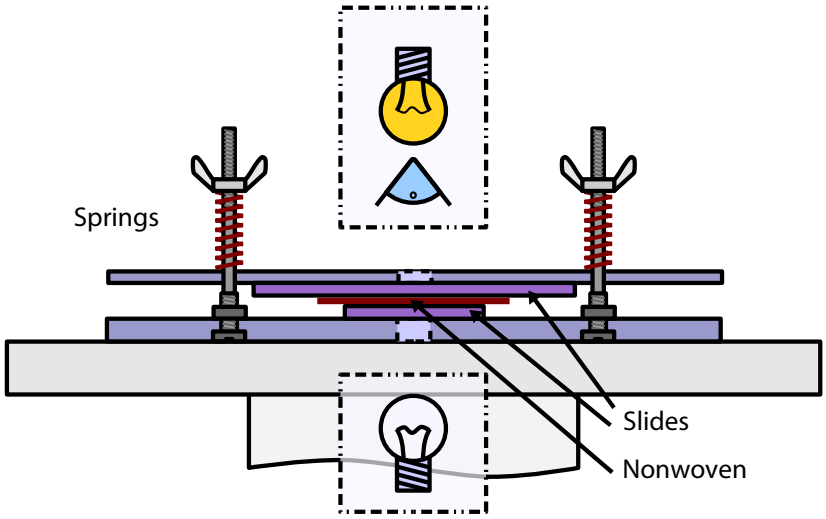

Figure 4.8: Simple apparatus used to apply pressures to nonwoven under a microscope. The upper and lower surfaces are drilled so that there is an entirely uninterrupted light path from the light source to the immediate environment of the nonwoven, and from there to the microscope lens. The slides and nonwoven are not attached to the rest of the assembly and can be freely positioned.

works well for low pressures, but the size of the required deadweight and the consequent instability that would be suffered make it inappropriate for higher pressures.

4.3.4 Method for raw data collection

The method for obtaining contact lengths and areas can be divided into two main stages: gathering raw micrographs; and processing those micrographs into distances. The former is addressed here; the latter is the subject of §4.3.5.

Before any data can be gathered, the nonwoven samples must be prepared. The samples are cut from each of the nonwovens, and are approximately 30 mm square and marked for orientation. Preliminary experiments (using a minor variant of the same method) have shown that nonwoven samples behave "plastically" within the pressure range used here; that is, contact images taken at a low pressure before and after subjecting the sample to a nominal 50 kPa pressure show significant differences, even to the eye without substantial processing (figure 4.9). Though a study of this plastic behaviour would itself be interesting, it is not within the remit of this work, so the problem is avoided by using each nonwoven sample only once before discarding it.

Micrographs have been gathered using a DMLM microscope and DFC 320 (both Leica Microsystems (UK) Ltd, Milton Keynes, UK) and QWin software (version 3.2.0, Leica Microsystems (UK) Ltd). The QWin "Mosaic" facility (for gathering multiple images and splicing them together) was used to enable large (approximately 5 mm square) micrographs to be obtained. Images were gathered in reflection mode so as to reduce variation in lighting that the "upper" nonwoven surface would suffer by virtue of the fibres beneath. In consequence, it was necessary to use shading correc-

(a)

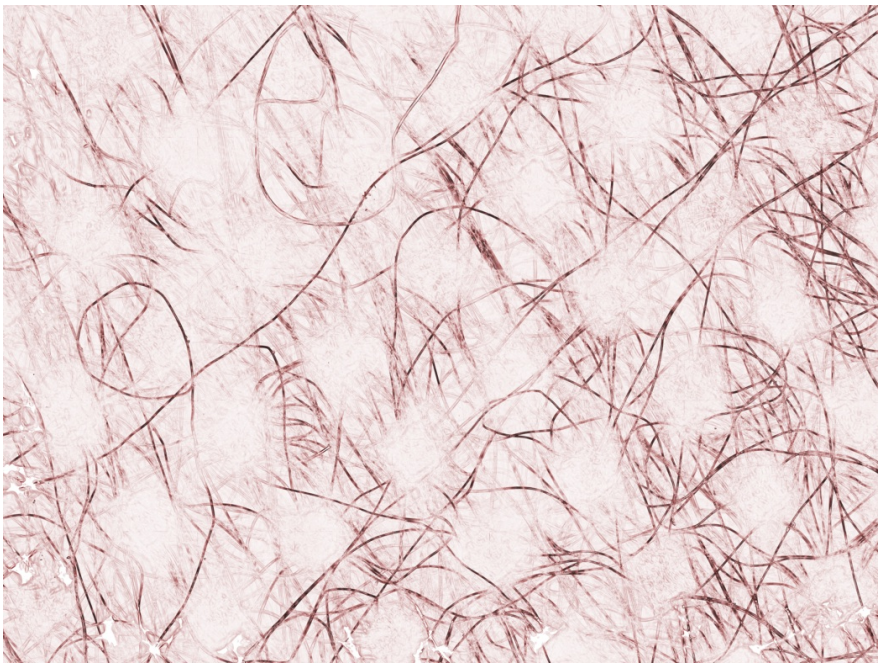

(b)

Figure 4.9: Images of nonwoven at 0.24 kPa (a) before and (b) after compression to 52 kPa, enhanced using the differential procedure described in §4.3.5. The reduction in the total length of contact fibres is apparent.

tion to ameliorate the otherwise marked darkening of off-axis image pixels; the procedure for this is described in the QWin documentation.

The method for gathering raw micrographs is as follows. It is assumed that at the start shading correction has been enabled; that the slides have been cleaned using alcohol and a soft cloth; and that the microscope's $\times 10$ lens is in position.

1. Place the lower slide symmetrically over the hole in the lower plate. Position the nonwoven sample *upside down* (surface of interest uppermost). Put the upper slide crossed over the lower one, carefully ensuring that it is symmetrically and squarely placed.

   For nominal pressures of 0.5 kPa and 1.5 kPa

2. Place the appropriate load symmetrically on the upper slide.

   For nominal pressures of 5 kPa, 15 kPa, and 50 kPa

2. Place the upper plate on the guide rods and lower it gently into position against the upper slide. Ensure that it is free to rock in all directions. Place any spacers needed on the rods, then the lower washers, springs, and upper washers. Finally, screw the wingnuts on until *nearly* in contact with the upper washers.
3. Carefully tighten each wingnut until the spring offers first resistance. Incrementally tighten each wingnut to the correct number of rotations, making sure always to keep the springs as balanced as possible. It is good practice to tighten diagonally opposite nuts directly sequentially.

   Continuing for all nominal pressures…

4. Focus the microscope on the lower surface of the upper slide. Move around the region of interest, checking that the surface remains in focus throughout (dust motes are helpful indicators). If this is not the case, inserts shims between the microscope stage and the lower surface until it is.

   Important: Judge focus based on the image shown on the computer screen: human eyes are much more accommodating of poor focus than a camera, and the latter records the results.
5. Use QWin's Mosaic feature to gather an image nominally 5 mm square (true dimensions 4316 µm × 4272 µm). Export it in the Tagged Image File Format (*TIFF*).
6. Use the differential enhancement Matlab routine given in listing D.1 to enhance the raw image. Check that the contact density is broadly constant across the image. If it is not the sample may not be level: check, and if necessary repeat the method from step 4.
7. Disassemble the upper plate assembly or remove the deadweights (as appropriate), then discard the nonwoven sample.

This procedure results in an enhanced image showing the contact fibres; an example is shown in figure 4.10. The procedure for converting this enhanced raw image into quantitative information on fibre contact segment conformation and length is given in the following section.

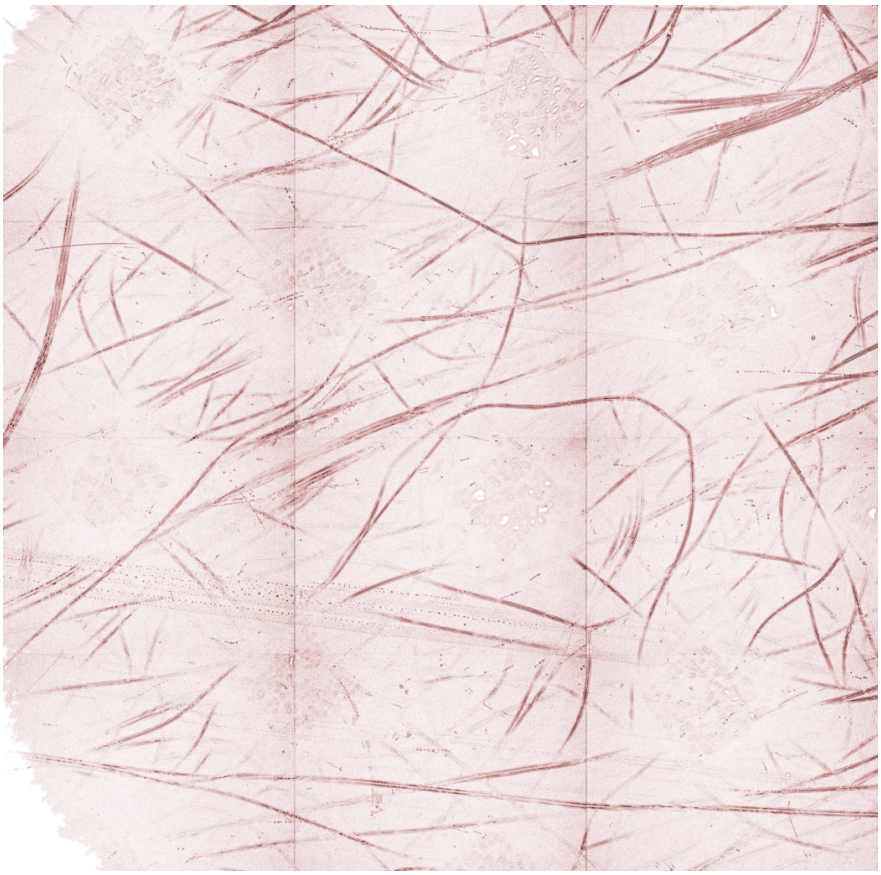

Figure 4.10: An example of an image collected and enhanced according to the procedure described in §4.3.4. The vertical lines correspond to imperfect splicing of the 12 constituent images; the white patches in the top and bottom left corners are obscured regions, but as the regions contain bonding points no fibres were missed because of them.

4.3.5 Method for processing raw data

Although the contact fibre segments shown in figure 4.10 are fairly clear to the human eye (especially when seen in conjunction with the original image), to a computer the task of identifying contact fibre segments is formidable. First, segments can have essentially any conformation; second, they are far from uniform in appearance and colouration; and third, the dust and other marks (which provide material assistance in focusing whilst remaining dilute enough to have negligible impact on the contact behaviour) which the human eye immediately discounts can in some cases superficially resemble fibres. It may well be possible to overcome some or all of these problems partially or totally, but it is by no means trivial, and certainly no "off the shelf" product will serve. In view of this and the comparative ease with which the human eye can identify the relevant segments, a semi-automated approach has been adopted.

In overview, this approach is to print out the enhanced raw images, manually trace them onto

acetate sheet, scan this back into the computer, and then use readily available software to perform the much simpler task of converting uniformly coloured lines on a blank background into Bézier curves. From this point, obtaining any desired information is relatively simple. By redigitising after manually tracing the fibre contact segments the onerous and time-consuming task of measuring each segment individually by hand is avoided, and the potential for obtaining much richer data is presented.

Raw and enhanced images have been printed out on A3 paper using a C203 Digital MFD (Konica Minolta Business Solutions (UK) Ltd, Basildon, UK). A3 acetate sheeting (Diacel 115 µm sheet A3, FLM400020, West Design Products Ltd, Folkestone, UK) was secured over the enhanced image with a pair of paper clips and the focused fibres traced using a Rotring Isograph pen (0.5 mm nib, Sanford GmbH, Hamburg, Germany) with red ink (Rotring Drawing Ink, Sanford GmbH); as in the validation experiments reported in §D.2, the fibres were considered to be out of focus as soon as blurring (equivalent here to reduction in intensity) was discernible. An assessment of the repeatability of the technique up to this point is described in §D.4.

The traced image was then scanned, again using a C203 Digital MFD and scanning at 200 dpi × 200 dpi[6] to a single page TIFF format. This image was initially processed using Gwenview (version 2.3.2, http://gwenview.sourceforge.net) to crop off the labelling and other uninformative regions and convert the image to bitmap format. The bitmap was then transferred to the GNU Image Manipulation Program (*the GIMP*, version 2.6.7, http://www.gimp.org), where the colour curves were adjusted to a step function (transition at 50 % intensity) to suppress grey noise and reduce intensity variation in the lines. Additionally, artefacts such as dust on the scanner glass and smudges on the acetate were removed at this stage. The "cleaned" bitmap was then saved and passed to a BASH[7] script which ran an open source bitmap tracer (AutoTrace, version 0.31.1, http://autotrace.sourceforge.net) to extract Bézier curves followed by a programme written by the present author which extracted curve lengths and mean curvatures from the Bézier curves; this script and the programmes it calls are described more thoroughly in §D.5.

Having passed through this process the data were in a form in which they could readily be interrogated.

4.3.6 Schedule of experiments

As all experiments were based on compression of nonwoven against glass, the schedule only includes variation of applied pressure and nonwoven, as well as repeats. As a corollary experiment to the pulling experiment described in §4.4 the pressure range here was chosen to cover that used there: the minimum pressure was 0.40 kPa and the maximum 43.7 kPa. As the full procedure of taking measurements, and especially tracing and processing the resultant images is time consuming, five pressures were selected across this range, spaced logarithmically at nominal values of 0.5 kPa, 1.5 kPa, 5 kPa, 15 kPa, and 50 kPa. Three repeats were run for each nonwoven at each pressure, giving a total

[6] This relatively low resolution scan is in fact superior for these purposes to a higher resolution scan because it does not detect the variability in hue and intensity that are inevitable in a line created by a narrow tube with a propensity to clog dispensing a suspension of pigments onto a potentially dirty surface with low surface energy.

[7] See http://www.gnu.org/software/bash/bash.html for a description of BASH.

Nominal pressure / kPa	True pressure / kPa	Method	Notes
0.5	0.404 ± 0.008	Deadweight	—
1.5	1.32 ± 0.03	Deadweight	—
5	4.7 ± 0.2	Plates; LP 016BC 03 springs	8 turns
15	13.8 ± 0.6	Plates; LC 020CD 07S springs	6 turns
50	43 ± 1	Plates; LC 020CD 07S springs	20 turns

Table 4.3: The true pressures applied during contact measurements corresponding to the nominal pressures used in the text, along with estimates of the error in each of the pressures and details of how they were applied.

of 45 experiments. Experiments which did not yield useful data were repeated, so a few more than 45 were run to obtain a full set of data.

Experiments were run by nonwoven; that is, (with the exception of faulty experiments later repeated) all NW1 experiments were done first, then NW3, and finally NW6. Since these runs have only the compression kit in common, and the springs were kept far from their yield points (specified by their manufacturer) this is unlikely to have introduced any error. Within each nonwoven run, complete sets of experiments covering all five pressures were completed before any were repeated, but the order in which the pressures were tested was randomly chosen for each set.

The exact pressures corresponding to the nominal pressures given above and the methods by which they were achieved are described in table 4.3. The errors given in this table are due to imperfect alignment of microscope slides, imperfect knowledge of weights (irrelevant for plate pressures), uncertainty over whether wingnuts were applying load, and error in the number of turns applied to the nuts. The last was principally due to uncertainty as to when the spring first began to compress. Details of the error calculations are given in §D.6.

4.3.7 Results

The complete raw results are very extensive and relatively uninformative, even to a practised eye, so they are included neither here nor in an appendix. However, a set of example images showing a single micrograph through its various stages of processing are shown in figure 4.11.

The contact length data from each micrograph can be represented as a single point on a graph of contact length against pressure. Such a graph has been produced for each nonwoven, showing three repeats at each of the five pressures; these graphs are shown in figure 4.12. Additionally, an example of the mean curvature graphs is given in figure 4.13; it corresponds to NW3 and has the highest correlation of all three fabrics ($R^2 = 0.17$), with NW1 and NW6 at $R^2 = 0.14$ and $R^2 = 0.05$, respectively. The curvatures are given in units of inverse contact length; in these units two similar curves return the same value irrespective of their scale.

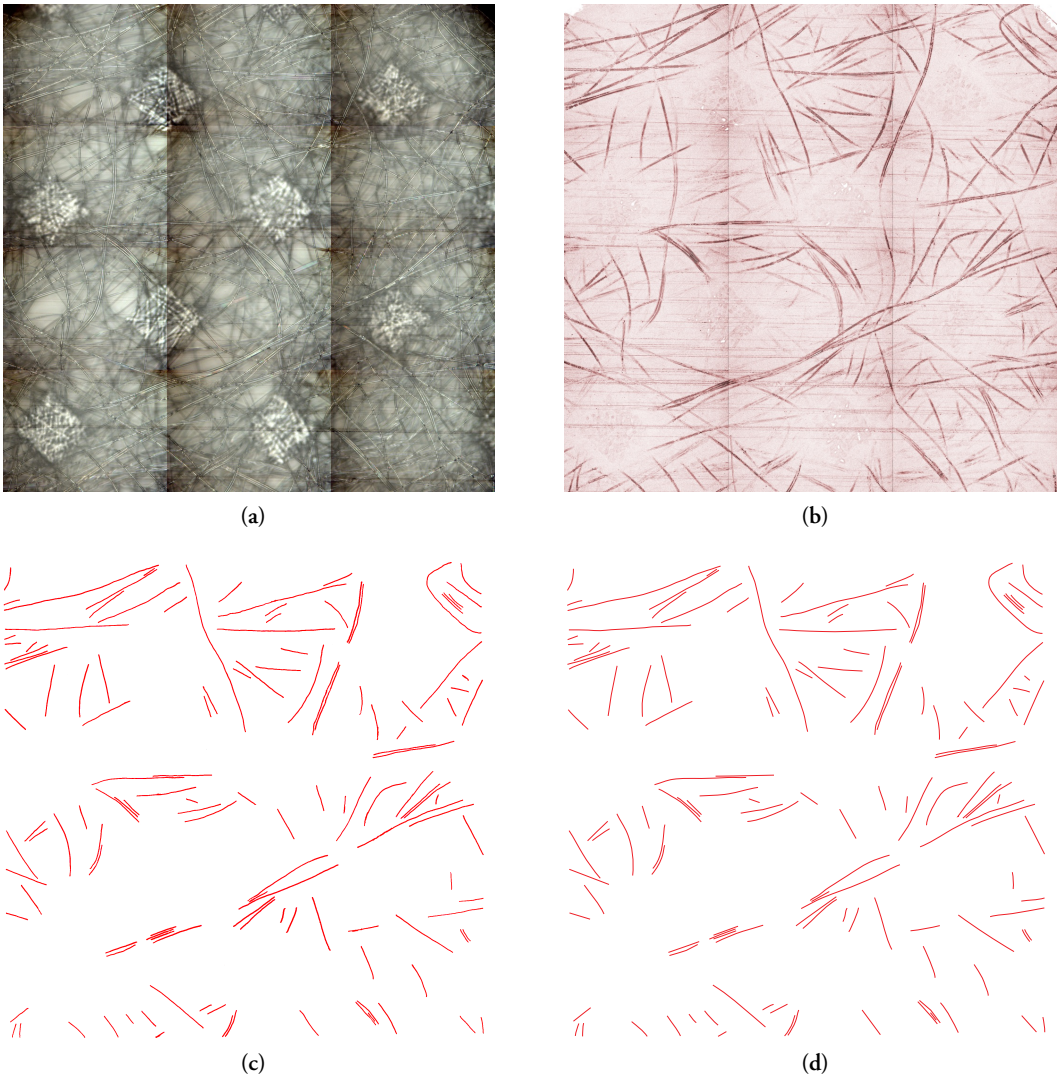

Figure 4.11: An example of a single micrograph image through its various stages of processing. (a) shows the raw image; (b) shows the images after differential enhancement; (c) shows the result of manual tracing; and (d) shows the image after conversion to Bézier curves. After this stage processing is limited to simple extraction of parameters from the curves.

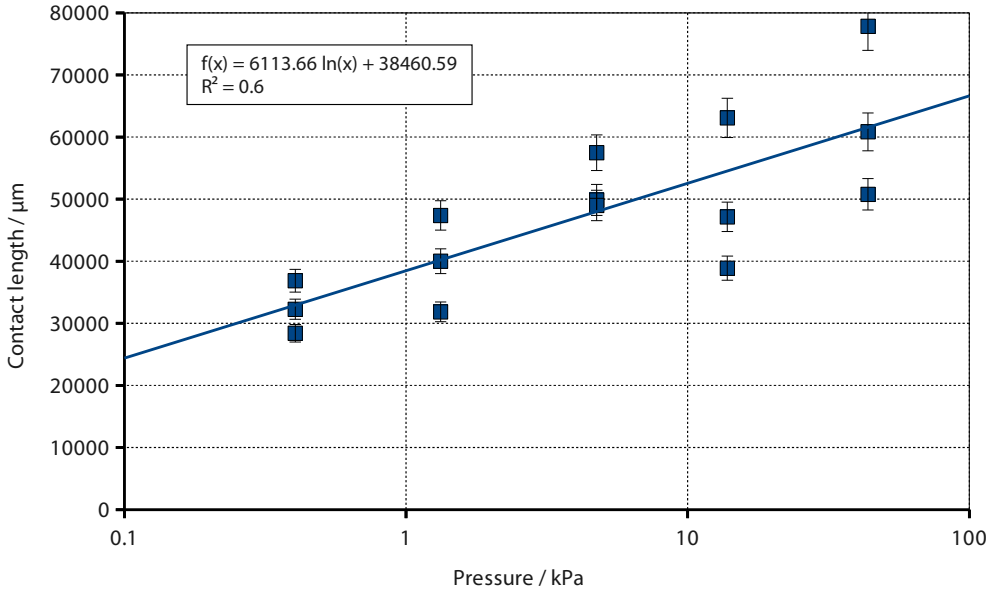

(a) NW1

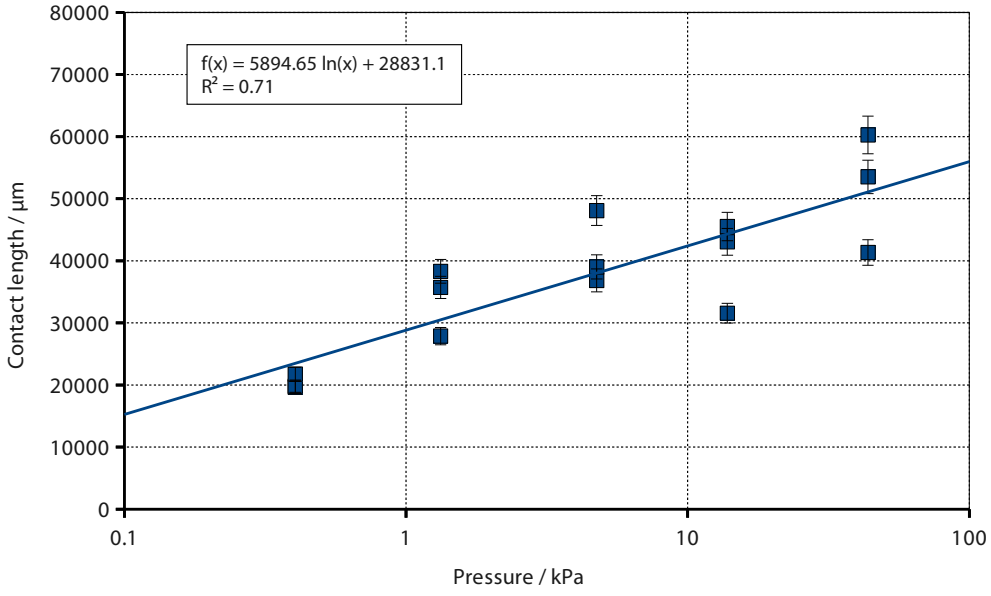

(b) NW3

Figure 4.12: Contact length against pressure for all nonwovens and glass. Each point corresponds to a single micrograph. In all cases the pressure error bars are smaller than the marker; contact length error bars are based upon the *approximate* ±5 % total process error identified in §D.4. *Continues…*

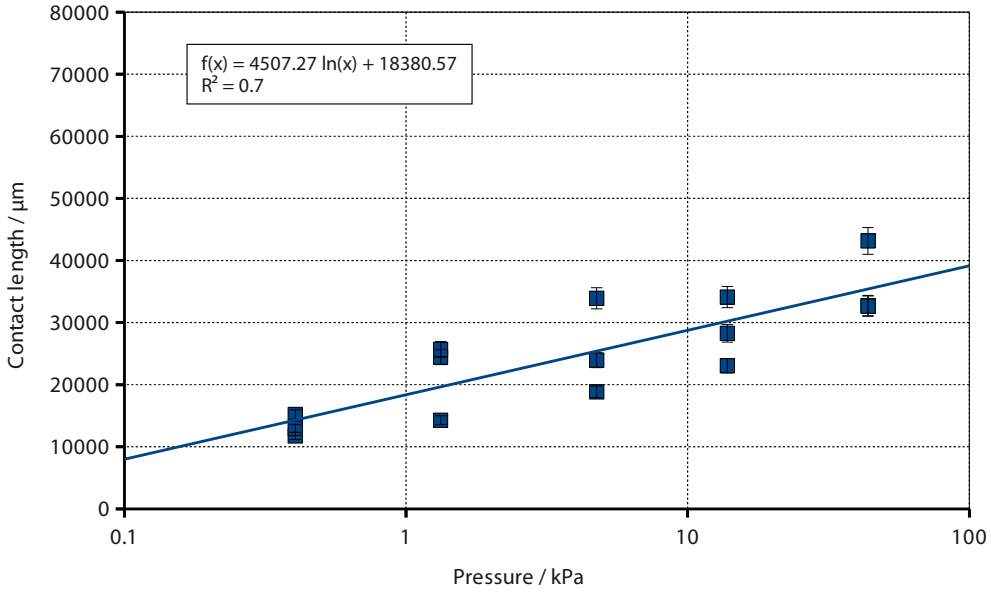

(c) NW6

Figure 4.12: *…Continued.*

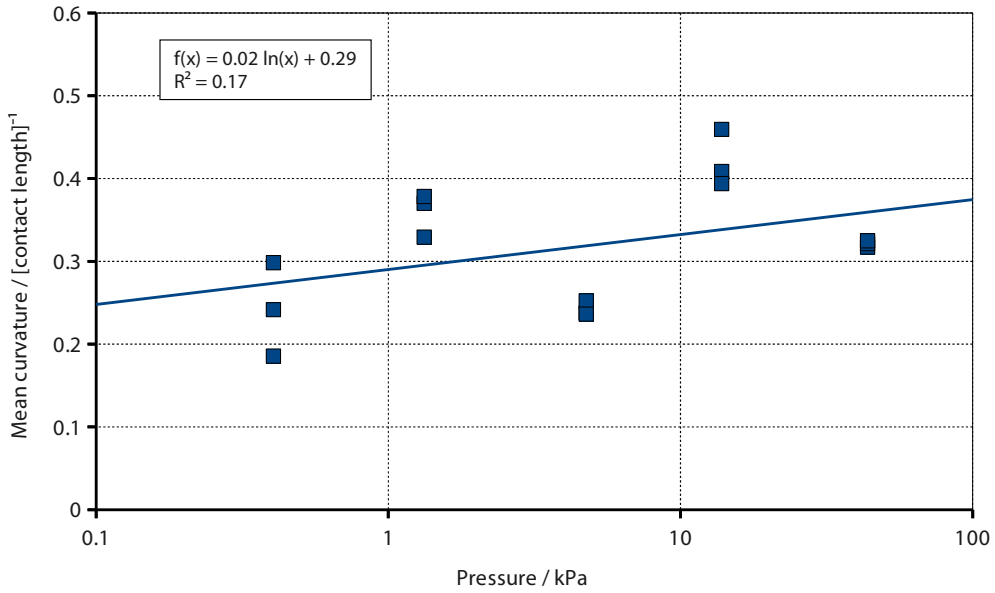

Figure 4.13: Mean curvature against pressure for NW3. Neither in this case nor in any other was there a strong correlation, nor was there any reason to expect one.

4.3.8 Analysis and comments

The contact data shown in figure 4.12 are interesting in their own right, and can be processed to provide still more information. Two features of the "raw" graphs are particularly interesting. First, at a given pressure the spread of contact lengths is much larger than can be attributed to the error in the technique (indicated by the error bars—§D.4). This implies that it is principally due to material variation. The second observation is the very slow (approximately logarithmic) increase of contact length with pressure: a pressure increase of two orders of magnitude leads to less than a factor of three increase in contact length in all cases. This is very surprising.

The combination of the two features noted is cause for a little concern: if the contact length increases only very slowly and the sample-to-sample variation is large, then any friction quantities that depend strongly on contact length will also vary more strongly with the random features of the particular sample at hand than with the independent variable of pressure. If this were indeed the case then in the context of this project very substantial noise would be anticipated on friction data. More broadly, when this work was applied and subtle changes made to nonwoven designs based upon it their effects would likely vanish in the noise created by the poor tolerance to which nonwovens seem to be produced.

Before proceeding, the issue of the relief of skin (surrogates) must be addressed. As alluded to many times, this feature is not present in glass, and the DoF technique would be blind to it if it were. In order to obtain an accurate assessment of the true contact lengths this must be taken into account. However, before undertaking substantial work it is wise to consider what the benefit might be. The way that such work would proceed would be to measure the relief of the skin (surrogate) and produce a statistical description of the proportion of the surface that is "at the top". The measured contact length would then be normalised to this (for both skin and Lorica Soft) and analysis of the corrected values would proceed. In other words, all of the nonwovens would be normalised in the same way for a given surface, and (following from the indentation analysis in §4.3.2) the normalisation would not vary with load. In consequence, neither the variation of length with load nor the comparisons between the nonwovens would appear any differently whether the lengths were corrected or not, other than by a change of scale. It has therefore been concluded that such a time-consuming and only mildly beneficial project should not be undertaken.

It is worth briefly considering a circumstance in which the founding assumptions of this contact work would be called into question. If the surface of the skin were *so* corrugated that the stiffness of the stratum corneum was *not* the principal stiffness determining deformation at the scale of tens of micrometres then both the earlier analysis and the conclusion of the previous paragraph would be in doubt. For example, if (in the extreme) the skin formed *villus*-like protrusions on scales substantially larger than the stratum corneum thickness then the behaviour of the skin surface would be determined by the bending stiffness of the *villi*, not by the stratum corneum compression modulus. This would invalidate the results of §4.3.2, and would mean that the skin relief was very variable with pressure, which would make contact results gathered on any surrogate surface of unclear applicability. Fortunately, the situation outlined is not the case, but it is not clear where on a spectrum between a smooth laminate and a *villus*-studded surface the skin really lies. This matter deserves more study in the future, but for now it is assumed that the "smooth laminate" description is more

accurate.

The principal shortcoming of the new experimental data is that they relate to contact *length* rather than contact *area*. No effective means of measuring contact width has been found, but by making some assumptions it is possible to infer the contact width and thus area from the length data already gathered. To do this, the same simple model can be used as was reported in §4.3.2, where it was used to estimate bulge height. However, whereas there (for simplicity) the contact length was assumed constant, here it is allowed to vary according to the logarithmic form observed.

To recapitulate, the model is a compromise between accuracy and solubility, assuming that contact fibres are straight and exert uniform pressure over their whole (rectangular) contact region and then (eliding the slight contradiction) determining the contact width by reference to an infinitely long Hertzian cylindrical contact with equivalent mean line loading. These isolated fibres are then combined (noting the linearity of simple elastic equations) by setting each of them to the mean length and arranging them in "ranks" of parallel fibres, separated so that the fibre contact length per unit area is correct. Clearly, several aspects of this approximate treatment are inaccurate: perfect accuracy is not claimed, nor indeed is it a primary aim; a guide as to the nature and variation of contact behaviour with contact pressure is the principal objective.

Referring to equation 4.6 and observing that $\lambda = 1/\hat{l}$, where $\hat{l}$ is the contact length normalised to sampled area,

$$a = \sqrt{\frac{4R}{\pi E^*}\frac{p_{nom}}{\hat{l}}}.$$

Since all of the contact length against pressure graphs are well-fit by $\hat{l} = \delta \log(p_{nom}) + \epsilon$ this can be written as

$$a = \sqrt{\frac{4R}{\pi E^*}\frac{p_{nom}}{\delta \log(p_{nom}) + \epsilon}}. \tag{4.7}$$

Since the two most commonly advocated models of skin-X friction are adhesion and "viscoelastic ploughing", it is interesting to predict the variation of contact fraction and a representative quantity for viscoelastic dissipation as functions of pressure. Considering first contact fraction, it is clear that by use of equation 4.7

$$\phi := \frac{A_{true}}{A_{nom}} = 2a\hat{l} = \sqrt{\frac{16R}{\pi E^*}}\sqrt{p_{nom}\hat{l}}.$$

Again, using the logarithmic fit to the experimental curves this becomes

$$\phi = \sqrt{\frac{16R}{\pi E^*}}\sqrt{p_{nom}\{\delta \log(p_{nom}) + \epsilon\}}.$$

In principle all of the quantities in this equation are determinable or known, but in practice the reduced modulus for the stratum corneum (the relevant layer—§4.3.2) is poorly known and very dependent upon ambient relative humidity. Fortunately, this merely represents a scaling factor, so although the graphs in figure 4.14 have assumed a reasonable value of 500 MPa [51] the form of the graph is not dependent on this value; the form equally applies to Lorica Soft. The graphs themselves are very interesting, both individually and in comparison with each other. All are similar in form;

a power law fit is good in all cases, with an exponent in the range 0.57–0.61. It is also informative to compare this to the behaviour that would be predicted for a single long fibre under load, where equation 4.5 shows a square root dependence of a (and thus $2aL$) on pressure. In moving from that simple system to the one at hand, the increase of contact length with nominal pressure causes line loading to increase sub-linearly with nominal pressure (acting to *slow* the increase of contact area) but itself directly acts to *increase* contact area; apparently the latter effect dominates.

Comparison *between* fabrics is fraught with uncertainty because the visibilities and depths of field of the fibres are not identical, but is nonetheless interesting, if limited. The three graphs are very similar; no clear distinction can be seen between NW3 and NW6, while NW1 gives rise to perhaps 20 % larger contact fractions. Since NW3 and NW6 have fibre diameters which differ by a factor of 1.6 this is interesting by itself; given the substantial difference between their respective contact lengths, it must be concluded that the flatter and wider contact of a larger diameter fibre roughly compensates. The larger contact fraction of NW1 appears to stem from it also having the largest contact length. This suggests that contact length is the more significant factor.

Regarding viscoelastic ploughing, there is little consensus in the literature as to the details of its origins, and the most coherent models are complicated. Since it would be very difficult and dubiously beneficial to apply any model in detail to the measured fibre contacts, but rather more sensible to deal with averaged quantities, the use of a beautifully detailed and intricate model would seem misguided. Instead, a very simple model after the original approach of Greenwood & Tabor [7] is used: the criticisms of this model reported and augmented in §2.4.5 stand, but given the small deformations and approximate nature of the application they are more than matched by the simplicity it offers.

Following the spirit of that model, the horizontal forces exerted on the front of a Hertzian impressed cylinder are calculated; the force considered as energy per unit distance, and the fact that γ of the energy is never regained at the back recalled; and the friction force thus given as γ times the "front" force. In this context it is more sensible to work with force per unit length, $\hat{f}$, and to assume an infinitely long cylinder for the purposes of calculations. Referring to figure 4.15,

$$d\hat{f} = p \sin\theta R d\theta,$$

where p is contact pressure, θ is the angle from vertical, and R is the cylinder radius. For Hertzian contact $p = (2P/\pi a)\sqrt{1 - r^2/a^2}$ [162], where $r = R\sin\theta$ is the distance from the centre, a is the limit of contact, and P is the line loading, and as argued in §4.3.2, obeys $P = p_{nom}/\hat{l}$. Substituting this distribution in and changing variables to r,

$$\hat{f} = \frac{2P}{\pi a R}\int_0^a \sqrt{1 - \frac{r^2}{a^2}}\, r\, dr.$$

This can be trivially solved using the substitution $\rho = \sqrt{1 - r^2/a^2}$ to give

$$\hat{f} = -\frac{2Pa}{3\pi R}\left[\left(1 - \frac{r^2}{a^2}\right)^{\frac{3}{2}}\right]_0^a = \frac{2Pa}{3\pi R},$$

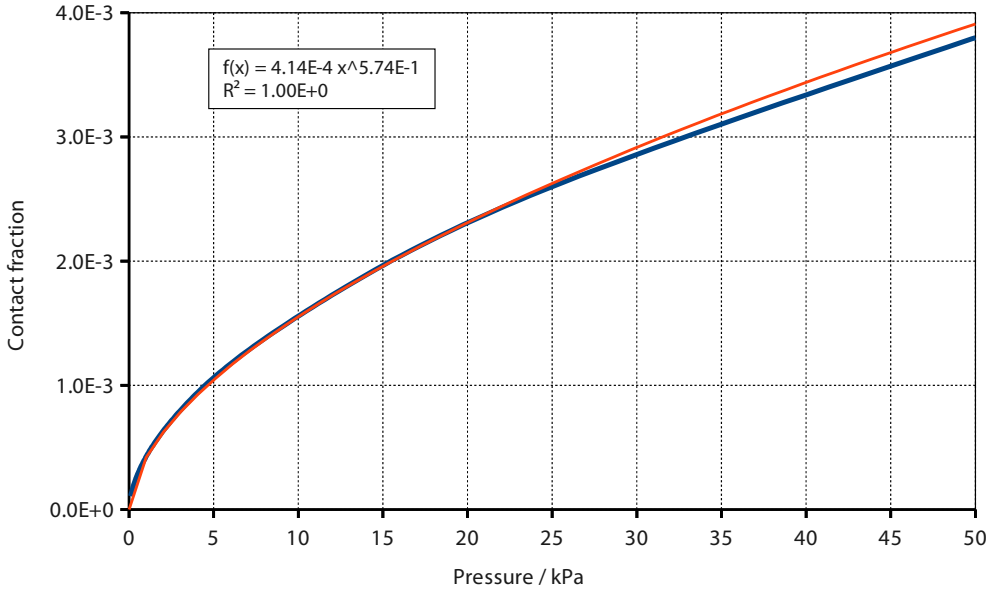

(a) NW1

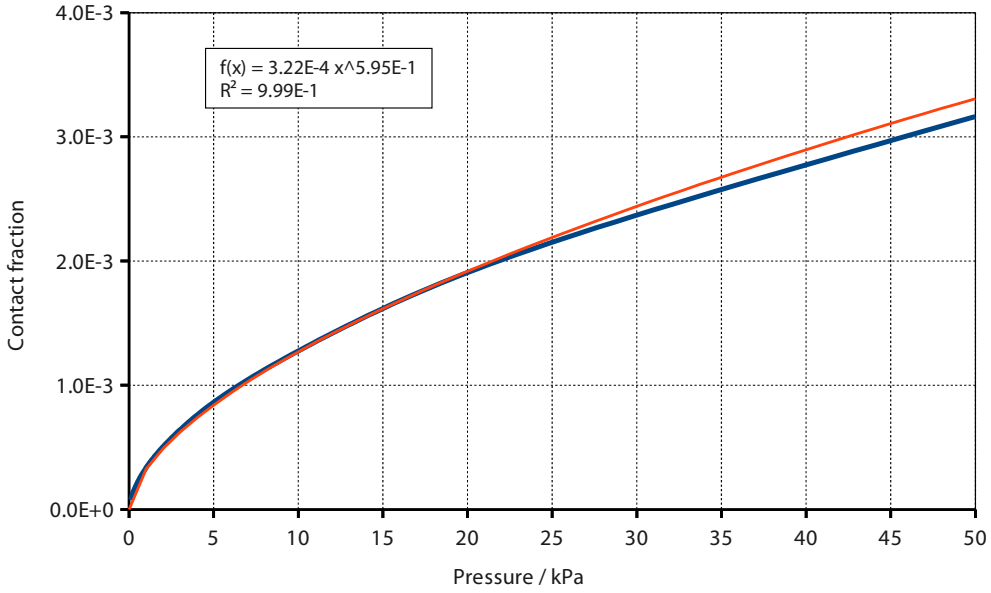

(b) NW3

Figure 4.14: Contact fraction, ϕ, for each nonwoven, as predicted from the assumption of Hertzian contact and the measured relationship between nominal pressure and contact length. Blue, thick lines are the prediction; orange, thin lines are power law fits. *Continues…*

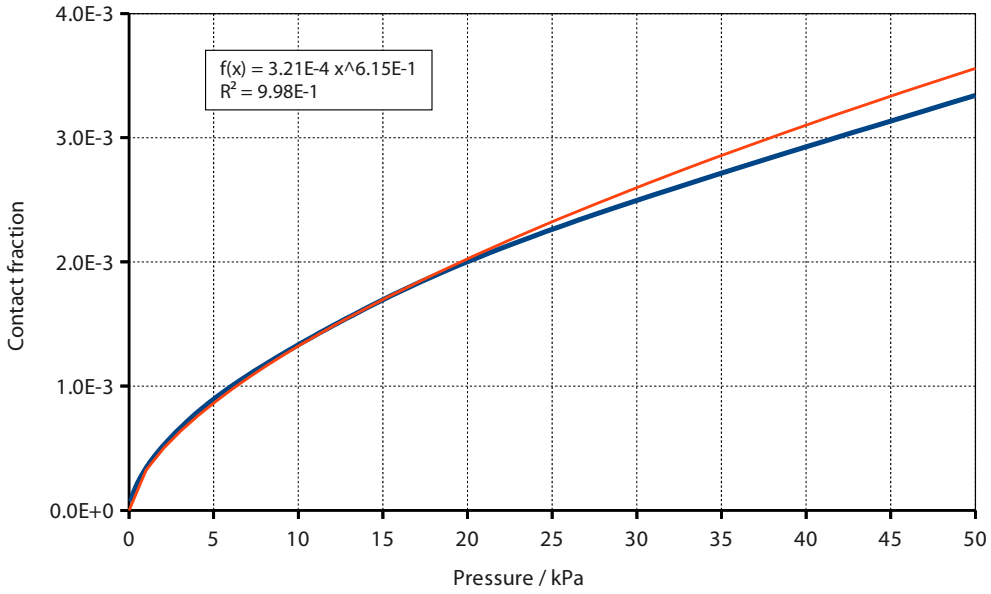

(c) NW6

Figure 4.14: *…Continued.*

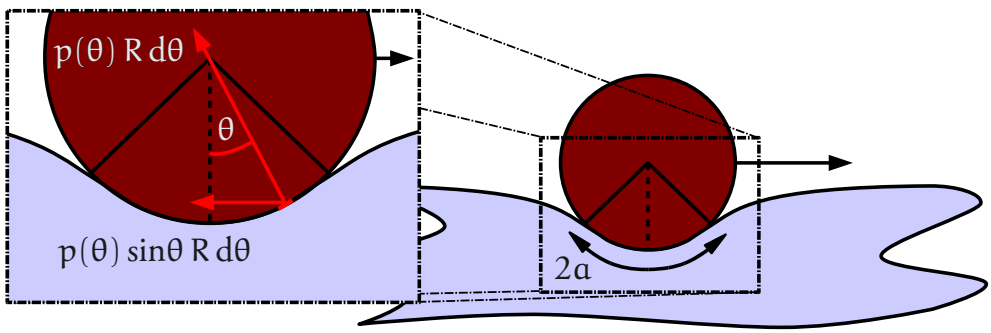

Figure 4.15: The horizontal force per unit length of fibre can be found by considering the horizontal component of the Hertzian pressure.

so the friction force per unit length is

$$\hat{f}_{fric} = \gamma \frac{2Pa}{3\pi R}.$$

This must now be moved from the situation of a single infinite cylinder to the collection of finite fibres that in fact occur. However, since introducing variation in orientation will merely give rise to a geometric prefactor of order unity for the price of considerable work, and the loss factor γ is in any case unknown, it will be assumed for simplicity that all fibres are broadside on to the direction of motion. As this is the case, subject to the assumption of uniformity of pressure along the length of the contact it follows that friction force per unit area is simply

$$\hat{f}_f = \gamma \hat{l} \frac{2Pa}{3\pi R} = \gamma \frac{2p_{nom} a}{3\pi R}.$$

Substituting for a using the expression in equation 4.7,

$$\hat{f}_f = \gamma \frac{2p_{nom}}{3\pi R} \sqrt{\frac{4R}{\pi E^*} \frac{p_{nom}}{\delta \log(p_{nom}) + \epsilon}} = \gamma \sqrt{\frac{16}{9\pi^3 R E^*} \frac{{p_{nom}}^3}{\delta \log(p_{nom}) + \epsilon}}. \tag{4.8}$$

Figure 4.16 shows plots of equation 4.8 for the same material parameters used before, and for $\gamma = 0.5$; the choice of γ merely scales the result. This should be emphasised: these predictions are *not* quantitative predictions of the magnitude of viscoelastic force in friction testing against the skin; they are indications of the rough form that it would be expected to take *if* simple viscoelasticity were important.

Again, the graphs are well-fit by power laws, with exponents varying in the range 1.38–1.43. Reiterating the caveats about comparisons between nonwovens, it is nonetheless unsurprising that again NW3 and NW6 behave very similarly, and (because of the form of the function) NW1 falls beneath them. Little more can be said about these graphs at this stage.

Comparing the two effects, it is interesting to note that the exponents in the power law relationships predicted for contact fraction (relating to adhesion) and viscoelastic dissipation are very different, around 0.6 and 1.4, respectively. In particular, coefficients of friction dominated by each would have qualitatively very dissimilar behaviour at low pressure, with the former diverging and the latter moving smoothly to zero. Comparison of friction results (§4.4.5) with these results is made in the following section.

Finally, it should of course be noted that both of these sets of predictions are based upon certain assumptions about the nature of the mechanisms; failure to follow them closely can equally be ascribed to the mechanisms' inapplicability or limitations of the simple models.

4.3.9 Comparison with independent contact measurements

During the period of the project reported in this thesis SCA Hygiene Products AB commissioned Toponova AB (Halmstad, Sweden) to use one of their surface scanning techniques to produce "surface maps" of two of the nonwovens used in this work (NW3 and NW6). The technique was based upon projecting a pattern of lines onto the nonwoven and observing the apparent distortion due to the

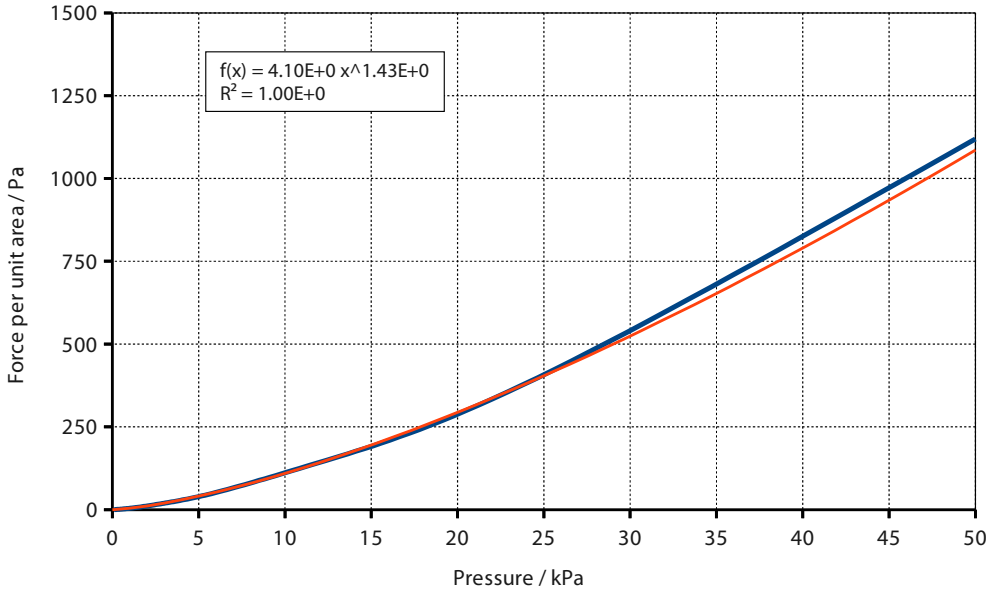

(a) NW1

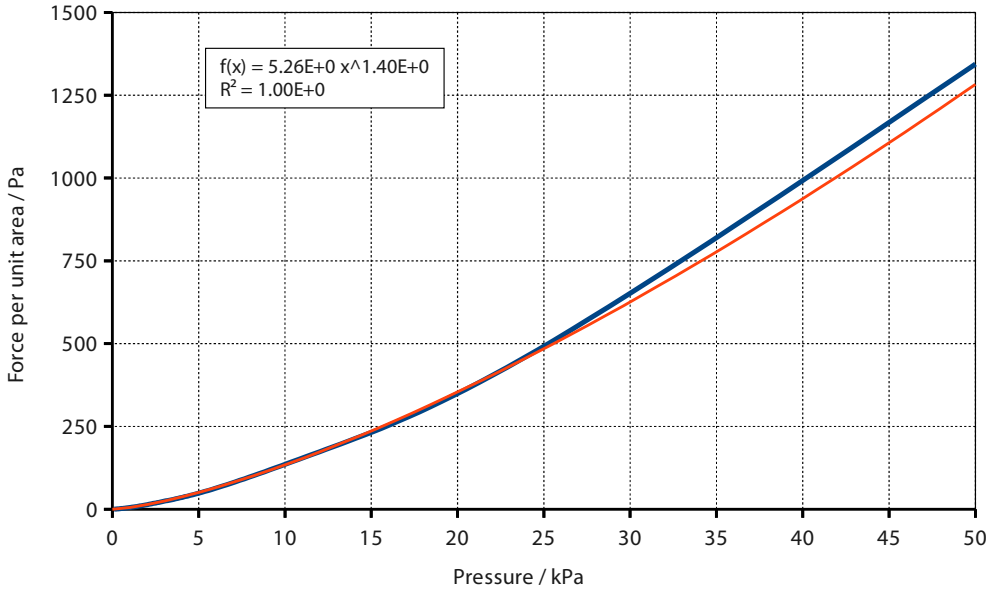

(b) NW3

Figure 4.16: Predictions for the form of viscoelastic dissipative forces following the spirit of Greenwood & Tabor [7], assuming Hertzian contact and using the contact length against pressure relationship observed experimentally. Blue, thick lines are the prediction; orange, thin lines are power law fits. *Continues…*

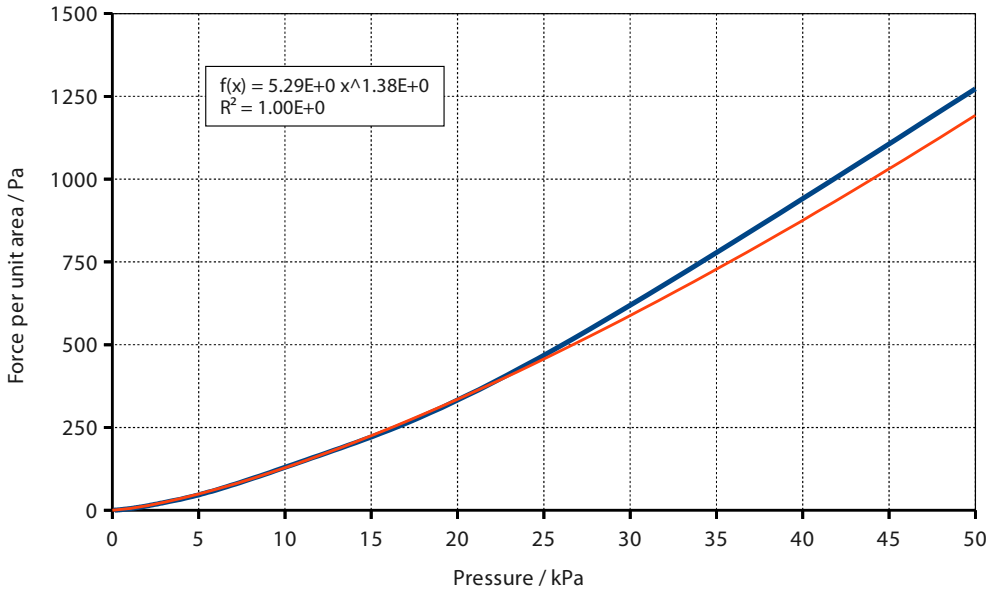

(c) NW6

Figure 4.16: *…Continued.*

relief. Measurements of this type are usually applied to objects with a well-defined surface—which nonwovens signally lack—so it would be expected that data gathered on materials so different from those for which the technique was designed would require more interpretation than would be the case for simpler materials. In particular since the "surface" is riddled with discontinuities any analysis based on derivatives would face significant challenges.

Allowing these difficulties, the data are interesting. They are in the form of maps (figure 4.17) showing where the "surface" is within 25 µm of the highest point gathered at 0.4 kPa, 4 kPa, and 16 kPa: given the approximate stratification of fibres in the studied nonwovens this corresponds to about 1½ and 1 fibre diameters for NW3 and NW6, respectively. It is thus a reasonable approximation to relate the area of the maps divided by the fibre diameter to contact length as measured using the DoF technique developed in this work. Such a comparison is made for NW3 in figure 4.18; the results for NW6 are very similar, though with the Toponova data proportionally slightly less. The Toponova data have additionally been scaled for equivalence with the smaller area measured using the DoF technique.

Comparison of the two sets of data shows that the Toponova data support the most interesting "raw" finding in this work: that the contact length increases approximately logarithmically with pressure. The most marked difference between the results is the absolute numerical value: the Toponova data have consistently around half of the numerical value of the DoF results. This is most likely attributable to the reasons cited above limiting the accuracy of a topographical technique to a material with no surface, and though it is possible that over-counting by the DoF technique may play a part, the generous selection depth of the Toponova data makes relative over-counting by the

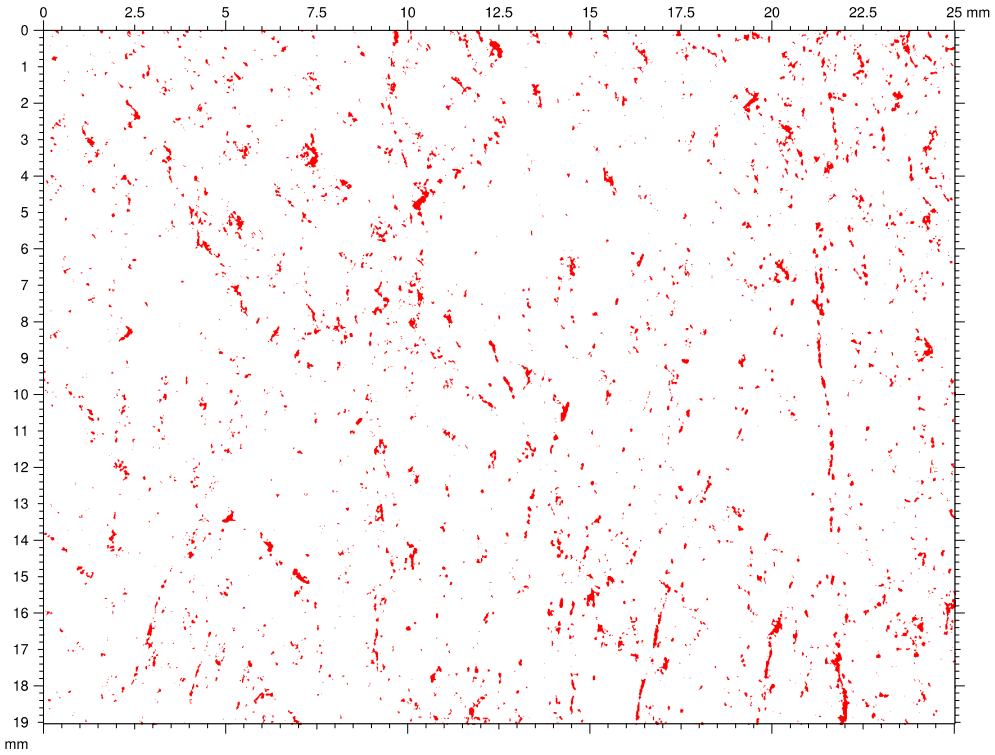

Figure 4.17: The results "map" from Toponova for NW3 at 16 kPa. By comparison with the DoF results obtained in this work it is quite sparse (the maps covers an area of 19 mm × 25 mm compared to a little less than a 5 mm square), and there are noticeably fewer extended linear features.

DoF technique unlikely. Qualitatively, although extended linear structures corresponding to fibres are visible in the Toponova data (figure 4.17) much of the contact area reported there is *not* of this type. Given that these data correspond to the uppermost 25 µm they certainly ought to look like fibres, so their more point-like nature also suggests that limitations of the technique are significant.

4.4 Force against displacement and low magnification microscopy

It was explained in §4.1.1 that in order to elucidate the mechanisms of friction pertinent to the skin (surrogate)-nonwoven interface simultaneous or cross-referable data on friction force, fibre and skin behaviour, and intimate contact area are needed. The latter has been accomplished in §4.3; this section addresses the former. The experiments performed are described in detail, the results are reported, and an initial analysis performed.

4.4.1 Apparatus

The apparatus for this experiment is designed to deliver uniform stress over the nonwoven-skin (surrogate) interface whilst driving it at a constant speed. Simultaneously, the force required to

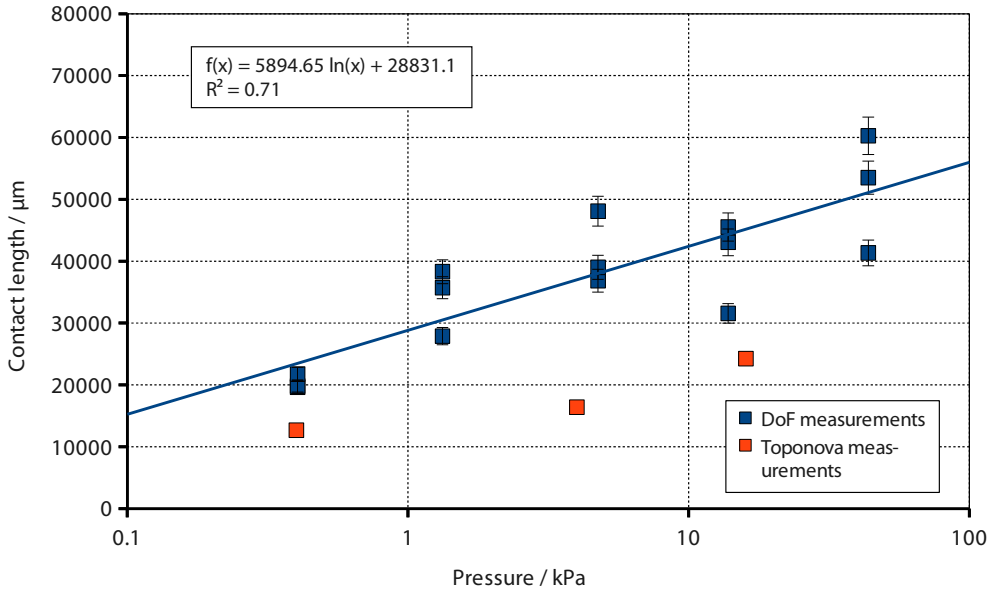

Figure 4.18: A copy of figure 4.12b for NW3 with the addition of the Toponova contact data. They show a similarly slow increase of contact length with pressure, but the values are about half of those found using the DoF method.

maintain motion, and the behaviour of the skin (surrogate) and nonwoven fibres must be observable. These requirements have all been met by the apparatus illustrated in figures 4.19 and 4.20. A detailed description of the equipment and the work done to characterise and validate it is given in appendix B, so only a brief description of the key features is given here.

The heart of the equipment is the contact between the skin (surrogate) and nonwoven itself: the transparent anvils[8]. These are made of epoxy resin, and shaped so that the normal and transverse force densities are constant. This requires a separate set of anvils for each pressure and material used; the method for making anvils is described in detail in appendix C. Nonwoven is fixed to the anvils at the periphery using red nail varnish[9], and skin (surrogate) to 2 mm thick perspex on either side of the slider using epoxy resin or cyanoacrylate; details are given in §4.4.2. The slider assembly is pulled between the anvils at a constant speed by a tensometer (MTT170, Diastron, Andover, UK) which measures the force required to maintain motion. By virtue of the transparency of the anvils and relatively sparse nature of the nonwoven it is possible to observe the fibres in the nonwoven and some of the skin surface using a microscope and camera (Leica DMLM and DFC295, Leica Microsystems (UK) Ltd, Milton Keynes, UK); a micrographic video of sliding is recorded for later evaluation using the LAS software for the microscope camera.

[8]There are two anvils, one corresponding to each of the two interfaces between nonwoven and skin (surrogate). Having two interfaces avoids the introduction of moments—more detail is given in §B.1.1.

[9]A readily available adhesive that is soluble in a common solvent (ethyl acetate) that does not damage any of the other materials used in the equipment. Further, since anvils are reused many times, the bright red colour of the adhesive means that it is easy to see if a residue is building up, something which is important but difficult with clear adhesives.

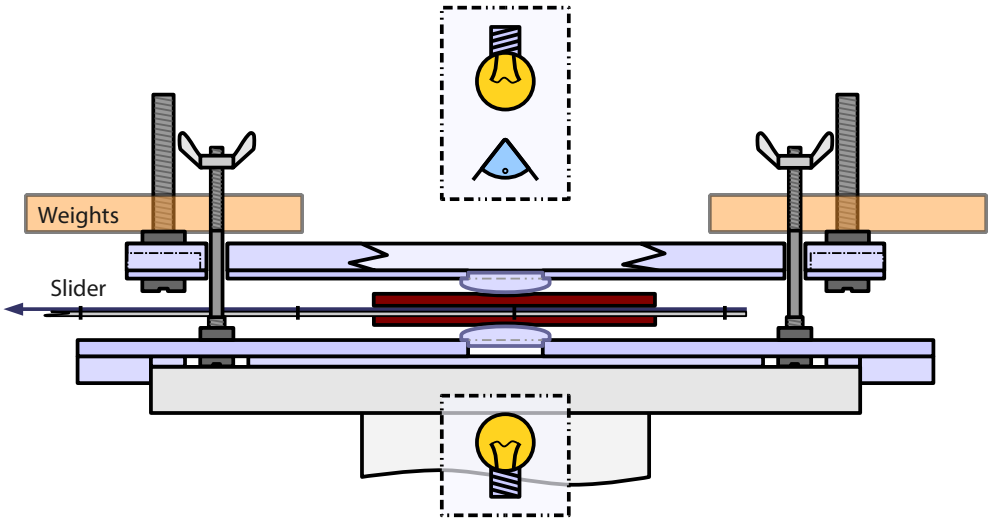

Figure 4.19: An overview of the apparatus for force and low magnification microscopy experiments. The upper surface slides freely on the rods, providing the pressure, but is fairly unconstrained in terms of orientation to enable it to adjust to any imperfections in the anvils. The anvils are faced with nonwoven (not shown) and are pressed against the slider assembly which bears the skin (surrogate); the slider is shown in more detail and plan view in figure 4.20. The whole assembly is shown mounted on the microscope stage for which it was designed.

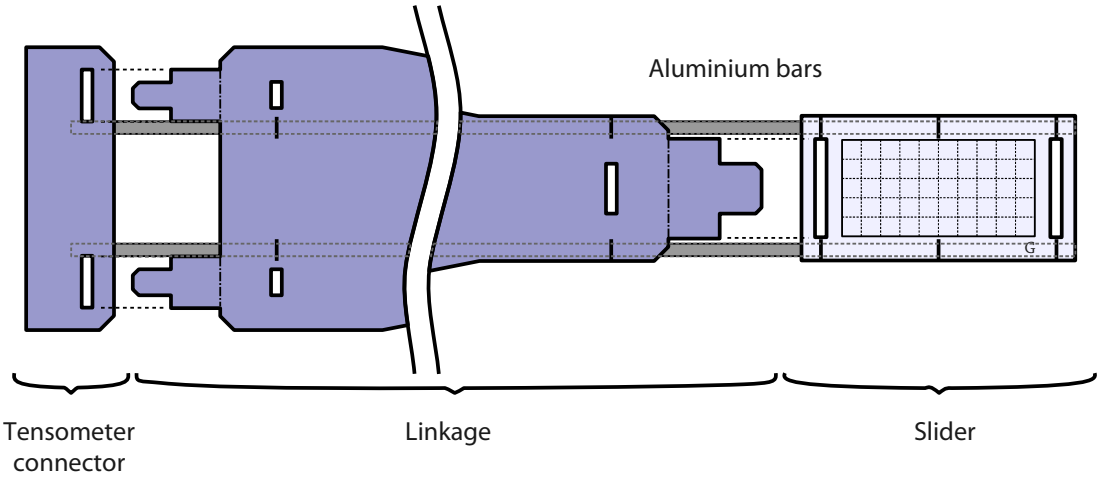

Figure 4.20: The slider assembly is composed of three distinct parts. The tensometer linkage is gripped in the tensometer's crosshead jaws and provides a means of repeatable and easy connection and disconnection of the remainder of the assembly. The linkage provides a stiff and laterally rigid connection between the tensometer and the slider. The slider is a simple piece upon which the skin (surrogate) sample is mounted. Aluminium bars are used to improve stiffness and are shown in position, located by staples.

4.4.2 Preparation of the equipment

Before each experimental run both the slider and the anvils are prepared with the relevant skin (surrogate) sample and nonwoven, respectively. Additionally, the anvils must be placed correctly in the apparatus and the apparatus assembled and located. The procedure for slider preparation is as follows.

1. For skin[10], cut the prepared sample into the two largest, nominally identical pieces possible that are at least 30 mm square (to accommodate the anvil width).
2. Bond the skin (surrogate) pieces to 2 mm thick perspex sheet stiffeners (100 mm × 50 mm) using cyanoacrylate (Loctite super glue, distributed by Henkel Consumer Adhesives, Winsford, Cheshire, UK) for skin and epoxy resin ("5 minute epoxy", ITW Performance Polymers, Riviera Beach, Florida, USA) for Lorica Soft. For skin, the samples were strained until a mark of known size (usually a 20 mm square) made before the sample's excision was of the correct size, thus allowing for shrinkage upon removal from the body (§2.2.1).
3. Connect the slider to the linkage piece, then slot the stiffening bars into place.
4. Before the first run fix the tensometer jaws over the tensometer connector using a piece of silicone rubber sheeting either side to increase friction.

The procedure for preparation of the nonwoven facing and fixing it to the anvils is as follows. It is important that the nonwoven is not stretched during this procedure to ensure repeatability. Two variants of the method are needed for the two different sizes of anvil (appendix C); this is indicated below.

1. All nonwovens are marked to fix their orientation in terms of machine direction and "up"; take the chosen nonwoven and make a small equivalent mark in the same orientation in the corner of the piece to be cut.
2. Cut (using sharp scissors) a swatch of nonwoven roughly 40 mm square including the orientation mark just drawn.
3. *For larger anvils:* Paint a thin band of red nail varnish (No. 7 "Stay Perfect" Pillar Box 98, Boots, Nottingham, UK) around the cylindrical outside edge of the anvil.

   For smaller anvils: Paint a thin band of nail varnish on the flat annulus on the anvil's face.
4. Place the nonwoven swatch *upside down*[11] on the anvil with the arrow of the orientation mark pointing towards the anvil's "front" mark.
5. *For larger anvils:* Push the cylindrical part of a ⌀30 mm casting cup (Seriform, Struers Ltd, Solihull, UK) over the nonwoven swatch and anvil. Leave the nail varnish to dry for half an hour.

   For smaller anvils: Place a silicone rubber annulus over the nonwoven (specially cut, relaxed internal diameter 19 mm) and push it down firmly onto the annular flat portion of the anvil.

[10] It will be recalled from §4.2.2 that, though no skin been been used in experiments all details for its use are given throughout this thesis to facilitate future experiments when skin *is* available.

[11] This ensures that the swatch is the correct way up when the anvil is upright and in contact with the skin (surrogate).

Place a 100 g weight on top, using an additional spacer if the anvil face extends beyond the top of the silicone rubber annulus.

6. *For larger anvils:* Push the casting cup off the anvil so that the anvil emerges from the cup nonwoven-covered face first.

   For smaller anvils: Remove the weight. Carefully free the silicone rubber annulus from the nail varnish by pulling it radially outwards (so as not to act to pull the nonwoven off). Once freed, remove the annulus.
7. Trim the excess nonwoven (including the nonwoven's orienting mark) from the sample using needle-nosed scissors. Fine trimming can be accomplished using a fresh scalpel.
8. Check the fixing; apply additional nail varnish to any insecure area.

It is known that surface contamination can alter friction at an interface considerably, so it is important that neither surface is touched at any stage during the preparation procedure, or during storage and use. Both anvils and the slider have always been kept in sealed containers when not in use to guard against contamination by dust and accidental damage.

The procedure for assembling and locating the equipment on the microscope stage, including placing "relief" springs and "trimming" load to allow for the weight of the upper surface is as follows.

1. Start with the upper surface separate from the lower and the equipment off the microscope.
2. Push the prepared anvils into the upper and lower surfaces with the "front" marks of the anvils aligned towards the tensometer end. Both should be a secure push fit, but not distort the surfaces themselves. No nail varnish or other material should be between the anvils and the surfaces.
3. Place the chosen slider (*not* attached to the linkage) symmetrically on the lower anvil and locate the upper surface on the rods, lowering it gently onto the slider. Be sure to avoid rubbing or twisting at the contact. Looking at the upper surface's distance up the four rods, take note of the lowest corner and how much higher each other corner is above this datum.
4. Remove the upper surface and slider. Place the relief springs on the rods. Put stiff spacers (annuli cut from polypropylene sheet are suitable) onto each spring top to raise it by the amount measured in step 3.
5. Place weights symmetrically on the upper surface until the upper anvil first contacts the slider; note the weight. This should be done to an accuracy of ± 2 g. Remove the weights.
6. Remove the upper surface and the slider. Attach the slider to the linkage and put it aside, ensuring that neither of the skin (surrogate) surfaces touch anything.
7. Relocate the upper surface on the lower; lower the supports to keep the anvils apart. Thread the wing nuts onto the M3 threaded part of the locating rods.
8. Place the 4 mm thick perspex spacer on the microscope stage (shown in figure 4.19); a further 2 mm spacer can be added if clearance needs to be increased. Place the main apparatus on the stage, taking care not to damage the microscope lenses.
9. Add the desired load *plus* the "trimming" load noted in step 5. This should be shared symmetrically between the two bolts on the upper surface.
10. Secure the apparatus to the stage at either end with two clips.

11. Lower the wing nuts along the rods until they prevent the upper surface from being pushed into the microscope lenses when the lenses are rotated out of position.

4.4.3 Method

To clarify the following description, some terminology must be introduced. The procedure in which the tensometer shuttles back and forth with the slider once is referred to as a *cycle*; a pre-programmed set of cycles (using a common "calibration"—defined below) is referred to as a *phase*; a set of phases designed to constitute a test of a particular combination of parameters and materials (for example, a chosen slider and nonwoven combination at a fixed speed) are referred to as a *run*. It is, of course, possible for a phase to consist of only one cycle, and a run to contain only one phase.

The methodology given here is for a single phase: this contains nuances that the method for a single cycle does not, whereas a run is simply a series of phases. Experiments on skin surrogates were conducted in an environmentally controlled room (*ECR*) held at 23 ± 1 °C and 50 ± 5 % relative humidity. Experiments on excised skin could not have been run in this room; requirements for dealing with biological samples precluded it, so the ambient conditions would have been noted for each experiment.

This procedure assumes that the anvils and slider have been prepared and the apparatus assembled and located in accordance with the procedures described in §4.4.2. The procedure is illustrated in figure 4.21.

1. Set the tensometer programme (see below) to the required speed, number of cycles, and run length. Prepare the microscope software to take continuous or periodic video, depending on the time the cycle requires[12].
2. Insert a simple wedge tool (figure 4.21a) onto the lower surface around the lower anvil from the end further from the slider. Insert the slider assembly between the surfaces from the other end and rest it on the wedges, continuing to support the free end of the slider (figure 4.21a). Take care not to touch the skin (surrogate) on either surface during this operation.
3. Instruct the tensometer to move to its starting position (if this is done before step 2 it is hard to locate the slider).
4. Instruct the tensometer programme to begin. Ensure that nothing touches the tensometer crosshead during the initial calibration period (always less than 10 s). After this, fit the slider linkage into the tensometer connector and secure the tabs (figure 4.21b).
5. Hold the slider securely and push the aluminium stiffening rods towards the tensometer crosshead until they butt up to it (figure 4.21c). This provides the principal lateral stiffness of the slider assembly, so must be done carefully. Ensure that the slider is parallel to the direction of travel of the tensometer crosshead.
6. Check that the anvils are central with respect to the slider. If they are not, adjust the position of the microscope stage until they are (figure 4.21d).

[12]In this work cycles using speeds of $5\,\mathrm{mm \cdot s^{-1}}$–$0.5\,\mathrm{mm \cdot s^{-1}}$ have been videoed continuously; slower cycles have been videoed periodically, ensuring that the start and end are included.

7. Remove the wedge tool from under the slider assembly, allowing the slider to drop into contact with the lower anvil. Raise the upper surface (holding both ends symmetrically), flip up the bistable supports, and lower the upper surface (figure 4.21e). Check that it is seated approximately horizontally; if this is not so it will be due to catching on the rods, and the surface should be raised and lowered again.
8. Shortly before the tensometer begins pulling, start the video capture on the microscope software.

   *All steps from 4 to 8 must be completed within the "*pre-wait*" period set in the tensometer programme (see below).*

9. The tensometer will pull the slider between the anvils. Note any contacts other than at the anvils, and any other interesting occurrences.
10. When the tensometer stops, raise the upper surface symmetrically and flip down the bistable supports. Insert the wedge tool under the slider, so raising the slider above the lower anvil. Stop the video capture. These processes must be completed within the "post-wait" time set in the tensometer programme.
11. In all but the final cycle of a phase, the tensometer will return the slider to its initial position. When it has done so, remove the wedge tool, raise the upper surface symmetrically, flip up the bistable supports, and lower the upper surface, checking as before that it is horizontal. This process must be completed within the "pre-wait" time set in the tensometer programme.

    Steps 9 to 11 are repeated as many times as set in the tensometer programme.

This procedure is repeated for each phase in a given run.

Technical note on the tensometer Each phase contains one "calibration"; that is, a period (variable, but always less than 10 s) in which the tensometer records the force that it is experiencing and subtracts that value from all subsequent forces reported in that phase. It is therefore important that the tensometer crosshead is not touched during the calibration period, as stated in step 4.

The tensometer requires a large number of parameters to be set, though many of them need never be changed. The key parameters for the interpretation of the above procedure are the offset, movement and wait parameters: start-point, initial-movement, pre-wait, main-movement, and post-wait[13]. initial-movement is invariably set to 0 mm. The wait times are set to the minimum time that enables the necessary adjustments to be made: pre-wait is usually 50 s; post-wait is usually 20 s; their values make no difference to the data, so are not reported with the results. The start-point and main-movement parameters are the most important varied parameters, controlling the initial position of the tensometer crosshead and its travel during a cycle, respectively. main-movement is set by the

[13]These terms have been coined for this work as they are descriptive of their functions here. The tensometer software terms them "sample size", "phase 1 movement", "phase 2 static", "phase 3 movement", and "phase 4 static", respectively. These terms are not used here as the start point is only tenuously related to the size of the sample, the word "phase" would introduce ambiguity, and the "static" periods that the software considers as full productive of data are merely waiting times to enable equipment to be adjusted in this context.

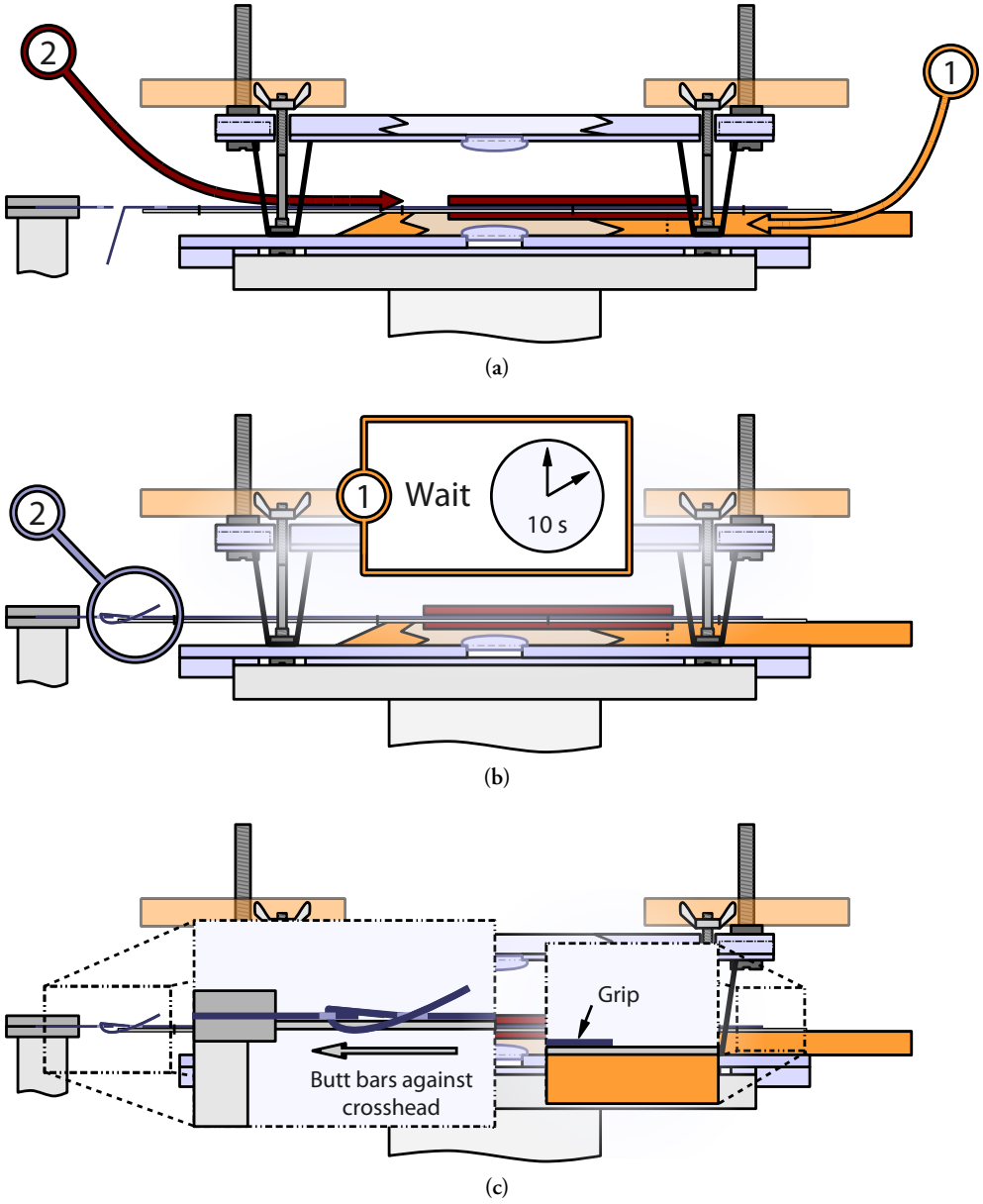

Figure 4.21: Illustrations of some of the steps in the force / low magnification microscopy method. (a) corresponds to step 2; one side of the wedge tool is cut away to show the anvil between its "arms". (b) goes with step 4. (c) illustrates step 5. *Figure continues…*

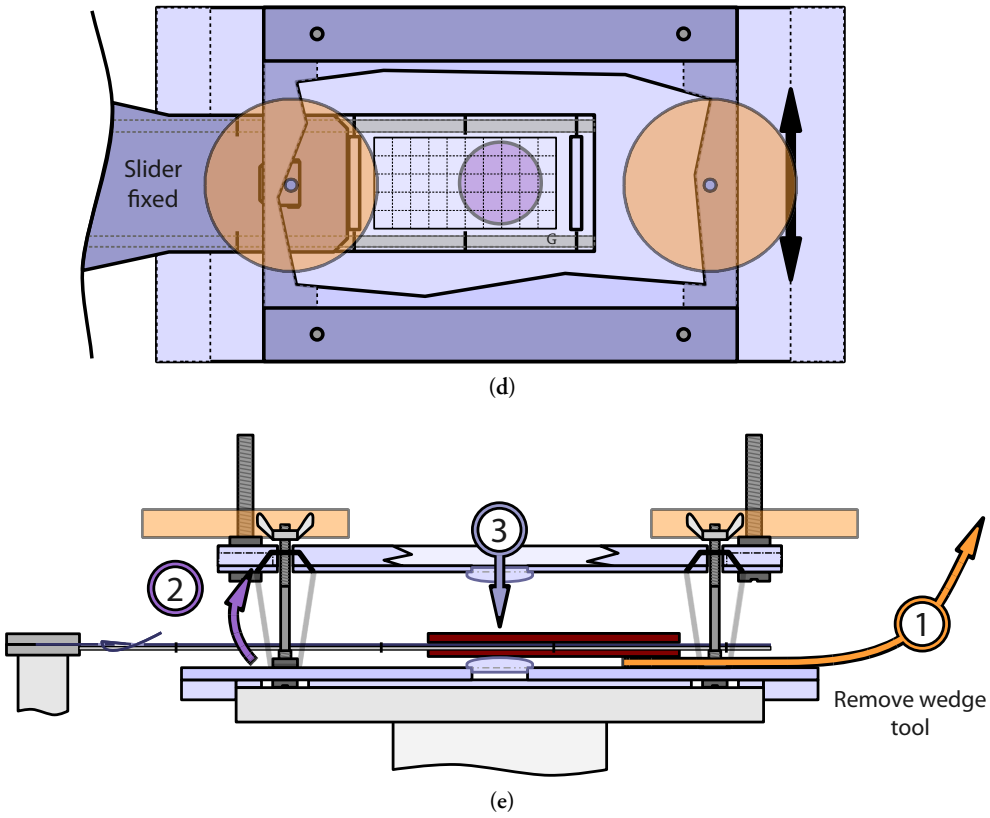

Figure 4.21: …*Continued* (d) corresponds to step 6; the view is plan, and the majority of the upper surface has been cut away to show the alignment of the slider and the anvil. The microscope stage can be translated as shown to improve the alignment if necessary. (e) corresponds to step 8.

length of the skin (surrogate) sample; to avoid edge effects so far as possible the anvils get no closer than about 10 mm to the sample edges. start-point is determined by the location that the sample is mounted on the slider; a scale is printed on the slider to aid in judging this.

A list of all of the tensometer programme parameters is given in table 4.4, along with their values or the basis on which a value is chosen for a specific experiment.

4.4.4 Schedule of experiments

Since no skin was available for experiments a thorough and complete set of experiments were run for each of the nonwovens and Lorica Soft. These enable not only a demonstration of the techniques and analysis, but also provide a substantial corpus of data that can be compared with equivalent skin data when they are available.

All experiments were carried out at one of five different velocities (0.05 mm · s^{-1}, 0.167 mm · s^{-1}, 0.5 mm · s^{-1}, 1.67 mm · s^{-1}, and 5 mm · s^{-1}; these are neater when expressed in the tensometer's

Parameter	Value or range	Notes
start-point / mm	—	Discussed in body text.
initial-movement / mm	0	—
pre-wait / s	Typically 50 s	Value not critical to results; can be changed if convenient.
main-movement / mm	—	Discussed in body text.
post-wait / s	Typically 20 s	Value not critical to results; can be changed if convenient.
Rate / mm · min^{-1}	3–300	Independent variable.
Maximum force / g	20—2000	The force beyond which the cycle will instantly terminate. It is used to select the size of force quanta, so should be set as low as practical.
Break detection	disable	—
Cycles	Usually 5	The number of cycles in a phase. A free choice, though 5 is usual.
Start each cycle at…	origin (*do* reset)	It is possible to instruct the tensometer not to return to start-point after each cycle, but this is never wanted in this work.
Gauge force / g	0	An additional force to add to the measured reading. Invariably set to 0 in this work.
Apply gauging to…	first cycle only	Check "zeroing" before the first run only.
Return sample to pick up position	true	—

Table 4.4: A summary of the parameters that are required by the tensometer control programme (MTTWin). Except where otherwise defined, the terminology used is the same as that used by MTTWin; where terms are unclear or misleading they have been clarified in the table. Note that MTTWin uses the curious units of "gram-force" for all forces; that is, it reports in multiples of the weight of one gram. This is not a sensible unit to use, so all forces reported in this work are given in newtons.

native units of mm · min^{-1}), covering the range of the tensometer[14]. The loads which would have been applied for skin differ from those used for Lorica Soft, principally because the anticipated small size of samples would have required the use of smaller anvils (and thus lower loads at a given pressure) for skin: Lorica Soft anvils remain larger to minimise the effect of nonwoven inhomogeneities. The exact loads and corresponding pressures are given in table C.1, but they vary from 0.25 N (0.6 kPa) to 19.0 N (32.1 kPa).

In general, the first phase with a slider or a nonwoven sample consisted of ten cycles—materials wore quite rapidly initially—with subsequent phases consisting of five cycles. The only exceptions to this were experiments at the slowest speed where only those cycles deemed strictly necessary were undertaken in order to save time. A given run continued until the majority of cycles in a five cycle phase were consistent; that is, they showed acceptably small random variation, and no longer any tendency for the force-displacement trace to drift up or down. In consequence mean

[14]The tensometer in fact nominally covers speeds down to 0.0167 mm · s^{-1}, but below 0.05 mm · s^{-1} movement is very obviously in discrete jerks.

traces—calculated as simple point-by-point arithmetic means—have usually been based on four or five individual cycles, with three quite common and two very rare.

Two different Lorica Soft sliders have been used, both cut in the same orientation but from different edges of the material roll and from different ends of the sample; these have been designated sliders L8 and L11; start-point was 28 mm for both. Nonwovens were arbitrarily considered in the order NW6, NW3, NW1. NW6 and slider L8 were tested thoroughly for all of the 25 combination of load and velocity in order to assess whether there were significant velocity-load interactions. NW6 and slider L11 were then treated more briefly, testing all velocities at the middle loading, followed by all loadings at the middle velocity. NW3 and NW1 were both treated in a similar way: L8 and L11 were alternated whilst testing different loads at the middle velocity, after which L8 was tested for all velocities at the middle load, and finally L11 was similarly tested for all velocities at the middle load.

4.4.5 Results

Before presenting the results, it should be noted that due to their very extensive nature, only *example* graphs are included in the main text to minimise disruption. All of the relevant data are included in appendix E. When referring to graphs in this section and the subsequent sections no comment will be made on where they are to be found; it is simple to infer this from the figure number.

The results for this experiment divide fundamentally into force data and microscopy data. The quantity of raw (individual cycle) data gathered is such that presenting them all would be impractical. In fact, since no insights have been derived from the individual cycles that have not been clearer or equally clear in the phase-means, only a single example of such graphs is included to exemplify the type (figure 4.22). These raw graphs give rise to mean-trace graphs, which are presented instead.

Since a whole run can be expressed as a single trace in this format it is most efficient to present several mean traces on a single graph, grouped in order to show variation with load or velocity clearly. To facilitate simple comparison between curves all friction forces have been normalised by the mean load on the two anvils (see §4.4.6 and §B.2.4). Traces showing variation with velocity are given in figures 4.23 and E.1. Graphs summarising the variation of the trace with load are shown in figures 4.24 and E.2. Since the slight difference in load between the two anvil faces complicates matters slightly, traces grouped by load are labelled with the letters of the anvils used—see table C.1.

It is immediately apparent that whilst in most cases there is very considerable similarity between the traces for a given slider against different nonwovens, traces for the two sliders against the same nonwoven often differ markedly. This is not unexpected: it is simply a reflection of the inhomogeneity of the Lorica Soft, and in fact provides a means by which to assess variation with sliding speed and load independently of the *shape* of the force-displacement curve.

Microscopy data from this experiment are very disappointing. Due to the very limited reflection from the Lorica Soft surfaces (skin could be expected to be similar) the contrast in the fibres is poor, and they have very limited visibility against the mottled backgrounds. The only general comment that can be made is that the fibres of all fabrics are seen to move in essentially all circumstances. Some also periodically "flash"; that is, they briefly reflect light before appearing dull again. It is conjectured

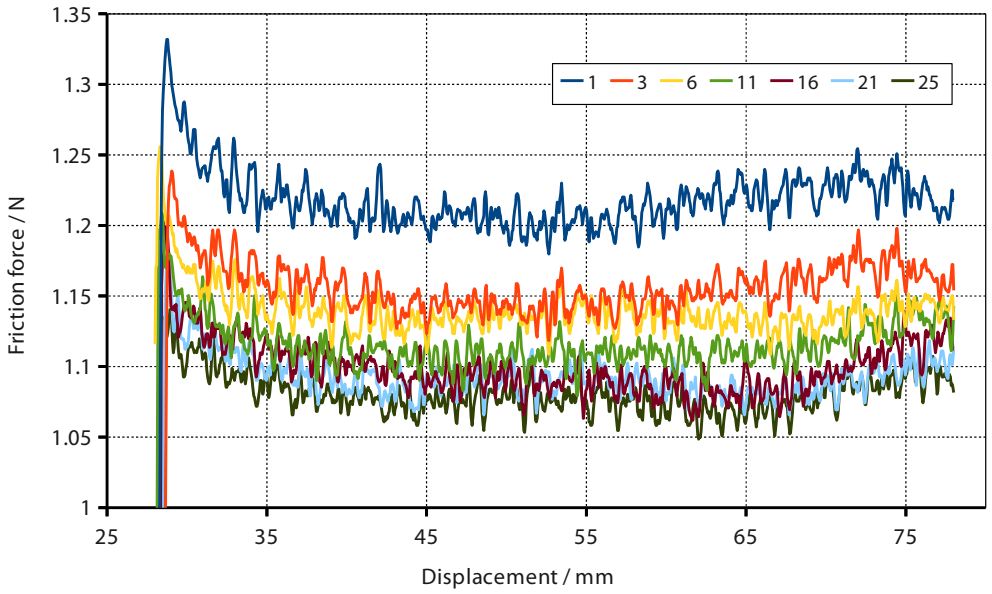

Figure 4.22: An example of a new slider (L11) "wearing in". This experiment used the τ-ψ combination of anvils, NW6, and a sliding speed of 1.67 mm · s^{-1}. The final five cycles (21–25; only 21 and 25 shown) can be clearly seen to have converged and the run-to-run force reading to have stabilised.

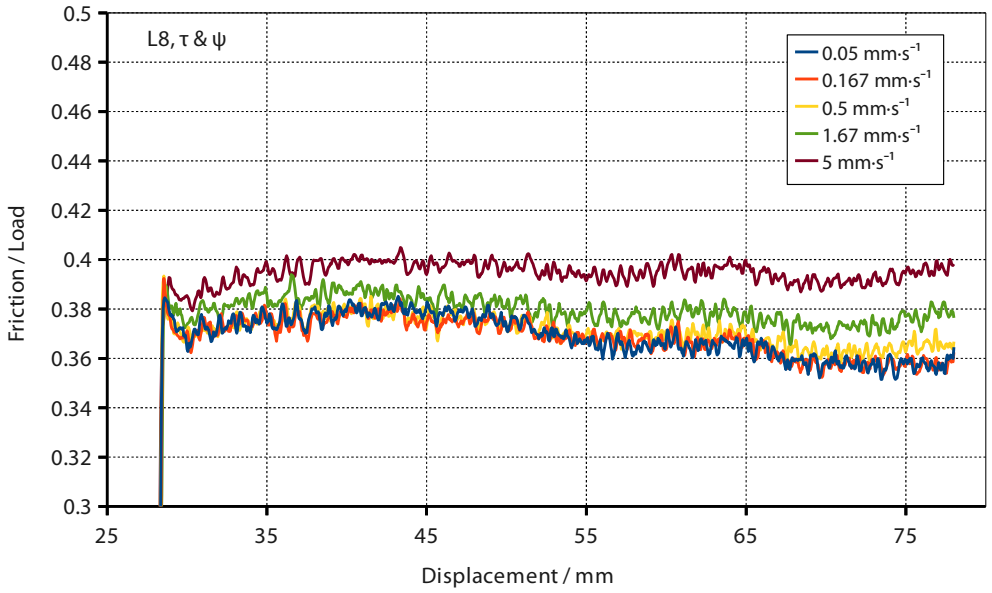

Figure 4.23: Comparison of normalised force-displacement curves at different sliding speeds for NW6 and the L8 Lorica Soft slider.

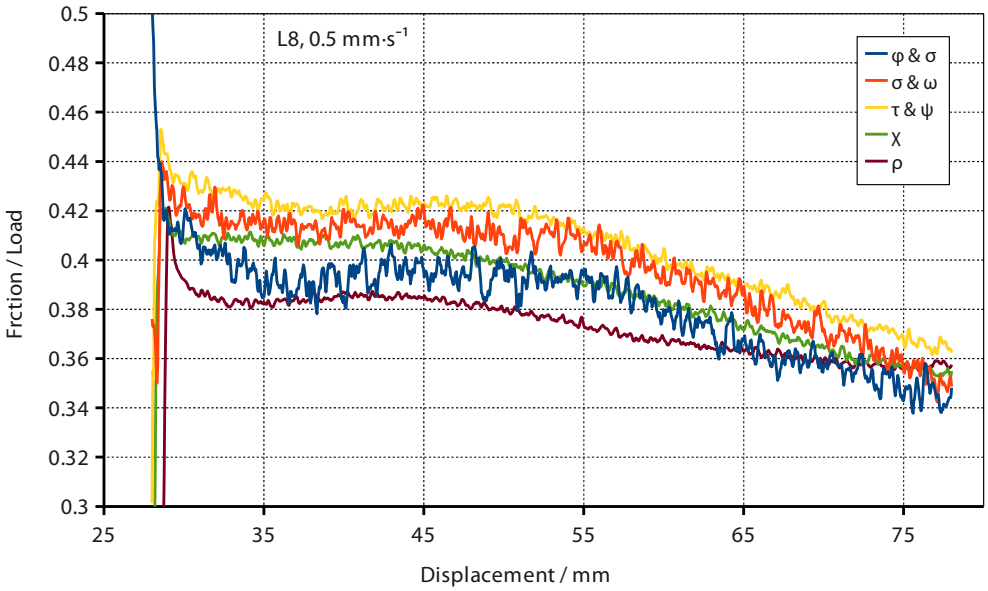

Figure 4.24: Comparison of normalised force-displacement curves at different loads for NW3 and the L8 Lorica Soft slider. The traces are labelled by the designation of the anvils used to take the measurements: the differential in load between the two surfaces precludes labelling them with a simple pressure, so this simple expedient has been adopted here and henceforth.

that this behaviour is due to the fibres being lifted up off the surface, thus changing their optical properties. However, "pinging"—that is, no movement followed by rapid correction—is not seen.

However, whatever their other shortcomings the constant focus of the videos corresponding to sliders L8 and L11 make it clear that the slider thicknesses were constant to less than 100 µm, which according to §B.2.5 means that systematic noise due to non-constant thickness will be no more than a few millinewtons and can thus be ignored.

4.4.6 Analysis and comments

Before embarking on a detailed quantitative analysis of the data, a brief qualitative analysis is worth while. Considering the data as a body, it is apparent that (a) the relative scale of the short-wavelength variation on the traces decreases with increasing load; (b) in general, friction increases with velocity, though not very much; (c) in several cases the first short distance of a trace does not conform to the patterns that the remainder does; and (d) in almost all cases the traces in a given graph share a strong family resemblance; that is, their shapes are discernibly alike. These observations are valuable guides to quantitative analysis.

In quantitative terms, the relationship between friction force and load, and friction force and sliding speed for the Lorica Soft data are the simplest to establish, so are addressed first. Considering friction force against load, it is useful to extract a single number from the friction trace so that a plot of friction force against load can be constructed. In all cases the traces are not uniform horizontal

lines, so some interpretation is required in order to extract such a characteristic. Fortunately, as noted it is apparent from the included graphs of friction force against displacement that in the majority of cases the traces for different loads applied to the same interface are not far from being mathematically similar; that is, when scaled they can be *approximately* superimposed; a more detailed discussion of this is given below. This means that, since the *relative* magnitude of the curves is of much more interest than the absolute values, any linear magnitude characteristic can be used for comparison. The chosen characteristic is (unnormalised) mean friction force over the interval 40 mm–78 mm: this excludes the sometimes atypical initial section of the traces but makes use of all of the remainder. This is plotted against the mean of the loads on the two anvils; further to the discussion in §B.2.5, for these purposes the difference in loads on either anvil was taken as the mean load due to the slider's weight over the interval 40 mm–78 mm.

Consideration of friction against load gives rise to the first instance of a derived graph, so a brief discussion of error bars is necessary. Since friction forces are determined from a mean friction-displacement curve based on several raw curves, the error on the extracted friction measure is simply taken as the standard deviation of the equivalent measures extracted from each of the raw curves. All errors of this type are calculated in this way; errors in coefficients of friction are normalised by the load. Error in load is more complicated. The error in the determination of actual load is negligible—the loads are correct to better than 0.1 g—but effective load variation due to slight imperfection in alignment, etc, is very difficult to estimate. The best assessment possible is the indirect one contained in §B.2.2, where the variation due to disassembly and reassembly of equipment was estimated as about ± 1 %; this will have comprised both random variation *and* variation due to imperfectly replicated imperfect alignment. This number is very similar to that found to be due to random error (§B.2.1), so it is reasonable to conclude that variation due to imperfect alignment is also negligible. In consequence, no load error bars are included on any subsequent graphs; error in sliding speed is also negligible so the quantity attracts no error bars.

Figures 4.25 and E.3 collectively show friction force against load (both calculated as discussed) for all three fabrics and both sliders. In each case a straight line fits the data with a coefficient of determination (R^2) of 0.999 *or higher*. Having established good agreement between a linear fit and the data, coefficients of dynamic friction, μ, can be meaningfully calculated (recalling that the measured friction is the sum of that from *two* interfaces). Considering graphs of pointwise-calculated[15] μ against load (figures 4.26 and E.4) it is clear that there is no coherent systematic variation of μ with load: the apparent *positive* correlation of coefficient of friction and load NW6-L11 stands against the *negative* correlation for NW6-L8. In view of this, so far as variation with normal force goes, the Lorica Soft-nonwoven system obeys Amontons' law to very high precision for the nonwovens considered here.

In spite of this excellent agreement it is nonetheless interesting to note that a *better* fit can be achieved at low loads by using a power law fit (index typically 0.98) rather than a linear fit; such fits are also shown in figures 4.25 and E.3. In many cases this actually *decreases* the coefficient of determination (never below 0.999) because the same absolute deviation at low loads gives rise to

[15] That is, based on the simple quotient of friction force and applied load for each individual load as opposed to a linear fit through all of the points.

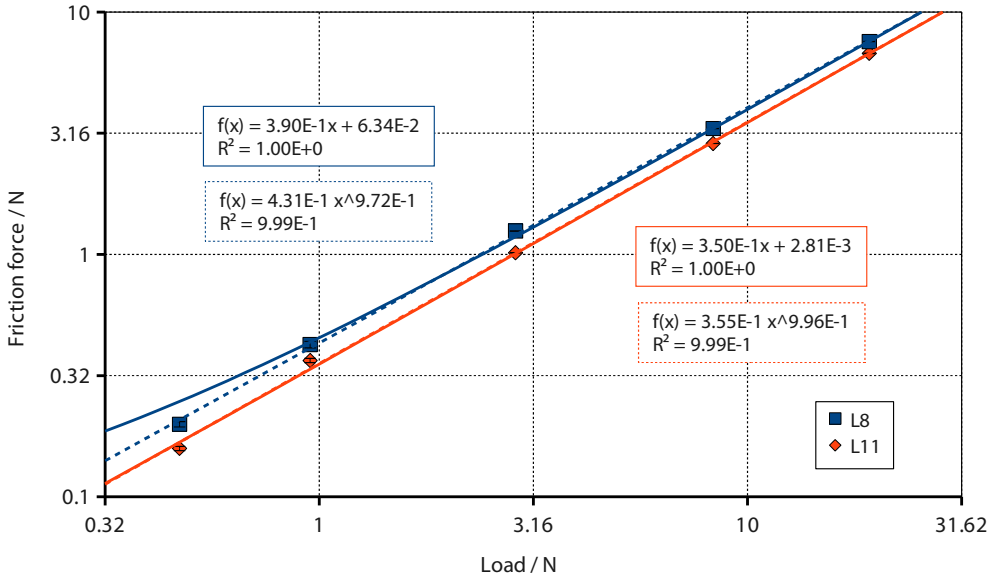

Figure 4.25: An example summary plot of friction force against load for NW1 against each Lorica Soft slider.

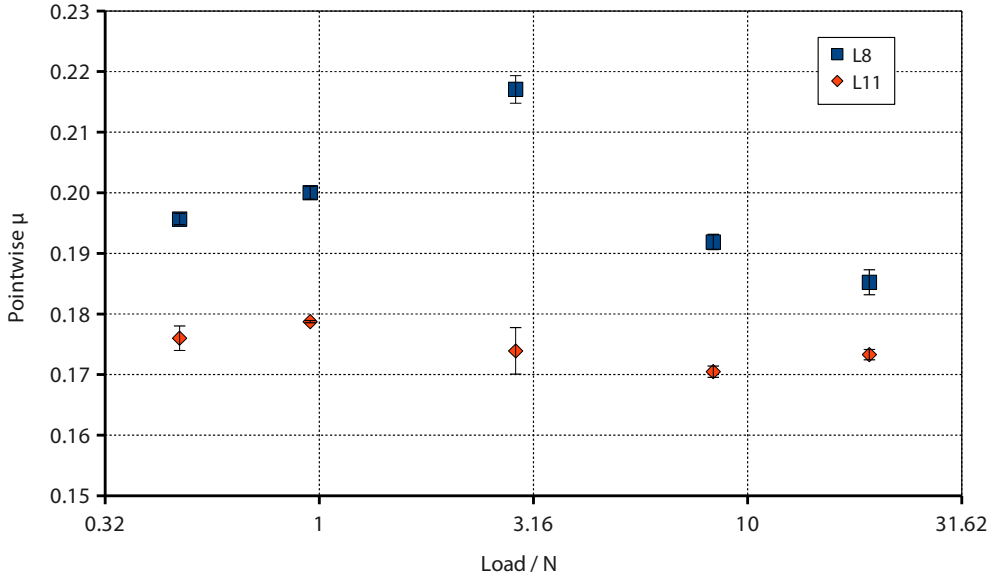

Figure 4.26: An example summary plot of pointwise calculated coefficients of friction against load for NW3 against each Lorica Soft slider.

the same absolute residual as at higher loads even though in absolute terms the conditions are more stringent at low loads. From the perspective of improving low-load agreement, the reduction in coefficient of determination means little. In favour of the power law fit is the fact that the error bars at low loads mandate a much closer agreement between data and fit than a linear fit can achieve; a power law fit passes within most[16] of the error bars on most graphs, whilst a linear fit frequently does not. This could be for two reasons: (1) this is the fundamental manner in which the interface behaves; or (2) a confounding factor that varies nonlinearly with load is complicating matters. It is impossible to distinguish between the two based on these data, but as the difference is very slight this does not present a practical problem for the remainder of the analysis.

All the preceding discussion relates to dynamic friction; static friction has not been considered. This is because of the already observed fact that the early portions of friction-displacement curves are not terribly reproducible. It would thus be impossible to perform an analysis in any depth on static friction; and in simple terms the initial portion of curves is broadly in proportion with the latter portions, so general statements about dynamic friction apply in good measure to static. It should be noted that the one clear pattern for the initial portions of friction-displacement curves—that the trace rises to higher loads and falls to lower ones—is simply a consequence of approximately the same force being used to set the equipment in the first place: it was higher than the smaller dynamic friction forces and lower than the higher ones. This reinforces the essentially uniform observation in all friction work that static friction exceeds dynamic friction, but also illustrates the futility of attempting a more rigorous analysis.

Having established that Amontons' law is at least a high-fidelity fit for dynamic friction, it becomes possible to correct friction-displacement traces for the known variation of load due to the slider's weight during sliding (established in §B.2.5). If friction data are pointwise multiplied by

$$\frac{2P}{2P + (-1.35 \times 10^{-3}x + 5.33 \times 10^{-1})}$$

(where P is the applied load) then they become representative of what *would* have been observed if there were *never* any contribution from the slider's weight; clearly the impact of this correction is larger for small applied loads. In all cases the effect of the correction is to relatively raise the "tail" of the friction-displacement traces.

Data discussed henceforth have had this correction applied. Friction against load graphs with the correction applied are shown in figure E.5.

Sliding speed has already been noted to correlate positively with friction. The easiest way to investigate this further is to plot coefficient of friction (determined pointwise, as previously explained) against sliding speed; such graphs are shown in figures 4.27 and E.6. From them it is clear that typical increases of μ with velocity are quite small, usually around 10 % of the value at the lowest speed over two orders of magnitude in sliding speed. Additionally, due to the small variation and substantial scatter it is not clear whether what variation does occur is linear or logarithmic with sliding speed. The principal inference that can be drawn from these observations is that viscoelasticity is

[16]Requiring that a fit pass within the error bars at all points would be to require overestimation of the error bars: at one standard deviation, only about two-thirds of error bars *ought* to bracket a fit.

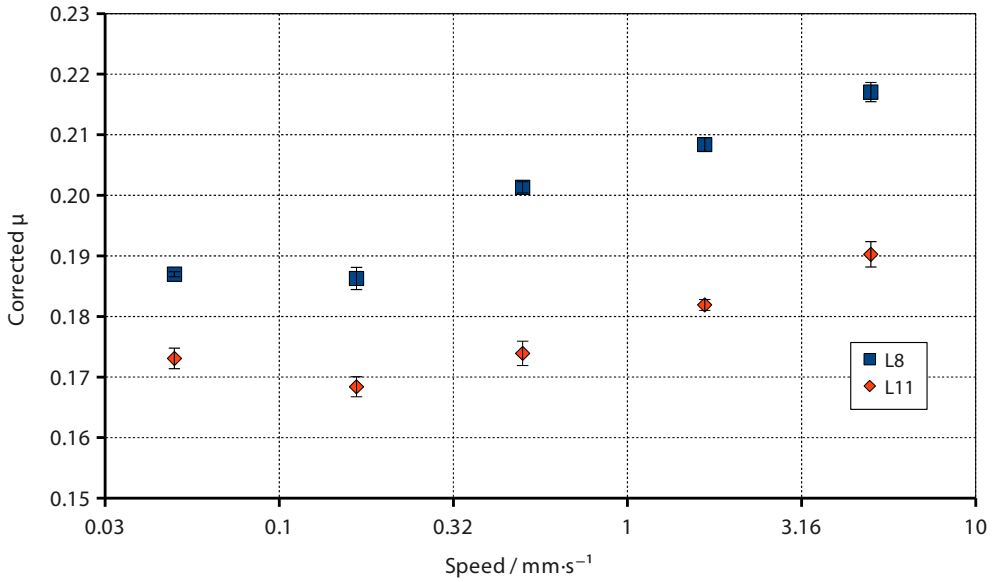

Figure 4.27: An example of variation of coefficient of friction with sliding speed for NW3 and each Lorica Soft slider with the τ & ψ anvils.

unlikely to be significant at this interface over any relevant speeds. A more subtle effect like geometric aging (§2.4.8) of contacts might conceivably explain this modest variation, though the requisite data to make any definite pronouncement are not currently available.

It has already been observed that the traces for a given interface bear a strong affinity to each other. Families of curves corresponding to different sliding speeds at the same load are mathematically similar; that is, simple scaling can bring the details of the traces into coincidence. This is *not* the case for traces corresponding to different loads at the same sliding speed. However, a linear transformation *can* bring most of the traces corresponding to different loads at most interfaces into good agreement. The linear mapping has two parameters, α and β, and maps the friction force F as

$$F(x) \rightarrow \alpha(F(x) + \beta); \tag{4.9}$$

note that neither α nor β are functions of x, the displacement. An example of the process of mapping traces onto each other is shown in figure 4.28.

The need for two parameters to describe this transformation suggests *two* underlying physical friction mechanisms, each corresponding to some proportion of the total friction and varying differently with applied load[17]. Using the transform to bring all of the traces at a given interface into agreement results in a set of α and β values which describe how the mechanisms responsible for friction which varies with displacement (*principal friction*) and friction which appears unrelated to this (*remainder friction*), respectively, vary with load. The collapsed traces are shown in figure E.7;

[17] If they varied in the same way then only one parameter would be required and the traces would be similar.

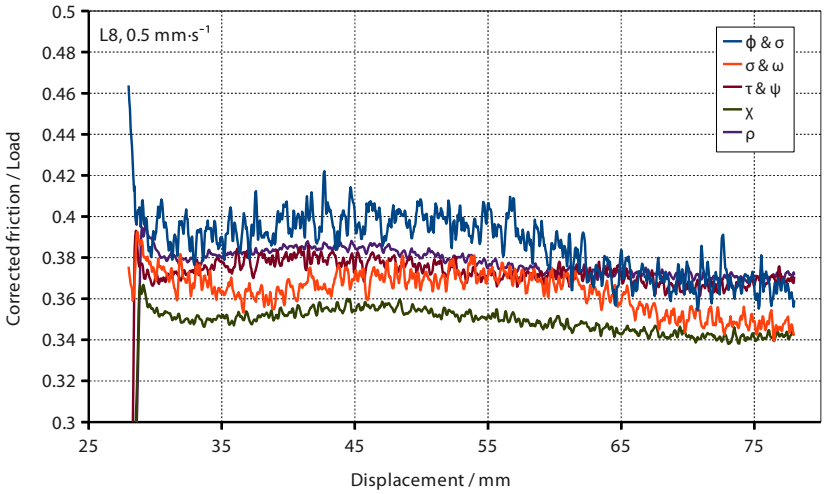

(a) Graph of corrected force against displacement for NW6-L8, sliding at 0.5 mm · s^{-1}.

Raw load / N	Anvils	α	β
0.25	ϕ & σ	1	0
0.73	σ & ω	—	—
2.65	τ & ψ	0.25	−0.61
8.09	χ	0.08	−1.64
19.01	ρ	0.03	−4.03

(b) Transform parameters for (a).

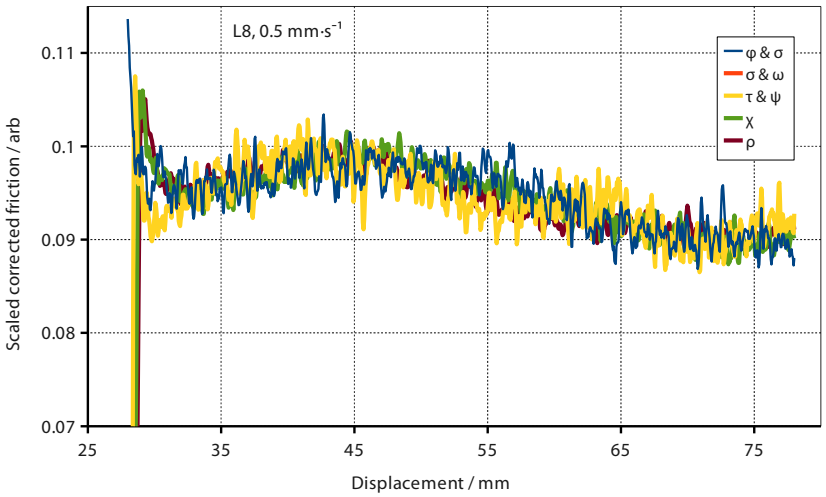

(c) Graph of force against displacement transformed according to the parameters in (b).

Figure 4.28: The process of mapping friction traces corresponding to different loads at a given interface onto a single master trace. Note the absence of σ & ω from (b) and (c): that trace did not fit.

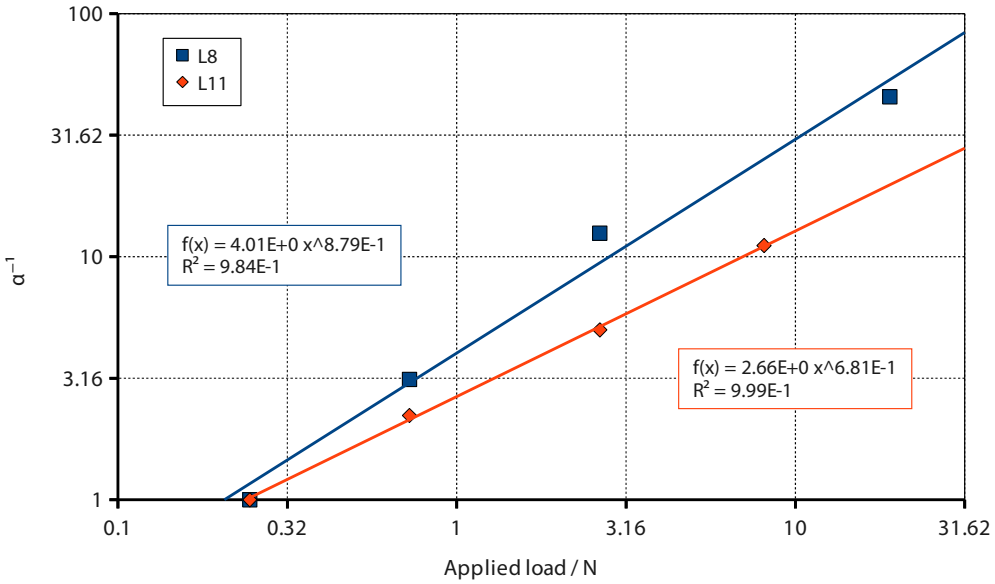

Figure 4.29: An example plot of α^{-1} against applied load for NW1 against each Lorica Soft slider, sliding at 0.5 mm $\cdot$ s^{-1}.

a missing trace indicates that no satisfactory fit was possible; emphasis was placed upon the latter, more reliable part of the curve during fitting.

Since α describes the scaling required to *collapse* the various traces onto a single trace, α^{-1} describes the way in which the principal friction scales with applied load. Plots of α^{-1} against applied load (figures 4.29 and E.8) show that (with one exception where neither of the two highest load traces could be fit) the principal friction varies sublinearly with load, in some cases with indices as low as ~ 0.6; the indices are tabulated for all experiments in table 4.5. As is clear from that table, the indices for NW6 are generally higher than for NW1 (no strong statements can be made for NW3 due to poorly fitting traces); and the indices for L8 are higher than for L11, in most cases quite markedly so. All trustworthy indices for principal friction are between 0.57 and 0.86.

Though it clearly is a measure of the amount of remainder friction, there are difficulties in the physical interpretation of β. The nature of the transformation described in equation 4.9 is that if an addition is made to each β value in inverse proportion to the corresponding α value then all of the traces simply move *en bloc*. In consequence, no significance can be attributed to absolute values of β. On the other hand, the change of β with applied load *is* meaningful. Figures 4.30 and E.9 show graphs of β against applied load; all but those corresponding to interfaces already identified as problematic are fit well by straight lines. However, the uncertainty in the offset prevents a direct assessment of the relative magnitudes of the principal and remainder components of friction.

Of course, another avenue is open in determining these relative scales: the overall relationship between total friction and load is known to be linear to high precision for each interface, so a simple computational experiment can be run to ascertain the proportions in which a power law with

Nonwoven	Slider	Speed / mm · s^{-1}	α^{-1} index
NW6	L8	0.05	0.797
		0.167	0.862
		0.5	0.789
		1.67	0.753
		5	0.761
	L11	0.5	0.568
NW3	L8	0.5	1.08
	L11	0.5	0.554
NW1	L8	0.5	0.879
	L11	0.5	0.681

Table 4.5: The scaling factor (α^{-1}) for principal friction has been found to vary as a power law with applied load. The indices for each of the tested interfaces and sliding speeds are shown in the table. Red indices indicate that something was wrong with the data which might make these numbers unreliable.

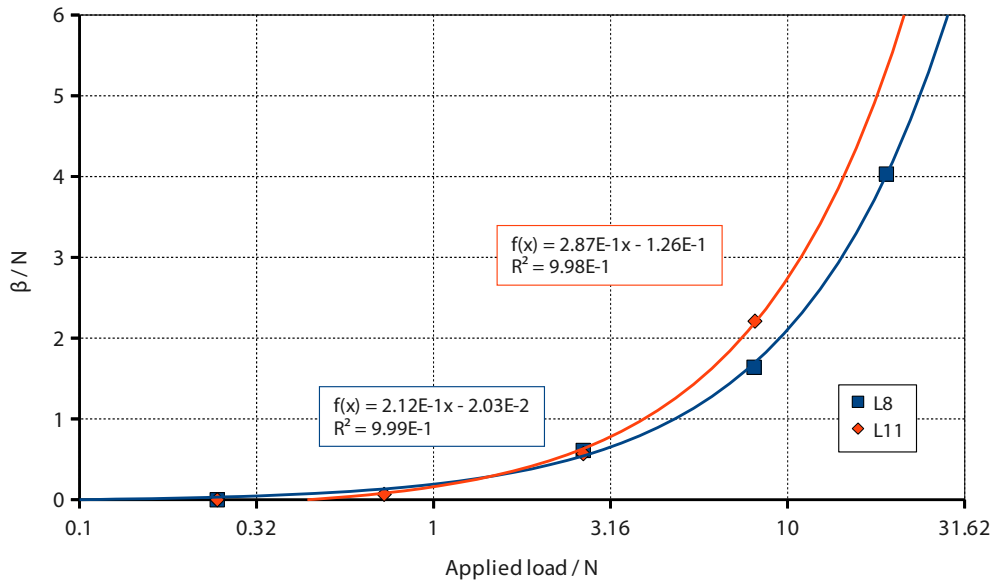

Figure 4.30: An example plot of β against applied load for NW6 sliding against each of the Lorica Soft sliders at 0.5 mm · s^{-1}

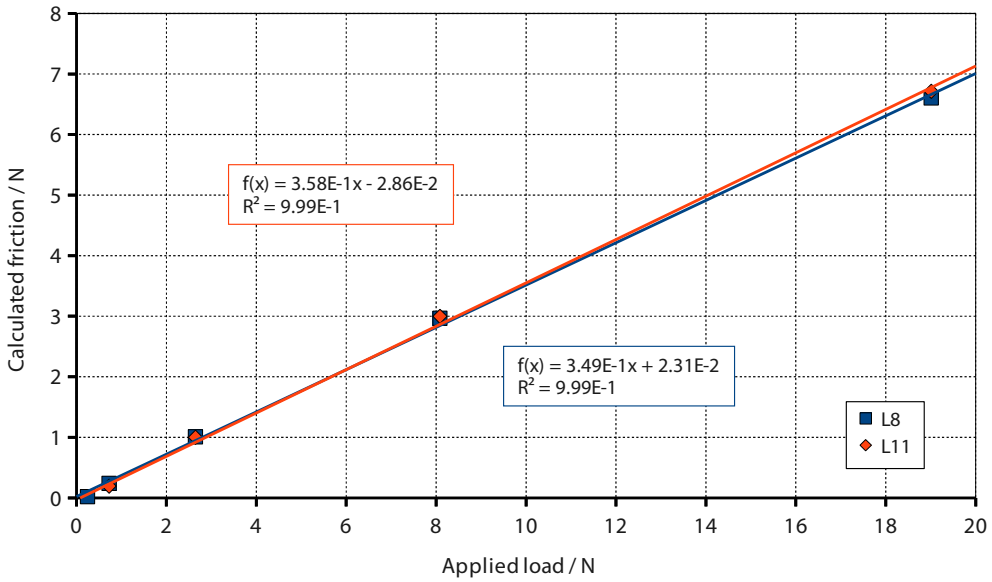

Figure 4.31: An example graph of calculated friction against load, comparing the models with the original linear fits from the data.

known index but unknown scale (corresponding to principal friction) should be added to a linear function with known gradient but unknown intercept (corresponding to remainder friction) in order to produce a function consistent with experimental results. This is achieved by fitting (least squares) a straight line to the sum of the two contributions, then manipulating first the coefficient of the principal friction term to obtain the correct gradient, and secondly adjusting the intercept of the remainder friction term to obtain the correct overall intercept. The results of this process are shown in figures 4.31 and E.10; in all cases the coefficient of determination (R^2) is at least 0.998. Though these values reflect a poorer fit than the same straight lines were to the original data, they remain good. It is perhaps not surprising that the fidelity of the fits is reduced: the data have been through several stages of processing before this, and though the fidelity of each has been *good*, they have inevitably not been perfect. That such agreement between calculated values and experimental fits is possible is strongly suggestive that the approach has merit. Typical proportions of the total friction ascribed to principal and remainder as a function of load are given in table 4.6.

Having established the relative scales and manners of variation with applied load of principal and remainder friction for the Lorica Soft-nonwoven interface, it remains to try to identify the mechanisms that they correspond to. This is considered in §4.5, where these data and those from §4.3 are compared.

4.5 Summary and conclusions

A brief summary of the main results presented in this chapter will be given before making connections between the two distinct experiments.

Anvils	Load / N	Remainder / N	Principal / N
ϕ & σ	0.25	−0.15	0.12
σ & ω	0.73	−0.05	0.25
τ & ψ	2.65	0.30	0.70
χ	8.09	1.6	1.5
ρ	19.01	4	3

Table 4.6: Approximate breakdown of friction into principal and remainder parts. It must be emphasised that these numbers are approximate indicators, averaging across interfaces and sliding speeds. In general, reducing the sliding speed relatively increases the importance of the remainder. At low loads the remainder component is negative; whilst clearly unphysical this is simply because the offset is attributed entirely to this term.

§4.3 found that the contact length of fibres constituting the interface between nonwoven and skin (surrogate) varied logarithmically with load, increasing by a factor of two to three (depending on the nonwoven) over two orders of magnitude of load. Assuming that the cylindrical fibres pressing into the skin (surrogate) obeyed Hertzian contact mechanics, predictions were made on the basis of the experimental data for the variation of adhesive friction (assuming no roughness on the scale of fibres) and viscoelastic friction (based on the Greenwood & Tabor model [7]) with load. Power law fits were good for both quantities; subject to their assumptions, adhesive friction was predicted to vary as $P^{0.6}$ and viscoelastic friction as $P^{1.4}$, with slight variations between nonwovens. NW1 had the highest contact fraction, followed by NW6, and then NW3. NW6 had the highest viscoelastic loss, followed by NW3, and finally NW1; however, this ranking is a little uncertain as the skin's loss factor may not be the same for all fibre diameters.

In §4.4 it was found that for Lorica Soft against each of the nonwovens overall friction against load could be well fit by a straight line, though there was a hint of sublinearity, especially at low loads. There was good evidence that the friction was composed of two different components (termed principal and remainder), the former varying with load sublinearly with a typical index around 0.75, and the latter varying linearly with load. Friction did generally increase with velocity, but only by about 10 % over two orders of magnitude velocity change; it was not possible to ascertain the manner of variation. Finally, under equivalent conditions NW1 had the highest friction, followed by NW3, and finally NW6.

Before comparing these two experiments, it is interesting to compare the Lorica Soft friction data with nonwoven-*in vivo* skin friction data obtained by SCA using the "curved pull" method described in §2.4.2. Experiments were run on four different arms using all three of the nonwovens used in this work, and coefficients of friction were calculated on the basis of three different applied loads. As commented before, this technique is not very sensitive to departures from Amontons' law, but it is an effective method for obtaining effective friction coefficients with low scatter. The method was used to obtain *static* friction coefficients, which took the values 0.38 ± 0.04, 0.36 ± 0.04, and 0.41 ± 0.03 for NW1, NW3, and NW6, respectively. In comparison to the *dynamic* nonwoven-Lorica Soft coefficients of friction, the most obvious difference is that the SCA nonwoven-skin

values are about twice the size: part of this is doubtless attributable to the comparison of dynamic and static data, but this will not account for the majority of the difference. Apart from the difference in magnitude, the trend between the nonwovens is not the same: the SCA data rank the nonwovens as NW3, NW1, NW6 in ascending order of friction coefficient against skin, whereas using comparable measurements the Lorica Soft data produce the ranking NW6, NW3, NW1. However, the error bars on the SCA data are of the same order as the differences, so it is difficult to be sure that NW3 and NW1 are in the correct order. Further, since comparison between nonwovens was not a primary objective of the Lorica Soft experiments there is potential for systematic error to influence the results; it is interesting that the ranking is the same as the order in which the nonwovens were tested. In summary, there is a clear difference in magnitude of coefficient of friction between the two tests which must be principally attributed to the difference in materials (though the tests were very different, so little more can be said), and though the ranking of nonwovens by coefficient of friction is not the same for the two it is not clear that *either* is significant, so the disparity cannot be interpreted. The former result is in marked distinction to the results of Derler *et al.* [60] comparing skin and Lorica Soft against a woven fabric.

Comparing the contact measurement and friction data obtained in this work, it is reasonable to conjecture that the principal friction is due to "nearly smooth" adhesion; that is, where the assumption that the skin and nonwoven fibres are smooth on the scale of a fibre diameter *nearly* holds. This is supported by the index of variation of principal friction with load only slightly exceeding the index found in §4.3 for contact fraction. According to the work of Archard and others (§2.4.1) roughness has the effect of increasing such indices towards unity; the slight difference in indices is thus attributed to slight roughness. Unfortunately, though this identification is quite plausible there is no *direct* evidence to support it.

Only two mechanisms are known which give rise to the linear relationship between friction and load that remainder friction demonstrates: plastic junction formation (following Bowden & Tabor [89]); and adhesion at rough, elastically deforming junctions (§2.4.1). The former is inconsistent with the lack of observed damage, apparently implicating the latter. This would suggest that Lorica Soft-nonwoven friction was all due to adhesion due to elastic deformation, but that two distinct populations of contacts took part: those corresponding to principal friction forming a fairly smooth interface; those corresponding to remainder friction forming a rough one. The lack of an explicitly viscoelastic friction mechanism is certainly consistent with the very limited variation of friction with sliding speed; what variation there is can perhaps be attributed to a rather more subtle viscoelastic effect like geometric aging (§2.4.8).

Considering again the mechanisms reviewed at the start of this chapter, some can be discounted for the Lorica Soft-nonwoven interface, and others shown probable.

Plastic dissipation. It has be shown that nonwovens *do* deform plastically from their initial state when they are loaded, both by direct observation of the behaviour of the fibres, and by the presence of a "run in" time for each new nonwoven or Lorica Soft sample. However, there is no evidence that plastic deformation continues to be an important mechanism of friction after this initial period; certainly there is no evidence of mounting damage, though it has not been searched for explicitly.

Viscoelastic dissipation. The very weak variation of friction with sliding speed suggests that if viscoelastic dissipation is present then it occurs to a very small extent.

Pinning. No "pinging" has been observed at interfaces: though fibres certainly were observed to move, their movement was fairly continuous and undulating (so far as could be established), implying that pinning is probably not an important mechanism.

Interfacial adhesion and dissipation. As discussed above, the data can be interpreted as suggesting two distinct populations of contact fibre[18] (one rough, one smooth) interacting with the skin (surrogate) surface by adhesion. This does not, of course, answer the question of where dissipation arises: adhesion is not, after all, intrinsically dissipative. It is, however, the most plausible of the identified interaction mechanisms on the basis of the available data.

Whilst both sets of experiments reported in this chapter have produced very interesting results and represent very substantial progress beyond what has been reported in the literature, they clearly represent only a beginning. They have *suggested* relationships that must in future work be further investigated and verified.

[18] It *is* possible that the two populations are instead features of the Lorica Soft, but considering the degree of variation of friction coefficient across the Lorica Soft, the proportions of the populations would have to be substantially more constant than their sum, which seems unlikely.

Chapter 5

Geometric friction

"As long as algebra and geometry have been separated, their progress have been slow and their uses limited; but when these two sciences have been united, they have lent each mutual forces, and have marched together towards perfection."

— Joseph-Louis Lagrange, 1736–1813

As explained in §3.2, geometric friction relates to how the normal forces introduced by a tense sheet over a curved surface induce frictional stresses on the surface, and in turn change the tension in the sheet, the shape of the surface, or both. Earlier work in this area has been reviewed in §2.4.2, but was limited to surfaces that were cylinders [100, 1], or at best convex prisms [107]. Work in this chapter provides a general framework within which more interesting surfaces can be approached, and considers some of these cases.

5.1 Introduction to the geometric friction work

Once the law relating local stresses and material properties to friction has been obtained for a given pair of material surfaces, the behaviour of an infinite, rigid, planar interface under normal loading is completely described. However, in practice most interesting situations fulfil none of these criteria, and so additional work relating complex stresses and geometries to friction is needed. For the skin-nonwoven interface considered in this work, stresses can either be in the form of directly applied stresses (reaction forces from a support surface, for example), or stresses induced by a tense nonwoven sheet and the geometry of the surface about which it is draped (figure 5.1). By their nature, the former (direct) stresses are relatively simple to describe and model as body forces applied at the surface. The latter type of stress is less easy to describe, and has been little studied. Such geometrically induced stresses and their effects on friction are the subject of this chapter.

For simplicity, direct stresses are neglected henceforth; their reintroduction is simple, but it is bought at the expense of clarity.

Given the general geometry, properties, and stresses in such systems, they are best described by continuum mechanics (§2.1). It is useful to recall Cauchy's law of motion (equation 2.2):

$$\nabla \cdot \mathbf{T} + \mathbf{f} = \rho \ddot{\chi} \qquad , \qquad \mathbf{T} = \mathbf{T}^{\mathsf{T}}$$

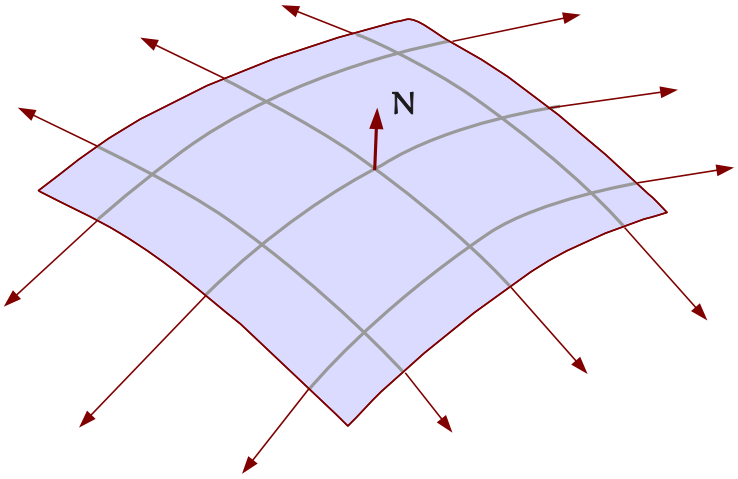

Figure 5.1: When a conformable sheet is placed in tension over a convex surface, a normal reaction force is generated. For "rough" surfaces, this causes friction, which in turn modifies the stress within the sheet.

where $\mathbf{T}$ is Cauchy stress, $\mathbf{f}$ is body force density, ρ is material density, and $\ddot{\chi}$ material acceleration. Before considering how to apply Cauchy's equation to the geometric friction problem, some assumptions are required. Assume that the nonwoven sheet:

1. has no through thickness, and can be represented as a two dimensional object;
2. always drapes, following the substrate surface without tearing or puckering;
3. is of sufficiently low density that its weight makes a negligible contribution to the forces acting; and
4. has no direct resistance to bending.

The last condition follows formally from the first, but is included for emphasis. These assumptions greatly simplify the analysis of this problem, and (but for the second) are very generally good assumptions. Assumption two is clearly *not* always true, though it is in many interesting cases. Its inclusion is essentially pragmatic: if a nonwoven sheet does *not* drape (in either way) then its behaviour is still more complicated to describe. The relaxation of this assumption would doubtless provide an interesting study, but it is not one which will be considered herein.

Representing the nonwoven sheet as a two dimensional object requires some interpretation of the three dimensional quantities in Cauchy's law of motion. Describing the nonwoven in this way is equivalent to assigning some finite thickness L, allowing no change through the thickness, and multiplying or dividing quantities by L, as relevant. For example, the nonwoven may be 200 µm thick and have a mass density of $20\,\mathrm{g}\cdot\mathrm{m}^{-2}$, so the mass density that would appear in the law of motion would be $20\,\mathrm{g}\cdot\mathrm{m}^{-2}\div 200\,\mu\mathrm{m} = 10^5\,\mathrm{g}\cdot\mathrm{m}^{-3}$. A further consequence of the lower dimension and the neglect of the nonwoven's weight is that the only body force ($\mathbf{f}$) to act is due only to the normal reaction from and frictional interaction with the substrate.

Cauchy's law of motion can now be interpreted into the geometric friction situation.

In *the nonwoven sheet*, Cauchy stress ($\mathbf{T}$) is caused by deformation of the sheet within the surface $\mathcal{S}$ defined by the substrate, and $\boldsymbol{\nabla}\cdot\mathbf{T}$ generally has both a normal component (due to surface curvature) and components within the surface. The frictional body forces act within $\mathcal{S}$, and the reaction from the substrate acts perpendicular to the surface. Clearly, in the case of a fixed substrate the normal reaction from the substrate will balance the normal component of $\boldsymbol{\nabla}\cdot\mathbf{T}$ and only the components of $\boldsymbol{\nabla}\cdot\mathbf{T}$ and $\mathbf{f}$ within $\mathcal{S}$ need be considered.

The *substrate* will generally not have a negligible weight density, so this cannot be ignored. However, the linearity of Cauchy's law of motion allows stress to be split into two components, $\mathbf{T} = \mathbf{T}' + \mathbf{T}_w$, where $\mathbf{T}_w$ balances the weight, so that both $\mathbf{T}_w$ and weight can be ignored in the subsequent consideration of the remaining $\mathbf{f}$ and $\mathbf{T}'$. It is important to note that this measure will cause a change in the apparent constitutive relationship for any nonlinear materials. Apart from any contact forces far from the interface, $\mathbf{f}$ in the substrate is now also purely due to normal reaction and friction, and thus acts only on the surface $\mathcal{S}$. The prime on $\mathbf{T}'$ will henceforth be discarded.

Having established the basic approach to the geometric friction problem, the details can be considered.

5.2 Description of the interacting bodies

Before the geometric friction system can be described at all notation for the bodies involved must be defined. This must extend the notation described in §2.1 and §2.1.2, and in some cases modify it, primarily to deal with the presence of *two* semi-independent material bodies, the substrate and the nonwoven sheet. Notation for the deformed and undeformed spaces and mappings between them is needed; and the qualitatively distinct regions of contact and non-contact must be considered.

5.2.1 Notation and terminology

By analogy with the notation defined in §2.1.1, the material body of the substrate is denoted $\mathfrak{L}$ with co-ordinates ν_ν, and similarly the manifold for the nonwoven sheet is described by $\mathfrak{S}$ and $\mathfrak{u}_\alpha$. These manifolds are mapped into space by $\boldsymbol{\lambda} : \mathfrak{L} \to \mathcal{L}$, $\boldsymbol{\sigma} : \mathfrak{S} \to \mathcal{S}$. Additionally, define $\mathcal{P} \subset \mathfrak{L}$ corresponding to the particles at the surface of the substrate, and the set $\mathcal{P}$ as the image of $\mathcal{P}$ under $\boldsymbol{\lambda}$. These mapping are illustrated in figure 5.2.

Again, after the convention adopted by Truesdell & Noll (apparently to facilitate more natural description of constitutive relationships) an *a priori* arbitrary reference configuration is selected for each of $\mathfrak{L}$ and $\mathfrak{S}$, denoted $\boldsymbol{\Lambda}$ and $\boldsymbol{\Sigma}$ respectively[1]. It should be emphasised that these are *not* fundamentally new quantities: they are merely specific instances of $\boldsymbol{\lambda}$ and $\boldsymbol{\sigma}$. It is also not the case that $\boldsymbol{\Lambda}$ and $\boldsymbol{\Sigma}$ *must* correspond to the same time, though they can do. In some instances it is more convenient to use locations in the reference configuration as co-ordinates, and in others to use the manifold co-ordinates. Again following the convention of Trusdell & Noll [10], the material description refers to a description in terms of positions in the reference configuration.

[1] $\boldsymbol{\Lambda}$ is chosen to denote the substrate reference configuration for the sake of regularity of relationship between general mappings and their reference configurations. This contrasts the earlier notation of Truesdell & Noll [10] who used $\varkappa$, apparently because it represented a further symbol of similar appearance to an "X".

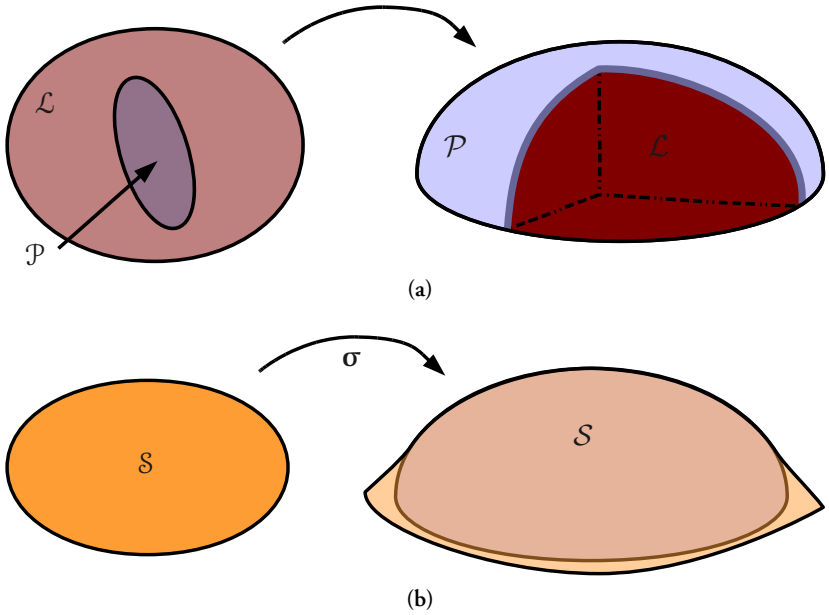

Figure 5.2: The manifolds for the two different material bodies and their subsets map into physical space as shown.

A general position vector in the current real space is denoted $\mathbf{x}$; if it is to be emphasised that the position is in any of $\mathcal{L}$, $\mathcal{P}$, or $\mathcal{S}$ then it is denoted $\mathbf{l}$, $\mathbf{p}$, or $\mathbf{s}$, respectively. Analogously, positions in the reference configurations $\boldsymbol{\Lambda}$ and $\boldsymbol{\Sigma}$ are denoted $\mathbf{L}$, $\mathbf{P}$, or $\mathbf{S}$.

A few additional articles of notation are needed to avoid ambiguity.

- Co-ordinates for $\mathcal{S}$ and $\mathcal{L}$ use Greek suffices; no other spaces use them.
- Bold ($\mathbf{T}$) script is reserved for denoting first and higher rank tensors in $\mathcal{S}$ and $\mathcal{L}$; matrices and columns in $\mathcal{S}$ and $\mathcal{L}$ are not emboldened.
- Contractions in $\mathcal{S}$ and $\mathcal{L}$ are denoted with a dot ($\cdot$); products in $\mathcal{S}$ and $\mathcal{L}$ receive no dot.
- Subscripts *are not* derivatives unless preceeded by the customary comma. This contrasts with notation commonly used in the study of fluids.

Following and improving on the convention stated by Pressley [11], components of tensors in $\mathcal{S}$ and $\mathcal{L}$ can be written in terms of the derivatives of the mappings $\boldsymbol{\sigma}$ and $\boldsymbol{\lambda}$ so that (using $\boldsymbol{\sigma}$ as an example)

$$\begin{aligned} \mathbf{t} = \mathsf{t}_\alpha \boldsymbol{\sigma}_{,\alpha} \quad &\Rightarrow \quad \mathbf{t}\cdot\mathbf{s} = \mathsf{t}_\alpha \mathcal{F}_{\mathrm{I}\,\alpha\beta}\mathsf{s}_\beta \\ \mathbf{T} = \mathsf{T}_{\alpha\beta}\boldsymbol{\sigma}_{,\alpha}\otimes\boldsymbol{\sigma}_{,\beta} \quad &\Rightarrow \quad \mathbf{T}\cdot\mathbf{S} = \mathsf{T}_{\alpha\beta}\mathcal{F}_{\mathrm{I}\,\beta\gamma}\mathsf{S}_{\gamma\delta}\boldsymbol{\sigma}_{,\alpha}\otimes\boldsymbol{\sigma}_{,\delta}, \end{aligned}$$

where $\mathcal{F}_{\mathrm{I}\,\alpha\beta} = \boldsymbol{\sigma}_{,\alpha}\cdot\boldsymbol{\sigma}_{,\beta}$, the first fundamental form of $\boldsymbol{\sigma}$.

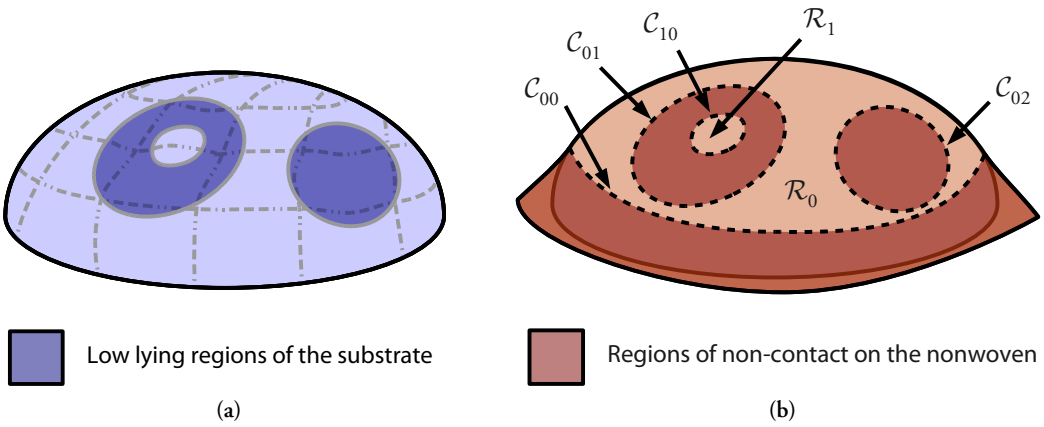

Figure 5.3: In general a non-uniform-convex surface contact cannot be described by a single simply connected region. (a) illustrates low-lying areas on the substrate. It is important to note that, depending on the limits of the nonwoven sheet, not all such low-lying areas will be regions of non-contact. (b) shows the regions of contact and non-contact on the nonwoven sheet.

5.2.2 Contact and non-contact

Clearly, both $\mathcal{S}$ and $\mathcal{P}$ are partitioned into regions of contact and regions of non-contact; in the regions of contact $\mathcal{S}$ and $\mathcal{P}$ are coincident. As behaviour is qualitatively different in the two types of region, notation must be defined to describe such regions, and a description of their behaviour must be derived.

In general both the nonwoven sheet and the substrate will be out of contact at the edges, so when considering contact it is logical to deal in terms of a set of loops $\{\mathcal{C}_{ij}\}$ which mark the limits of regions of contact $\{\mathcal{R}_i\}$. In the case of a uniformly convex surface the region $\mathcal{R}_0$ is the only region, and it is simply connected. The more general situation of a non-uniform-convex surface is illustrated in figure 5.3. In the general situation of several disjoint connected regions, the outermost limit of each connected contact is defined as the curve $\mathcal{C}_{i0}$. Within each of these regions other bounding curves are denoted $\mathcal{C}_{ij}$. In the case of concentric contact regions (for example, $\mathcal{R}_0$ and $\mathcal{R}_1$ in figure 5.3) the outer bounding curve $\mathcal{C}_{10}$ is within the region enclosed by $\mathcal{C}_{01}$; this pattern would continue if there were further concentric contact regions.

The evolution of the contact regions with time is not simple to describe in the general case: Poisson contraction means that "free" nonwoven surfaces are not generally ruled surfaces[2]; the possibility for stress to depend on strain *rate* breaks the one-to-one correspondence between deformation and stress; and for a nonwoven with non-negligible inertia there would be no unique solution for a surface with fixed forces at its boundaries in any case. Fortunately, in fundamental terms, the evolution of the curves $\{\mathcal{C}_i\}$ is determined by the instantaneous velocity fields. It is simplest to see the essence

[2]A ruled surface is a surface composed of the union of a set of straight lines [11]. Prisms (fairly clear), cones (lines through the apex), and planes (again clear) are examples of ruled surfaces.

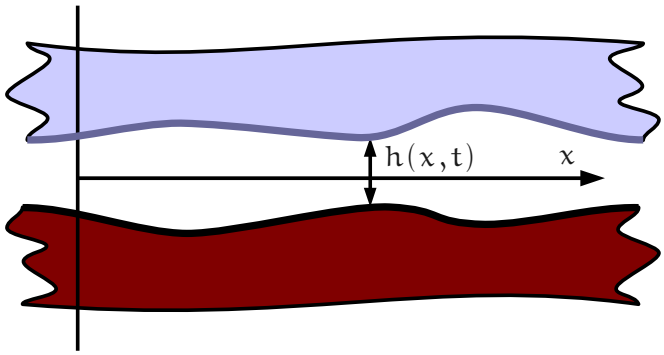

Figure 5.4: A simple two dimensional model of the movement of contact edges. The mechanisms involved here are identical to those which control the behaviour of the real system of interest.

of this argument by considering a "toy" two dimensional model before going on to consider the more complicated case at hand.

The simplest model that captures the essential mechanism at play is the two-dimensional motion of a pair of lines separated by a distance $h(x,t)$ (figure 5.4). The motion of any point on a $\mathcal{C}_{ij}$ can be considered in these terms: how must a point $x_l(t)$ move if $l = h(x_l(t),t)$, where l is a constant? This is fairly trivial to solve:

$$\frac{dl}{dt} = \frac{d}{dt}h(x_l(t),t) \qquad \Rightarrow \qquad 0 = \partial_t h + \dot{x_l}\partial_x h$$
$$\dot{x_l} = -\frac{\partial_t h(x_l)}{\partial_x h(x_l)}. \tag{5.1}$$

Although this is apparently complete, the situation of parallel incidence and matched velocities at $\mathcal{C}_{ij}$ does not immediately fit into the "toy" model as it stands: equation 5.1 represents the quotient of two zeros. Fortunately, l'Hôpital's rule [163] provides a simple means to evaluate such a quotient:

$$\dot{x_l} = -\frac{\partial_x \partial_t h(x_l)}{\partial_x{}^2 h(x_l)} \qquad \text{if } \partial_t h(x_l) = \partial_x h(x_l) = 0. \tag{5.2}$$

This is readily confirmed and clarified by considering the example function

$$h(x,t) = \begin{cases} a(x - L(t))^2 & x > L(t) \\ 0 & x \leq L(t) \end{cases}.$$

Equation 5.2 gives that $\dot{x_l} = \dot{L}(t)$, as it should, so long as the derivatives are evaluated at $x = \lim_{\epsilon \to 0}(L(t) + \epsilon)$; that is, infinitesimally outside the contact region. This point is important, and it applies for all such models. Having considered a simplified model where the same mechanisms operate it is now straight forward to extend this model to consider the more general problem.

Two generalisations must be made in moving from the "toy" model to a realistic one. The first involves defining $\mathbf{h} = \boldsymbol{\sigma} - \boldsymbol{\lambda}$; the second involves identifying an analogue for x. This is most readily

done by considering the tangent spaces of $\mathcal{S}$ and $\mathcal{P}$ at $\mathbf{x} \in \mathcal{C}_{ij}$. Since only a small region near the point $\mathbf{x}$ is considered, the tangent space is an adequate substitute for x. Now, consider the behaviour of $\boldsymbol{\epsilon}(t)$:

$$\frac{d\mathbf{l}}{dt} = \frac{d}{dt}\mathbf{h}(\boldsymbol{\epsilon}(t), t) \qquad \Rightarrow \qquad \mathbf{0} = \partial_t \mathbf{h} + \dot{\boldsymbol{\epsilon}} \cdot \boldsymbol{\nabla}_{\boldsymbol{\epsilon}} \mathbf{h}$$
$$\dot{\boldsymbol{\epsilon}} = -(\boldsymbol{\nabla}_{\boldsymbol{\epsilon}} \mathbf{h})^{-T} \cdot \partial_t \mathbf{h}.$$

As in the toy model, it will often be the case that both $\boldsymbol{\nabla}_{\boldsymbol{\epsilon}} \mathbf{h}$ and $\partial_t \mathbf{h}$ are zero on a bounding curve, and as with that model l'Hôpital's rule enables a result still to be extracted:

$$\mathbf{0} = (\hat{\boldsymbol{w}} \cdot \boldsymbol{\nabla}_{\boldsymbol{\epsilon}}) \partial_t \mathbf{h} + \dot{\boldsymbol{\epsilon}} \cdot \boldsymbol{\nabla}_{\boldsymbol{\epsilon}} (\hat{\boldsymbol{w}} \cdot \boldsymbol{\nabla}_{\boldsymbol{\epsilon}}) \mathbf{h}$$
$$\dot{\boldsymbol{\epsilon}} = -(\partial_\perp \boldsymbol{\nabla}_{\boldsymbol{\epsilon}} \mathbf{h})^{-T} \cdot (\partial_\perp \dot{\mathbf{h}}) \qquad \text{if } \boldsymbol{\nabla}_{\boldsymbol{\epsilon}} \mathbf{h} = \partial_t \mathbf{h} = \mathbf{0},$$

where the direction $\hat{\boldsymbol{w}}$ was chosen as to be perpendicular to the curve and $\partial_\perp \coloneqq \hat{\boldsymbol{w}} \cdot \boldsymbol{\nabla}_{\boldsymbol{\epsilon}}$; in this situation the derivative *along* the curve is zero, so this is the most sensible choice of direction. As before, these quantities must be evaluated infinitesimally outside of the curve so that the higher order discontinuities do not cause problems.

5.3 Equations of motion in contact regions

In §5.1 the general form of Cauchy's law of motion was restated. Subject to the conventions and assumptions regarding weight, away from the contact regions of $\mathcal{P}$ and $\mathcal{S}$ no body forces act. These regions thus each obey

$$\boldsymbol{\nabla} \cdot \mathbf{T} = \rho_\dagger \ddot{\boldsymbol{\chi}}.$$

The behaviour in the contact regions of $\mathcal{P}$ and $\mathcal{S}$ is much more complicated due to the non-zero contact force.

This section considers *only* contact regions, and in them relates the contact force to the local geometry, stresses, and dynamics. It starts by considering the nature of a frictional interface in more detail (§5.3.1), then relates contact forces to stresses and acceleration (§5.3.2). Normal components of stress are then related to local geometry (§5.3.3), before finally considering a concrete example of a classic friction law in §5.3.4. After a brief discussion of static friction in §5.3.1 attention is focused on dynamic friction; the reason for this is made clear in §5.3.1.

Note that, since contact is assumed throughout, locally $\mathcal{S} = \mathcal{P}$ and so the two symbols may be used interchangeably. However, this will only be done where it simplifies rather than complicates or obscures.

5.3.1 Instantaneous isotropic interfaces

In order to progress with the study of frictional interfaces, some further details must be specified. A wide class of interfaces can be defined so:

Definition — "Instantaneous isotropic interface (III)" An interface composed of a pair of surfaces which have no intrinsically preferred directions and no directional memory effects, so that the frictional force acts in the opposite direction to the *current* relative velocity vector $\boldsymbol{\nu}$ (for $\boldsymbol{\nu} \neq \mathbf{0}$), or to the sum of *current* applied forces parallel to the interface acting to initiate motion (for $\boldsymbol{\nu} = \mathbf{0}$).

The last aspect of this definition addresses the ambiguity of direction mentioned is §2.4.1, which is of great importance. Based on this definition and the preceding discussion of laws of motion (§5.1) it is possible to write down a general friction law for IIIs, which depends only on two materially determined functions, the friction scalar functions, one for statics and one for dynamics:

$$\mathbf{P}_{\mathcal{S}} \cdot \mathbf{f} = \begin{cases} -\psi_{\mathrm{s}} \hat{\mathbf{F}} & \boldsymbol{\nu} = \mathbf{0} \\ -\psi_{\mathrm{d}} \hat{\boldsymbol{\nu}} & \boldsymbol{\nu} \neq \mathbf{0} \end{cases},$$

where $\mathbf{P}_{\mathcal{S}}$ is a projection matrix which removes components outside of the surface $\mathcal{S}$, $\mathbf{F}$ is the force parallel to the interface in the particles' own frame—that is, allowing for their acceleration—, $\boldsymbol{\nu}$ is sliding velocity parallel to the interface, and the superposed circumflex indicates normalisation. Substituting these definitions into Cauchy's law of motion gives

$$\boldsymbol{\nabla} \cdot \mathbf{T}_1 + \mathbf{P}_{\hat{\mathbf{N}}} \cdot \mathbf{f}_1 - \psi_{\mathrm{s}\,1} \left\{ \frac{\mathbf{P}_{\mathcal{S}} \cdot (\boldsymbol{\nabla} \cdot \mathbf{T}_1 + \mathbf{P}_{\hat{\mathbf{N}}} \cdot \mathbf{f}_1 - \rho_1 \ddot{\boldsymbol{\chi}}_1)}{\|\mathbf{P}_{\mathcal{S}} \cdot (\boldsymbol{\nabla} \cdot \mathbf{T}_1 + \mathbf{P}_{\hat{\mathbf{N}}} \cdot \mathbf{f}_1 - \rho_1 \ddot{\boldsymbol{\chi}}_1)\|} \right\} = \rho_1 \ddot{\boldsymbol{\chi}}_1 \quad , \quad \boldsymbol{\nu} = \mathbf{0} \tag{5.3}$$

$$\boldsymbol{\nabla} \cdot \mathbf{T}_1 + \mathbf{P}_{\hat{\mathbf{N}}} \cdot \mathbf{f}_1 - \psi_{\mathrm{d}\,1} \left\{ \frac{\mathbf{P}_{\mathcal{S}} \cdot (\dot{\boldsymbol{\chi}}_1 - \dot{\boldsymbol{\chi}}_2)}{\|\mathbf{P}_{\mathcal{S}} \cdot (\dot{\boldsymbol{\chi}}_1 - \dot{\boldsymbol{\chi}}_2)\|} \right\} = \rho_1 \ddot{\boldsymbol{\chi}}_1 \quad , \quad \boldsymbol{\nu} \neq \mathbf{0}, \tag{5.4}$$

where the subscript "1" indicates the body in question, "2" the contacting body, $\boldsymbol{\chi}_\dagger$ denotes either $\boldsymbol{\lambda}$ or $\boldsymbol{\sigma}$, and $\mathbf{P}_{\hat{\mathbf{N}}}$ is a projection matrix onto the normal to the surface $\mathcal{S}$. The right hand side of equation 5.3 need not be zero since a lack of relative motion does not preclude motion entirely. From these equations it is clear that the static case is underdetermined: within the surface both friction and non-friction terms are proportional to the same vector, so reducing equation 5.3 to the scalar equation

$$\|\mathbf{P}_{\mathcal{S}} \cdot (\boldsymbol{\nabla} \cdot \mathbf{T}_1 + \mathbf{P}_{\hat{\mathbf{N}}} \cdot \mathbf{f}_1 - \rho_1 \ddot{\boldsymbol{\chi}})\| = \psi_{\mathrm{s}}. \tag{5.5}$$

Clearly, since the stress is fundamentally determined by the deformation *vector* field and its derivatives [10], this *scalar* equation cannot be solved. Further, ψ_{s} is generally not a single valued function of local pressure; it scales with applied force up to a limit, beyond which slip occurs. These observations imply that for an III there is not a unique stable static stress field, *even if the materials show no memory effects and are linear elastic*: information on the history of the interface is required[3]. It is still, of course, possible to determine whether a particular configuration is stable, most simply by allowing ψ_{s} to denote its maximum value and considering

$$\|\mathbf{P}_{\mathcal{S}} \cdot (\boldsymbol{\nabla} \cdot \mathbf{T}_1 + \mathbf{P}_{\hat{\mathbf{N}}} \cdot \mathbf{f}_1 - \rho_1 \ddot{\boldsymbol{\chi}})\| \leq \psi_{\mathrm{s}};$$

[3]It is interesting to compare this result with other non-uniqueness results for frictional interfaces, for example those of Hild [164, 165] and Hasani *et al.* [166, 167]. These arise from an entirely different source (and are based on an unphysical but mathematically convenient approximation that friction opposes deformation rather than motion), suggesting that non-uniqueness is an unavoidable features of friction problems, and arises from multiple sources.

if this is true then local slip will not occur. The only case in which the static system may be solved is at the limit of slip in the case of high symmetry in which the problem is really one dimensional. In this case, the equilibrium form of equation 5.3 reduces to the low density limit of equation 5.4 as there is only one possible direction for any vector to point.

The dynamic equation is, at this stage, in principle solvable for any dimension.

5.3.2 Contact forces at a dynamic interface

In general, both the nonwoven sheet and the substrate that constitute an interface will deform in response to the tensile forces imposed upon the sheet. In the presence of acceleration the simple "equal and opposite" relationship between normal components of $\boldsymbol{\nabla} \cdot \mathbf{T}$ and normal reaction from the facing surface alluded to in §5.1 breaks down: a more general relationship must be considered.

Consider the forms of equation 5.4 for the nonwoven sheet (n) and the substrate (s):

$$\boldsymbol{\nabla} \cdot \mathbf{T}_n + \mathbf{P}_{\hat{\mathbf{N}}} \cdot \mathbf{f}_n - \psi_d \left\{ \frac{\mathbf{P}_{\mathcal{S}} \cdot (\dot{\boldsymbol{\sigma}} - \dot{\boldsymbol{\lambda}})}{\|\mathbf{P}_{\mathcal{S}} \cdot (\dot{\boldsymbol{\sigma}} - \dot{\boldsymbol{\lambda}})\|} \right\} = \rho_n \ddot{\boldsymbol{\sigma}} \tag{5.6}$$

$$\boldsymbol{\nabla} \cdot \mathbf{T}_s + \mathbf{P}_{\hat{\mathbf{N}}} \cdot \mathbf{f}_s - \psi_d \left\{ \frac{\mathbf{P}_{\mathcal{S}} \cdot (\dot{\boldsymbol{\lambda}} - \dot{\boldsymbol{\sigma}})}{\|\mathbf{P}_{\mathcal{S}} \cdot (\dot{\boldsymbol{\lambda}} - \dot{\boldsymbol{\sigma}})\|} \right\} = \rho_s \ddot{\boldsymbol{\lambda}} \quad , \quad \boldsymbol{\varkappa} \in \mathcal{P}, \tag{5.7}$$

since friction scalars relating to the same interface must be equal. Newton's third law applies irrespective of acceleration, so $\mathbf{f}_s = -\mathbf{f}_n$. Further, where the surfaces $\mathcal{S}$ and $\mathcal{P}$ are in contact both $\dot{\boldsymbol{\sigma}} \cdot \hat{\mathbf{N}} = \dot{\boldsymbol{\lambda}} \cdot \hat{\mathbf{N}}$ and $\ddot{\boldsymbol{\sigma}} \cdot \hat{\mathbf{N}} = \ddot{\boldsymbol{\lambda}}_s \cdot \hat{\mathbf{N}}$: appendix F justifies and discusses these equations further. Consider the dot product of equations 5.7 and 5.6 with $\hat{\mathbf{N}}$:

$$(\boldsymbol{\nabla} \cdot \mathbf{T}_s) \cdot \hat{\mathbf{N}} + \mathbf{f}_s \cdot \hat{\mathbf{N}} = \rho_s \ddot{\boldsymbol{\lambda}} \cdot \hat{\mathbf{N}} \tag{5.8}$$

$$(\boldsymbol{\nabla} \cdot \mathbf{T}_n) \cdot \hat{\mathbf{N}} + \mathbf{f}_n \cdot \hat{\mathbf{N}} = \rho_n \ddot{\boldsymbol{\sigma}} \cdot \hat{\mathbf{N}}. \tag{5.9}$$

Summing these equations,

$$(\boldsymbol{\nabla} \cdot \mathbf{T}_s + \boldsymbol{\nabla} \cdot \mathbf{T}_n) \cdot \hat{\mathbf{N}} = (\rho_s + \rho_n) \ddot{\boldsymbol{\chi}}_\dagger \cdot \hat{\mathbf{N}},$$

where $\ddot{\boldsymbol{\chi}}_\dagger \cdot \hat{\mathbf{N}} \coloneqq \ddot{\boldsymbol{\sigma}} \cdot \hat{\mathbf{N}} = \ddot{\boldsymbol{\lambda}} \cdot \hat{\mathbf{N}}$ because normal acceleration is equal on both sides of the interface. $\ddot{\boldsymbol{\chi}}_\dagger \cdot \hat{\mathbf{N}}$ is thus obtained:

$$\ddot{\boldsymbol{\chi}}_\dagger \cdot \hat{\mathbf{N}} = \frac{(\boldsymbol{\nabla} \cdot \mathbf{T}_s + \boldsymbol{\nabla} \cdot \mathbf{T}_n) \cdot \hat{\mathbf{N}}}{\rho_s + \rho_n}.$$

Substituting this result back into equations 5.8 and 5.9 gives

$$-\mathbf{f}_n \cdot \hat{\mathbf{N}} = \mathbf{f}_s \cdot \hat{\mathbf{N}} = \left\{ \frac{\rho_s \boldsymbol{\nabla} \cdot \mathbf{T}_n - \rho_n \boldsymbol{\nabla} \cdot \mathbf{T}_s}{\rho_s + \rho_n} \right\} \cdot \hat{\mathbf{N}},$$

the normal force per unit area exerted by the substrate on the sheet. Further substituting this result

into the equations of motion (5.7 and 5.6),

$$\boldsymbol{\nabla}\cdot\mathbf{T}_s+\mathbf{P}_{\hat{\mathbf{N}}}\cdot\left\{\frac{\rho_s\boldsymbol{\nabla}\cdot\mathbf{T}_n-\rho_n\boldsymbol{\nabla}\cdot\mathbf{T}_s}{\rho_s+\rho_n}\right\}-\psi_d\left\{\frac{\mathbf{P}_{\mathcal{S}}\cdot(\dot{\boldsymbol{\lambda}}-\dot{\boldsymbol{\sigma}})}{\|\mathbf{P}_{\mathcal{S}}\cdot(\dot{\boldsymbol{\lambda}}-\dot{\boldsymbol{\sigma}})\|}\right\}=\rho_s\ddot{\boldsymbol{\lambda}}\quad,\quad\mathbf{x}\in\mathcal{P}\tag{5.10}$$

$$\boldsymbol{\nabla}\cdot\mathbf{T}_n-\mathbf{P}_{\hat{\mathbf{N}}}\cdot\left\{\frac{\rho_s\boldsymbol{\nabla}\cdot\mathbf{T}_n-\rho_n\boldsymbol{\nabla}\cdot\mathbf{T}_s}{\rho_s+\rho_n}\right\}-\psi_d\left\{\frac{\mathbf{P}_{\mathcal{S}}\cdot(\dot{\boldsymbol{\sigma}}-\dot{\boldsymbol{\lambda}})}{\|\mathbf{P}_{\mathcal{S}}\cdot(\dot{\boldsymbol{\sigma}}-\dot{\boldsymbol{\lambda}})\|}\right\}=\rho_n\ddot{\boldsymbol{\sigma}}.\tag{5.11}$$

The situation of negligible nonwoven inertia ($\rho_n\approx 0$) is interesting to consider. In this case the above equations simplify considerably to

$$\boldsymbol{\nabla}\cdot\mathbf{T}_s+\mathbf{P}_{\hat{\mathbf{N}}}\cdot\{\boldsymbol{\nabla}\cdot\mathbf{T}_n\}-\psi_d\left\{\frac{\mathbf{P}_{\mathcal{S}}\cdot(\dot{\boldsymbol{\lambda}}-\dot{\boldsymbol{\sigma}})}{\|\mathbf{P}_{\mathcal{S}}\cdot(\dot{\boldsymbol{\lambda}}-\dot{\boldsymbol{\sigma}})\|}\right\}=\rho_s\ddot{\boldsymbol{\lambda}}\quad,\quad\mathbf{x}\in\mathcal{P},$$

and

$$\boldsymbol{\nabla}\cdot\mathbf{T}_n-\mathbf{P}_{\hat{\mathbf{N}}}\cdot\{\boldsymbol{\nabla}\cdot\mathbf{T}_n\}-\psi_d\left\{\frac{\mathbf{P}_{\mathcal{S}}\cdot(\dot{\boldsymbol{\sigma}}-\dot{\boldsymbol{\lambda}})}{\|\mathbf{P}_{\mathcal{S}}\cdot(\dot{\boldsymbol{\sigma}}-\dot{\boldsymbol{\lambda}})\|}\right\}=\mathbf{0},$$

where the latter simplifies to

$$\mathbf{P}_{\mathcal{S}}\cdot\{\boldsymbol{\nabla}\cdot\mathbf{T}_n\}-\psi_d\left\{\frac{\mathbf{P}_{\mathcal{S}}\cdot(\dot{\boldsymbol{\sigma}}-\dot{\boldsymbol{\lambda}})}{\|\mathbf{P}_{\mathcal{S}}\cdot(\dot{\boldsymbol{\sigma}}-\dot{\boldsymbol{\lambda}})\|}\right\}=\mathbf{0},$$

since $\mathbf{P}_{\mathcal{S}}+\mathbf{P}_{\hat{\mathbf{N}}}=\mathbf{I}$, the identity tensor. In this limit it is therefore the case that the nonwoven sheet behaves precisely as it would if there were no normal acceleration at all (setting $\ddot{\boldsymbol{\sigma}}\cdot\hat{\mathbf{N}}=0$ in equation 5.9). This is perhaps as would be expected: in the absence of inertia all systems respond instantaneously, and all of their states are steady.

These equations are complete but for the specification of the friction scalars. They generally depend on normal force density (for example, Amontons' law asserts proportionality between frictional stress and normal force density), and, as shown above, the normal force density depends on the normal components of $\boldsymbol{\nabla}\cdot\mathbf{T}_s$ and $\boldsymbol{\nabla}\cdot\mathbf{T}_n$. The substrate has through thickness, and provides normal forces by deforming; the nonwoven sheet provides them by virtue of the curvature of the surface. This is considered further in §5.3.3

5.3.3 Normal stress from the curved nonwoven sheet

It is hard to imagine friction scalars that would *not* depend upon normal stress. Earlier models have related this quantity to tangential stress and curvature; a similar result should be obtainable here. The fundamental mechanism by which a normal stress is generated by tension in a nonwoven sheet draped over a general curved surface is the same as that advanced by Cottenden *et al.* [107] for their simple, two-dimension model (figure 5.5): normal components of tension are introduced by the surface curvature.

In two dimensions there is no question of how to describe the local curvature of a surface: as shown in figure 5.5 it is a simple matter to define the angle through which the surface turns as a function of

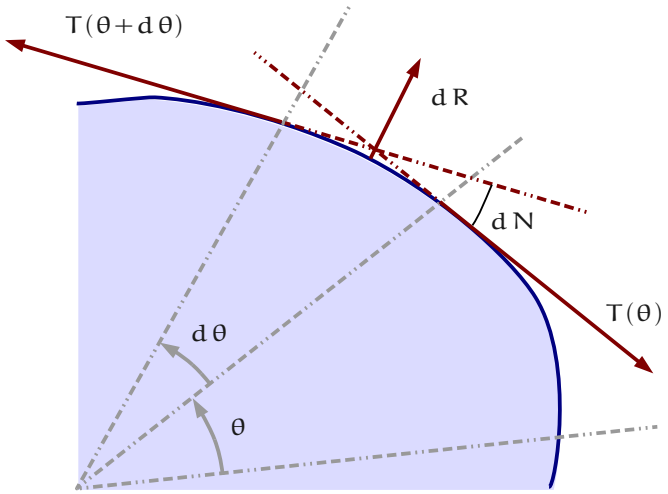

Figure 5.5: The tension forces in a draped sheet over a curved surface are always parallel to that surface. It therefore follows that the two forces $\mathsf{T}(\theta)$ and $\mathsf{T}(\theta + \mathrm{d}\theta)$ will not be parallel to each other and so exert a net force on an inwards normal, exciting a normal reaction force $\mathrm{d}\mathsf{R}$.

some co-ordinate. For a one dimensional surface—that is, a curve in two dimensions—the identity between change in surface angle and change in a unit normal is an article of trivia, but as the unit normal generalises well to two dimensional surfaces this parenthetic identity becomes the pillar of the new theory. The change in surface unit normal (analogous to angle change in two dimensions) between two locations $\mathbf{x}$ and $\mathbf{x}+\boldsymbol{\eta}$ is

$$\delta\hat{\mathbf{N}} = \hat{\mathbf{N}}(\mathbf{x}+\boldsymbol{\eta}) - \hat{\mathbf{N}}(\mathbf{x}) = \boldsymbol{\eta}\cdot\boldsymbol{\nabla}\hat{\mathbf{N}} + \mathcal{O}(\|\boldsymbol{\eta}\|^2).$$

Note that $\hat{\mathbf{N}}$ is a vector: its direction is as shown in figure 5.6. Having recognised the role of $\hat{\mathbf{N}}$, two derivations of normal force density as a function of tangential stress and surface curvature are offered. The first is physically intuitive, though a little longer and less rigorous; the second is shorter and neater, but owes nothing to physical reasoning at all. Both are presented for their mutual support.

It should be emphasised that this mechanism only applies to points at which the surfaces $\mathcal{S}$ and $\mathcal{P}$ are in contact.

For the first derivation, consider a small area of the surface, $\mathcal{A}$ bounded by $\partial\mathcal{A}$ (figure 5.7). The component of force $\mathrm{d}\mathsf{R}$ along an *inward pointing* normal is

$$\begin{aligned}\mathrm{d}\mathsf{R}(\mathbf{x}) &= \lim_{\|\boldsymbol{\eta}\|\to 0} \oint_{\partial\mathcal{A}} \mathrm{d}\mathbf{F}(\mathbf{x}+\boldsymbol{\eta})\cdot\hat{\mathbf{N}}(\mathbf{x}+\boldsymbol{\eta}) \\ &= \lim_{\|\boldsymbol{\eta}\|\to 0} \oint_{\partial\mathcal{A}} \mathrm{d}\mathbf{F}(\mathbf{x}+\boldsymbol{\eta})\cdot\left[(\boldsymbol{\eta}\cdot\boldsymbol{\nabla})\hat{\mathbf{N}}(\mathbf{x})\right], \end{aligned} \tag{5.12}$$

where terms of order $\|\boldsymbol{\eta}\|^2$ in the integrand have been neglected on the basis of the limit. Recalling

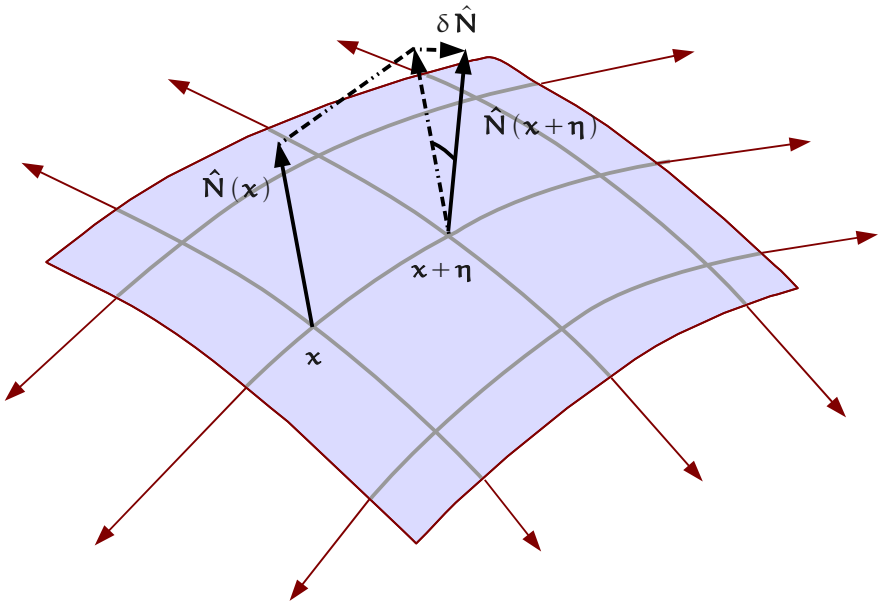

Figure 5.6: The "angle" $\delta\hat{\mathbf{N}}$ is equal to the change in unit normal between $\mathbf{x}$ and $\mathbf{x}+\boldsymbol{\eta}$. Its direction is generally not the same as that of $\boldsymbol{\eta}$.

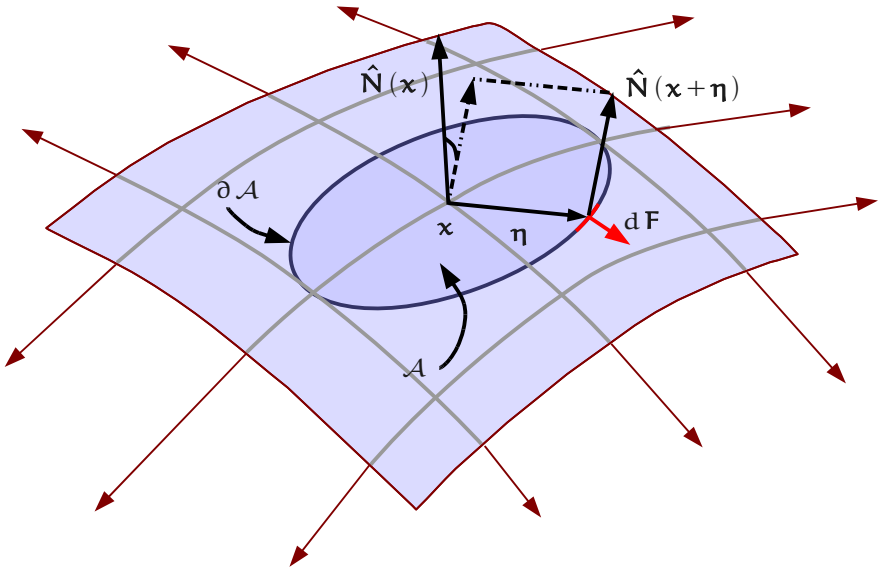

Figure 5.7: The region considered when calculating the pressure at a point. $\mathrm{d}\mathbf{F}$ is the element of force that acts along the coloured portion of the boundary $\partial\mathcal{A}$.

that the nonwoven sheet is modelled as a two dimensional entity, the Cauchy stress $\mathbf{T}_n$ within the nonwoven and an element of force $d\mathbf{F}$ are related by $d\mathbf{F} = L\mathbf{T} \cdot d\check{\mathbf{x}}$, where $d\check{\mathbf{x}}$ is an axial distance vector and L is the nonwoven sheet thickness. Substituting this into equation 5.12,

$$\begin{aligned} dR(\mathbf{x}) &= L \lim_{\|\boldsymbol{\eta}\| \to 0} \oint_{\partial \mathcal{A}} [\mathbf{T}(\mathbf{x}) \cdot d\check{\boldsymbol{\eta}}] \cdot \left[(\boldsymbol{\eta} \cdot \boldsymbol{\nabla}) \hat{\mathbf{N}}(\mathbf{x}) \right] \\ &= L \lim_{\|\boldsymbol{\eta}\| \to 0} \int_{\mathcal{A}} \boldsymbol{\nabla}_{\boldsymbol{\eta}} \cdot \left[(\boldsymbol{\eta} \cdot \boldsymbol{\nabla}) \hat{\mathbf{N}}(\mathbf{x}) \cdot \mathbf{T}(\mathbf{x}) \right] dS, \end{aligned}$$

where the latter step involves applying the divergence theorem in two dimensions. Note that the divergence contracts between $\boldsymbol{\nabla}$ and the second index of $\mathbf{T}$, which is the only free index inside the square brackets. The divergence can be expanded using the product rule, and in the limit given only the term in which $\boldsymbol{\eta}$ is differentiated survives:

$$dR(\mathbf{x}) = L \int_{\mathcal{A}} \mathrm{Tr} \left[\boldsymbol{\nabla} \hat{\mathbf{N}}(\mathbf{x}) \cdot \mathbf{T}(\mathbf{x}) \right] dS \qquad \Rightarrow \qquad \frac{dR(\mathbf{x})}{dS} = L\,\mathrm{Tr} \left[\boldsymbol{\nabla} \hat{\mathbf{N}}(\mathbf{x}) \cdot \mathbf{T}(\mathbf{x}) \right].$$

Defining the *curvature tensor* $\mathbf{C} \coloneqq \boldsymbol{\nabla} \hat{\mathbf{N}}(\mathbf{x})$ and recognising $dR(\mathbf{x})/dS = -L(\boldsymbol{\nabla} \cdot \mathbf{T}) \cdot \hat{\mathbf{N}}$,[4]

$$(\boldsymbol{\nabla} \cdot \mathbf{T}_n) \cdot \hat{\mathbf{N}} = -\mathrm{Tr} \left[\mathbf{C}(\mathbf{x}) \cdot \mathbf{T}(\mathbf{x}) \right]. \tag{5.13}$$

A more rigorous but less physical method for obtaining the normal component of stress is simply to calculate $(\boldsymbol{\nabla} \cdot \mathbf{T}_n) \cdot \hat{\mathbf{N}}$. Representing $\mathbf{T}$ as described in §5.2.1,

$$\begin{aligned} \boldsymbol{\nabla} \cdot \mathbf{T}_n &= (\boldsymbol{\nabla} u_\gamma \partial_\gamma) \cdot (T_{n\,\alpha\beta}\, \boldsymbol{\sigma}_{,\alpha} \otimes \boldsymbol{\sigma}_{,\beta}) \\ &= (\boldsymbol{\nabla} u_\gamma \cdot \boldsymbol{\sigma}_{,\beta}) (T_{n\,\alpha\beta,\gamma} \boldsymbol{\sigma}_{,\alpha} + T_{n\,\alpha\beta} \boldsymbol{\sigma}_{,\alpha\gamma}) + (\boldsymbol{\nabla} u_\gamma \cdot \boldsymbol{\sigma}_{,\beta\gamma})\, T_{n\,\alpha\beta} \boldsymbol{\sigma}_{,\alpha} \\ &= (T_{n\,\alpha\beta,\beta} \boldsymbol{\sigma}_{,\alpha} + T_{n\,\alpha\beta} \boldsymbol{\sigma}_{,\alpha\beta}) + (\boldsymbol{\nabla} u_\gamma \cdot \boldsymbol{\sigma}_{,\beta\gamma})\, T_{n\,\alpha\beta} \boldsymbol{\sigma}_{,\alpha}, \end{aligned}$$

since $\boldsymbol{\nabla} u_\gamma \cdot \boldsymbol{\sigma}_{,\beta} = \delta_{\beta\gamma}$. The normal component of the stress force is thus

$$(\boldsymbol{\nabla} \cdot \mathbf{T}_n) \cdot \hat{\mathbf{N}} = T_{n\,\alpha\beta} \boldsymbol{\sigma}_{,\alpha\beta} \cdot \hat{\mathbf{N}} = T_{n\,\alpha\beta} \mathcal{F}_{\mathrm{II}\,\alpha\beta},$$

where $\mathcal{F}_{\mathrm{II}\,\alpha\beta}$ is the second fundamental form of the surface patch $\boldsymbol{\sigma}$.

The equivalence of the two expressions for $(\boldsymbol{\nabla} \cdot \mathbf{T}_n) \cdot \hat{\mathbf{N}}$ is most easily shown by manipulation of equation 5.13. Weingarten's theorem, a standard theorem of differential geometry (see Pressley [11] or others) relates $\mathcal{F}_{\mathrm{II}\,\alpha\beta}$ to the derivative of the unit normal:

$$\hat{\mathbf{N}}_{,\alpha} = -\mathcal{F}_{\mathrm{II}\,\alpha\theta} {\mathcal{F}_{\mathrm{I}}}^{-1}{}_{\theta\beta}\, \boldsymbol{\sigma}_{,\beta} \quad \Rightarrow \quad \mathbf{C} = \boldsymbol{\nabla} \hat{\mathbf{N}} = -\mathcal{F}_{\mathrm{II}\,\alpha\theta} {\mathcal{F}_{\mathrm{I}}}^{-1}{}_{\theta\beta}\, \boldsymbol{\nabla} u_\alpha \otimes \boldsymbol{\sigma}_{,\beta}$$

(Note that in his excellent book Pressley [11] mysteriously chooses to multiply column vectors by matrices on the right in his statement of Weingarten's theorem—the above statement has reordered the matrices so as to adopt the more usual convention on matrix multiplication.) Substitution of this equation and the component form of $\mathbf{T}_n$ into equation 5.13 demonstrates the equivalence of

[4] The minus sign here arises because inward pointing forces have been considered, whilst $\hat{\mathbf{N}}$ points outwards.

the two expressions:

$$\begin{aligned}\mathrm{Tr}(\mathbf{C}\cdot\mathbf{T}_\mathrm{n}) &= -\mathcal{F}_{\mathrm{II}\,\alpha\theta}{\mathcal{F}_\mathrm{I}}^{-1}{}_{\theta\beta}\mathsf{T}_{\mathrm{n}\,\gamma\delta}(\boldsymbol{\nabla}\mathfrak{u}_\alpha\cdot\boldsymbol{\sigma}_\gamma)(\boldsymbol{\sigma}_{,\beta}\cdot\boldsymbol{\sigma}_\delta)\\ &= -\mathcal{F}_{\mathrm{II}\,\alpha\theta}{\mathcal{F}_\mathrm{I}}^{-1}{}_{\theta\beta}\mathsf{T}_{\mathrm{n}\,\gamma\delta}\delta_{\alpha\gamma}\mathcal{F}_{\mathrm{I}\,\beta\delta}\\ &= -\mathcal{F}_{\mathrm{II}\,\alpha\theta}\delta_{\delta\theta}\mathsf{T}_{\mathrm{n}\,\alpha\delta}\\ &= -\mathcal{F}_{\mathrm{II}\,\alpha\delta}\mathsf{T}_{\mathrm{n}\,\alpha\delta}.\end{aligned}$$

The two expressions are thus equal, with $\mathsf{C}_{\alpha\beta} = -{\mathcal{F}_\mathrm{I}}^{-1}{}_{\alpha\gamma}\mathcal{F}_{\mathrm{II}\gamma\delta}{\mathcal{F}_\mathrm{I}}^{-1}{}_{\delta\beta}$.

5.3.4 Amontons' law

As a key motivation for the definition of an instantaneous isotropic interface, it would be helpful to consider Amontons' law as a concrete example. By differentiating both sides of the classic expression $\mathsf{F} = \mu_* \mathsf{N}$ with respect to contact volume, and requiring that there is only any force on the surface $\mathcal{S}$,

$$\psi_* = \mu_* |\mathbf{f}_\dagger \cdot \hat{\mathbf{N}}|,$$

where $\mathbf{f}_\dagger$ is the force per unit volume on the appropriate surface, and the asterisk denotes either d or s. Thus

$$\begin{aligned}\boldsymbol{\nabla}\cdot\mathbf{T}_\mathrm{s} + \mathbf{P}_{\hat{\mathbf{N}}}\cdot\left\{\frac{\rho_\mathrm{s}\boldsymbol{\nabla}\cdot\mathbf{T}_\mathrm{n} - \rho_\mathrm{n}\boldsymbol{\nabla}\cdot\mathbf{T}_\mathrm{s}}{\rho_\mathrm{s}+\rho_\mathrm{n}}\right\} - \mu_\mathrm{d}\left|\hat{\mathbf{N}}\cdot\left\{\frac{\rho_\mathrm{s}\boldsymbol{\nabla}\cdot\mathbf{T}_\mathrm{n} - \rho_\mathrm{n}\boldsymbol{\nabla}\cdot\mathbf{T}_\mathrm{s}}{\rho_\mathrm{s}+\rho_\mathrm{n}}\right\}\right|\hat{\boldsymbol{\nu}} &= \rho_\mathrm{s}\ddot{\boldsymbol{\lambda}}\\ \boldsymbol{\nabla}\cdot\mathbf{T}_\mathrm{n} - \mathbf{P}_{\hat{\mathbf{N}}}\cdot\left\{\frac{\rho_\mathrm{s}\boldsymbol{\nabla}\cdot\mathbf{T}_\mathrm{n} - \rho_\mathrm{n}\boldsymbol{\nabla}\cdot\mathbf{T}_\mathrm{s}}{\rho_\mathrm{s}+\rho_\mathrm{n}}\right\} + \mu_\mathrm{d}\left|\hat{\mathbf{N}}\cdot\left\{\frac{\rho_\mathrm{s}\boldsymbol{\nabla}\cdot\mathbf{T}_\mathrm{n} - \rho_\mathrm{n}\boldsymbol{\nabla}\cdot\mathbf{T}_\mathrm{s}}{\rho_\mathrm{s}+\rho_\mathrm{n}}\right\}\right|\hat{\boldsymbol{\nu}} &= \rho_\mathrm{n}\ddot{\boldsymbol{\sigma}},\end{aligned}$$

where $\hat{\boldsymbol{\nu}} = (\mathbf{P}_\mathcal{S}\cdot(\dot{\boldsymbol{\lambda}} - \dot{\boldsymbol{\sigma}}))/\|\mathbf{P}_\mathcal{S}\cdot(\dot{\boldsymbol{\lambda}} - \dot{\boldsymbol{\sigma}})\|$ and the first equation applies only for $\mathbf{x} \in \mathcal{P}$. Clearly it would be simple to substitute for $(\boldsymbol{\nabla}\cdot\mathbf{T}_\mathrm{n})\cdot\hat{\mathbf{N}}$, but this would simply generate an unreadable expression without adding any clarity.

In the commonly applicable $\rho_\mathrm{n} \approx 0$ limit there is again a dramatic simplification.

$$\begin{aligned}\boldsymbol{\nabla}\cdot\mathbf{T}_\mathrm{s} + \mathbf{P}_{\hat{\mathbf{N}}}\cdot\{\boldsymbol{\nabla}\cdot\mathbf{T}_\mathrm{n}\} - \mu_\mathrm{d}\left|\hat{\mathbf{N}}\cdot\{\boldsymbol{\nabla}\cdot\mathbf{T}_\mathrm{n}\}\right|\hat{\boldsymbol{\nu}} &= \rho_\mathrm{s}\ddot{\boldsymbol{\lambda}}\\ \boldsymbol{\nabla}\cdot\mathbf{T}_\mathrm{n} - \mathbf{P}_{\hat{\mathbf{N}}}\cdot\{\boldsymbol{\nabla}\cdot\mathbf{T}_\mathrm{n}\} + \mu_\mathrm{d}\left|\hat{\mathbf{N}}\cdot\{\boldsymbol{\nabla}\cdot\mathbf{T}_\mathrm{n}\}\right|\hat{\boldsymbol{\nu}} &= 0\end{aligned}$$

The proposed substitution is now quite enlightening:

$$\begin{aligned}\boldsymbol{\nabla}\cdot\mathbf{T}_\mathrm{s} - \hat{\mathbf{N}}\mathrm{Tr}(\mathbf{T}_\mathrm{n}\cdot\mathbf{C}) - \mu_\mathrm{d}|\mathrm{Tr}(\mathbf{T}_\mathrm{n}\cdot\mathbf{C})|\frac{\mathbf{P}_\mathcal{S}\cdot(\dot{\boldsymbol{\lambda}}-\dot{\boldsymbol{\sigma}})}{\|\mathbf{P}_\mathcal{S}\cdot(\dot{\boldsymbol{\lambda}}-\dot{\boldsymbol{\sigma}})\|} &= \rho_\mathrm{s}\ddot{\boldsymbol{\lambda}}\\ \mathbf{P}_\mathcal{S}\cdot(\boldsymbol{\nabla}\cdot\mathbf{T}_\mathrm{n}) + \mu_\mathrm{d}|\mathrm{Tr}(\mathbf{T}_\mathrm{n}\cdot\mathbf{C})|\frac{\mathbf{P}_\mathcal{S}\cdot(\dot{\boldsymbol{\lambda}}-\dot{\boldsymbol{\sigma}})}{\|\mathbf{P}_\mathcal{S}\cdot(\dot{\boldsymbol{\lambda}}-\dot{\boldsymbol{\sigma}})\|} &= 0.\end{aligned} \tag{5.14}$$

This example illustrates first the manner in which friction laws can be used in this framework, and second the significant simplification that can be wrought by the assumption of negligible nonwoven inertia.

5.4 Material and spatial descriptions of the equations of motion

The material and spatial descriptions of fields in continuum mechanics have been defined in §2.1.1 and specialised to the geometric friction model in §5.2. Equations 5.10 and 5.11 use a mixture of the two: the gradients use the spatial description, but the velocities and acceleration are couched in the material description. Whilst providing a compact form in which to state the result, equations 5.10 and 5.11 are not in a form from which a general solution could be obtained. The equations must be transformed so that they are expressed entirely in one description or the other.

5.4.1 Material description

Two changes must be made to equations 5.10 and 5.11 in order that they are expressed in the material description: the gradients must be re-expressed over the reference space; and subsidiarily, the point-equilibrium version of the equations—that is, where fields at a fixed point in space are static—must be transformed into the material description. In this description the fundamental fields are the deformation functions $\boldsymbol{\lambda}(\mathbf{L})$ and $\boldsymbol{\sigma}(\mathbf{S})$.

The gradient operator transforms as a tensor [163] so for an example function $f(\mathbf{L})$,

$$\boldsymbol{\nabla} f(\mathbf{L}) = \boldsymbol{\nabla}\mathbf{L} \cdot \boldsymbol{\nabla}_{\mathbf{L}} f(\mathbf{L}) \qquad \Rightarrow \qquad \boldsymbol{\nabla} f(\mathbf{L}) = [\boldsymbol{\nabla}_{\mathbf{L}}\boldsymbol{\lambda}]^{-1} \cdot \boldsymbol{\nabla}_{\mathbf{L}} f(\mathbf{L}), \tag{5.15}$$

since $\boldsymbol{\nabla}\mathbf{L} = [\boldsymbol{\nabla}_{\mathbf{L}}\boldsymbol{\lambda}]^{-1}$ by the product rule. The general dynamic equations of motion for an instantaneous isotropic interface in the material description can thus be written as in equations 5.16 and 5.17. However, as suggested above, an intuitive definition of stable sliding does not naturally fit into these equations as they stand. Stable sliding "seems like it ought to mean" a situation in which an acute observer of a small neighbourhood in physical space would see no changes occurring. This definition is itself a mixture of the material and spatial descriptions; using the notation defined in §2.1.1, it requires that

$$\partial_t \dot{\chi}_\dagger = 0,$$

for some relevant deformation function $\chi_\dagger$; that is, the spatial description time derivative of the material description velocity (the particle "flow velocity", to borrow from fluid mechanics) vanishes. Since this quantity does not appear in the equations as they stand, it must be introduced.

In §2.1.1 equation 2.1 relates material and spatial description time derivatives. Applied to the deformation functions $\dot{\boldsymbol{\lambda}}(\mathbf{L})$ and $\dot{\boldsymbol{\sigma}}(\mathbf{S})$, it gives

$$\ddot{\boldsymbol{\lambda}} = \partial_t \dot{\boldsymbol{\lambda}} + \dot{\boldsymbol{\lambda}} \cdot \boldsymbol{\nabla}\dot{\boldsymbol{\lambda}} \quad , \quad \ddot{\boldsymbol{\sigma}} = \partial_t \dot{\boldsymbol{\sigma}} + \dot{\boldsymbol{\sigma}} \cdot \boldsymbol{\nabla}\dot{\boldsymbol{\sigma}},$$

and by transforming the spatial gradient operators

$$\ddot{\boldsymbol{\lambda}} = \partial_t \dot{\boldsymbol{\lambda}} + \dot{\boldsymbol{\lambda}} \cdot ([\boldsymbol{\nabla}_{\mathbf{L}}\boldsymbol{\lambda}]^{-1} \cdot \boldsymbol{\nabla}_{\mathbf{L}})\dot{\boldsymbol{\lambda}} \quad , \quad \ddot{\boldsymbol{\sigma}} = \partial_t \dot{\boldsymbol{\sigma}} + \dot{\boldsymbol{\sigma}} \cdot ([\boldsymbol{\nabla}_{\mathbf{S}}\boldsymbol{\sigma}]^{-1} \cdot \boldsymbol{\nabla}_{\mathbf{S}})\dot{\boldsymbol{\sigma}}.$$

By setting $\partial_t \dot{\boldsymbol{\lambda}} = \partial_t \dot{\boldsymbol{\sigma}} = 0$, the material description equations for point equilibrium of two bodies $\mathcal{L}$ and $\mathcal{S}$ interacting via an instantaneous isotropic interface are obtained; they are equations 5.18 and

$$\begin{cases} ([\boldsymbol{\nabla}_{\mathbf{L}}\boldsymbol{\lambda}]^{-1}\cdot\boldsymbol{\nabla}_{\mathbf{L}})\cdot\mathbf{T}_{\mathrm{s}}+\mathbf{P}_{\hat{\mathbf{N}}}\cdot\left\{\dfrac{\rho_{\mathrm{s}}([\boldsymbol{\nabla}_{\mathbf{S}}\boldsymbol{\sigma}]^{-1}\cdot\boldsymbol{\nabla}_{\mathbf{S}})\cdot\mathbf{T}_{\mathrm{n}}-\rho_{\mathrm{n}}([\boldsymbol{\nabla}_{\mathbf{L}}\boldsymbol{\lambda}]^{-1}\cdot\boldsymbol{\nabla}_{\mathbf{L}})\cdot\mathbf{T}_{\mathrm{s}}}{\rho_{\mathrm{s}}+\rho_{\mathrm{n}}}\right\}-\psi_{\mathrm{d}}\left\{\dfrac{\mathbf{P}_{\mathcal{S}}\cdot(\dot{\boldsymbol{\lambda}}-\dot{\boldsymbol{\sigma}})}{\|\mathbf{P}_{\mathcal{S}}\cdot(\dot{\boldsymbol{\lambda}}-\dot{\boldsymbol{\sigma}})\|}\right\}=\rho_{\mathrm{s}}\ddot{\boldsymbol{\lambda}} & \boldsymbol{\lambda}(\mathbf{L}),\boldsymbol{\sigma}(\mathbf{S})\in\bigcup_{\mathrm{i}}\mathcal{R}_{\mathrm{i}} \\ ([\boldsymbol{\nabla}_{\mathbf{L}}\boldsymbol{\lambda}]^{-1}\cdot\boldsymbol{\nabla}_{\mathbf{L}})\cdot\mathbf{T}_{\mathrm{s}}=\rho_{\mathrm{s}}\ddot{\boldsymbol{\lambda}} & \boldsymbol{\lambda}(\mathbf{L})\notin\bigcup_{\mathrm{i}}\mathcal{R}_{\mathrm{i}} \end{cases} \tag{5.16}$$

$$\begin{cases} ([\boldsymbol{\nabla}_{\mathbf{S}}\boldsymbol{\sigma}]^{-1}\cdot\boldsymbol{\nabla}_{\mathbf{S}})\cdot\mathbf{T}_{\mathrm{n}}-\mathbf{P}_{\hat{\mathbf{N}}}\cdot\left\{\dfrac{\rho_{\mathrm{s}}([\boldsymbol{\nabla}_{\mathbf{S}}\boldsymbol{\sigma}]^{-1}\cdot\boldsymbol{\nabla}_{\mathbf{S}})\cdot\mathbf{T}_{\mathrm{n}}-\rho_{\mathrm{n}}([\boldsymbol{\nabla}_{\mathbf{L}}\boldsymbol{\lambda}]^{-1}\cdot\boldsymbol{\nabla}_{\mathbf{L}})\cdot\mathbf{T}_{\mathrm{s}}}{\rho_{\mathrm{s}}+\rho_{\mathrm{n}}}\right\}-\psi_{\mathrm{d}}\left\{\dfrac{\mathbf{P}_{\mathcal{S}}\cdot(\dot{\boldsymbol{\sigma}}-\dot{\boldsymbol{\lambda}})}{\|\mathbf{P}_{\mathcal{S}}\cdot(\dot{\boldsymbol{\sigma}}-\dot{\boldsymbol{\lambda}})\|}\right\}=\rho_{\mathrm{n}}\ddot{\boldsymbol{\sigma}} & \boldsymbol{\lambda}(\mathbf{L}),\boldsymbol{\sigma}(\mathbf{S})\in\bigcup_{\mathrm{i}}\mathcal{R}_{\mathrm{i}} \\ ([\boldsymbol{\nabla}_{\mathbf{S}}\boldsymbol{\sigma}]^{-1}\cdot\boldsymbol{\nabla}_{\mathbf{S}})\cdot\mathbf{T}_{\mathrm{n}}=\rho_{\mathrm{n}}\ddot{\boldsymbol{\sigma}} & \boldsymbol{\sigma}(\mathbf{S})\notin\bigcup_{\mathrm{i}}\mathcal{R}_{\mathrm{i}} \end{cases} \tag{5.17}$$

$$\begin{cases} ([\boldsymbol{\nabla}_{\mathbf{L}}\boldsymbol{\lambda}]^{-1}\cdot\boldsymbol{\nabla}_{\mathbf{L}})\cdot\mathbf{T}_{\mathrm{s}}+\mathbf{P}_{\hat{\mathbf{N}}}\cdot\left\{\dfrac{\rho_{\mathrm{s}}([\boldsymbol{\nabla}_{\mathbf{S}}\boldsymbol{\sigma}]^{-1}\cdot\boldsymbol{\nabla}_{\mathbf{S}})\cdot\mathbf{T}_{\mathrm{n}}-\rho_{\mathrm{n}}([\boldsymbol{\nabla}_{\mathbf{L}}\boldsymbol{\lambda}]^{-1}\cdot\boldsymbol{\nabla}_{\mathbf{L}})\cdot\mathbf{T}_{\mathrm{s}}}{\rho_{\mathrm{s}}+\rho_{\mathrm{n}}}\right\} & \\ \qquad -\psi_{\mathrm{d}}\left\{\dfrac{\mathbf{P}_{\mathcal{S}}\cdot(\dot{\boldsymbol{\lambda}}-\dot{\boldsymbol{\sigma}})}{\|\mathbf{P}_{\mathcal{S}}\cdot(\dot{\boldsymbol{\lambda}}-\dot{\boldsymbol{\sigma}})\|}\right\}=\rho_{\mathrm{s}}\dot{\boldsymbol{\lambda}}\cdot([\boldsymbol{\nabla}_{\mathbf{L}}\boldsymbol{\lambda}]^{-1}\cdot\boldsymbol{\nabla}_{\mathbf{L}})\dot{\boldsymbol{\lambda}} & \boldsymbol{\lambda}(\mathbf{L}),\boldsymbol{\sigma}(\mathbf{S})\in\bigcup_{\mathrm{i}}\mathcal{R}_{\mathrm{i}} \\ ([\boldsymbol{\nabla}_{\mathbf{L}}\boldsymbol{\lambda}]^{-1}\cdot\boldsymbol{\nabla}_{\mathbf{L}})\cdot\mathbf{T}_{\mathrm{s}}=\rho_{\mathrm{s}}\dot{\boldsymbol{\lambda}}\cdot([\boldsymbol{\nabla}_{\mathbf{L}}\boldsymbol{\lambda}]^{-1}\cdot\boldsymbol{\nabla}_{\mathbf{L}})\dot{\boldsymbol{\lambda}} & \boldsymbol{\lambda}(\mathbf{L})\notin\bigcup_{\mathrm{i}}\mathcal{R}_{\mathrm{i}} \end{cases} \tag{5.18}$$

$$\begin{cases} ([\boldsymbol{\nabla}_{\mathbf{S}}\boldsymbol{\sigma}]^{-1}\cdot\boldsymbol{\nabla}_{\mathbf{S}})\cdot\mathbf{T}_{\mathrm{n}}-\mathbf{P}_{\hat{\mathbf{N}}}\cdot\left\{\dfrac{\rho_{\mathrm{s}}([\boldsymbol{\nabla}_{\mathbf{S}}\boldsymbol{\sigma}]^{-1}\cdot\boldsymbol{\nabla}_{\mathbf{S}})\cdot\mathbf{T}_{\mathrm{n}}-\rho_{\mathrm{n}}([\boldsymbol{\nabla}_{\mathbf{L}}\boldsymbol{\lambda}]^{-1}\cdot\boldsymbol{\nabla}_{\mathbf{L}})\cdot\mathbf{T}_{\mathrm{s}}}{\rho_{\mathrm{s}}+\rho_{\mathrm{n}}}\right\} & \\ \qquad -\psi_{\mathrm{d}}\left\{\dfrac{\mathbf{P}_{\mathcal{S}}\cdot(\dot{\boldsymbol{\sigma}}-\dot{\boldsymbol{\lambda}})}{\|\mathbf{P}_{\mathcal{S}}\cdot(\dot{\boldsymbol{\sigma}}-\dot{\boldsymbol{\lambda}})\|}\right\}=\rho_{\mathrm{n}}\dot{\boldsymbol{\sigma}}\cdot([\boldsymbol{\nabla}_{\mathbf{S}}\boldsymbol{\sigma}]^{-1}\cdot\boldsymbol{\nabla}_{\mathbf{S}})\dot{\boldsymbol{\sigma}} & \boldsymbol{\lambda}(\mathbf{L}),\boldsymbol{\sigma}(\mathbf{S})\in\bigcup_{\mathrm{i}}\mathcal{R}_{\mathrm{i}} \\ ([\boldsymbol{\nabla}_{\mathbf{S}}\boldsymbol{\sigma}]^{-1}\cdot\boldsymbol{\nabla}_{\mathbf{S}})\cdot\mathbf{T}_{\mathrm{n}}=\rho_{\mathrm{n}}\dot{\boldsymbol{\sigma}}\cdot([\boldsymbol{\nabla}_{\mathbf{S}}\boldsymbol{\sigma}]^{-1}\cdot\boldsymbol{\nabla}_{\mathbf{S}})\dot{\boldsymbol{\sigma}} & \boldsymbol{\sigma}(\mathbf{S})\notin\bigcup_{\mathrm{i}}\mathcal{R}_{\mathrm{i}} \end{cases} \tag{5.19}$$

5.19. These formulae are given for completeness; no further deductions can be gleaned from them at this stage.

5.4.2 Spatial description

The transformation of equations 5.10 and 5.11 into the spatial description requires more substantial changes. Essentially, this is because it has been implicitly assumed to this point that the fundamental fields are $\lambda(\mathbf{L})$ and $\sigma(\mathbf{S})$: stresses have been assumed to depend upon these functions, and they appear several times in the equations of motion. However, if the fields are to be defined over physical space then this must change. Additionally, the particle velocities $\dot{\lambda}$ and $\dot{\sigma}$ must be written as functions of position.

To proceed, it must be recognised that an arbitrary deformation function $\chi(\mathbf{X}, t)$ is a mapping into physical space, $\mathbf{x} = \chi(\mathbf{X}, t)$, and as it is an invertible mapping, it is equally valid to invert this equation and use $\mathbf{X}(\mathbf{x}, t)$ as the fundamental field over physical space. It is a simple matter to write material description gradients of χ in terms of spatial description gradients of $\mathbf{X}$; as noted in §5.4.1, $\boldsymbol{\nabla}\mathbf{X} = [\boldsymbol{\nabla}_{\mathbf{X}}\chi]^{-1}$, and higher derivatives can be simply obtained by applying the operator identity given in equation 5.15.

The particle velocity for the arbitrary deformation function must also be determined in terms of $\mathbf{X}$. This is most easily accomplished by considering that $\dot{\mathbf{X}} = \mathbf{0}$ by definition, and transforming the material description time derivative to the spatial description:

$$\mathbf{0} = \dot{\mathbf{X}} = \partial_t \mathbf{X} + \dot{\chi} \cdot \boldsymbol{\nabla}\mathbf{X},$$

whence it follows that

$$\dot{\chi} = -\partial_t \mathbf{X} \cdot (\boldsymbol{\nabla}\mathbf{X})^{-1}. \tag{5.20}$$

This result, and equation 2.1 enable equations 5.10 and 5.11 to be written in the spatial description as equations 5.21 and 5.22; $\dot{\lambda}[\mathbf{L}]$ and $\dot{\sigma}[\mathbf{S}]$ are as given by equation 5.20. For the spatial description the point equilibrium variants of these equations are easy to obtain.

It is interesting to consider the case of point equilibrium of a sheet which is uniform in its reference configuration. This is equivalent to proposing that density and ψ_d at a point are functionals of $\boldsymbol{\nabla}\mathbf{L}$ and $\boldsymbol{\nabla}\mathbf{S}$ *only*, and not of $\mathbf{L}$ or $\mathbf{S}$ themselves. Noting that stress depends only upon the deformation gradient and higher derivatives—that is, $\mathbf{T}_s[\boldsymbol{\nabla}\mathbf{L}]$, $\mathbf{T}_n[\boldsymbol{\nabla}\mathbf{S}]$—all terms in all of the spatial description equations depend only on $\boldsymbol{\nabla}\mathbf{L}$, $\boldsymbol{\nabla}\mathbf{S}$, $\dot{\lambda}[\mathbf{L}]$, and $\dot{\sigma}[\mathbf{S}]$. Represent this as

$$\mathbf{g}[\boldsymbol{\nabla}\mathbf{L}, \boldsymbol{\nabla}\mathbf{S}, \dot{\lambda}, \dot{\sigma}] = \mathbf{0}. \tag{5.23}$$

By the assumption of point equilibrium it follows that $\partial_t \dot{\lambda} = \partial_t \dot{\sigma} = \mathbf{0}$, so the derivative of equation 5.23 with respect to the spatial description time can be written as

$$\mathrm{Tr}\left(\partial_t \boldsymbol{\nabla}\mathbf{L} \cdot \frac{\delta \mathbf{g}}{\delta \boldsymbol{\nabla}\mathbf{L}}\right) + \mathrm{Tr}\left(\partial_t \boldsymbol{\nabla}\mathbf{S} \cdot \frac{\delta \mathbf{g}}{\delta \boldsymbol{\nabla}\mathbf{S}}\right) = \mathbf{0}. \tag{5.24}$$

It is certainly the case that the variations of stress with respect to deformation gradient are non-

$$\begin{cases} \boldsymbol{\nabla}\cdot\mathbf{T}_{s}+\mathbf{P}_{\hat{\mathbf{N}}}\cdot\left\{\dfrac{\rho_{s}\boldsymbol{\nabla}\cdot\mathbf{T}_{n}-\rho_{n}\boldsymbol{\nabla}\cdot\mathbf{T}_{s}}{\rho_{s}+\rho_{n}}\right\}-\psi_{d}\left\{\dfrac{\mathbf{P}_{\mathcal{S}}\cdot(\dot{\boldsymbol{\lambda}}[\mathbf{L}]-\dot{\boldsymbol{\sigma}}[\mathbf{S}])}{\|\mathbf{P}_{\mathcal{S}}\cdot(\dot{\boldsymbol{\lambda}}[\mathbf{L}]-\dot{\boldsymbol{\sigma}}[\mathbf{S}])\|}\right\}=\rho_{s}\left(\partial_{t}\dot{\boldsymbol{\lambda}}[\mathbf{L}]+\dot{\boldsymbol{\lambda}}[\mathbf{L}]\cdot\boldsymbol{\nabla}\dot{\boldsymbol{\lambda}}[\mathbf{L}]\right) & \mathbf{l}=\mathbf{s}\in\bigcup_{i}\mathcal{R}_{i} \\ \boldsymbol{\nabla}\cdot\mathbf{T}_{s}=\rho_{s}\left(\partial_{t}\dot{\boldsymbol{\lambda}}[\mathbf{L}]+\dot{\boldsymbol{\lambda}}[\mathbf{L}]\cdot\boldsymbol{\nabla}\dot{\boldsymbol{\lambda}}[\mathbf{L}]\right) & \mathbf{l}\notin\bigcup_{i}\mathcal{R}_{i} \end{cases} \tag{5.21}$$

$$\begin{cases} \boldsymbol{\nabla}\cdot\mathbf{T}_{n}-\mathbf{P}_{\hat{\mathbf{N}}}\cdot\left\{\dfrac{\rho_{s}\boldsymbol{\nabla}\cdot\mathbf{T}_{n}-\rho_{n}\boldsymbol{\nabla}\cdot\mathbf{T}_{s}}{\rho_{s}+\rho_{n}}\right\}-\psi_{d}\left\{\dfrac{\mathbf{P}_{\mathcal{S}}\cdot(\dot{\boldsymbol{\sigma}}[\mathbf{S}]-\dot{\boldsymbol{\lambda}}[\mathbf{L}])}{\|\mathbf{P}_{\mathcal{S}}\cdot(\dot{\boldsymbol{\sigma}}[\mathbf{S}]-\dot{\boldsymbol{\lambda}}[\mathbf{L}])\|}\right\}=\rho_{n}\left(\partial_{t}\dot{\boldsymbol{\sigma}}[\mathbf{S}]+\dot{\boldsymbol{\sigma}}[\mathbf{S}]\cdot\boldsymbol{\nabla}\dot{\boldsymbol{\sigma}}[\mathbf{S}]\right) & \mathbf{l}=\mathbf{s}\in\bigcup_{i}\mathcal{R}_{i} \\ \boldsymbol{\nabla}\cdot\mathbf{T}_{n}=\rho_{n}\left(\partial_{t}\dot{\boldsymbol{\sigma}}[\mathbf{S}]+\dot{\boldsymbol{\sigma}}[\mathbf{S}]\cdot\boldsymbol{\nabla}\dot{\boldsymbol{\sigma}}[\mathbf{S}]\right) & \mathbf{s}\notin\bigcup_{i}\mathcal{R}_{i} \end{cases} \tag{5.22}$$

Spatial description	Material description
Surface geometry is also naturally defined over physical space.	The deformation function would be needed to interpret geometry in the reference configuration.
—	The form of the governing equation is simpler.
Boundary conditions are more naturally expressed in terms of the spatial description.	—
Point equilibrium for a uniform sheet results in an $\mathbf{X}$ that is time independent.	The deformation function relates to the motion of physical particles.

Table 5.1: A summary of the main advantages and disadvantages for the material and spatial descriptions of the equations of motion for geometric friction.

zero, and further that since the constitutive behaviour of the sheet and substrate are almost surely different there is no potential for them to cancel. It is also highly unlikely that the variations of density will be the same for both bodies, and there is no reason why friction should relate neatly to any of the aforementioned quantities. In view of these points, although it is mathematically *possible* for the manifold terms of equation 5.24 to cancel out whilst being individually non-zero, it is phenomenally unlikely. In consequence, for non-degenerate systems, it follows that $\partial_t \boldsymbol{\nabla} \mathbf{L} = \partial_t \boldsymbol{\nabla} \mathbf{S} = \mathbf{0}$, and since the time and spatial derivatives both belonging to the spatial description commute, $\boldsymbol{\nabla} \partial_t \mathbf{L} = \boldsymbol{\nabla} \partial_t \mathbf{S} = \mathbf{0}$. Representing mappings for both bodies by the generic χ and $\mathbf{X}$, it thus follows from the definition of point equilibrium that

$$\begin{aligned} \mathbf{0} = \partial_t \dot{\chi}[\mathbf{X}] &= \partial_t \left[-\partial_t \mathbf{X}(\mathbf{x}, t) \cdot [\boldsymbol{\nabla} \mathbf{X}]^{-1} \right] \\ &= -\partial_t{}^2 \mathbf{X}(\mathbf{x}, t) \cdot [\boldsymbol{\nabla} \mathbf{X}]^{-1} - \partial_t \mathbf{X}(\mathbf{x}, t) \cdot \partial_t \left[\boldsymbol{\nabla} \mathbf{X} \right]^{-1}. \end{aligned}$$

Observing that the latter term is zero by the argument advanced above, it follows that

$$\partial_t{}^2 \mathbf{X}(\mathbf{x}, t) \cdot [\boldsymbol{\nabla} \mathbf{X}]^{-1} = \mathbf{0} \quad \Rightarrow \quad \partial_t{}^2 \mathbf{X}(\mathbf{x}, t) = \mathbf{0},$$

where the latter step follows because $\boldsymbol{\nabla} \mathbf{X}(\mathbf{x})$ is always invertible. This result means that for a uniform sheet in point equilibrium without highly degenerate material characteristics, $\partial_t \mathbf{X}$ has a single value for all positions $\mathbf{x}$ and times t. All variation in particle velocity $\dot{\chi}$ is thus due to spatial variation in deformation as described by $\boldsymbol{\nabla} \mathbf{X}$.

5.4.3 Benefits of each description

The two descriptions advanced each have advantages and disadvantages, both practical and more abstract. These are summarised in table 5.1 and discussed here.

As demonstrated in §5.3.3, local normal force density depends on local geometry. For the simplest example of a rigid substrate this geometry is fixed in physical space; that is, it is easily described as

a time-invariant field over $\mathbf{x}$. It is thus most naturally allied to the spatial description; the material description would require that the geometry field was composed with the deformation function, $\mathbf{C} \circ \boldsymbol{\chi}(\mathbf{x}) := \mathbf{C}(\boldsymbol{\chi}(\mathbf{X}))$, which adds complexity. However, the forms of the material description equations are simpler, which in part offsets this.

An important consideration for obtaining a solution is that the boundary conditions of the problem often apply at fixed points in physical space. As for the case of geometry, this speaks in favour of the spatial description, though it is always possible at the cost of some complexity to compose the boundary conditions with the deformation function and so move to the material description.

A more potent argument in favour of the spatial description is that noted at the end of §5.4.2: the modulation of particle velocity across an instantaneous isotropic interface including a uniform sheet in point equilibrium is purely due to deformation. In consequence, the entire differential equation (and thus solution) is in terms of $\boldsymbol{\nabla}\mathbf{X}$, which is time-independent. This situation is of considerable interest, and is certainly best approached in the spatial description.

5.5 Solutions

The equations of geometric friction are too complicated to allow an analytical, general solution. Since this is the case, a number of approaches could be taken to produce useful solutions. Analytical solutions provide more information about what is and is not important than numerical solutions, so it is worth developing even approximate analytical solutions in any situations found to be amenable. Numerical solutions have their place in providing some insight into circumstances where no analytical solutions have even approximate validity, and are generally much more robust in allowing generalisations, but are not considered in this work due to limited time. Finally, it is important wherever possible to verify by experiment that solutions obtained by any method correspond to the true behaviour of the systems at hand.

Before attempting to generate any solutions, it is as well to consider the factors that can be varied.

Constitutive relations. Both the nonwoven sheet and the substrate have constitutive relations, and their natures will dramatically affect any solution. For example, in the limit of infinite substrate stiffness the substrate ceases to display transients, and normal acceleration is zero, leading to a simplification of the equations; in the case of zero substrate stiffness the nonwoven sheet flattens any curvature out and no friction occurs.

Force loading. The forces present at the periphery of the nonwoven sheet will affect the solutions. The simplest scenario involves uniform loading on either end of the sheet a long way from the contact region, but the converse situation of static loading varying around the entire periphery could also be considered.

Undeformed substrate geometry. Clearly, the initial geometry is very important: a flat surface experiences no friction, whilst a cusp generates enormous frictional stresses.

Initial conditions. It is not *a priori* obvious that a complicated constitutive relationship over a complicated surface will reach the same equilibrium irrespective of the initial strain fields. More mundanely, the path and time to equilibrium will certainly depend on the initial conditions.

In order to develop analytical solutions many simplifications will be required. It is however important to re-emphasise that the strength of an analytical solution in a problem of this type does not primarily subsist in perfect accuracy, but rather in the possibility of interrogating the solution to establish trends, and identify what is and is not important.

The additional assumptions made for all analytical solutions are given here, along with a brief discussion of their scope of validity.

Static substrate steady state. The substrate is assumed to be in a steady state, and not to be moving. This could be achieved by the substrate being rigid, or it could simply be that any transients have passed. The assumption of statics covers many interesting situations. Only the flow of the nonwoven sheet need therefore be calculated.

Non-inertial nonwoven. The nonwoven is assumed to have a very low density so that its inertia can be neglected, as discussed in §5.3.2. As nonwovens typically have an area density in the range $15\,\mathrm{g}\cdot\mathrm{m}^{-2}$–$25\,\mathrm{g}\cdot\mathrm{m}^{-2}$ [168] this is reasonable.

Distant, end-only forces. The assumption that the only forces acting on the nonwoven sheet act at the "ends" and at a distance (figure 5.8) arises primarily from the experimental origin of this work. As reviewed in §2.4.2, a method used by various authors to measure friction between skin and nonwoven involved dragging a strip of nonwoven around an arm or a finger. One of the primary uses of this model is thus to interpret such experiments more accurately over a wider range of surface geometries.

Uniformly convex substrate. If the surface is not uniformly convex then, as noted in §5.2.2, the contact and non-contact regions must be treated differently, and before that, be calculated. This degree of complexity would render any analytical model uninformative, even if such a solution could be obtained. In practice, many interesting surfaces *are* convex.

Amontons' law. As noted in chapter 4 no friction data on skin are available, but for an established friction surrogate Amontons' law is obeyed to very high precision. It thus seems probable that it will remain at least a fair approximation for skin itself. So long as it is at least a *fair* description, in this context the simplicity of Amontons' law makes up for relatively minor inaccuracies: a reasonable solution is preferable to no solution.

The simplification effected by "turning off" Poisson contraction (setting Poisson's ratio $\nu = 0$) is discussed (§5.5.1), then solutions are developed for sliding at any angle on prismical substrates (§5.5.2) and conical substrates (§5.5.3), surfaces chosen both for their simplicity and their applicability to limbs and portions of the torso.

Note that since all work in this section assumes a steady, static substrate the subscript n will be dropped from quantities associated with the nonwoven sheet for the sake of brevity and typographic clarity.

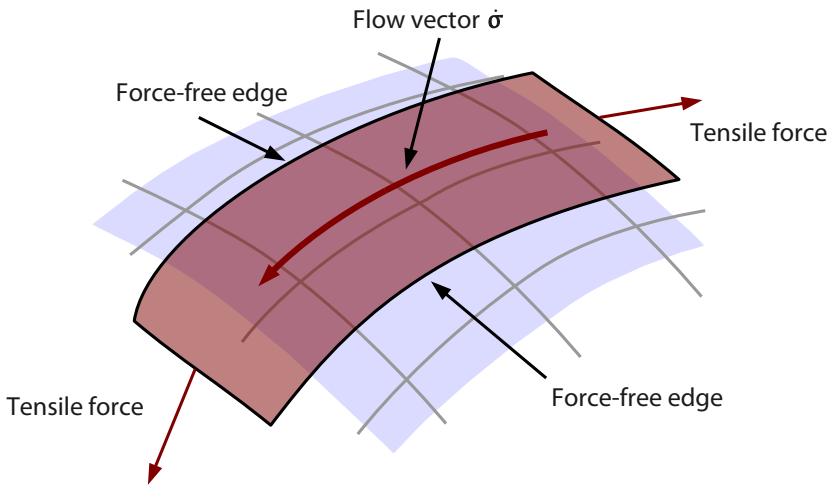

Figure 5.8: A simple situation in which a strip of conformable nonwoven is draped over the surface $\mathcal{S}$ and subjected only to tensile forces at a distance.

5.5.1 Geodesic flow around surfaces isomorphic to the plane

Most materials exhibit Poisson contraction: a positive tensile strain produces a lateral contraction [13]. This has the effect of linking the components of strain together, and thus rendering material behaviour much more complicated and interesting. However, this effect is not included in either the classic cylinder model [105] or the newer model of Cottenden *et al.* [107] (both assume tangential flow), and yet they give excellent agreement with experiment. Further, although no measurement of the Poisson ratio of any appropriate nonwoven is known, experimental experience shows that it is not large. This suggests that to a first approximation materials may be modelled without Poisson contraction.

Additionally, attention will be limited to surfaces which are isomorphic to the plane; that is, those which have the same first fundamental form as the plane (using the same co-ordinates); this is the identity matrix for plane Cartesian co-ordinates.

In the absence of Poisson contraction, situations similar to the experimental methods of Gwosdow *et al.* [100] and Cottenden *et al.* [1] (figure 5.8) simplify considerably. There are no forces along the "sides" of the samples, and in the absence of Poisson contraction longitudinal forces cannot generate them. There cannot therefore be any lateral forces; $\mathbf{T} \cdot \dot{\boldsymbol{\sigma}}_{\perp} = 0$: all forces are tensile.

An important feature of unidirectional stretches is that geodesics parallel to the principal stretch axis are mapped onto themselves. Further, if the surface $\mathcal{S}$ is isomorphic to the plane then geodesics on $\mathcal{S}$ are also geodesics of the plane. This implies that geodesics of the deformed sheet are identical to those of the plane, which are straight lines and thus readily parametrised.

Under these assumptions, $\hat{\dot{\boldsymbol{\sigma}}}$ is known, and as the substrate is static this fixes the direction of friction as well. Further, since the flow lines follow straight lines in the plane, a surface patch can be

chosen so that $\boldsymbol{\sigma}_{,y}$ is parallel to $\hat{\dot{\boldsymbol{\sigma}}}$ and $\boldsymbol{\sigma}_{,x}$ is parallel to $\hat{\dot{\boldsymbol{\sigma}}}_{\perp}$, so the lateral force condition implies

$$\mathbf{T}\cdot\dot{\boldsymbol{\sigma}}_{\perp}=0 \quad\Rightarrow\quad \mathbf{T}\cdot\boldsymbol{\sigma}_{,x}=T_{\alpha\beta}\boldsymbol{\sigma}_{,\alpha}\otimes\boldsymbol{\sigma}_{,\beta}\cdot\boldsymbol{\sigma}_{,x}=0 \quad\Rightarrow\quad T_{\alpha x}\boldsymbol{\sigma}_{,\alpha}=0,$$

and hence that

$$T_{\alpha x}=0 \quad \forall\alpha$$

since $\mathcal{F}_I = I$. By the symmetry of $T_{\alpha\beta}$ under exchange of suffices (which follows immediately from its usual symmetry) this condition requires that its only non-zero component is T_{yy}. This great simplification reduces the governing equation 5.14 to

$$\begin{aligned}\mu_d|\mathrm{Tr}(\mathbf{T}\cdot\mathbf{C})|\hat{\dot{\boldsymbol{\sigma}}} &= \mathbf{P}_{\mathcal{S}}\cdot(\boldsymbol{\nabla}\cdot\mathbf{T}) = \mathbf{P}_{\mathcal{S}}\cdot[\,(\boldsymbol{\nabla}u_\gamma\partial_\gamma)\cdot(T_{\alpha\beta}\boldsymbol{\sigma}_{,\alpha}\otimes\boldsymbol{\sigma}_{,\beta})\,]\\ &= \mathbf{P}_{\mathcal{S}}\cdot[T_{\alpha\beta,\gamma}\boldsymbol{\nabla}u_\gamma\cdot\boldsymbol{\sigma}_{,\beta}\boldsymbol{\sigma}_{,\alpha}+T_{\alpha\beta}\boldsymbol{\nabla}u_\gamma\cdot\boldsymbol{\sigma}_{,\beta\gamma}\boldsymbol{\sigma}_{,\alpha}+T_{\alpha\beta}\boldsymbol{\sigma}_{,\beta}\cdot\boldsymbol{\nabla}u_\gamma\boldsymbol{\sigma}_{,\alpha\gamma}]\\ &= \mathbf{P}_{\mathcal{S}}\cdot[T_{\alpha\beta,\beta}\boldsymbol{\sigma}_{,\alpha}+T_{\alpha\beta}\boldsymbol{\nabla}u_\gamma\cdot\boldsymbol{\sigma}_{,\beta\gamma}\boldsymbol{\sigma}_{,\alpha}+T_{\alpha\beta}\boldsymbol{\sigma}_{,\alpha\beta}] \qquad (5.25)\end{aligned}$$

since $\boldsymbol{\nabla}u_\gamma\cdot\boldsymbol{\sigma}_{,\beta}=\delta_{\gamma\beta}$ for all patches. Further, when $\mathcal{F}_I = I$ it follows that $\boldsymbol{\nabla}u_\gamma=\boldsymbol{\sigma}_{,\gamma}$. Considering $\boldsymbol{\sigma}_{,\gamma}\cdot\boldsymbol{\sigma}_{,\beta\gamma}=(\frac{1}{2}\boldsymbol{\sigma}_{,\gamma}\cdot\boldsymbol{\sigma}_{,\gamma})_{,\alpha}=(\frac{1}{2}I)_{,\alpha}=0$, the second term of equation 5.25 vanishes, so.

$$\begin{aligned}\mu_d|\mathrm{Tr}(\mathbf{T}\cdot\mathbf{C})|\hat{\dot{\boldsymbol{\sigma}}} &= (\boldsymbol{\sigma}_{,\gamma}\otimes\boldsymbol{\sigma}_{,\gamma})\cdot[T_{\alpha\beta,\beta}\boldsymbol{\sigma}_{,\alpha}+T_{\alpha\beta}\boldsymbol{\sigma}_{,\alpha\beta}]\\ &= \boldsymbol{\sigma}_{,\gamma}[T_{\gamma\beta,\beta}+T_{\alpha\beta}\boldsymbol{\sigma}_{,\alpha\beta}\cdot\boldsymbol{\sigma}_{,\gamma}]. \qquad (5.26)\end{aligned}$$

Using

$$\begin{aligned}\boldsymbol{\sigma}_{,\alpha\beta}\cdot\boldsymbol{\sigma}_{,\gamma} &= (\boldsymbol{\sigma}_{,\alpha}\cdot\boldsymbol{\sigma}_{,\gamma})_{,\beta}-\boldsymbol{\sigma}_{,\alpha}\cdot\boldsymbol{\sigma}_{,\beta\gamma}=-\boldsymbol{\sigma}_{,\alpha}\cdot\boldsymbol{\sigma}_{,\beta\gamma},\\ \boldsymbol{\sigma}_{,\alpha}\cdot\boldsymbol{\sigma}_{,\beta\gamma} &= (\boldsymbol{\sigma}_{,\alpha}\cdot\boldsymbol{\sigma}_{,\beta})_{,\gamma}-\boldsymbol{\sigma}_{,\alpha\gamma}\cdot\boldsymbol{\sigma}_{,\beta}=-\boldsymbol{\sigma}_{,\alpha\gamma}\cdot\boldsymbol{\sigma}_{,\beta},\end{aligned}$$

and $T_{\alpha\beta}=T_{\beta\alpha}$, it follows that

$$T_{\alpha\beta}(\boldsymbol{\sigma}_{,\alpha\beta}\cdot\boldsymbol{\sigma}_{,\gamma})=-T_{\alpha\beta}(\boldsymbol{\sigma}_{,\alpha}\cdot\boldsymbol{\sigma}_{,\beta\gamma})=-\tfrac{1}{2}T_{\alpha\beta}(\boldsymbol{\sigma}_{,\alpha}\cdot\boldsymbol{\sigma}_{,\beta\gamma}+\boldsymbol{\sigma}_{,\beta}\cdot\boldsymbol{\sigma}_{,\alpha\gamma})=0.$$

It therefore follows from (5.26) that

$$\mu_d|\mathrm{Tr}(\mathbf{T}\cdot\mathbf{C})|\hat{\dot{\boldsymbol{\sigma}}}=\boldsymbol{\sigma}_{,\gamma}T_{\gamma\beta,\beta}.$$

This equation simplifies after recalling that the only non-zero component of stress is T_{yy}:

$$\mu_d|T_{yy}C_{yy}|\boldsymbol{\sigma}_{,y}=T_{yy,y}\boldsymbol{\sigma}_{,y}.$$

By assumption $T_{yy}\geq 0$, so the equation can be further simplified and solved in integral form:

$$T_{yy,y}-\mu_d|C_{yy}|T_{yy}=0 \quad\Rightarrow\quad T_{yy}=T_0\exp\left(\mu_d\int|C_{yy}|dy\right), \qquad (5.27)$$

where the integrating factor $\exp\left(-\mu_d\int|C_{yy}|dy\right)$ was used to write the equation as a perfect differen-

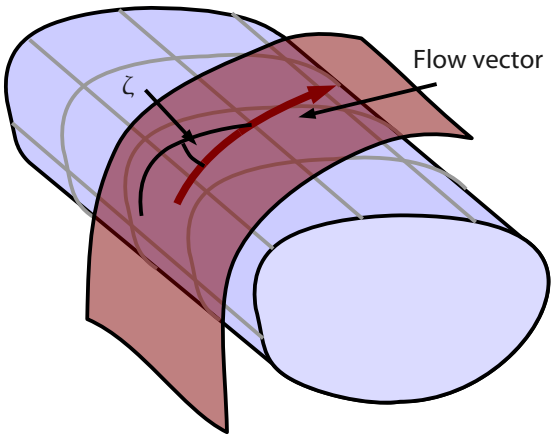

Figure 5.9: The angle ζ is defined as the angle between the flow vector and the projection of the prism's plane of cross section onto the surface.

tial. This form is valid for any surface isomorphic to the plane (with an appropriate choice of patch) for a fabric with $\nu = 0$. Solutions for specific examples of such surfaces can now be considered.

5.5.2 Prism solutions

New models must consist with older, established ones. It is therefore important to derive the solution for tangential flow around a prism, of which flow around a cylinder is clearly a special case. The assumptions made hitherto in this section are essentially those made for the "classic" solution [105] and by Cottenden *et al.* [107], so agreement should be obtained. It is simple with this model to generalise the previous models slightly and consider flow at an angle ζ to the prism's plane of cross section (figure 5.9), so this generalisation is made.

In essence, once a patch $\boldsymbol{\sigma}(x, y)$ has been defined all subsequent quantities up to and including T_{yy} itself follow by formal manipulation and substitution into equation 5.27. A few intermediate steps are noted for ease of reading. Define

$$\boldsymbol{\sigma}(x, y) = (R(\phi)\cos(\phi), R(\phi)\sin(\phi), x\cos(\zeta) + y\sin(\zeta))$$
$$d\phi = \frac{\cos\zeta dy - \sin\zeta dx}{\sqrt{R(\phi)^2 + R'(\phi)^2}},$$

with respect to a standard Cartesian basis. In principle ϕ could be calculated for a given $R(\phi)$, but in practice this is not required. By differentiation and the cross product it is easy to determine $\boldsymbol{\sigma}_{,x}$, $\boldsymbol{\sigma}_{,y}$, and the outward pointing normal, $\hat{\mathbf{N}}$:

$$\boldsymbol{\sigma}_{,x} = \phi_{,x}(R'\cos\phi - R\sin\phi,\ R'\sin\phi + R\cos\phi,\ 0) + (0, 0, \cos\zeta)$$
$$\boldsymbol{\sigma}_{,y} = \phi_{,y}(R'\cos\phi - R\sin\phi,\ R'\sin\phi + R\cos\phi,\ 0) + (0, 0, \sin\zeta)$$

$$\hat{\mathbf{N}} := \pm\frac{\boldsymbol{\sigma}_{,x}\times\boldsymbol{\sigma}_{,y}}{\|\boldsymbol{\sigma}_{,x}\times\boldsymbol{\sigma}_{,y}\|} = -\frac{1}{\sqrt{R^2+R'^2}}(-\{R'\sin\phi+R\cos\phi\},\ R'\cos\phi-R\sin\phi,\ 0)$$

From these it is simple to confirm the isomorphism between the plane and a general prism by checking that $\mathcal{F}_{\mathrm{I}} = \mathrm{I}$:

$$\begin{aligned}\boldsymbol{\sigma}_{,x}\cdot\boldsymbol{\sigma}_{,x} &= \phi_{,x}{}^2(R^2+R'^2)+\cos^2\zeta = 1\\ \boldsymbol{\sigma}_{,y}\cdot\boldsymbol{\sigma}_{,y} &= \phi_{,y}{}^2(R^2+R'^2)+\sin^2\zeta = 1\\ \boldsymbol{\sigma}_{,x}\cdot\boldsymbol{\sigma}_{,y} = \boldsymbol{\sigma}_{,y}\cdot\boldsymbol{\sigma}_{,x} &= \phi_{,x}\phi_{,y}(R^2+R'^2)+\cos\zeta\sin\zeta = 0.\end{aligned}$$

To obtain the second fundamental form, and thus $C_{\alpha\beta}$, further differentiation of the patch is required:

$$\begin{aligned}\boldsymbol{\sigma}_{,xx} &= \frac{\phi_{,xx}}{\phi_{,x}}\boldsymbol{\sigma}_{,x}-\frac{\phi_{,xx}}{\phi_{,x}}(0,\ 0,\ \cos\zeta)\\ &\qquad+\phi_{,x}^2\left(\{R''-R\}\cos\phi-2R'\sin\phi,\ \{R''-R\}\sin\phi+2R'\cos\phi,\ 0\right)\\ \boldsymbol{\sigma}_{,yy} &= \frac{\phi_{,yy}}{\phi_{,y}}\boldsymbol{\sigma}_{,y}-\frac{\phi_{,yy}}{\phi_{,x}}(0,\ 0,\ \sin\zeta)\\ &\qquad+\phi_{,y}^2\left(\{R''-R\}\cos\phi-2R'\sin\phi,\ \{R''-R\}\sin\phi+2R'\cos\phi,\ 0\right)\\ \boldsymbol{\sigma}_{,xy}=\boldsymbol{\sigma}_{,yx} &= \frac{\phi_{,xy}}{\phi_{,x}}\boldsymbol{\sigma}_{,x}-\frac{\phi_{,xy}}{\phi_{,x}}(0,\ 0,\ \cos\zeta)\\ &\qquad+\phi_{,x}\phi_{,y}\left(\{R''-R\}\cos\phi-2R'\sin\phi,\ \{R''-R\}\sin\phi+2R'\cos\phi,\ 0\right).\end{aligned}$$

Contraction with the unit normal produces the second fundamental form, so observing

$$\left(\{R''-R\}\cos\phi-2R'\sin\phi,\{R''-R\}\sin\phi+2R'\cos\phi,0\right)\cdot\hat{\mathbf{N}} = -\frac{-R\{R''-R\}+2R'^2}{\sqrt{R^2+R'^2}}$$

it follows that

$$\mathcal{F}_{\mathrm{II}} = -\left[\frac{-R(R''-R)+2R'^2}{(R^2+R'^2)^{\frac{3}{2}}}\right]\begin{pmatrix}\sin^2\zeta & -\sin\zeta\cos\zeta\\ -\sin\zeta\cos\zeta & \cos^2\zeta\end{pmatrix},$$

where the matrices are with respect to the $\{x,y\}$ co-ordinates of the plane. The prefactor of the matrix of components can be simplified somewhat by observing that

$$\frac{R'^2-RR''}{R^2+R'^2} = \left[\frac{R^2}{R^2+R'^2}\right]\left[\frac{R'^2-RR''}{R^2}\right] = \frac{\mathrm{d}}{\mathrm{d}(R'/R)}\left[\tan^{-1}\left(\frac{R'}{R}\right)\right]\frac{\mathrm{d}}{\mathrm{d}\theta}\left[\frac{-R'}{R}\right]$$

whence

$$\mathcal{F}_{\mathrm{II}} = -\left[\frac{\frac{\mathrm{d}}{\mathrm{d}\phi}(\phi-\tan^{-1}(R'/R))}{\sqrt{R^2+R'^2}}\right]\begin{pmatrix}\sin^2\zeta & -\sin\zeta\cos\zeta\\ -\sin\zeta\cos\zeta & \cos^2\zeta\end{pmatrix},$$

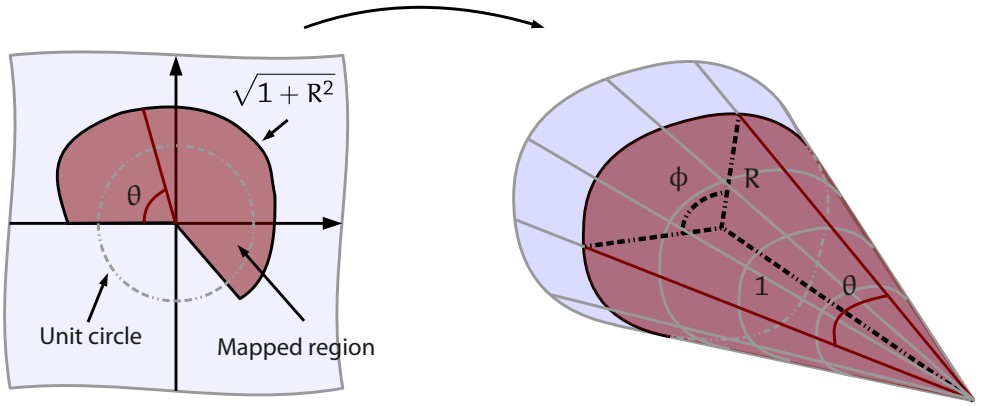

Figure 5.10: The plane maps onto a general cone as shown. The plane polar co-ordinates $\{r, \theta\}$ relate to the plane Cartesian co-ordinates as specified in equation 5.29.

Further simplification can be effected by changing the differentiation variable to y:

$$\mathcal{F}_{II} = -\frac{d}{dy}\left[\frac{\phi - \tan^{-1}(R'/R)}{\cos\zeta}\right]\begin{pmatrix} \sin^2\zeta & -\sin\zeta\cos\zeta \\ -\sin\zeta\cos\zeta & \cos^2\zeta \end{pmatrix}.$$

Since $\mathcal{F}_I = I$, $C_{\alpha\beta} = -\mathcal{F}_{II\,\alpha\beta}$. Substituting into equation 5.27 produces

$$\begin{aligned} T_{yy} &= T_0 \exp\left(\mu_d \cos\zeta \int \frac{d}{dy}[\phi - \tan^{-1}(R'/R)]dy\right) \\ &= T_0 \exp\left(\mu_d \cos\zeta \left[\phi - \tan^{-1}(R'/R)\right]_{\phi_0}^{\phi_1}\right), \end{aligned} \tag{5.28}$$

where ϕ_0, ϕ_1 are the limits of contact, which is the result derived by Cottenden *et al.* [107] for $\zeta = 0$, and reduces to the classic cylindrical solution for $\zeta = 0$, $R' = 0$. As noted by Cottenden *et al.* [107] for their model, for fixed ϕ_0 and ϕ_1 the co-ordinate centre can be chosen so that the arctangent term vanishes at both limits; this result clearly also holds here.

5.5.3 Conical solutions

The simplest generalisation of a prism that remains isomorphic to the plane is a cone, so it is a logical surface to consider for an analytical solution. Again, the starting point for a solution is to state the patch for a general cone. This is specified by a cylindrical polar function $R(\phi)$ (the radius at unit distance along the axis from the cone apex), so by considering figure 5.10 the patch is

$$\sigma = \frac{r}{\sqrt{1 + R(\phi(\theta))^2}}(R(\phi(\theta))\cos(\phi(\theta)), R(\phi(\theta))\sin(\phi(\theta)), 1),$$

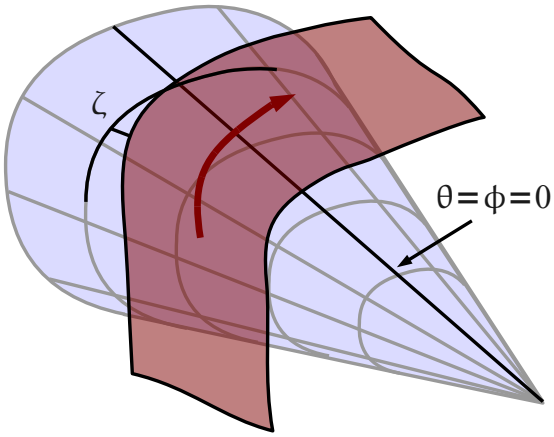

Figure 5.11: The angle ζ is defined as the angle between the flow vector and the cone's cross sectional plane at $\theta = \phi = 0$.

where $\{r, \theta\}$ are plane polar co-ordinates derived from the Cartesian $\{x, y\}$ co-ordinates by

$$r = \sqrt{x^2 + y^2} \qquad , \qquad \theta = \tan^{-1}\left(\frac{y}{x}\right) - \zeta, \tag{5.29}$$

where ζ is the angle between the direction of slip and the tangential direction when $\theta = \psi = 0$ (figure 5.11). The connection between ϕ and θ is more subtle, but consideration of figure 5.12 shows that

$$d\theta = \frac{\sqrt{R^2 + R'^2 + R^4}}{1 + R^2} d\phi = \frac{R\sqrt{1 + R^2}}{\sqrt{(1 + R^2)^2 - R_{,\theta}^2}} d\phi, \tag{5.30}$$

where the second equality follows by writing $R_{,\theta} = \phi_{,\theta} R'$ and rearranging. Differentiate the patch:

$$\begin{aligned} \boldsymbol{\sigma}_{,\alpha} = \left\{ r_{,\alpha} - \frac{RR' r\theta_{,\alpha}\phi_{,\theta}}{1 + R^2} \right\} \frac{1}{\sqrt{1 + R^2}} (R\cos\phi, R\sin\phi, 1) \\ + \frac{\theta_{,\alpha}\phi_{,\theta} r}{\sqrt{1 + R^2}} (R'\cos\phi - R\sin\phi, R'\sin\phi + R\cos\phi, 0). \end{aligned} \tag{5.31}$$

It is more convenient in the ensuing derivation to change to the non-constant orthonormal basis

$$\{(\cos\phi, \sin\phi, 0), (-\sin\phi, \cos\phi, 0), (0, 0, 1)\},$$

and in this basis the components of $\boldsymbol{\sigma}_{,\alpha}$ read

$$\boldsymbol{\sigma}_{,\alpha} = \frac{1}{\sqrt{1 + R^2}} \left[R r_{,\alpha} + \frac{r\theta_{,\alpha}\phi_{,\theta} R'}{1 + R^2}, R\theta_{,\alpha}\phi_{\theta} r, r_{,\alpha} - \frac{RR' r\theta_{,\alpha}\phi_{,\theta}}{1 + R^2} \right].$$

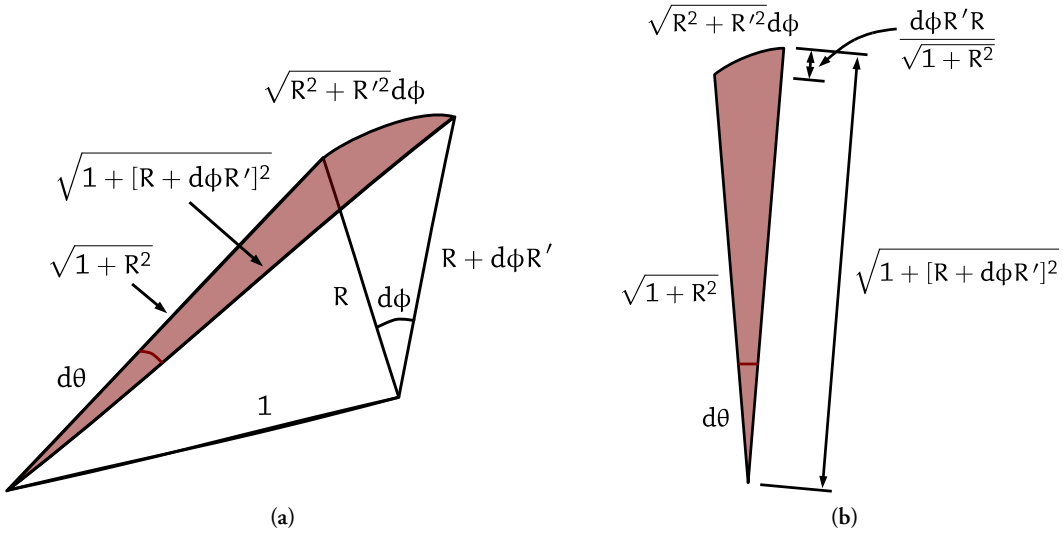

Figure 5.12: Elemental increases in ϕ and θ are connected by the two interrelated triangles shown in (a). (b) shows the relationship between $\sqrt{1+R^2}d\theta$ (the arc length at constant radius) and the other quantities.

Again, it is easy to show from here that $\mathcal{F}_I = I$, as expected:

$$\begin{aligned}\boldsymbol{\sigma}_{,\alpha}\cdot\boldsymbol{\sigma}_{,\beta} &= \frac{1}{1+R^2}\left\{(1+R^2)r_{,\alpha}r_{,\beta} + \frac{(1+R^2)r^2\phi_{,\theta}{}^2R'^2\theta_{,\alpha}\theta_{,\beta}}{(1+R^2)^2} + R^2r^2\phi_{,\theta}{}^2\theta_{,\alpha}\theta_{,\beta}\right\}\\ &= r_{,\alpha}r_{,\beta} + \frac{r^2\phi_{,\theta}{}^2\theta_{,\alpha}\theta_{,\beta}}{(1+R^2)^2}\left\{R'^2+R^2(1+R^2)\right\}\\ &= r_{,\alpha}r_{,\beta} + r^2\theta_{,\alpha}\theta_{,\beta},\end{aligned}$$

where the last step made use of equation 5.30. Finally,

$$r_{,x} = \frac{x}{r} \quad , \quad r_{,y} = \frac{y}{r} \quad , \quad \theta_{,x} = \frac{-y}{r^2} \quad , \quad \theta_{,y} = \frac{x}{r^2}, \tag{5.32}$$

so

$$\boldsymbol{\sigma}_{,x}\cdot\boldsymbol{\sigma}_{,x} = 1 \quad , \quad \boldsymbol{\sigma}_{,y}\cdot\boldsymbol{\sigma}_{,y} = 1 \quad , \quad \boldsymbol{\sigma}_{,x}\cdot\boldsymbol{\sigma}_{,y} = \boldsymbol{\sigma}_{,y}\cdot\boldsymbol{\sigma}_{,x} = 0.$$

A normal vector can again be obtained by taking the cross product of the two $\boldsymbol{\sigma}_{,\alpha}$:

$$\begin{aligned}\tilde{\mathbf{N}} = (1+R^2)\boldsymbol{\sigma}_{,x}\times\boldsymbol{\sigma}_{,y} = &\left[Rr_{,x} + \frac{r\theta_{,x}\phi_{,\theta}R'}{1+R^2},\, R\theta_{,x}\phi_\theta r,\, r_{,x} - \frac{RR'r\theta_{,x}\phi_{,\theta}}{1+R^2}\right]\\ &\times\left[Rr_{,y} + \frac{r\theta_{,y}\phi_{,\theta}R'}{1+R^2},\, R\theta_{,y}\phi_\theta r,\, r_{,y} - \frac{RR'r\theta_{,y}\phi_{,\theta}}{1+R^2}\right]\end{aligned}$$

$$
\begin{aligned}
&= r\phi_{,\theta}\begin{bmatrix} R(\theta_{,x}r_{,y} - \theta_{,y}r_{,x}), \\ \dfrac{R'}{1+R^2}\left\{-r_{,y}\theta_{,x}(1+R^2) + r_{,x}\theta_{,y}(1+R^2)\right\}, & R^2(r_{,x}\theta_{,y} - r_{,y}\theta_{,x}\end{bmatrix} \\
&= r\phi_{,\theta}(\theta_{,y}r_{,x} - \theta_{,y}r_{,x})\left[R, -R', -R^2\right].
\end{aligned}
$$

This must be normalised to produce $\hat{\mathbf{N}} = \tilde{\mathbf{N}}/\|\tilde{\mathbf{N}}\|$, the outward pointing unit normal for the surface.

$$
\hat{\mathbf{N}} = \frac{1}{\sqrt{R^2 + R'^2 + R^4}}\left[R, -R', -R^2\right].
$$

For the general cone it is useful to note that since by definition $\boldsymbol{\sigma}_{,\alpha}\cdot\hat{\mathbf{N}} = 0$ it follows that $\boldsymbol{\sigma}_{,\alpha}\cdot\hat{\mathbf{N}}_{,\beta} + \boldsymbol{\sigma}_{,\alpha\beta}\cdot\hat{\mathbf{N}} = 0$, so $\boldsymbol{\sigma}_{,\alpha\beta}\cdot\hat{\mathbf{N}} = -\boldsymbol{\sigma}_{,\alpha}\cdot\hat{\mathbf{N}}_{,\beta}$, which (given the relative complexities of $\boldsymbol{\sigma}_{,\alpha}$ and $\hat{\mathbf{N}}$) somewhat simplifies the derivation of $\mathcal{F}_{\mathrm{II}}$. Recalling that the new basis is not constant,

$$
\begin{aligned}
\hat{\mathbf{N}}_{,\beta} &= A\hat{\mathbf{N}} + \frac{\phi_{,\theta}\theta_{,\beta}}{\sqrt{R^2 + R'^2 + R^4}}\left[R', -R'', -2RR'\right] + \frac{\phi_{,\theta}\theta_{,\beta}}{\sqrt{R^2 + R'^2 + R^4}}\left[R', R, 0\right] \\
&= A\hat{\mathbf{N}} + \frac{\phi_{,\theta}\theta_{,\beta}}{\sqrt{R^2 + R'^2 + R^4}}\left[2R', R - R'', -2RR'\right].
\end{aligned}
$$

where the function A has not been calculated since $\hat{\mathbf{N}}$ is orthogonal to $\boldsymbol{\sigma}_{,\alpha}$. Proceeding formally with the calculation of $\boldsymbol{\sigma}_{,\alpha}\cdot\hat{\mathbf{N}}_{,\beta}$, the terms depending upon $r_{,\alpha}$ cancel, leading to

$$
\begin{aligned}
\boldsymbol{\sigma}_{,\alpha}\cdot\hat{\mathbf{N}}_{,\beta} &= \frac{\phi_{,\theta}\theta_{,\beta}}{\sqrt{1+R^2}\sqrt{R^2 + R'^2 + R^4}} \\
&\qquad \left\{\frac{2R'^2 r\theta_{,\alpha}\phi_{,\theta}}{1+R^2} + R\theta_{,\alpha}\phi_{,\theta}r(R - R'') + \frac{2R^2R'^2 r\theta_{,\alpha}\phi_{,\theta}}{1+R^2}\right\} \\
\mathcal{F}_{\mathrm{II}\alpha\beta} &= -\boldsymbol{\sigma}_{,\alpha}\cdot\hat{\mathbf{N}}_{,\beta} = \frac{r\phi_{,\theta}^2\theta_{,\alpha}\theta_{,\beta}}{\sqrt{1+R^2}\sqrt{R^2 + R'^2 + R^4}}(RR'' - 2R'^2 - R^2),
\end{aligned}
$$

Only the yy component is relevant, so consider that component, recalling that $\theta_{,y} = x/(x^2+y^2) = \cos(\theta+\zeta)/r$:

$$
\mathcal{F}_{\mathrm{II}yy}dy = (\theta_y dy)\cos(\theta+\zeta)\phi_{,\theta}\sqrt{1+R^2}\left\{\frac{RR'' - 2R'^2 - R^2}{R^2 + R'^2 + R^4}\right\}. \tag{5.33}
$$

Observing that

$$
\frac{d}{d\phi}\left(\tan^{-1}\left[\frac{R'}{R\sqrt{1+R^2}}\right]\right) = \sqrt{1+R^2}\left\{\frac{RR'' - 2R'^2 - R^2}{R^2 + R'^2 + R^4}\right\} + \frac{1}{\sqrt{1+R^2}},
$$

equation 5.33 can be further simplified to

$$
\mathcal{F}_{\mathrm{II}yy}dy = d\theta\cos(\theta+\zeta)\left\{\frac{d}{d\theta}\left(\tan^{-1}\left[\frac{R'}{R\sqrt{1+R^2}}\right]\right) - \frac{\phi_{,\theta}}{\sqrt{1+R^2}}\right\}. \tag{5.34}
$$

This expression has several shortcomings. Most obviously, it is not directly integrable; even the perfect differential is accompanied by a cosine. Additionally, although it splits off a term that vanished in the case of circular cross section, the second term is *not* independent of R'. However, equation 5.34 is the most compact and enlightening form so far obtained.

In the absence of a generally integrable form for $\mathcal{F}_{II}$, it is worth looking at the simpler situation of a circular cone, where R is a constant. In this situation $\phi = (\sqrt{1+R^2}/R)\theta$, and equation 5.34 reduces to

$$\mathcal{F}_{II\,yy}\,dy = -d\theta\cos(\theta+\zeta)\frac{1}{R}.$$

Since the first fundamental form is the identity, $C_{yy} = -\mathcal{F}_{II\,yy}$, so substituting this expression into equation 5.27,

$$\begin{aligned} T_{yy} &= T_0 \exp\left(\mu_d \int \frac{\cos(\theta+\zeta)}{R} d\theta\right) \\ &= T_0 \exp\left(\frac{\mu_d}{R}\left[\sin(\theta+\zeta)\right]_{\theta_0}^{\theta_1}\right), \end{aligned} \tag{5.35}$$

where θ_0, θ_1 are the limits of contact. This expression is compared to equation 5.28 in §5.5.4.

5.5.4 Comparison of the analytical solutions

A prism is the limit of a cone with similar cross section as the conical angle tends to zero. It is thus necessarily the case that the solution for circular cones (equation 5.35) should reduce to the cylindrical solution with $\zeta = 0$ (equation 5.28) as $R \to 0$. It is also interesting to consider how rapidly the two solutions part company as R increases.

To compare the two solutions, it is useful to change variables to ϕ and then expand the exponent of equation 5.35 in terms of ϕ and R; take $\zeta = 0$ for simplicity. Thus, in equation 5.35, using $\sin\theta = \theta - \theta^3/6 + \mathcal{O}(\theta^5)$ and $\theta = R\phi/\sqrt{1+R^2}$ gives

$$\begin{aligned} T_{yy} &= T_0 \exp\left(\frac{\mu_d}{R}\left[\sin\left(\frac{R\phi}{\sqrt{1+R^2}}\right)\right]_{\phi_1}^{\phi_2}\right) \\ &= T_0 \exp\left(\frac{\mu_d}{R}\left[\left\{\frac{R\phi}{\sqrt{1+R^2}}\right\} - \frac{1}{3!}\left\{\frac{R\phi}{\sqrt{1+R^2}}\right\}^3 + \mathcal{O}\left(\left\{\frac{R\phi}{\sqrt{1+R^2}}\right\}^5\right)\right]_{\phi_1}^{\phi_2}\right) \\ &= T_0 \exp\left[\mu_d\phi\left\{1 - \tfrac{1}{2}R^2\left(1+\tfrac{1}{3}\phi^2\right) + \mathcal{O}\left(R^4\right)\right\}\right]_{\phi_1}^{\phi_2}. \end{aligned} \tag{5.36}$$

(If $\zeta \neq 0$ then the exponent in (5.36) attracts a factor of $\cos\zeta$, and another term of order $\phi^2 R\sin\zeta$ arises.) Comparing equations 5.36 and the cylindrical solution, it is clear that as $R \to 0$ the solution for a circular cone collapses to that for a cylinder.

Using equation 5.36 it is possible to examine why Karavokyros [169] found that his experiments (using a minor variant of the "curved pull" method reported by Cottenden *et al.* [1]) on Neoprene-covered plaster of Paris circular cones showed good agreement with the cylindrical friction model at their error level (around ±10 % for most samples). Seeking to examine anatomically relevant

situations, Karavokyros tested only cones with small conical half-angles, in no case exceeding 12°; he used ϕ in the range [70°, 120°]. Considering the most extreme cone, substitute $R = \tan(12^\circ) \approx 0.20$ into equation 5.36:

$$T_{yy} = T_0 \Big[\exp(\mu_d \phi) \exp\left(-0.02\mu_d \phi \left(1 + \tfrac{1}{3}\phi^2\right)\right) \Big]_{\phi_1}^{\phi_2} \tag{5.37}$$

(to quadratic order in R). In the range $[70°, 120°] \approx [1.2, 2.1]$ radians the exponent in the second exponential varies in the range $[-0.104\mu_d, -0.036\mu_d]$, so the exponential function itself varies in $[\sim 0.90^{\mu_d}, \sim 0.96^{\mu_d}] \approx [0.95, 0.98]$ (in these experiments $\mu \approx 0.5$). This degree of variation is small in comparison with the experimental error, so the agreement of Karavokyros' conical experiments with the prismical theory is consistent with the conical theory presented here.

It is also interesting to consider a corresponding comparison for much more extreme cones and larger angles of contact. In these circumstances, before any comparison can be made it is first necessary to address the question of what quantity should be identified with the cylindrical contact angle for a geometry that is fundamentally not cylindrical. It should be emphasised that there is *not* a "correct" answer to this question; in the purest sense it is somewhat ill-posed; it is considered out of curiosity as to how far a wonderfully simple model can be stretched before ceasing to be at all helpful.

The angle in the cylindrical friction model arises from resolution of forces around the curve, so it is perhaps most natural to relate the cylindrical contact angle to the angle between the incoming and outgoing directions of the sheet over the cone. It would be reasonable to object that, as the path of a strip around a cone is not planar[5], this association is erroneous; the objection is allowed, but the ansatz is defended on the grounds that even for large angles of contact the normal deviation from a plane is small compared to the length of the contact curve. The quantity proposed can easily be computed; considering the patch $\boldsymbol{\sigma}$ for a circular cone, the proposed equivalent cylindrical contact angle, φ, is given by

$$\varphi = \cos^{-1}\left(\boldsymbol{\sigma}_{,y}(\theta_0) \cdot \boldsymbol{\sigma}_{,y}(\theta_1)\right),$$

where the inverse cosine takes the appropriate branch. This may be calculated by taking the Cartesian expression for the conical patch derivative (equation 5.31), specialising to a circular cone, and evaluating it at both extremes of contact.

$$\boldsymbol{\sigma}_{,\alpha} = \frac{r_{,\alpha}}{\sqrt{1+R^2}}(R\cos\phi, R\sin\phi, 1) + \frac{\theta_{,\alpha}\phi_{,\theta} r}{\sqrt{1+R^2}}(-R\sin\phi, R\cos\phi, 0),$$

so by substituting from equations 5.32,

$$\boldsymbol{\sigma}_{,y} = \frac{\sin\theta}{\sqrt{1+R^2}}(R\cos\phi, R\sin\phi, 1) + \frac{\cos\theta}{R}(-R\sin\phi, R\cos\phi, 0),$$

where the symbol ϕ has been retained for compactness only; as before it is $\phi = \theta\sqrt{1+R^2}/R$.

[5]If the path were planar then it would by necessity be an ellipse (the path of such a plane cutting a cone); the possibility of cusps in the case of very large contact angles clearly contradicts this, so the path cannot be planar.

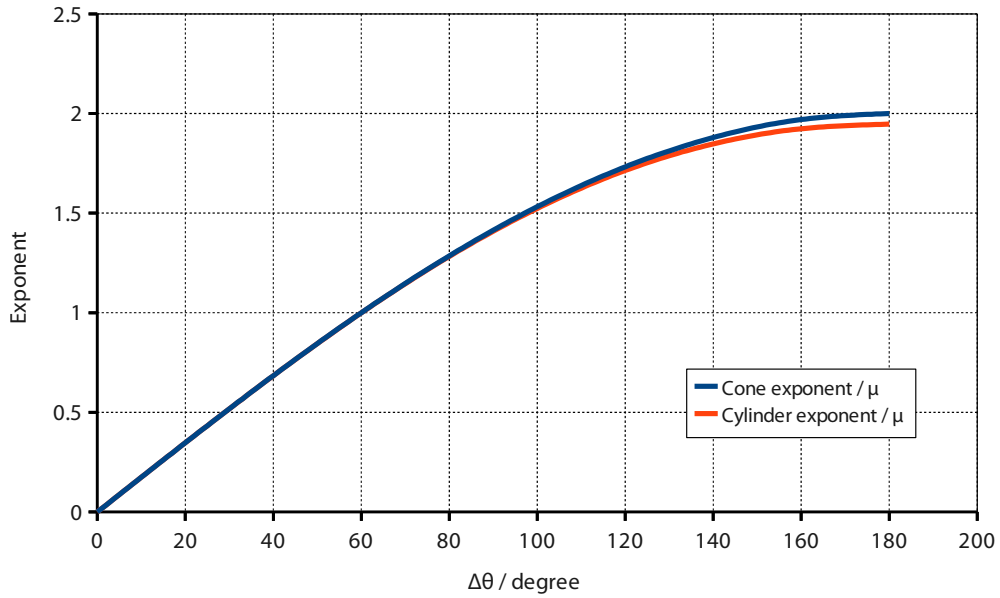

Figure 5.13: A comparison of the exponents for the model for circular cones and that for cylinders, where the latter uses the angle between the incoming and outgoing strips as its contact angle. The similarity is striking, even for a conical half angle of 45° and very large contact angles.

Symbolic calculation of φ in not enlightening due to the complexity of the expression generated and its lack of similarity of form to any portion of the conical friction expression, so a numerical comparison has been performed instead (figure 5.13). Taking advantage of the (limited) similarity of form between the two models, figure 5.13 compares $\log(T_{yy}/T_0)/\mu$ for each model; that is, between

$$\varphi = \cos^{-1}\left(\boldsymbol{\sigma}_{,y}(\theta_0)\cdot\boldsymbol{\sigma}_{,y}(\theta_1)\right) \qquad \text{and} \qquad \left[\frac{\sin(\theta)}{R}\right]_{\theta_0}^{\theta_1}.$$

Clearly, a numerical comparison must select specific values for R and the balance of θ_0 and θ_1; figure 5.13 takes a cone with half-angle of 45° to accentuate any differences, and sets $\theta_0 = -\theta_1$ for simplicity; $\zeta = 0$ without loss of generality.

The similarity between the two curves is quite striking; the difference is never greater than 3 % of the value of the true conical value, which for a typical value of $\mu = 0.5$ leads to a discrepancy of *less* than 3 % between T_{yy}/T_0 calculated using each method. Since this is at the better end of the usual experimental error on that quantity, this result implies that using the simple cylindrical theory to interpret experimental results (defining the contact angle as explained above) will be acceptable in most experimental circumstances, even for the cones with half-angles in the region of 45°.

5.6 Experimental verification

The nature of the scientific method is that theories should produce predictions, and these predictions should be tested experimentally. In the case of the theory presented here, the *ideal* form of experimental test would be a test of the equation of motion; that is, the differential form of the theory. However, in this case (as in most) it is not practical to do so, so specific solutions must be tested instead. Since the prism solutions are a minor generalisation of previously published and experimentally verified solutions [107], it is the new, conical solutions that merit most attention. A series of tests have been carried out by Asimakopoulos [170], testing the prediction obtained for circular cones (equation 5.35). As this work is yet to be published, a brief description is given here.

The work was carried out using a variant on the "curved pull" method (described by Cottenden *et al.* [1]), pulling a nonwoven coverstock (not one of those investigated in this work) over plaster of Paris circular cones; the equipment is shown in figure 5.14. The additional complexity in this equipment over previous instances of the "curved pull" method is due to the more complicated geometry of a cone compared to a prism, and the requirement that the pulled strip remains geometrically flat. Because the pulled strip moves around two cylinders (variously, unspecified "plastic" tubes or chromium plated piping) a correction must be made to the force data reported by the tensometer before using them to test the new model; this is a simple matter given the long-understood behaviour of material wrapped around a cylinder.

This correction having been made, Asimakopoulos has plotted his data in the form of $[\sin(\theta)]_{\theta_0}^{\theta_1}/R$ against T_{yy}/T_0; the data for two different cone half-angles are shown in figure 5.15, where $R = \tan(35°)$, or $R = \tan(45°)$. The method of plotting means that the new conical model predicts a straight line with gradient μ passing through the origin. The graph shows that Asimakopoulos' data support the theoretical work well: the gradients differ by less than 10 %, and both lines are close to passing through the origin. The non-zero intercept is thought to be due to inaccuracies in the measurement of friction between the nonwoven strip and the pipes, perhaps exacerbated by progressive polishing during the course of the experiments, and a serendipitous linear relationship between the wrapping angles around the pipes and the contact angles on the cone.

5.7 Summary

This chapter has shown the derivation of equations of motion for a conformable sheet over a general, flexible, curved substrate when the two are coupled by a friction force of a very general type (III). Based upon nothing more than this general assumption, it has been shown that with non-degenerate pairs of materials, for a uniform sheet sliding in point equilibrium the rate at which undeformed sheet passes is constant in time and space.

Further assumptions have then been made in order to enable some solutions to be extracted. Limiting focus to static substrates, very low density sheets, forces exerted only at the ends of a strip, and convex substrates, and further assuming Amontons' law holds, a general solution in the form of an integral has been derived for sheets with zero Poisson ratio and substrates with zero Gaussian curvature. Closed-form solutions have then been obtained for convex prisms (with any sliding angle) and circular cones. All solutions have been demonstrated to be consistent with each other and with

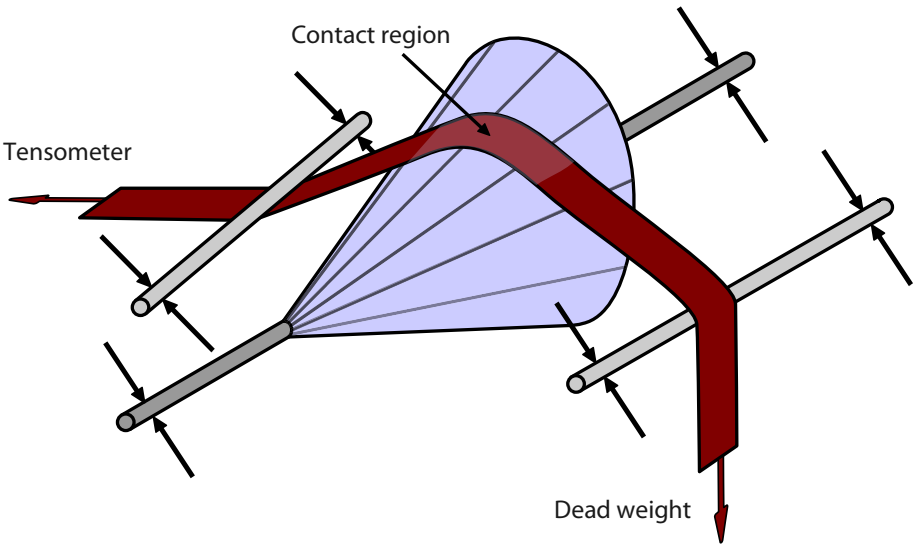

Figure 5.14: The equipment used by Asimakopoulos to experimentally test the new conical friction model. A nonwoven strip was pulled around a circular cone of large half-angle; the additional pipes ensure that the geometry remains correct.

previous solutions from the literature. Further, by defining a "reasonable" correspondence between conical geometry and circular geometry it has been shown that using the "classic" solution for a cylinder to interpret data from even an extreme cone introduces no substantial error. Experimental evidence supports both the prism solution (by identification with a previously extant solution) and the conical solution (new experiments).

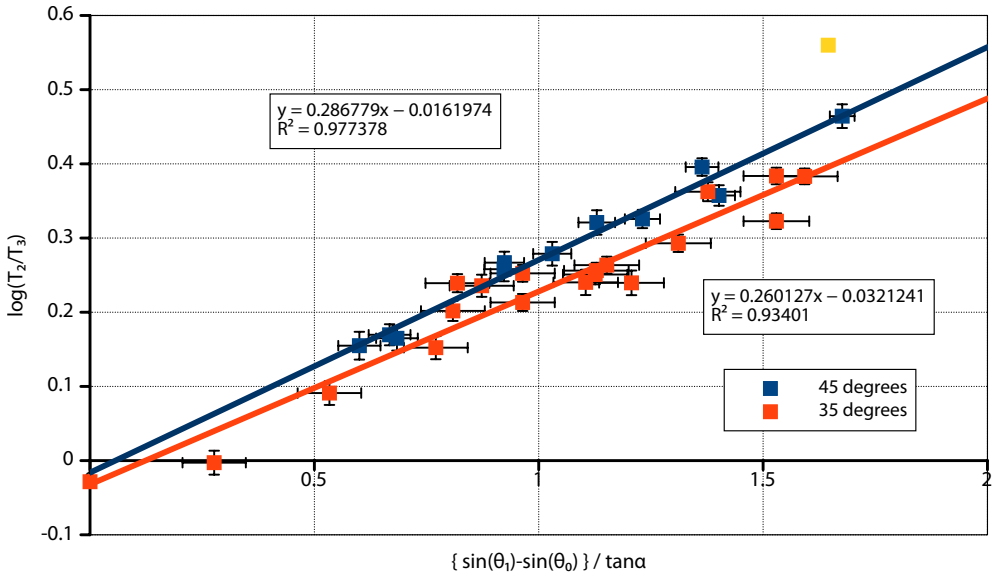

Figure 5.15: Asimakopoulos' results [170]. Without loss of generality Asimakopoulos took $\xi = 0$. Data for two different cones are shown, with half angles of 45° and 35°. The additional point (shown in yellow, and relating to the 45° cone) is clearly an outlier, and has not been included in the fits.

Chapter 6

Conclusions

"You get a wonderful view from the point of no return."
— Terry Pratchett, 1948–

Since the work presented in chapters 4 and 5 of this thesis has been so varied in terms of techniques used and the specific aspects of the skin-nonwoven friction problem addressed, it has made far more sense to summarise and analyse the results, and explain their scientific implications at the end of the relevant chapters. In consequence, such analysis and explanation is not needed here. Instead, a summary of what has been found and achieved is given, along with detailed recommendations for follow-up work.

6.1 Summary of findings and achievements

The most practical achievements have been in regard to the development of experimental equipment and techniques which introduce little error, and are well characterised so that data can be interpreted with confidence.

Contact fibre length can be determined to within about ±5 %. Contact between "skin" and nonwoven occurs at discrete fibre locations. The length of these fibre contacts can now be measured with a variation of about ±5 %. Since no other reliable and more direct method for measuring the fibre contacts has been found it has not been possible to prove that the contacts measured are not systematically different from the true contacts, but there are good indirect reasons for believing the two to be very similar.

Friction force has random and systematic error of about 1 % each. The friction-displacement equipment has been thoroughly characterised after a careful development. The validation experiments showed that random variation is typically a little more than 1 %, and that all of the identified sources of systematic error total to about the same.

This equipment has enabled accurate experiments to be conducted. Unfortunately, as explained in §4.2.2, it has not been possible to obtain any skin samples to experiment on within the time frame of this project. However, all equipment has been designed with this material in mind, and

a request for ethics and local research and development approval to obtain and work on skin made and granted. As explained before, some experiments are impacted by this and others are not. In this following summary of experimental findings it is made clear which are which.

Contact length between fibres and "skin" varies logarithmically with pressure. Despite fair scatter due to the inconsistency of nonwoven as a material, the large pressure range over which measurements were conducted showed that the total contact fibre length varied logarithmically with pressure, increasing only by about a factor of three over two orders of magnitude in pressure. This is a property of the nonwoven, and as such applies to the nonwoven-X interface for all facing materials above a certain stiffness (§4.3.2), including both skin and Lorica Soft.

Predictions for viscoelasticity and adhesion have been derived from contact measurements. Assuming some simple models from the literature for adhesive and viscoelastic friction, and invoking Hertzian deformation of the skin (surrogate) surface, predictions were made for how each mechanism would scale with load. Power laws were fitted to both (the fits were good) and the indices taken as "fingerprints" of the mechanisms for later comparison with friction data. Though the numerical values of the predictions (where possible) depend upon the mechanical and surface properties of the X surface, they appear only in scaling factors so the indices are universal.

Amontons' law applies to high precision to Lorica Soft-nonwoven dynamic friction. Experiments have shown that linear fits to dynamic friction force-normal load data have a coefficient of determination of 0.999 *or higher* for all Lorica Soft-nonwoven interfaces. There is, however, a slight suggestion of sublinearity on the basis of the low-load results. However, this effect is not pronounced enough to lead to a discernible trend in point-calculated coefficients of friction with load, so it is hard to be sure if it is simply a reflection of the sensitivity of low-force results to environmental noise, or a true effect. Either way, in pragmatic terms Amontons' law has been verified to high precision.

Lorica Soft-nonwoven friction varies very weakly with sliding speed. Friction force varies very weakly with velocity, typically increasing by 10 % over two orders of magnitude change in sliding speed. This suggests that viscoelasticity is probably not a significant contributor to friction in this velocity range. The variation that has been observed may perhaps be attributable to "geometric aging" (§2.4.8), but this has not been investigated.

Variation in friction with distance implies two significant mechanisms. Attempts to collapse all of the friction-displacement curves for a given interface at a given sliding speed showed that a single scaling parameter was inadequate; *two* parameters were needed, with corresponding contributions that varied differently with load. This implies that *two* friction mechanisms are significant. The indices of power law fits provide circumstantial evidence (by comparison with the contact results) that two families of contacts are created, one "smooth" and one "rough", but the evidence is certainly not conclusive.

As well as primarily experimental findings, several mainly theoretical findings relating to the sliding of a generic compliant sheet over a substrate have been derived. Some have been experimentally verified by others' work.

A framework and equation of motion for general sheet-sliding has been derived. The problem of a compliant sheet sliding over a generally shaped substrate has been considered in detail. Evolution of contact areas in the case of non-uniform convexity has been described, and equations of motion for both sheet and substrate have been derived from Cauchy's law of motion and a very general assumption about the direction of friction forces, notably not prescribing their magnitude.

Change in local sliding velocity for a uniform sheet is only due to deformation. Based on no further assumptions, it has been shown that for a sheet which is uniform in its relaxed state and sliding in equilibrium, change in the local sliding velocity is only due to deformation in the sheet. It is thus possible in the spatial description to represent particle velocity with a single vector rather than a field, representing a substantial efficiency in the case of numerical solutions.

An integral-form solution has been found for certain sheets on "flat" surfaces obeying Amontons' law. By assuming Amontons' law and that both the density and Poisson's ratio for the compliant sheet are negligible, a general solution for a strip sliding in steady-state over a general convex surface with zero Gaussian curvature has been found in integral form. It takes the form of a functional of the curvature tensor of the surface.

Solutions for Amontons' law on a prism have been obtained. By determining the curvature tensor for a prism the general solution has been specialised and calculated in closed form. The result is consistent with that previously published for sliding over a prism, but generalises it by allowing sliding at any angle relative to the axis.

Solutions for Amontons' law on a circular cone have been obtained. The curvature tensor for a general cone has been calculated, and the general solution adapted to the special case of a circular cone integrated to give a solution in closed form. It has been demonstrated that this reduces to the known solution for a cylinder for a shallow-angled cone, and further that the two solutions diverge slowly. This solution is significant as substantial regions of the body can be well approximated as portions of cones.

Subject to suitable mapping, the conical solution can be approximated by the cylindrical. By defining the "equivalent" cylindrical wrapping angle to be that between the incoming and outgoing strips, a numerical comparison of the exact result for the circular cone with the "equivalent" cylindrical result shows that the two are in excellent agreement even on a cone with a half-angle of 45°. This somewhat surprising result implies that (subject to measuring the angles "correctly") the very simple equation for friction around a cylinder can be applied to large angle cones without introducing error beyond that usually associated with such experiments. This will be of great practical use.

Experimental evidence supports the prism and conical solutions. A colleague's experimental work has gone some substantial way towards verifying the conical result, and thus to some extent the equations of motion.

6.2 Evaluation of the project against the objectives (§3.3)

At the beginning of this thesis is was explained that the long-term goal towards which this project has made the first moves is to understand how and why friction between skin and fabric occurs, so

that manufacturers of hygiene products (and other interested parties) to are able to engineer their coverstocks for specific friction properties against skin, so minimising both slippage and unnecessary abrasion. The microfriction aspect of this work has made an important first step in discounting certain friction mechanisms and generating testable hypotheses as to which mechanisms *are* important. Further work to verify and further explore these hypotheses will enable nonwovens to be designed for task, as intended. Further, the geometric friction work has laid out a complete and coherent framework within which simulations relating global product structure to local friction can be run: useful simulations based upon this work could be developed *now*, and used to inform product design.

Since the long-term objective was rather remote and lofty, more immediate and concrete objectives for this project were set out in the light of the literature review. Most have been achieved. They are evaluated one by one.

6.2.1 Microfriction

To develop and characterise friction and interface apparatus. These have both been achieved. The friction equipment is an order of magnitude more sensitive than any other apparatus found in the literature, and—more importantly—has been thoroughly validated. It is a complete success. The interface apparatus and associated procedures give very *reproducible* results for the conformation and length of the contact between the surfaces, but has had to make a number of compromises (notably it uses a glass substrate instead of skin (surrogate), though theory implies this does not matter) and has not been verified against any very direct standard, though it is thought to be a good measure.

To gather data at various relevant interfaces. Complete data have been gathered for the Lorica Soft-nonwoven interface for three different and relevant nonwovens. As explained in §4.2.2, it has not been possible to obtain skin for experimental use. This is a serious omission, and one which must be amended in future work.

To analyse the interface and friction data to identify mechanisms. Friction data for the Lorica Soft-nonwoven interface have been analysed and have produced a tentative identification of two different friction mechanisms, plausibly corresponding to adhesion between rough and smooth populations of contacts. The evidence remains circumstantial, and the mechanisms should be verified by more specifically targeted experiments.

To relate models of identified mechanisms to material properties and make predictions. Adhesion is both an easy and a difficult mechanism to make predictions for. On the one hand, it relates to the simple quantity, "contact area", but this contact area must be intimate (hence the importance of roughness). Set against this, surface free energies must be known, and though they are not hard to measure they are not trivial to predict. Moreover, adhesion is not intrinsically dissipative, so the actual dissipation mechanism must be found before quantitative predictions can be be. Good progress has been made on this objective, but it is not complete.

6.2.2 Geometric friction

To describe friction for a simple substrate and sheet. This is achieved, and much more. A full *description* for any compliant sheet and substrate coupled by almost any friction law has been given.

To be based on a small number of meaningful parameters. The general model uses whatever parameters are required to describe the deformation of the materials and whatever is needed to describe the friction law. The specific solutions require only geometric parameters for the substrate and a coefficient of friction. All are meaningful in the sense intended.

To be solvable, at least numerically. Some closed form solutions have been obtained, and a more general integral form solution. These are for very simple scenarios, but ones which are relevant to the problem at hand.

Some additional properties were identified as useful, though less necessary.

To permit the use of an accurate constitutive equation for the sheet. The equations of motion allow anything to be used. However, only a very specialised subset of constitutive behaviour has enabled a solution at this stage.

To permit a range of microfriction laws. Again, subject to a very reasonable assumption on the direction in which friction acts any law can be used, though only Amontons' law has so far enabled solutions.

To allow for substrate deformation. The equations of motion allow for any substrate behaviour, but only steady state has generated solutions.

To allow for concave portions of a surface. A complete description enabling the areas of contact to be calculated as they change has been given. As with the previous "desirable" points, no solutions have been generated in this case, but for all of these more general situations it would—at least in principle—be simple to construct a numerical model to obtain solutions.

6.3 Recommendations for future work

No project can ever answer all of the questions that it produces; there is always further work to be done. To facilitate such future work, a brief description of the key areas which would benefit from future work is given here. The first few relate to areas identified in the literature review.

Anisotropic skin stiffness. In the literature review it was observed that it appears not to have been widely realised (and certainly not studied thoroughly) that the laminar structure of skin will give rise to anisotropic stiffness. In consequence it appears that received wisdom in the medical community is that the dermis is the principal contributor to skin stiffness, which is almost certainly not the case. A thorough, layer-by-layer study coupled with a careful treatment of the skin-laminate itself are needed to clarify matters.

Skin friction against contact area. In the literature review an attempt was made to bring the majority of skin-X friction results into a single picture by means of discussion of the deformation of different skin layers at different loadings. It was acknowledged freely that the picture had no solid evidence to support it, but it seems to make enough sense to be worth a some further study.

The majority of the recommendations relate to the microfriction work, either in terms of further apparatus or technique development, putative results or hypotheses, or new materials or situations which should be considered.

Contact measurement during motion. Contact measurements were made statically in this work. It would be interesting to see whether relative motion between the nonwoven and the substrate caused any changes to the observed results.

Contact measurement against other materials. Although theoretical results gave emphatic approval to the substitution of glass for skin or Lorica Soft, it would be comforting to obtain experimental verification of this. This may perhaps be achieved by casting high optical quality silicone rubber pads of various stiffnesses and examining to what extent the observed behaviour changed.

Where is skin along the smooth–villus-ridden spectrum? The interpretation of contact results depends upon how accurately skin may be assumed to be "flat" on the scale of the fibres. This is not clear at present, and could do with clarifying.

Can low magnification microscopy be improved? The results from the low magnification microscopy work conducted simultaneously with the friction measurements were disappointingly unclear. This is probably principally due to lighting conditions, so further work into somehow enabling transmission microscopy, or perhaps illuminating the samples from the side would likely substantially improve contrast.

Greater focus on static friction. The main focus of this work has been dynamic friction. In consequence, experimental scatter on static friction results has not received much attention in the development of the equipment and procedures described herein, so such scatter is substantially larger than for dynamic friction. It would be helpful to address this.

Can the rough / smooth population hypothesis be proven? As a result of the data it has been hypothesised that there are two populations of contacts at the nonwoven-Lorica Soft interface, one interacting via smooth adhesion, the other via rough adhesion. This should be investigated further with experiments more pointedly targeted at adhesion, though it is not immediately clear how.

Can lower loads be accessed? It would be helpful from the point of view of clarifying linearity of friction with load to be able to access lower contact loads than has been possible in this work to date. The principal problem has been the weight of the slider, so somehow relieving this without also coupling it to the environment would be a promising approach.

Experiments must be done on skin. All of the friction and low magnification microscopy work *must* be repeated on real skin samples.

Finally, some aspects of the geometric friction work would benefit from further consideration, mostly in terms of generalising existing solutions in some way.

Geometric solutions for a general linear elastic sheet. Current geometric friction solutions assume that Poisson's ratio is zero. It seems likely that by invoking some type of conservation of sheet flow it should be possible to find the flow lines for the sheet and thus produce a more general solution.

Perturbative solutions? It may be possible to use the entirely general equations of motion to construct perturbative solutions for rather more general cases around the simple solutions already obtained.

6.4 Project outputs

A fair number of identifiable outputs have issued from this project in its duration. These are listed here with brief explanations.

Two papers published. Two papers on geometric friction have been written and published in the period of this project [107, 171]. The former covers work on prisms that was completed (but not written up) prior to this project. The latter is essentially a condensed version of chapter 5.

Three to four papers in preparation. A further paper on the experimental verification of the conical solutions in geometric friction is in active preparation. One or two (decision yet to be made) papers on the methods and illustrative results from the microfriction work have also been started, but are in an earlier stage of preparation. Finally, a review paper based on the literature review is in *very* early stages; a likely journal must be identified before much further work is invested.

Two conference presentations. The work in this thesis has been presented with varying slants at two different conferences ("Innovating for continence: the engineering challenge", Simon Foundation, Chicago, April 2009; "Incontinence: the engineering challenge", IMechE, London, December 2009).

Two lectures to the industrial sponsors. Results and application to industry have been presented to substantial audiences at SCA's headquarters in Gothenburg on two occasions in September 2009 and Ocober 2010.

Posters. Posters have been entered for both the Dept. Medical Physics & Bioengineering and the UCL Graduate School poster competitions on two successive years (2009, 2010), on the first occasion winning the departmental competition and running up in the Graduate School competition.

Lecture at a Medical Modelling Group colloquium. A "virtual group" of researchers with an interest in mathematical modelling of the body exists within UCL. Upon invitation, a presentation of the geometric friction work was given to them in May 2009.

In addition to these outputs on the topic of this work, during the same period several other outputs with different foci have been made. Most have related to the study of water vapour flux from the skin, and on this theme one paper is in preparation, another awaiting submission, and a conference

presentation has been given. In other veins, work done some years ago has been incorporated into a recently published book chapter [172], and a poster on *in vivo* friction measurement techniques was given at a conference.

Appendix A

Experimental protocol submitted for ethics committee approval

It is a statutory requirement that all research that involves human tissue must be approved by the relevant Research Ethics Committee (*REC*). In accordance with this, a successful application to gather and experiment on breast skin was made to the Hammersmith and Queen Charlotte's REC which involved a substantial form and supporting paperwork. Much of the paperwork relates to the researchers, and the form is somewhat ponderous, but the protocol for the research provides a good summary of it. The protocol is thus reproduced verbatim on the following pages.

As noted in the body of this thesis, the protocol was assembled before all of the experimental methods were finalised. Because of this, some of the details of the experimental methods given here are different from those presented in chapter 4. Where there is a difference, the version in the thesis body is correct. Successful applications for permission to modify the protocol were made as necessary.

Protocol for a study of friction between human skin and nonwoven fabrics

Alan Cottenden[1], David Cottenden[1], James Malone-Lee[2], Jayant Vaidya[2], and Alan Wilson[2]

[1]Department of Medical Physics & Bioengineering, University College London, UK
[2]Department of Medicine, University College London, UK

April 29, 2009, Version 2.1

Full title of study An experimental study of the friction between excised, healthy, blemish-free human skin and nonwoven coverstock fabrics, preparatory to theoretical modelling of this interaction.

Short title A study of friction between human skin and nonwoven fabrics

Chief investigator Dr. Alan Cottenden

Co-investigators Mr. David Cottenden, Prof. James Malone-Lee, Mr. Jayant Vaidya, Mr. Alan Wilson

Sponsor University College London

Abstract

Wearers of incontinence pads and sanitary towels frequently experience skin abrasion due to friction. The Continence and Skin Technology Group has worked for some years to develop techniques for measuring this friction *in vivo*. In order to deepen our understanding of how this friction works, we now need to conduct a study on excised skin.

The study will involve taking residual skin from routine mastectomy operations and performing microscopy and some mechanical tests on it. There will be no interaction between the investigators and the participants; all interaction will be via the participants' surgeons, who will make the initial approach to their patients, and obtain informed consent.

Contents

1 Introduction

The work described in this document follows a series of *in vivo* experimental studies of friction between skin and nonwoven coverstock fabrics (similar to teabag material, and commonly used as topsheets in incontinence pads and feminine hygiene products) which have provided the immediate motivation for this study (§1.1). The eventual aim of the project of which this study forms a part is to develop a mathematical model that can predict (at least semi-quantitatively) the friction between a particular person's skin and a certain nonwoven fabric on the basis of their material properties.

The procedures proposed (§2.3.1 and §2.3.2) have been trialled as far as possible using an unverified skin surrogate (§1.2), and so it has been established that it is very likely that the study described here will meet its stated objectives (§1.3).

1.1 Background

Three million people in the UK are incontinent of urine, and the prevalence is anticipated to increase further as the population ages [1]. Whilst many sufferers can be at least partially cured, the significant minority who cannot be fully cured require products to manage their condition. The most common product type is absorbent pads. When pad materials and skin are wet the coefficient of friction between the wearer and their pad increases [2], increasing the vulnerability of the skin to abrasion damage [3].

An improved understanding of the mechanisms of friction between skin and typical nonwoven pad coverstocks is needed in order to design products that are less damaging to the skin.

The Continence and Skin Technology Group (*CSTG*) have been researching friction between human skin and nonwoven fabrics (such as those commonly used in incontinence pads and other hygiene products) for a number of years. In the course of this research we have developed and

published methods for repeatably measuring this friction, and using these methods have discovered that under the same nominal conditions the friction between a given fabric and equivalent sites on different people can be quite different [4]. Further, a set of subjects ordered by increasing friction against fabric A will not generally be in the same order for fabric B. This represents a significant advance in the study of the skin / nonwoven system.

We now wish to understand why this is, and to model it mathematically in terms of the material properties of skin and nonwovens, and so in the long term to understand how to design fabrics that are kinder to the skin. This requires that we gain a microscopic understanding of the interface between the two surfaces and the nature of sliding. This is not possible using *in vivo* skin (as in previous work) due to subject movement and the requirements of microscopy: excised skin is needed for the research to progress.

1.2 Preliminary experiments

In preparation for the acquisition of human skin, experimental methodologies for investigating the interface between nonwovens and thin ($\sim$ 1 mm) silicone rubber have been preliminarily developed. These have included methods for (a) examining the nonwoven-silicone interface under a microscope; and (b) determining the force required to drive the interface at a constant speed, whilst simultaneously observing the interface under a microscope. It is hoped that as silicone rubber has many comparable mechanical properties to skin its behaviour will be similar enough that experiments developed using silicone will be readily adaptable to use skin.

The experiments are described in detail in §2.3.1 and §2.3.2.

1.3 Aims and objectives

The role of this study is to elucidate the mechanism by which friction arises. To this end, the immediate objectives are as follows.

1. *To establish the nature of the skin-nonwoven interface across an anatomically representative pressure range.* This will require a small number (roughly five) of varied skin samples to be observed using the method described in §2.3.1.
2. *To establish the relationship between intersurface intimate contact and friction across the speed and pressure ranges specified.* This constitutes the most substantial and quantitative objective of this study, and will require ten or fifteen skin samples. The method for obtaining these data is described in §2.3.2, where the reason for the adequacy of a relatively small sample is further explained.

Experiments relating to each of these objectives must give an indication of the extent to which the mechanisms and rules identified are common to all people. Consequently, the individuals from whom the skin is taken should vary in ethnicity and age if possible so that any important features that are identified can be established as likely universal, or not. However, though this would be desirable, it is not of primary importance for the present project.

2 Methodology

This section describes all procedures and methods that will be employed in the execution of this work, including the identification of subjects, obtaining consent, and the sourcing of skin (§2.1);

the transport, storage, and disposal of skin (§2.2); and the experimental methodologies that will make use of the excised skin (§2.3).

The timing of different stages in the skin acquisition and storage, and the experiments are given in §2.5.

2.1 Identification of subjects, consent, and tissue sourcing

This study will involve working with two surgeons based at the Whittington Hospital: Mr Jayant Vaidya (JSV), and Mr Alan Wilson (AJW). Both surgeons routinely perform mastectomy operations, the skin from which is generally smooth and free from hair. This makes it well suited to our experiments: in this exploratory work it is more important that skin is uniform and simple than that it is from the diaper area.

Criteria for *inclusion* in this study are as follows.

- The patient is on the operating list of JSV or AJW for a mastectomy: less major breast surgery will not yield skin samples of sufficient size to be usable in the study's experiments. A minimum size for a sample to be used in this study is 2 cm $\times$ 2 cm.
- The patient is 18 years old or above.
- The patient is capable of understanding the information given them about the study, and is fit to give informed consent themselves.

It is possible that patients who have consented to participate in this study will not yield any suitable samples in consequence of the details of their surgery. This is unavoidable, and necessary so that normal surgical procedures are not interrupted.

Criteria for *exclusion* from this study are as follows:

- The patient is under 18 years old.
- The patient is incapable of understanding the information about the study or or giving informed consent themselves.

All interaction with the patient will be via JSV and AJW, from first identification of patients scheduled for mastectomy on the operating list, through initial approach and information, to consenting. The researchers will never meet any of the patients, and will have access to no personal information pertaining to them.

The procedure from first identification to the skin being handed to the researchers is as follows.

1. Operating lists are provisionally decided on a Monday morning. JSV and AJW identify any mastectomy patients, and contact David Cottenden (DJC) if any suitable patients are scheduled, for organisational purposes. The identity of any such patient is not passed on.
2. JSV and AJW conduct clinics on Monday and Wednesday mornings, during which they will see patients on their forthcoming lists. During these sessions they will make the initial approach to the patient, and provide them with all the information that they will need to make an informed decision as to whether or not to participate (see appendix A).
3. Surgery is conducted on Tuesday mornings (AJW), Tuesday afternoons (JSV, AJW), and Monday afternoons (JSV or AJW). Normal practice is for the patient to consent to the operation immediately before it; at the same time they will be asked whether they consent to take part in this study also (see appendix B). This will give each patient at least 24 hours (Monday clinic) or five days (Wednesday clinic) to consider the information given them.

4. JSV and AJW will contact DJC immediately prior to the relevant operation so that he can be waiting outside the theatre. When the operation is complete, skin from an unafffected part of the breast will be taken by the surgeon and given to DJC, who will begin experiments as soon a possible. The Whittington Hospital Pathology laboratory have consented to this sample bypassing them. All samples will be anonymous, though the hospital notes will carry the study number.

This will be continued until sufficient samples have been gathered: as discussed in §1.3, the number of samples needed is expected to be about 20, and will not exceed 30. No more precise figure is possible due to the exploratory nature of this work.

2.2 Transport, preparation, storage, and disposal of tissue

Our procedures for transporting, preparing, storing, and disposing of samples are as follows.

1. Having received the skin sample from JSV / AJW, DJC will transport it on foot to our laboratory on the Archway Campus, Highgate Hill in a sealed, refrigerated container. This is a five minute walk.
2. Having been given at least a day's warning by DJC, Mr Samuel Bishara (SB), a surgeon based in the same laboratory, will separate the dermis and epidermis from subcutaneous layers. This will be conducted in a laboratory which routinely handles tissue samples, and is clearly marked as such.
3. The skin will be kept in a clearly marked refrigerator whenever it is not being used. As freezing would alter the mechanical structure of the skin sample, all work upon a given sample will be undertaken within 24 hours of its removal, with all efforts made to complete work as fast as possible.
4. Upon the expiry of 24 hours, or the completion of experiments the sample will be disposed of using the clinical waste bins in the laboratory used by SB. These are emptied daily, and the contents incinerated according to the NHS system.

2.3 Experiment methodology

The experimental methodology presented here is the result of initial tests in which silicone rubber has been substituted for skin (§1.2). As such, the methods may well need some adjustment before they can be applied to skin: there is no way of avoiding this; the nature of this study is exploratory. It may also be necessary to undertake experiments similar in character to those described here, but which differ in details. It is also likely that some of the early samples will be rendered unusable whilst the techniques for mounting are perfected.

However, all reasonable measures have been taken to anticipate any additional problems that may arise.

The experimental methods required to achieve the objectives stated in §1.3 are detailed below.

2.3.1 Simple microscopy (objective 1)

The objective in this work is to establish the nature of the interface between skin and nonwoven, in particular where the points of intimate contact lie. This will be conducted for pressures in the range 100 Pa–100 kPa, or a subset of this range. This is achieved by simple optical microscopy of

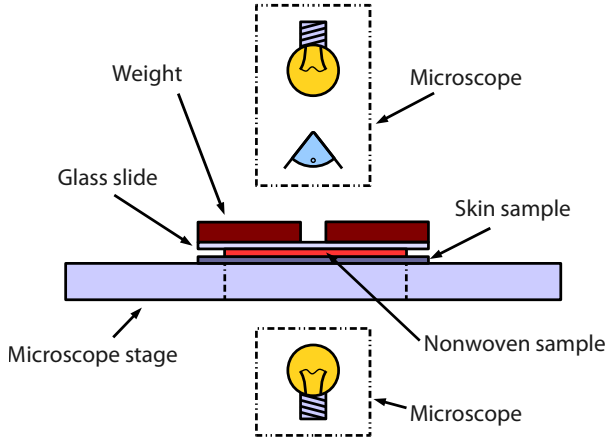

Figure 1: Simple optical microscopy should enable the nature of the interface between skin and nonwoven material to be established.

the nonwoven-skin interface, compressed by a weight above a glass slide, and viewed through the nonwoven (figure 1). This technique has been established for the silicone surrogate, and it seems unlikely that significant modification will be needed when skin is substituted.

It may be necessary to cast the sample in resin to facilitate microscopy, but it is not thought likely at this stage.

2.3.2 Simultaneous friction measurement and simple microscopy (objective 2)

This experiment is intended to supply detailed information on the relationship between intimate surface contact and friction. It is proposed following preliminary work using a silicone surrogate. If experimental results from §2.3.1 are entirely different from those corresponding to silicone then the details of this experiment may require reasonable modification; for example, it may be necessary to reorient the experiment. However, it will remain in essence the same, involving observing an interface during sliding, and will involve similar equipment and a similar method.

The method proposed is illustrated in figure 2. Two pieces of the skin sample will be fixed to either side of a carrier membrane or sheet, which will enable horizontal forces to be applied to the skin, and will keep the tensometer providing the force distant from the skin itself. This three layer composite will then be placed between two transparent anvil faces, in turn fixed into a cantilever device which will enable a wide range of pressures to be applied, and the skin / nonwoven interface to be observed through the anvil face. A tensometer will then be used to move the skin / carrier composite between the anvil faces at a constant velocity, and to measure the force required to do so. This will be repeated for pressures in the range 100 Pa–100 kPa, and velocities in the range $5\,\mu m \cdot s^{-1}$–$5\,mm \cdot s^{-1}$.

The information provided by this experiment should enable the key mechanisms for skin / nonwoven friction to be identified from qualitative observation of the interface during sliding, as it

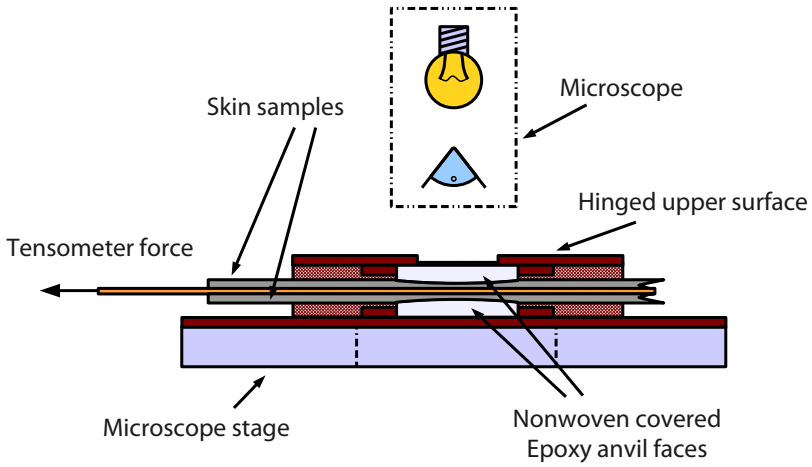

Figure 2: Skin samples are fixed to both sides of a carrier membrane and placed between the two faces of a transparent anvil, through which the interface can be observed. The carrier is then pulled at a constant speed by a tensometer, which measures the frictional force, enabling moment-by-moment comparisons of the frictional force and the microscopic behaviour of the skin / nonwoven interface.

already has for the silicone / nonwoven interface. Further, the digital micrograph videos recorded during sliding will also enable the contact area and geometry to be established instantaneously, and as a time series that can be linked to the force measurements. This can be expected to confirm identified mechanisms quantitatively, and to provide information as to how variation of friction between subjects is manifested at the microscopic level.

It is hopefully now clear why a small sample will be sufficient: the objective is to establish mechanisms and to gain some appreciation of their ubiquity; the objective is *not* to obtain a measure of the variation of any quantity in the population.

2.4 Health and safety

All tissue must be regarded as both a bacterial and viral hazard, so its safe handling is of the highest importance. The samples are covered by the Whttington Hospital's usual health and safety policy until the time that they are handed to DJC after surgery, and are covered by existing procedures when they have been deposited in a clinical waste bin. The period in between is covered here.

Elementary precautions The laboratory and fridge are marked as food and drink free. Gloves are worn at all times when handling specimens, removed, and deposited in clinical waste bins when finished with. All surfaces touched with gloves are considered contaminated. Hands are washed thoroughly with soap and water after working with specimens.

Cleaning All equipment and surfaces that come into contact with skin samples will be cleaned with alcohol spray afterwards, in accordance with normal procedures.

Equipment design The equipment that has been specially built for this study or its preliminaries will be adapted for suitability for use with skin samples. For example, where wooden surfaces are used they will be thoroughly varnished so as to render cleaning with alcohol effective.

Appropriate training and experience Procedures which incur a heightened risk are carried out by people fitted by training to do them. The principal example in this study is deferring to SB and his surgical training for the preparation of skin.

No other significant health and safety issues are raised by this study.

2.5 Projected timing

The purposes of this section are to clarify the rather complex train of events which follows the surgeons' receipt of their operating lists, and to give an approximate guide to the start and end dates of the work.

The sequence and timing of events following the surgeons' receipt of a week's operating list early on Monday is laid out in table 1. It is important to note that in all cases the patient will have at least 24 hours to consider whether or not they wish to take part, and in most cases several days. The relatively small number of mastectomies on any given list means that most of sessions during which the surgeons operate will not result in any skin, and so no action will be needed. For this reason, it will be possible for one person (DJC) to conduct all of the experiments.

As stated in §2.2, no samples will be retained beyond 24 hours after their removal; there are therefore no issues pertaining to tissue storage.

Mr Jayant Vaidya estimates that he and Mr Alan Wilson perform a total of three or four mastectomies per month, so it is to be expected that 20 samples will take in the region of five to ten months, depending upon the uptake rate. The PhD project that this work forms part of currently has well in excess of a year to run, so it is very likely that the study will be completed in good time for the end of the project.

3 Ethics

This study involves very little interaction with the participants that would not otherwise take place, and none on the part of the investigators. All samples and the data generated from them are anonymised prior to supply, with no links remaining to the participant other than the recond of the study number in the hospital notes. Samples will not be retained for substantial periods of time; all will have been destroyed by the end of the study; indeed, they will not be kept beyond the period that experiments take, which will be no more than 24 hours (§2.5). Samples will be obtained from residual material from normal, scheduled operations that would be undertaken without reference to this study; no additional procedures or alterations to existing ones are required. The skin would otherwise be disposed of by the Whittington Hospital.

In consequence of this, the primary ethical requirement is to obtain informed consent from participants. As described in §2.1, this will be managed by the prospective participant's surgeon using materials prepared by us (see appendices A and B). At least 24 hours will be given to the prospective participants in which to consider the information, before they are given the opportunity to take part or not when consent is sought for their surgery (§2.1); consent forms for this study will be kept with the patients' notes.

	Monday	Tuesday	Wednesday	Thursday	Friday
< 09:30	JSV, AJW receive operating list	—	—	—	—
AM	JSV, AJW clinic: initial approach made and information given	AJW surgery	JSV, AJW clinic: initial approach made and information given DJC completes experiments and disposes of skin SB prepares skin; DJC experiments	—	—
PM	—	JSV, AJW surgery SB prepares skin; DJC experiments	DJC completes experiments and disposes of skin	—	—
AM	—	AJW surgery SB prepares skin; DJC experiments	DJC completes experiments and disposes of skin SB prepares skin; DJC experiments	—	—
PM	JSV or AJW surgery	DJC completes experiments and disposes of skin SB prepares skin; DJC experiments JSV, AJW surgery	DJC completes experiments and disposes of skin	—	—

Table 1: A guide to the timing of the study, taking the surgeons' receipt of an operating list as the starting point. As explained in §2.1, patients on the operating list received on a Monday are seen in clinic on either Monday or Wednesday AM, when JSV or AJW will introduce the study to them and provide information. Patients at the Monday AM clinic will come back in for surgery on either Tuesday AM or later; patients at the Wednesday clinic will come back for the following Monday PM, or later: in either case they will have at least 24 hours to consider the information. For each of the possible surgery slots, the timing of sample preparation and experiments is shown in the same colour; the low frequency of mastectomies makes it unlikely that the substantial overlap of tasks relating to each possible surgery slot will be a problem.

Though the samples will be anonymised, they will be kept in a keypad secured laboratory. The data obtained by experiment will be entirely untraceable to the participant, but will be kept on password secured computers; our practice with experimental data of this type is to keep them indefinitely. Samples will be coded with a single number, and linked to the gender, ethnicity, and age of the participant, as well as a general description of other skin conditions and medical interventions which may significantly alter the skin.

4 Expertise

Dr Alan Cottenden is a Medical Physicist with 25 years' experience working on incontinence technology. He has managed, directed, or participated in around 25 clinical trials of incontinence products and clinical studies involving *in vivo* measurements on skin.

David Cottenden is a PhD student in the Continence and Skin Technology Group, a joint venture of the departments of Medical Physics and Medicine. His previous training is in physics and mathematics. His direct supervisor is Alan Cottenden.

Prof. James Malone-Lee is Professor of Medicine at University College London, and has been working on incontinence for about 25 years. In this time he has overseen 15 clinical trials, and has considerable experience in this respect. He is head of the centre within which this work will be undertaken.

Mr Jayant Vaidya is a Fellow of the Royal College of Surgeons, and is presently a Consultant Surgeon and Senior Lecturer at UCL, based in the Whittington Hospital. He has recently taken up this post, having previously practised in the University of Dundee for five years.

Mr Alan Wilson is also a Fellow of the Royal College of Surgeons, and is a Senior Consultant Surgeon based at the Whittington Hospital.

Mr Samuel Bishara is a Member of the Royal College of Surgeons, and works with Prof. James Malone-Lee in his research group. He has worked on a number of clinical trials in this context.

Appendix A Participant information sheet

As mentioned in §2.1, after the surgeon has informally assessed a prospective participant for suitability, they will be given the relevant information about this study in order that they can make an informed choice as to whether or not to take part. The information sheet is attached at reduced scale to make the layout explicit; it will be issued to prospective participants at full A4 scale.

UCL Department of Medical Physics and Bioengineering
Continence & Skin Technology Group

Archway Campus
Clerkenwell Building
Highgate Hill
London N19 5LW
England

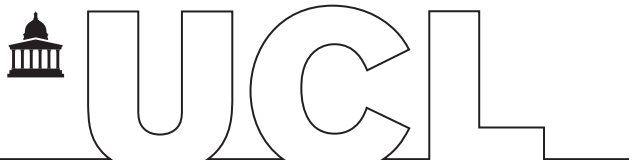

University College London Continence & Skin Technology Group study into friction between excised human skin and nonwoven fabrics

Prospective participant information sheet

(prepared June 15, 2009, Version 2.2)

Rubbing between skin and fabric can cause irritation, and in some cases cause sores to develop. This causes significant discomfort to a wide range of people of all ages. Hopefully, if the friction force which causes skin damage can be understood, better fabrics can be designed.

This research study, undertaken as part of a Ph.D project and funded by SCA Hygiene Products AB, will involve using small portions of skin removed as part of mastectomy operations at the Whittington Hospital in experiments to help us understand friction (the force which opposes movement) between skin and fabric. Please read this information carefully before deciding whether or not to donate your tissue.

What is the purpose of this study?

The purpose of this study is to find out how friction between skin and some fabrics works. These fabrics are similar to those used in the outer layers of nappies and sanitary towels, and so are often against the skin. At the moment, some users of these products suffer skin problems caused by rubbing against their nappy or towel. This is partly due to friction. If we can understand how this friction works then it will hopefully be possible for us to improve these products.

Why have I been chosen?

Some skin will be removed as part of your mastectomy. This skin would be suitable for the study, so a portion of it could be used.

What do I have to do?

If you take part in this study then you will not need to do anything differently, and your operation will proceed as normal. After your operation, rather than disposing of all the skin that is removed, your surgeon will give some of it to us. We will conduct our experiments, and then dispose of it ourselves according to legal guidance on disposing of tissue samples that have been used for research. No extra skin will be removed. All skin removed during your operations would normally be disposed of by the hospital.

Do I have to take part?

No, you are under no obligation to take part. If you decide not to then your operation will go ahead as normal, and all skin that is removed will be disposed of within the hospital. Your treatment will be identical whether you take part or not.

What if I change my mind?

You are free to change you mind and withdraw from the study right up to your operation. If you do withdraw then your surgeon will not give us any skin that is removed.

What are the possible disadvantages or risks of taking part?

There are no risks to you from taking part, as no part of your treatment will change.

What are the possible benefits of taking part?

There are no direct benefits to you from taking part. Longer term, you or others may benefit from any improvements to fabrics that we are able to make as a result of this study.

What types of experiments will you be doing?

The experiments we will be doing will involve looking at skin and fabric under a microscope, and at the same time measuring the force that is needed to make skin and fabric slide over one another.

What will happen to the skin when the study is finished?

When the study is finished, all skin will be disposed of, using the same procedure that would have been used by the pathology laboratory in the hospital under strict guidelines.

What happens if something goes wrong?

This study has nothing to do with your operation itself, and your treatment will not be affected in any way by choosing to take part in this study, so nothing can go wrong because you took part in this study. This does not change any risks that are to do with the surgery itself.

Will my taking part in this study be kept confidential?

If you choose to take part in this study, your choice will be kept confidential. Very limited information about you will be passed from your surgeon to us, none of which would identify you. The data that we obtain from our experiments will not identify you in any way. No DNA, genetic material, or other identifying biological features will be extracted from any skin samples.

What will happen to the results of the study?

The results gathered from our experiments on skin will be used to help us understand how friction between skin and fabrics works. We hope to be able to use this understanding to make suggestions to manufacturers about how they should change the fabrics that they use in sanitary towels and nappies so that they are kinder to the skin. Results may be published, but the data that are published will be completely anonymous and untraceable.

Who is organising and funding the study?

This study is organised by research staff at University College London, and it is funded by SCA Hygiene Products AB and the Engineering and Physical Sciences Research Council.

Who has reviewed the study?

The study has been reviewed by the Hammersmith and Queen Charlotte's Research Ethics Committee.

What happens next?

You should think about whether you are happy to take part in this study. When you come back into hospital for your operation your surgeon will ask you if you are happy to take part in this study. If you are, then you will be asked to sign a consent form. You will receive a copy, and the original will be kept by the hospital in your medical notes.

Further information

If you would like to discuss any aspect of this study, please contact your surgeon, who will either provide the information that you need themselves, or forward your question to us. We will provide the information that you want to your surgeon, who will pass it onto you.

Thank you very much for your help.

Appendix B Participant consent form

Following a period for a prospective participant to consider the information sheet that they have been given, they will be asked whether they wish to take part in the study (§2.1). If they do, they will be asked to sign a consent form. The consent form is attached at reduced scale to make the layout explicit; it will be issued to prospective participants at full A4 scale.

UCL Department of Medical Physics and Bioengineering
Continence & Skin Technology Group

Archway Campus
Clerkenwell Building
Highgate Hill
London N19 5LW
England

University College London Continence & Skin Technology Group study into friction between excised human skin and nonwoven fabrics

Participant consent form - confidential

(prepared March 24, 2010, Version 2.1)

Investigator's name: Alan Cottenden

Investigator's address: Continence & Skin Technology Group, Third Floor, Clerkenwell Building, Highgate Hill, London N19 5LW

To be completed by the participant:

1. I have read the information sheet about the study that was given to me. YES / NO
2. I have been given the opportunity to ask questions and discuss the study. YES / NO
3. I have been given enough information about the study and all my questions have been given a satisfactory answer. YES / NO

   Member of staff providing information: _____
   Position: _____
4. I am aware of the nature of the study and that by signing this document I agree to be entered into the study. YES / NO
5. I agree that the a sample of tissue (that would be otherwise discarded after my operation) can be used as described in the information sheet. YES / NO
6. I agree to take part in the study. YES / NO

Participant:	**Person taking consent:**
Signature: _____	Signature: _____
Print name: _____	Print name: _____
Date: _____	Position: _____
	Date: _____

When complete: one copy for the participant; original to be kept in medical notes.

Appendix C Sample information form

After surgery, DJC will collect the skin sample, labelling the box with the form attached here so ensure that the information pertaining to the sample remains with it, and no confusion can arise. The information will be transferred to computer subsequently. No sensitive personal information is written on the form, and the subject could not be identified from it.

Information sheet for subject #_____

Collection date: _____

Collection time: _____

Limited patient information

Age: _____

Ethnicity: _____

Gender: FEMALE / MALE

Previous relevant medical interventions: _____
_____
_____

Concurrent skin conditions: _____
_____
_____

Comments: _____
_____
_____

References

[1] Good practice in continence services. Tech. Rep., Department of Health, UK, London (2000).

[2] Hong, K. H., Kim, S. C., Kang, T. J. & Oh, K. W. Effect of abrasion and absorbed water on the handle of nonwovens. *Textile Res. J.* **75**, 544–550 (2005).

[3] Zimmerer, R. E., Lawson, K. D. & Calvert, C. J. The effects of wearing diapers on skin. *Pediatric Dermatology* **3**, 95–101 (1986).

[4] Cottenden, A. M., Wong, W. K. R., Cottenden, D. J. & Farbrot, A. Development and validation of a new method for measuring friction between skin and nonwoven materials. *J. Eng. Med.* **222**, 791–803 (2008).

Appendix B

Description and characterisation of force / low magnification microscopy apparatus

The apparatus used to observe the nonwoven-skin (surrogate) interface during sliding and simultaneously measure friction was described only briefly in the body of this thesis, and no characterisation or validation were provided there. Since the latter is vital for the experiments described to be reproduced and the former is the key to interpretation of the data they are given in detail in this appendix. The apparatus is described in detail (§B.1) along with explanations of the key design decisions, followed by an account of experiments performed to characterise the mechanical measurements and noise (§B.2).

B.1 Description of apparatus and justification of design

The apparatus that was designed, built, and used to gather the friction and low magnification microscopy data described in §4.1.1 is shown in figure B.1. It consists of a slider with either side faced with skin (surrogate) that is pulled at a constant speed by a tensometer (MTT170, Diastron, Andover, UK) between two transparent "anvils", each of which is faced with nonwoven. The anvils are held in place by two perspex surfaces, the lower of which is clamped to a microscope stage (DMLM with DFC295 camera, Leica Microsystems (UK) Ltd, Milton Keynes, UK), and the upper of which is laterally restrained by four smooth guiding rods attached to the lower. The upper surface is loaded with deadweights and the microscope stage translated such that the upper nonwoven-skin (surrogate) interface can be observed through the upper anvil. In order to enable lower pressures to be accessed a spring is fitted around each of the guiding rods to bear the weight of the upper surface (LP 012BC 06 ($k = 0.028\,N \cdot mm^{-1}$, $l_0 = 31.75\,mm$), Lee Spring, Wokingham, UK); the weight of the upper surface is "trimmed" for each experiment so that the unladen upper surface *just* contacts the slider. The springs were selected for their precision and extremely low stiffness: an additional compression of 1 mm results in an additional force of only 0.112 N, equivalent to a load of about 11 g; such a displacement is easily observed and thus is compensated for.

The key features of the apparatus are (1) the double interface; (2) the shaped, transparent anvils; (3) the smooth guides for the upper surface; (4) and the laterally stiff, reversible slider assembly. These are described in detail in the following sections.

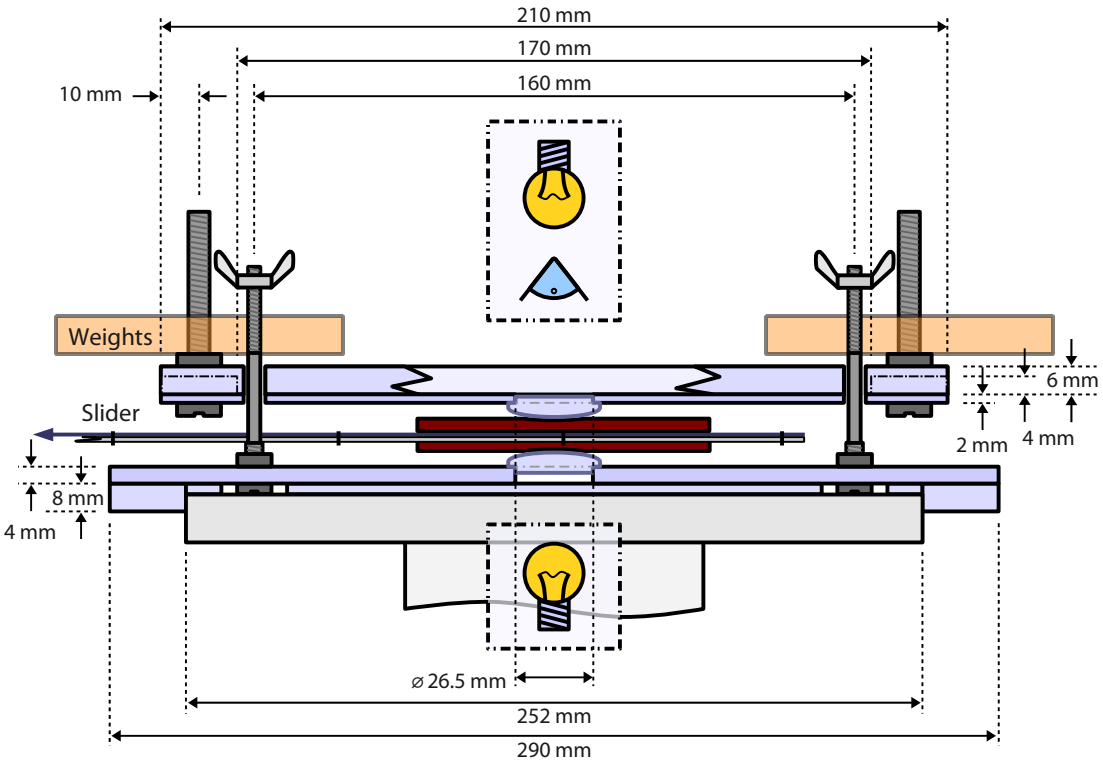

Figure B.1: The friction and microscopy apparatus. It is built entirely of perspex sheet for ease of cleaning, and shown sitting on a microscope stage, as intended. The design has two lines of symmetry, so missing dimensions can be inferred. Bistable props that clip onto the upper surface to support it when no slider is present have been omitted for clarity, as have large clips that retain the apparatus on the microscope stage. The guide rods for the upper surface are described elsewhere; the weight bolts are M5×60 mm. Part of one of the stiffening bars on the upper surface has been removed for clarity. Both upper and lower surfaces are 150 mm from front to back; guide rods pairs are 110 mm from centre to centre; and the longitudinal stiffening bars on the upper surface are 20 mm wide. The springs that bear the weight of the upper surface are not shown for the sake of visual clarity.

B.1.1 Double interface

The "double interface" design is motivated by early exploratory experiments on a basic, single interface "classic" slider design which showed that significant artefacts in the force against displacement data were attributable to moments generated by the non-colinearity of the friction and tensometer driving forces. Two key problems arose: a systematic decrease of friction force with distance of the order of 10 %; and a marked tendency for the slider to tip over. Analysis of the system implied that the first effect was due to limited torsional stiffness in the rig, and thus could in principle be ameliorated, though in consideration of the "soft" materials under investigation it could not be eliminated. However, the tipping was still apparent when the point of action of the tensometer force was lowered to within a few millimetres of the contact; no further lowering was possible.

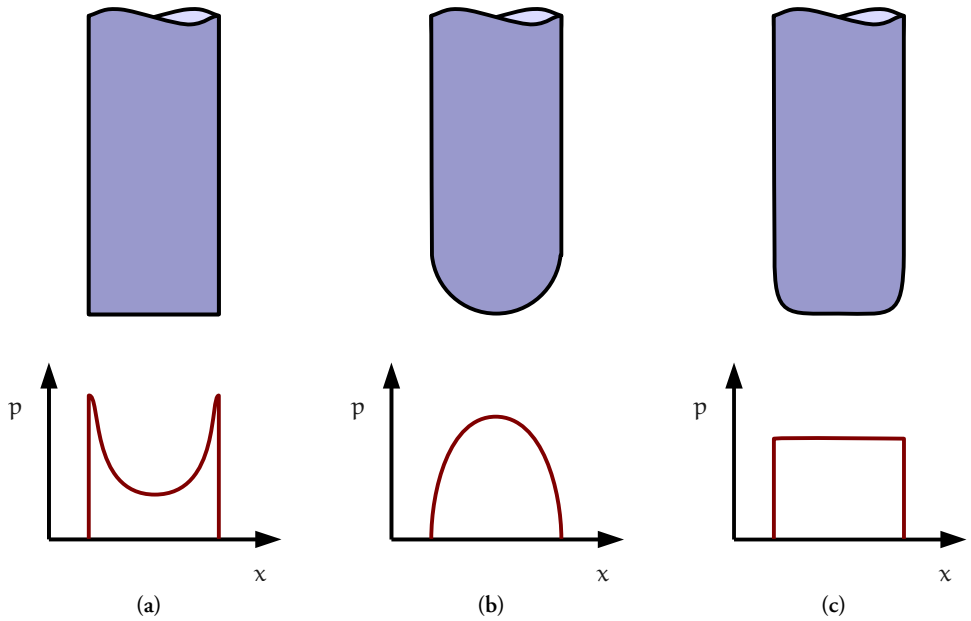

Figure B.2: Pressure distributions below a "punch" are substantially determined by its geometry. (a) A square punch has a low pressure in the middle and a high pressure at the periphery. (b) The classic Hertz solution for a spherical punch has a pressure that is high in the middle and low at the edges. (c) Somewhere between the two there will exist a shape that gives a uniform pressure under normal loading.

A double interface intrinsically avoids large net moments by having two equivalent interfaces contributing opposite and nearly equal moments. The only inequality is due to the weight of the slider adding to the normal force at the lower interface; this can be minimised by careful slider design.

B.1.2 Shaped, transparent anvils

If the force against displacement data are to be maximally useful it is important to make all regions of the nonwoven-skin (surrogate) contact as close to equivalent as possible. As the distribution of stresses below a "punch" pressed into an elastic surface is principally determined by the shape of the punch, the shape of the anvils in the friction apparatus must be carefully considered.

It is not universally appreciated that the pressure distribution below a flat punch pressed into a uniform surface is itself *not* uniform (figure B.2). For a material with a non-zero shear modulus a discontinuity in the shape of an impressed punch causes (in an idealised material) a divergence in the local normal stress [173]. Hertz's famous solution for the normal stress distribution below a sphere shows that, whereas the square punch is in some sense "too square" (with divergent normal stress at the periphery of contact) a sphere is "not square enough" (with normal stress maximal in the centre of contact). Clearly a shape somewhere between the two will result in a uniform pressure.

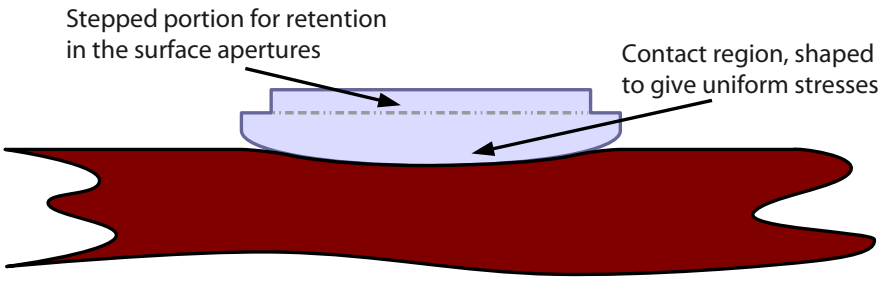

Figure B.3: The key features of an anvil. The lower portion is shaped so as to provide the necessary uniform stresses, and the upper to interface with the rest of the apparatus.

An additional complexity is caused by lateral friction forces. Bousinesq's exact solution for surface shape as a function of applied forces [174] for small displacements of a linear elastic material makes it clear that this shape is influenced by *all* components of surface force. It is therefore not valid to assume that the shape which leads to uniform pressure under normal loading will also work when a tangential force component is added. Further, even if the contact area remains the same, increasing any or all of the forces alters the required shape, though in some cases it is purely by a scaling factor.

Substantial work has been done to ensure that the shapes used are correct, which may be found in appendix C, along with a description of the method used to produce them. A diagram showing the key features is given in figure B.3.

B.1.3 Smooth guide rods

Following §B.1.2 it is clear that the anvil faces must be parallel[1] if the required uniformity of stresses are to be attained. This is most readily achieved by allowing the upper surface to determine its own orientation to a fair extent, thus relaxing the otherwise exacting tolerance that would be required of the anvils; provided an anvil's face and the plane of the stepped portion which locates it in its aperture match to within a degree or so, any mismatch should readily be accommodated by the upper surface.

The apparatus described here is accordingly intended to constrain the lateral movement of the upper surface and anvil, but not to place any limits on its vertical movement, and only lightly to constrain its pitch and roll orientations. Since this must remain the case when substantial lateral forces are acting the four vertical rods that provide the lateral constraint must be smooth, so avoiding any reduction in apparent load applied to the skin (surrogate) when the upper surface is pressed against the rods. Additionally, if the rods are corrugated on a millimetre scale (for example, retaining any of the thread from the bolts from which they were machined—figure B.5) the upper surface "locks in" to one of the corrugations on each bolt, but *not always the same ones*. This results in several similar but distinct families of curves (variation between families substantially exceeds variation within each) appearing in a series of force against displacement repeats (figure B.4). This is clearly unacceptable and indicative of a problem, so care has been taken to ensure that the rods are smooth.

[1] Or rather, be in the same relative orientations.

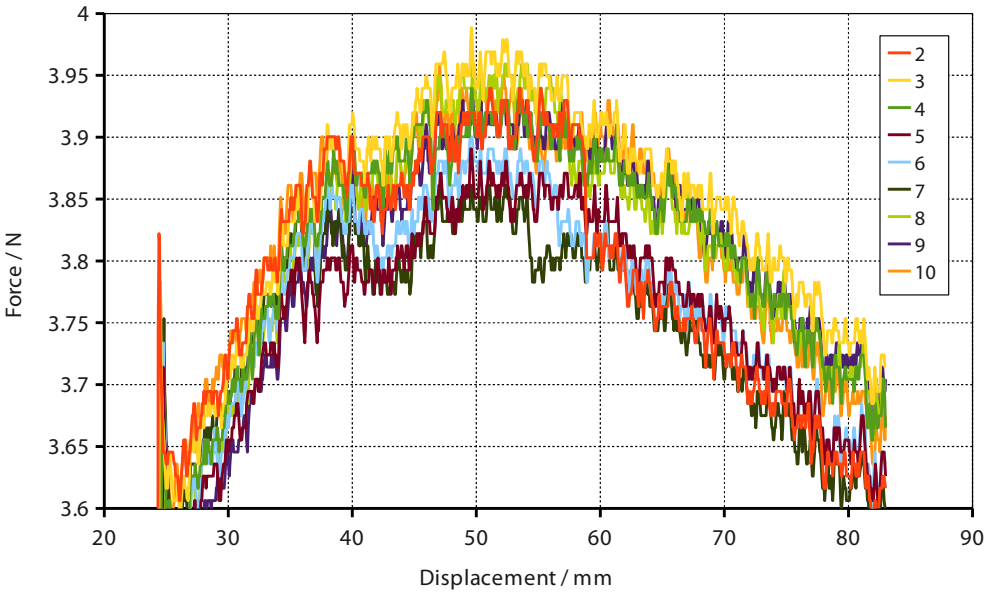

Figure B.4: Force against displacement data gathered using a version of the apparatus where the rods were fully threaded (~5.7 N load; 5 mm · s^{-1}; NW1 against Lorica Soft). The curves group fairly neatly into two groups: repeats 5, 6, and 7; and repeats 3, 4, 8, 9, and 10; repeat 2 jumps from one family to the other part way through the experiment. These distinct families vanish when the threads are removed, which along with the clearly quantised nature and the possibility (though low probability) of transition between families implicates the thread. The gross shape is characteristic of the interface and is not relevant here. The first repeat is an outlier and so is not included; first repeats are commonly outliers.

In addition to smoothness over the range along which the upper surface makes contact, the rods are attached to the lower surface, and mount a wing nut on their upper extremity to prevent the upper surface accidentally being dislodged during use. In view of these requirements the simplest way to produce the rods is to begin with an M4 bolt and machine it to specifications. The original and final bolts are illustrated in figure B.5.

B.1.4 Slider assembly

The fundamental job of the slider assembly is to support the skin (surrogate) surfaces and link them to the tensometer. It must make it possible to conduct repeat experiments and be sure that the region of skin (surrogate) tested remains the same. It must also avoid altering the pressure distribution between the skin (surrogate) and the anvils, and must not add any significant additional forces due, for example, to sagging under its own weight.

In view of these requirements, the design described in the main body of this thesis has been adopted. The three part design (in which one part remains fixed to the tensometer crosshead at all times) ensures that the slider can be repeatably placed with respect to the tensometer, and means that the slider portion (which is disposable when used with skin) can be simple and quick to make.

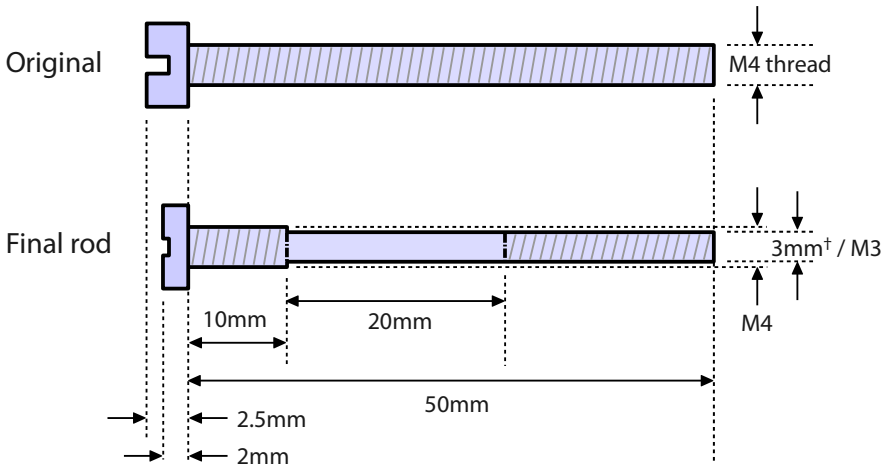

Figure B.5: The smooth rods are machined from 50 mm M4 bolts. The 10 mm closest to the head is left unchanged; the next 20 mm are turned to a smooth 3 mm; the final 20 mm have an M3 thread cut on. †Although the ISO standard dictates that an M4 thread should not cut down to a diameter of 3 mm, mass produced bolts usually cut beyond this, so the central portion has a diameter slightly less than 3 mm.

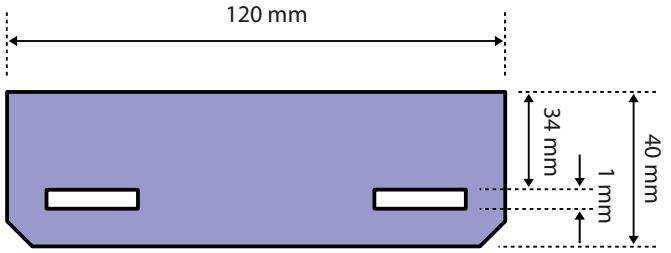

Figure B.6: The tensometer connector is a simple piece designed to remain in the tensometer jaws and facilitate the quick, easy, and repeatable attachment and removal of the linkage via its lugs.

The details of the portions are as follows.

Tensometer connector (figure B.6) This part was designed to prevent the linkage from rotating about a vertical axis and so ensure that the same portion of the slider contacted the anvils in each successive run. This was achieved by simply spacing the connecting lugs widely. The orientation of the linkage is determined by the line of the (scored) bend in the linkage; the folded-back lugs simply maintain the bend so their position is not of first importance. The part is made from stiff 0.52 mm polyethylene sheet (RS Components Ltd, Corby, UK).

Linkage (figure B.7) The linkage maintains the lateral stiffness established by the tensometer connector, prevents sagging, and provides a connection between the slider and the tensometer that is stiff in tension. Tensile stiffness is achieved simply by cutting the linkage from the same polyethylene sheet as the tensometer connector, and using the same scored fold connection to join to the slider as is used between the tensometer connector and the linkage. Lateral stiffness is maintained by a pair

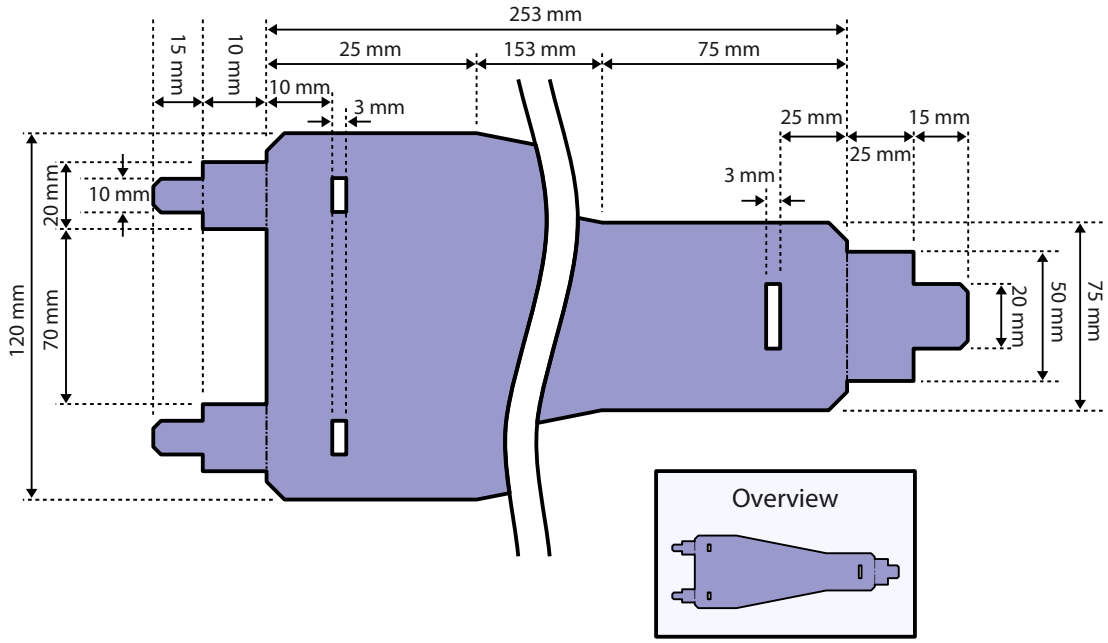

Figure B.7: The linkage is relatively complicated to enable other things to be simple. It is symmetric about an axis along its length. To make details visible it has been "cut" in the main diagram; the overview shows the true shape.

of aluminium bars (rectangular cross section, 2 mm × 6 mm) stapled along the linkage and slider and butted up to the tensometer crosshead; they can be removed to change the slider, but are a snug push fit.

Slider (figure B.8) Since many different sliders are required—and for skin samples they must be considered as disposable—the slider has been designed to be as simple and quick to make as possible. Its principal function is to hold the skin (surrogate) samples and prevent bending, and transmit the tensometer force without appreciable stretching. Sliders are printed onto 240 µm acetate sheet with a grid included to aid with positioning samples and determining the displacement ranges. Both skin and skin surrogates are mounted on 2 mm thick perspex which is then glued to the acetate slider; this increases bending stiffness considerably.

B.2 Characterisation of mechanical apparatus

All experimental equipment colours the data it provides in some way. This is unavoidable, but so long as the way in which the data are coloured and the relationship between the reported data and the "true" data (so far as these can be discerned) is known it need not be a serious problem. The objective of the experiments reported here was not to measure the characteristics of the interfaces tested, but rather to establish the repeatability of force data and to ascertain which (if any) of the

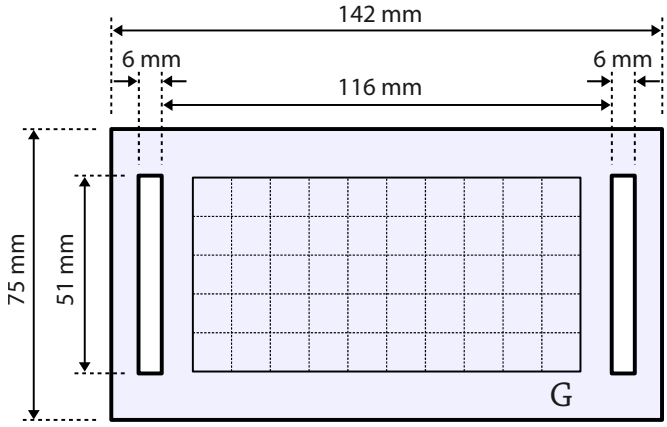

Figure B.8: Sliders are simply printed onto acetate and cut out. The "G" mark is to fix orientation: the symbol has no reflectional or rotational symmetry, and by convention the "positive" direction is taken to the left when the symbol is oriented. The slider is symmetric about its length and width axes.

features of the force against displacement graphs were due to the equipment, and which must be ascribed to the material interface.

Artefacts on the data can be divided into random errors ("noise") and systematic errors characteristic of the system. The extent of the former can be measured by simply running an experiment several times and considering the variation between repeats (§B.2.1); the latter is a more complicated matter. For this equipment systematic errors could be due to one or more of the surfaces and rods (§B.2.2); the anvils (§B.2.3); the weight of the slider (§B.2.4); or some other non-interfacial aspect of the slider (§B.2.5). These are considered sequentially.

All experiments made use of a variant of the standard pull method described in §4.4.3 which omitted any microscopy.

B.2.1 Random variation

Clearly a prerequisite of any experiment designed to measure random variation is that the underlying measured quantity is constant. Consequently, any "run in" for materials must be allowed for before taking the results used to assess variation. The materials used in this test were Lorica Soft (mounted on 2 mm perspex sheet—L6 slider) and NW6 on the μ anvils (§C.4); these choices are essentially arbitrary as the objective is to characterise equipment rather than materials.

Many instances of this experiment have been undertaken (it is incidental in essentially all subsequent tests), but only data from a single phase (five cycles) are included here (figure B.9). It is immediately apparent that the run-to-run variation is very small; numerically, the area between a curve composed of the maximum reading at any point and the equivalent minimum curve is 2.5 % of the area below the mean curve; that is the full scale variation is on average ± 1.25 %. In terms of practical application, this degree of random variation is significantly less than the amount by which the curves vary throughout the displacement. In consequence, the shape of the curve must be at-

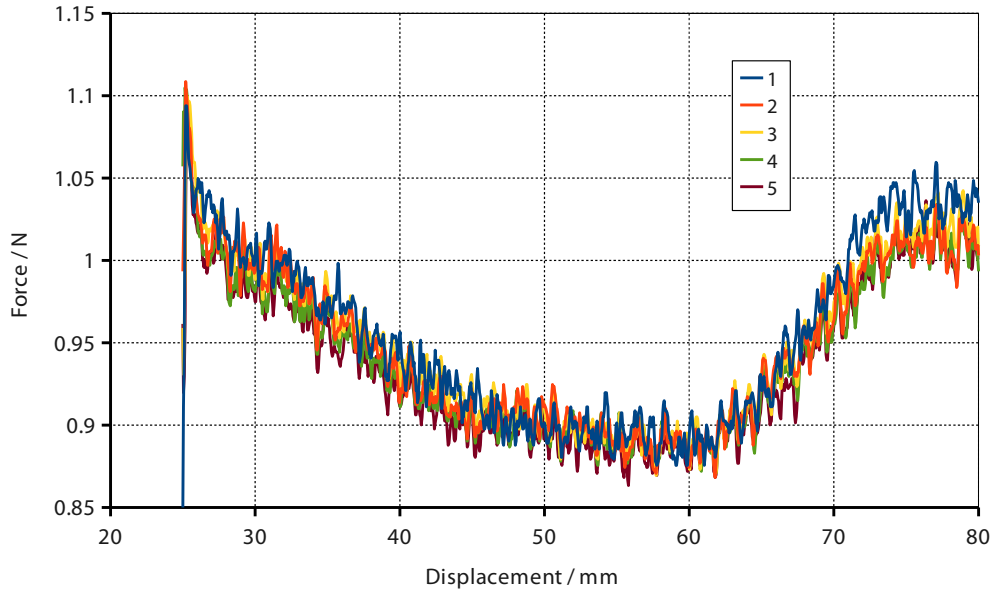

Figure B.9: A typical example of the extent of random variation during a phase of pulling experiments (2.55 N load; 0.5 mm · s^{-1}; NW6 against Lorica Soft L6). The total variation is substantially less than the signal variation. Note that the underlying friction will have changed slightly during his experiment, so the true extent of random variation will be a little less than it appears here. Also note the y axis scale does not start at zero.

tributed to some mixture of true interface properties and artefact introduced by the apparatus. The following experiments assess the contributions of each source to the observed curves.

B.2.2 Variation due to surfaces, rods, and disassembly

This test is based on running a three phase test: the first phase is "normal"; the second phase reverses the surface and rods whilst maintaining the orientation of the slider and anvils; and the third phase is a repeat of the first to assess the extent of material drift and the extent to which nominally resetting the original conditions reproduces the original results. All tests use a contact load of 260 g ⇔ 2.55 N ⇔ 5.9 kPa with the μ anvils (§C.4), and are pulled at 0.5 mm · s^{-1}. The materials used are Lorica Soft for the slider facing and NW6 for anvil covering.

If the surfaces and rods were introducing a signal into the results then reversing the arrangement would cause the signal to be reversed along the run; comparison of the phases 1 and 3 traces with the phase 2 traces would show a significant difference. In the case of no discernible difference above the random variation it would be reasonable to conclude that no important systematic error is introduced by the surface and rods. If there is close agreement between the traces from phases 1 and 3 then it is reasonable to conclude that material drift has not been significant, and also that when the equipment is disassembled and reassembled in the same configuration no important change is introduced.

This experiment has been completed with three sliders; the results are shown in figure B.10. The agreement between phases is very impressive: the areas between maximum and minimum curves as proportions of the areas under the mean curves are 2.3 %, 3.4 %, and 4.0 %, respectively.

More can be learned from these results than the simple fact of excellent agreement. First, observing that in all cases the results from the three phases progress slowly down the force axis, it is likely that much of the variation seen is in fact due to material wear; nonwovens wear continually, so this cannot be avoided. If this is indeed the case then the inter-curve areas would probably fall in all cases to less than 2 % of the area below the mean curve. This should be emphasised: the repeatability when everything is disassembled and put back together either way around is probably *less than* ± 1 *%*. This is unprecedented in "soft" friction work.

Second, the sliders move from fairly flat to fairly undulating through the series L4, L5, L6. The non-flatness of L6 provided an excellent test of the likely performance of the equipment when faced with skin, which is far less regular than Lorica Soft and much less easy to glue down flat.

The random variation is very small; the variation due to the surfaces and the rods is very small. It only remains to determine the effect of the anvils and non-interfacial aspects of the slider assembly.

B.2.3 Variation due to anvils

This issue is more complicated than variation due to surface and rods: the surfaces and rods ought not to make any difference irrespective of their configuration; the anvils clearly will make a difference to the result depending on their shape. As explained in §B.1.2 the anvils are designed to give uniform stresses over their surfaces, which is the distribution in which the macroscopic data can be most accurately applied to mesoscopic scales.

The shape of the anvils *does* impact the force data, and has been chosen to maximise their usefulness.

B.2.4 Systematic variation due to the weight of the slider

It has not been possible to design the equipment so that the weight of the slider does not act upon the lower anvil. In view of this, two measures have been necessary: to minimise the weight of the slider assembly; and to measure the load that it exerts upon the lower anvil at different phases of its travel. Weight *has* been minimised; the load exerted by the slider during sliding is reported here.

The load due to slider weight has been measured simply by securing an anvil to a balance and programming the tensometer to pull a slider over its usable length in 5 mm increments, with brief stops between each movement. The load was recorded before sliding and then during each stop, thus elucidating the relationship between load due to the slider and the distance slid. This procedure has been undertaken with both of the Lorica Soft sliders used in the experiments reported in §4.4; the results are shown in figure B.11. Three repeats were taken for each slider, with the aluminium bars slackened and repositioned between each run.

The results show clearly that there is no appreciable difference between the two (nominally identical) sliders: the straight line $\mathrm{P} = -1.35 \times 10^{-3}\mathrm{x} + 5.33 \times 10^{-1}$ is characteristic for both sliders, where P is measured in newtons and x in millimetres.

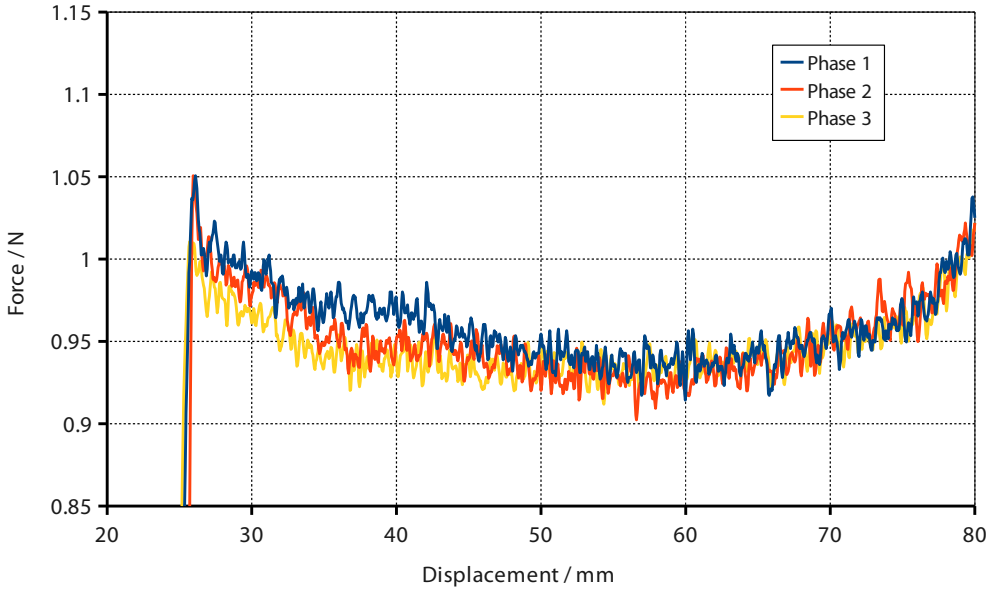

(a) Lorica Soft L4

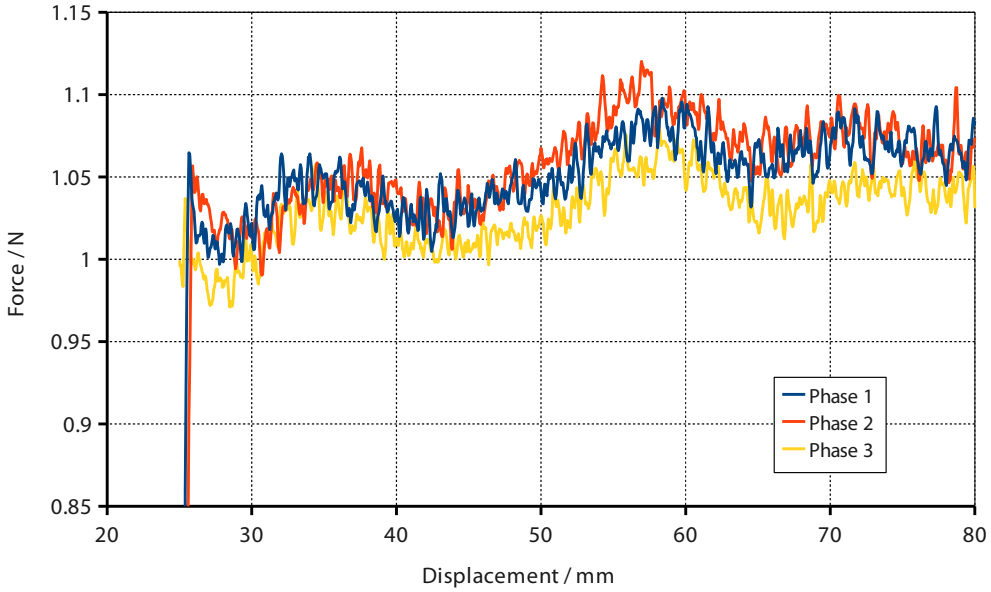

(b) Lorica Soft L5

Figure B.10: Comparisons of the mean curves from a three phase experiment in which the first and third phase are nominally identical and the second has the rods and surfaces reversed (2.55 N load; 0.5 mm · s^{-1}; NW6 sliding on Lorica Soft). Note the the y axis scale does not start at zero. *Continues…*

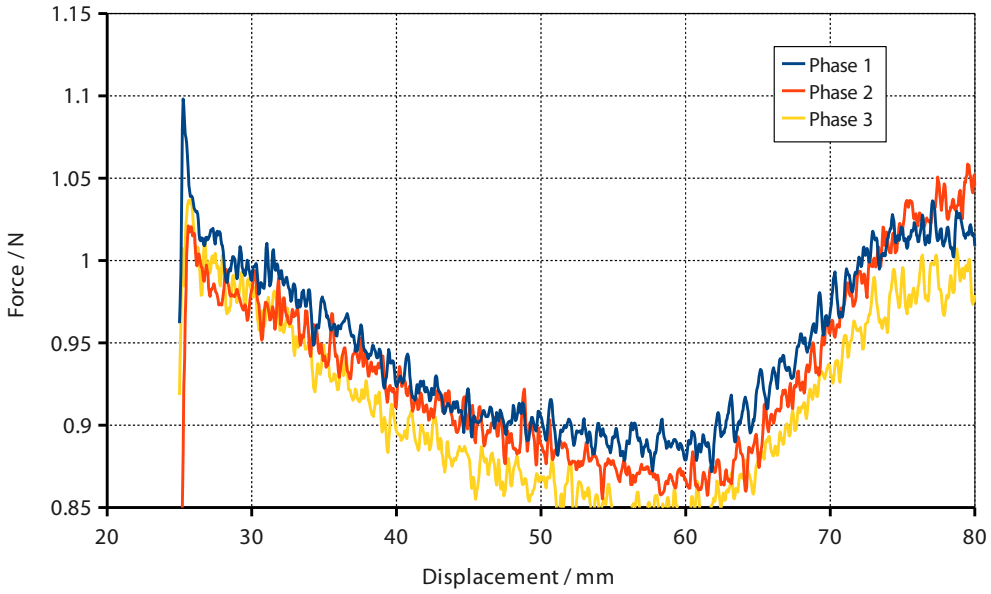

(c) Lorica Soft L6

Figure B.10: *...Continued.*

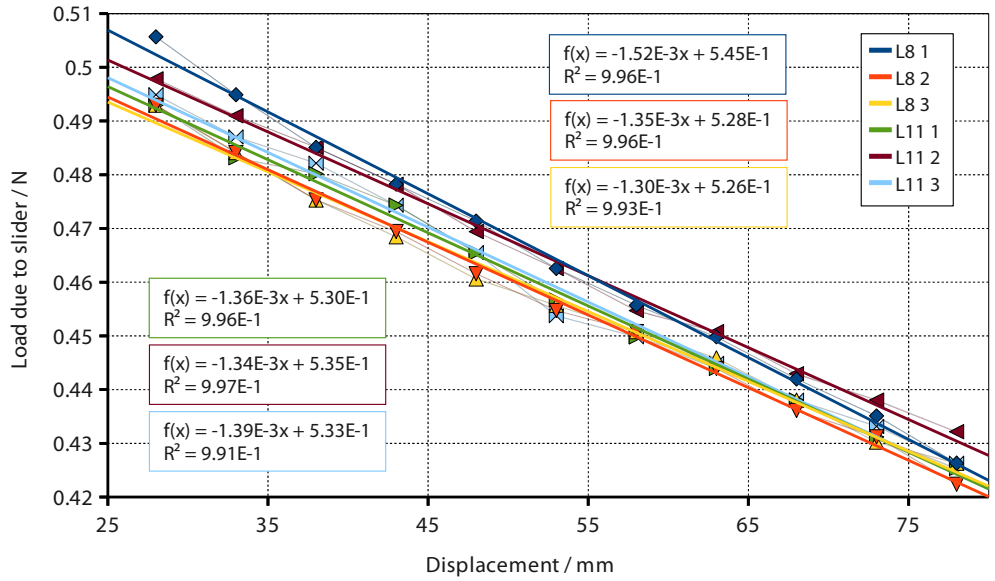

Figure B.11: Load due to the slider assembly (fitted with Lorica Soft sliders L8 and L11) as a function of displacement.

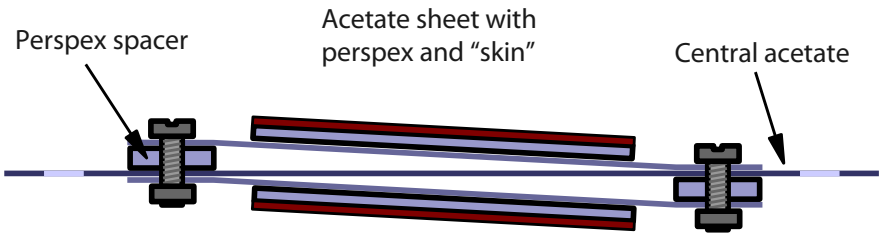

Figure B.12: The "tilting" slider used to assess the impact of non-parallel or non-horizontal slider faces. The spacers can be moved to either end, stacked, or removed entirely.

B.2.5 Variation due to the slider assembly

As the surfaces and rods make little difference to the data and the anvils have been designed to render them maximally interpretable, the only remaining source of systematic error is in the non-interfacial aspects of the slider assembly. Possible sources of error include co-linearity of the slider assembly with the direction of travel of the tensometer crosshead; sagging of the slider fore and aft of the anvil contacts; and variation of thickness of the sample along its length. The second has been designed against both with the aluminium bars, and by using perspex supports for the skin (surrogate). The remaining two possible effects have been explored experimentally, and are reported here.

With regards to co-linearity of the slider with the direction of travel, any fixed rotation around a vertical axis (yaw) is essentially unimportant so long as it is indeed fixed to high precision: the track taken by the anvils will be different from the case of perfect alignment, but the data will be perfectly valid for the *de facto* track. Imperfect orientation around a horizontal axis perpendicular to the direction of pull (pitch) and around a horizontal axis parallel to the direction of pull (roll) require further consideration as they are likely to alter force distributions, at least for large rotations. In fact, non-zero roll has already been considered: due to imperfect "right angles" and slightly non-flat materials used in construction of the equipment, the "reverse" experiments of §B.2.2 had approximately 5° roll compared to the "forward" experiments; figure B.10 shows no significant distinction between them. In terms of co-linearity, pitch alone remains to be considered.

Both variation due to slider pitch and due to variation of sample width have been accessed and assessed with the same experiment. It differs from the method described in §4.4.3 only in the nature of the slider: rather than simply glueing mounted Lorica Soft samples to the slider template, the samples were bolted on using nylon M3 bolts, thus making it possible for spacing shims to be inserted and removed as desired (figure B.12). By inserting shims at only one end experiments to assess the impact of non-flat sliders were possible; by inserting shims on opposite sides and ends a systematic pitch could be introduced whilst maintaining the slider thickness.

Experiments were run in the order shown in table B.1: missing phase numbers correspond to phases in which something went wrong, causing the phase to be abandoned. The results of these phases are shown in figure B.13, where each trace is the mean of all "clean" cycles in the corresponding phase. Phases 1–11 were completed in quick succession and internally agree well; the interval between phase 11 and phase 12 appears to have seen a degree of material drift, so phase 14 was

Phase number	Motivation	Front packing	Rear packing
1	Control	—	—
2	Impact of a downward slope?	upper 2 mm	—
3	Does the "side" of the slope matter?	lower 2 mm	—
4	Control	—	—
5	Impact of an upward slope?	—	upper 2 mm
6	As phase 3	—	lower 2 mm
10	If the slope doubles, does the effect?	upper 4 mm	—
11	Control	—	—
12	Control	—	—
14	Impact of constant thickness and tilt	upper 2 mm	lower 2 mm
15	Control	—	—

Table B.1: List of the phases during which the impact of no-uniform thickness and slider tilt were assessed. The phases above the line were completed in quick succession; an interval passed before those below the line were completed, again in quick succession.

bracketed by two "flat" phases to guard against any further drift.

These experiments can be interpreted as a combination of work done against / received from gravity—that is, the load is raised or lowered by any slope that is introduced, requiring or providing a force—and friction against the rods. The former effect can be readily predicted:

$$\Delta f = \frac{\Delta h}{\Delta l} m g \quad \Rightarrow \quad \begin{cases} \Delta f_{u,2} = \frac{2\,\mathrm{mm}}{80\,\mathrm{mm}} \times 0.260\,\mathrm{kg} \times 9.8\,\mathrm{N \cdot kg^{-1}} = 0.06\,\mathrm{N} & \text{(upper, 2 mm)} \\ \Delta f_{l,2} = \frac{2\,\mathrm{mm}}{80\,\mathrm{mm}} \times 0.315\,\mathrm{kg} \times 9.8\,\mathrm{N \cdot kg^{-1}} = 0.07\,\mathrm{N} & \text{(lower, 2 mm)} \\ \Delta f_{u,4} = \frac{4\,\mathrm{mm}}{80\,\mathrm{mm}} \times 0.260\,\mathrm{kg} \times 9.8\,\mathrm{N \cdot kg^{-1}} = 0.13\,\mathrm{N} & \text{(upper, 4 mm)} \end{cases},$$

where the force on the lower interface is slightly elevated due to the weight of the slider (§B.2.5). Due to the excellent repeatability of the technique, all three control phases in the first block (1, 4, and 11) are in very close agreement and provide a reliable datum for comparison.

Considering first the downward slopes (phases 2, 3, and 10), comparison with the control phases shows a fairly constant offset for each curve; table B.2 shows that a constant shift of 0.06 N, 0.09 N, and 0.19 N bring phases 2, 3, and 10 (respectively) into good agreement with phase 1. The first two values are very close to the offset predicted on the basis of work done by a falling load; the third offset is approaching 50 % greater than the value predicted. This latter discrepancy is probably due to friction at the rods supporting some of the weight of the upper surface, thus reducing the normal load at the interfaces. It is interesting to note that, in accordance with predictions, the bigger shift of phases 2 and 3 is seen with phase 3, corresponding to the lower interface.

The upward sloping phases (phases 5 and 6) are notably different from the downward slopes in that the difference between them and phase 1 is clearly not constant. Table B.2 quantifies the difference as the root mean square (*RMS*) difference between the control curves and the curve at hand, normalised by the mean of the former: error A (allowing only constant correction) is around

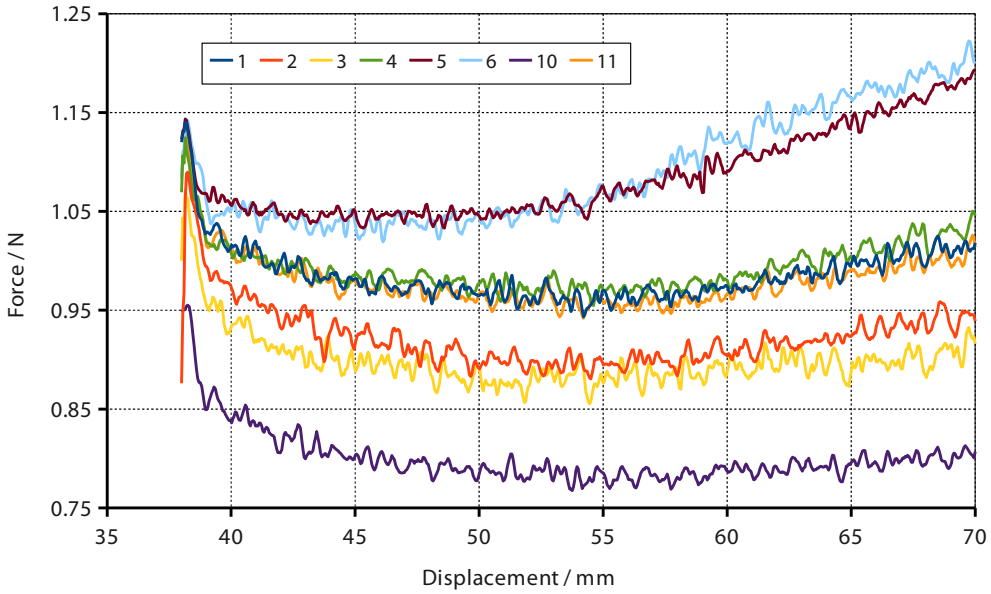

(**a**) Phases 1–11

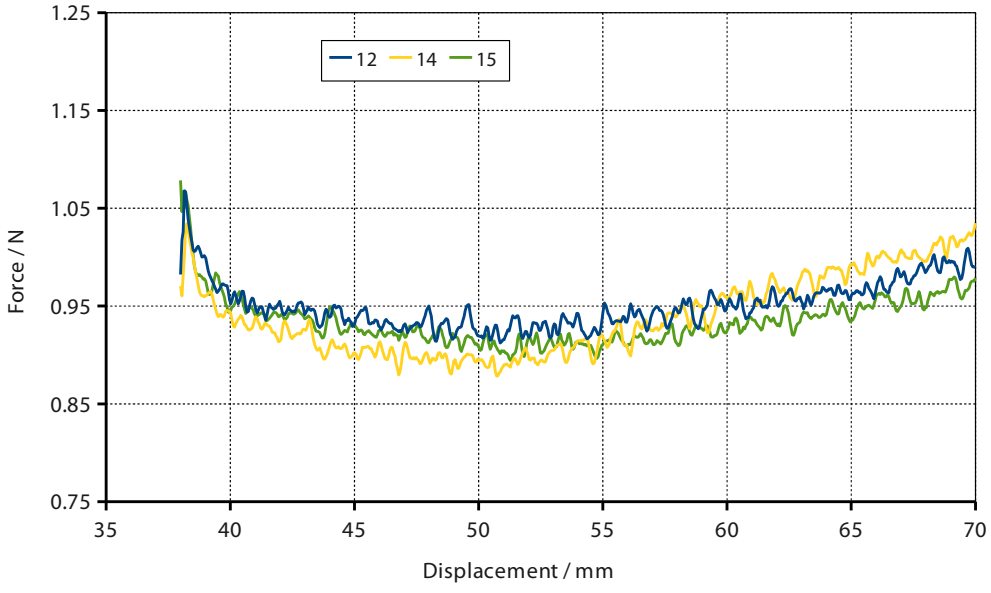

(**b**) Phases 12–15

Figure B.13: Results from the experiment to establish the sensitivity of the apparatus to non-uniform thickness and and a tilted slider (2.55 N load; 0.5 mm · s^{-1}; NW6 sliding on Lorica Soft L7). (a) shows the result from the first block of experiments; (b) shows the second block. Descriptions of the phases are given in table B.1.

Phase	Mean offset	Error A / %	Linear fit to $(f_\# - f_1)$		Error B / %
			Gradient / N · mm^{-1}	Intercept / N	
2	-0.06	1.3	-6.2×10^{-4}	-0.03	1.1
3	-0.09	1.4	-6.7×10^{-4}	-0.05	1.2
10	-0.19	1.3	-1.2×10^{-3}	-0.12	0.7
5	0.10	3.8	4.2×10^{-3}	-0.12	0.8
6	0.11	5.1	5.6×10^{-3}	-0.20	1.3
14	-0.01	2.5	2.3×10^{-3}	-0.14	1.5

Table B.2: A summary of the differences between each phase and phase 1 (phases 2–10) or phase 12 (phase 14), taken as the prototypical control phases. For each phase both the mean difference and a linear fit to the difference was found. For each phase, an approximation to the difference was added back on and the RMS difference between phase 1 and each "corrected" phase was calculated, normalised to the mean of phase 1 or phase 12; error A corresponds to the constant shift and error B to the linear shift. Numbers in red are not considered to correspond to plausible fits, but are included for completeness.

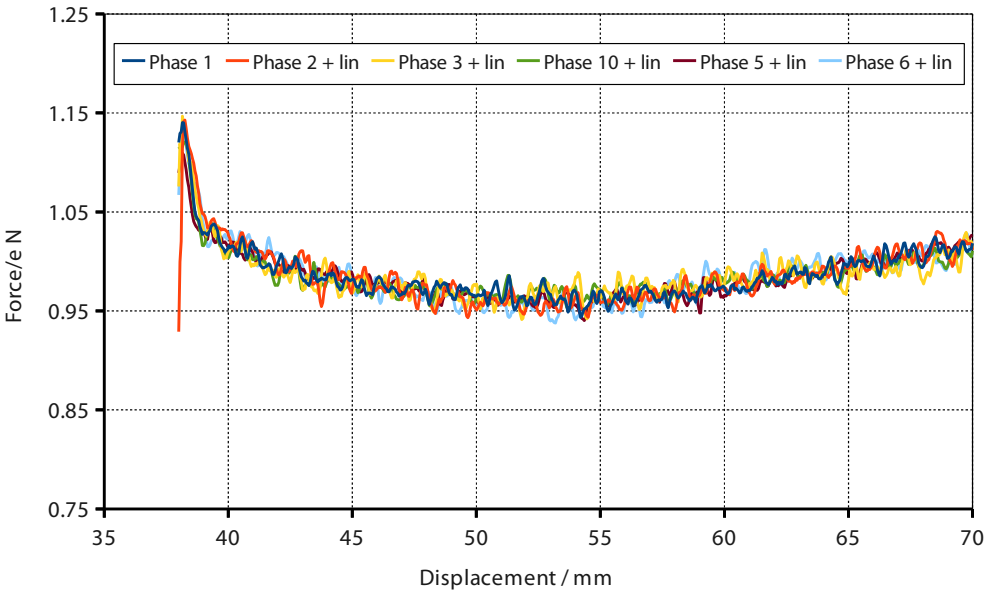

Figure B.14: A comparison of the curves from the first block of testing (phases 1–11) having applied linear "corrections" to them. Correlation coefficients and the corrections themselves are given in table B.2.

four times error B (allowing linear correction) is both cases. Additionally, the mean differences (0.10 N and 0.11 N for phase 5 and 6, respectively) are substantially larger than those predicted by a simple rising weight model. This is again probably due to friction at the rods, in this case "jamming" of the upper surface against them. This is a complicated phenomenon and cannot be explored in depth here. It is, however, interesting to note that despite the complexity of jamming, the greater deviation again lies with the phase corresponding to the lower interface, as predicted by the simple model.

The final class, a tilted slider with constant thickness corresponds to phase 14 (using phase 12 as the datum). The simple rising / falling weight model would predict that this would have a small positive offset of 0.01 N, but this is not seen; in fact, table B.2 shows that the offset is about that size but of the opposite sign. Considering the magnitude, this is unlikely to be significant. Of more interest is the discernible "wave" that phase 14 shows, starting below the control curve and switching over approximately half way through the cycle. Given the complex forces acting on the slider due to the aluminium bars and other parts of the equipment a detailed analysis would be difficult, and would in any case be of little help.

In summary, these results principally show that estimating the degree of deviation caused by a non-flat slider on the basis of a simple model involving weights and inclined planes provides a reasonable estimate of the magnitude of the deviations that are in fact seen; in most cases the estimate is no more than 50 % inaccurate, and in the worst of all cases (the end of phases 5 and 6) the deviation was only about twice what would have been predicted. Possibly more interesting is the excellent agreement that can be reattained when a linear correction is made: even many of the incidental "bumps" are retained! The degree of non-flatness in these sliders was deliberately much larger than would be likely in a normal sample, so taking this reassurance along with the ability to estimate deviation on the basis of thickness measurements and the resilience of small scale features, the technique may be considered fully validated.

B.2.6 Comparison of flat anvils with curved anvils

It is interesting to note a brief experiment conducted during the final stages of development of the method described in this appendix in which the friction traces obtained using a near-flat anvil and a normal, curved anvil with the same (Lorica Soft faced) slider, nonwovens, and load were compared. This experiment was motivated by the relative complexity and time commitment of producing transparent curved anvils: if equivalent traces could be obtained using anvils with flat faces (which can be cast simply in one stage in pots) then this would correspond to a significant time saving. Given the very limited curve observable on the face of anvils corresponding to Lorica Soft, the suggestion is *a priori* plausible.

The experiment was conducted according to the method described in §4.4.3, though without any microscopy. In order to exacerbate any differences between the two anvils, a large load of 17.84 N was used; the upper surface was "trimmed" independently for each pair of anvils; and the sliding speed was $0.5\ \mathrm{mm} \cdot \mathrm{s}^{-1}$. The "flat" anvil was of the same diameter and similar thickness to the curved one, and had as flat a face as was possible to achieve over the majority of its area, with the peripheral

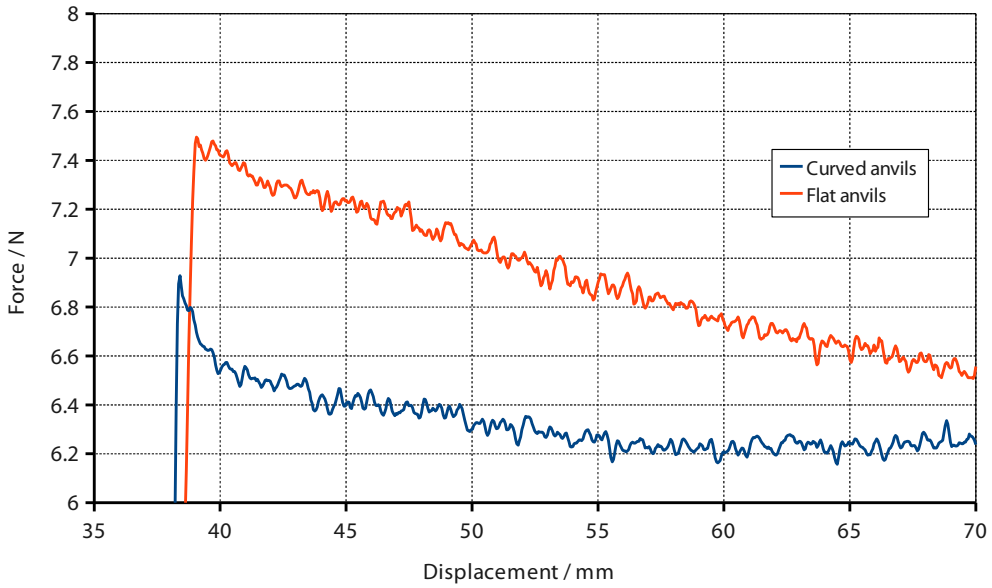

Figure B.15: A comparison of the friction trace from a "flat" pair of anvils and from a normal, curved pair. All other particulars of the sliding equipment were the same between the two.

millimetre chamfered into a gentle curve so as to avoid the abrupt edges contributing the bulk of the friction. The results are shown in figure B.15.

Comparison of the curves is fascinating. Experience of such curves from the main experimental runs of this type preclude the attribution of such differences in magnitude and shape to differences between nominally equivalent nonwoven samples, and as the slider was well worn-in at the time of this experiment slider material variation in not credible. The only remaining explanation of the substantial differences between the two traces is that curved anvils do indeed make a substantial difference to the results of friction experiments, and must thus be used in all cases.

Appendix C

Production of anvils for uniform stress

The importance of the shape of the anvils used in friction tests in determining the stress distribution between nonwoven and skin (surrogate) has been mentioned briefly in appendix B. It was made clear there that the extent to which bulk force measurements could be taken as indicative of the local stresses thus also depends strongly on the shape of the anvils. This appendix describes how anvils which provide uniform stresses can be made.

C.1 The issue of stress distributions

To briefly recapitulate the argument put forward elsewhere, it is clear that the bulk force against displacement data that are obtained from the tensometer are only representative of a "small" region of the interface if the stresses are uniform across the region of contact. As illustrated in §B.1.2, the shape of the anvils (in conjunction with the mechanical properties of the skin (surrogate)) is the principal determinant of the stress distribution, and uniform stress is not obtained by using a square-ended punch. The anvils must therefore be carefully shaped so as to ensure the stress distribution is uniform.

There are two main approaches that could be taken to achieve this: theoretical calculation of the shape followed by fabrication; or identification of a method whereby the shape is produced without prior knowledge of it. The former has various problems associated with it, chief amongst them being the complexity of solving the descriptive equations subject to mixed boundary conditions; the merely approximate agreement between the linear elastic constitutive model and the true mechanical properties of skin (surrogate); and the difficulty of manufacturing an essentially arbitrarily shaped object to the precision of tens or hundreds of micrometres. In consequence, the latter approach has been adopted.

The approach taken is based upon the well-known fact that Newtonian fluids cannot statically support shear stresses, and thus always exert a uniform[1], isotropic pressure against any container. This suffices to produce anvils that correspond to uniform normal stress; shear stress can be added using a thin sheet pulled laterally parallel to the interface.

[1] It is true that a differential hydrostatic head means would lead pressure will vary slightly with location. However, as is subsequently explained, the relevant height difference in the equipment developed in this work was a matter of a perhaps 3 mm, so the non-uniformity in pressure was only s.g. $\times$ 3 Pa, where s.g. is the specific gravity of the fluid at the anvil face (using water as a reference). This is negligible in all cases.

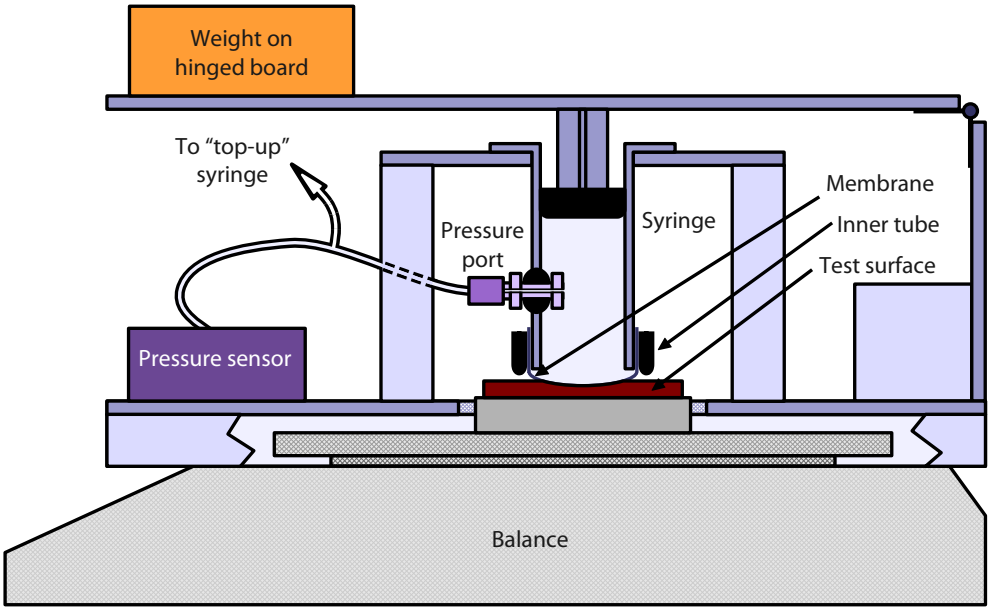

Figure C.1: The apparatus used to produce uniform-stress anvil shapes. The equipment is built onto a balance; part of one side has been cut away for visual clarity.

C.2 Apparatus and methodology for anvil shape production

The key to producing appropriate anvils is to turn the problem on its head: instead of trying to produce the shape that gives rise to a set of forces, apply the set of forces and take note of the shape. Further, given the complex materials involved, it is far easier to use the materials and configurations themselves (where possible) than to try to imitate them. Following these principles, the equipment illustrated in figure C.1 has been built to implement the correct force fields.

The apparatus provides a known normal stress against the test surface via fluid pressure; applies a corresponding shear stress by pulling a strip of nonwoven between the retaining membrane and the aforementioned surface (figure C.2); and measures the normal force with a balance. The equipment is built upon a balance (A&D GF-2000, A&D Engineering, San Jose, CA, USA): the test surface (along with necessary spacers) is fixed to the balance pan with double sided tape; the remainder of the equipment rests upon the balance surround. Depending on the desired contact area for the final anvil, one of two different diameter syringes are used (BD Plastipak 300613 (20 ml, ⌀ 19.0 mm), BD Plastipak 300865 (50 ml, ⌀26.5 mm, discontinued), BD Becton Dickinson UK Ltd, Oxford, UK), each with their corresponding mounting plate; syringes have been cut roughly to length and then polished flat and square using a rotary polishing machine (LaboPol-5, Struers Ltd, Solihull, UK). The open end of the syringe is covered with latex taken from surgical gloves (Profeel DHD Platinum power free surgical gloves, WRP Asia Pacific Sdn Bhd, Sepang, Malaysia; size 8; the outside faces outwards on the syringe) held in place by a double layer of bicycle inner tube (Race 28 Light (42 mm Presta) for ⌀19.0 mm syringe, Tour 26 (40 mm Schrader) for ⌀26.5 mm

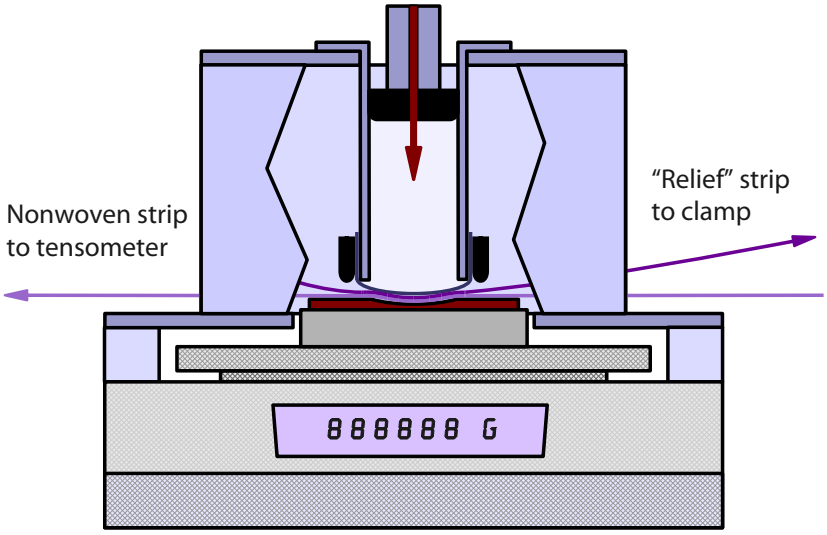

Figure C.2: The shear force required to obtain the correct anvil shape is provided by a nonwoven strip pulled along at a constant rate by the tensometer used in all other experiments. In order to prevent the membrane from shearing unduly a "relief strip" is also included which pulls in the opposite direction and is pre-tensioned before sliding begins.

syringe, Continental AG, Korbach, Germany), which also serves to prevent the membrane bulging out the side. The pressure within the syringe is measured via a port cut in the side within which a small grommet (OD 9.53 mm, ID 6.35 mm, stock number 543-204, RS Components Ltd, Corby, UK) is sealed using bathroom sealant (785 silicone, Dow Corning Europe SA, Seneffe, Belgium). A nylon M5 bolt with an axial hole (⌀1.5 mm) is passed through the grommet and retained using an M5 nut that is tightened against the grommet so as to provide a good seal. A tube terminating in a threaded pneumatic connector is screwed onto the bolt, at the other end of which is an electronic pressure sensor (MPXM2051GS, Freescale Semiconductor, East Kilbride, UK; rated to cover the range 0 kPa–50 kPa). All other components are built of 4.3 mm plywood or pine deal, as shown in figure C.1.

The membrane must be fixed onto the squared-off syringe with great care in order to avoid introducing uneven or excessive tension which would lead to poor reproducibility and other problems. To achieve this, the inner tube is pulled half onto another squared-off, "applicator" syringe of the same diameter, the outside lubricated with silicone grease, and then the overhanging portion of the tube folded back over the portion already on the applicator syringe. The latex is then placed on the (inverted) pressure syringe under no tension, and the "loaded" applicator placed on top of it so the two syringes align. The outer layer of the inner tube is then rolled down onto the pressure syringe, securing the latex membrane in the process. The inner tube still on the applicator is then rolled down over the top of the layer on the pressure syringe, leaving a double layer of inner tube holding the latex membrane in place on the pressure syringe, and the membrane with little or no tension.

The equipment is designed to produce a depression in the test surface corresponding to uniform

normal and shear stress. It is the case that in a static fluid (such as within the syringe) stress is isotropic, so under its influence alone its boundaries experience a pure and constant normal force density. This simple situation is slightly complicated in this equipment by the membrane that has been introduced between the fluid and test surface in order to make the arrangement fluid-tight; it is unavoidably under some tension, so by the arguments set out in chapter 5 it contributes a normal force density of its own. Its contribution is equal to the product of the tension in the membrane and curvature tensor, so if this remains low the contribution is small. The product of the latex sheet's Young's Modulus and thickness is $100\,\mathrm{N \cdot m^{-1}}$–$200\,\mathrm{N \cdot m^{-1}}$ (determined by uniaxial extension tests; the range is due to the significant nonlinearity of the stress-strain curve; thickness is approximately 100 µm), and the mean strain[2] for the larger anvils is always less than 0.2; the mean strain for the smaller anvils is never more than 0.3. These numbers give rise to membrane stresses not exceeding $40\,\mathrm{N \cdot m^{-1}}$ and $60\,\mathrm{N \cdot m^{-1}}$ for large and small anvils, respectively. Coupled with corresponding maximum curvatures within the contact region of $10\,\mathrm{m^{-1}}$ for larger and $50\,\mathrm{m^{-1}}$ for smaller[3] anvils, the normal stress contribution of the membrane does not exceed 0.4 kPa for large anvils or 3 kPa for small ones. For large anvils the maximum "curvature" pressure is thus significant compared to the lowest applied pressure (0.5 kPa), but although the lower applied pressures correspond to the larger curvatures, the strain in this case is more like 0.02 so the contribution is still less than 10 % of the intended pressure. A similar reduction argument applies for the smaller anvils, but since the maximum "curvature" pressure is much larger it is likely that, at the lowest applied pressures, the "curvature" pressure is approximately equal to the intended applied pressure. This is certainly not ideal, but is unlikely to cause substantial error due to the very limited depression created in the substrate at such low pressures. At higher applied pressures the "curvature" pressure makes a much smaller relative contribution, as intended.

There is also a normal force contribution by a similar mechanism from the relief strip and main strip. This is readily analysed by considering that the tension forces on the both are of the order $\mu_{\mathrm{eff}} p A$, where p is applied pressure, A is contact area, and μ_{eff} are the effective coefficients of friction between test surface and main strip and main strip and relief strip, and between main strip and relief strip for the main strip and relief strip, respectively. Division by the cross-sectional area of the strips and multiplication by the curvature gives the pressure contribution from each strip. Overestimating each μ_{eff} as unity, and the contact area as $10^{-3}\,\mathrm{m^2}$, the contribution from each strip is about $3 \times 10^{-3} p$, so the total contribution from both strips is substantially less than 1 % of the applied pressure: it can also be neglected.

For all Lorica Soft anvils and most skin anvils, the normal force density supplied by the test surface must therefore be the principal component to balance the fluid pressure; uniform normal force density has been achieved to a good approximation. The shear is implemented using the equipment shown in figure C.2; if a strip of the "correct" fabric is pulled across the test surface under a uniform

[2] In an analysis of this type it would be most appropriate to use the *maximum* strain rather than the mean. This cannot, however, readily be determined. Fortunately since the action of the relief strip is to make the anvils grossly roughly symmetric, and the "noise" from the sliding strip below will make unstable equilibria untenable it seems likely that the extrema are not that far from the mean, an assertion corroborated by qualitative observation.

[3] This number is almost certainly an overestimate, but the exact figure is very difficult to estimate given the size of the anvil; a larger figure is quoted out of caution.

normal force density (which is true to a good approximation) then by definition the shape adopted by the test surface will correspond to the shear force density distribution below a uniform normal force density! This shear distribution is itself uniform for interfaces obeying Amontons' law, and substantial generalisations of it. Arguing as before, the shape adopted by the test surface when a given stress distribution and sliding velocity are applied will produce that stress distribution if pressed into the surface and made to slide to the same velocity. This shape is not unique: uniform stresses over different areas generally give rise to different shapes.

The issue of friction between the "shear strip" and the membrane should be mentioned. Up to the point where stress and curvature within the membrane become simultaneously large the normal force density at the test surface remains close to the uniform value required to match the fluid pressure *irrespective of any shearing that the membrane suffers*. In fact, it is the nature of shear that where it increases it acts to reduce curvature, so its effect is limited. This means that shearing the membrane (within limits) has no impact on the fidelity of the shape impressed in the test surface. It *does*, however, lead to contact regions that are asymmetric with respect to the anvil, which may cause complications. It is therefore desirable to avoid membrane shearing to the greatest extent possible. This is achieved with the "relief strip" shown in figure C.2. This is nothing more than a strip of nonwoven clamped at the opposite end to the tensometer and at a very low angle relative to the test surface that sits between the membrane and the moving "main" nonwoven strip. If the relief strip is tensioned before pressure is applied and sliding begins (to strain it to the degree that it experiences *during* sliding) then it effectively insulates the membrane from any shearing that it would otherwise have experienced.

Finally, the equipment described is not constructed from pieces designed for the role they fulfil herein, and most of them have not been manufactured to exacting tolerances. In consequence, although it has been possible to reduce air leakage over a 20 min period (see §C.3) so that pressure usually drops by no more than 10 % of its initial value, it has not been possible to routinely obtain substantially better performance than this. In consequence, a small additional syringe has been introduced along the tube to the pressure sensor (shown in figure C.1) which is adjusted to maintain pressure at its initial value.

Having achieved the correct interface shape, it only remains to make an anvil to match it. This can be managed by introducing any material into the syringe that is initially a fluid but (unlike air) progressively and fairly slowly changes to a stiff solid; candidate materials include solids with a low melting temperature which can be introduced molten (wax, for example) and resins that cure from a Newtonian fluid to a stiff solid.

C.3 Casting of anvils

The final anvil must be highly transparent and polished so that microscopy can be carried out through it. This would appear to favour the use of a highly transparent and hard resin (slow curing epoxy has been found to work well) to capture the interface shape. However, the time taken for such a resin to cure at room temperature (24 h or more) is prohibitive in view of the number of different anvils that are needed, the difficulties of producing a seal that maintains pressure within the syringe

effectively for that period, and the degree of variation of atmospheric pressure over this time frame; variation by 1 kPa is common in a day. Because of this, multi-stage casting procedures have been developed that reduce the time period of which pressures must be maintained by around two orders of magnitude to around ten minutes.

The technique developed is a two stage process. The first stage involves introducing a small quantity of a fast-curing resin (polyurethane (*PUR*), Axson F16, Axson UK, Newmarket, UK; found to be one of the coolest fact-curing resins available) into the syringe *before* pressurising it, applying pressure, and removing the cast shape one the resin has cured (typically around ten minutes). The second stage involves stretching smooth latex rubber over the blank[4] and producing a counter-cast. Finally, a clear anvil is cast in epoxy using the counter-cast as a mould.

The method for introducing PUR and applying tensions and pressures is quite intricate; the details are as follows. It is assumed that at the start, the membrane is in position and the balance and pressure sensors turned on (the former tared without any strips in place); that both the main and relief strips are laid out (the former secured at the non-tensometer end with a small weight to prevent it from being slack) and the tensometer programme ready; that the pipework is all connected up; that the top plate is in position and secured; and that both syringe plungers are *not* in position.

1. Mix approximately 8 g of PUR. Stir thoroughly, then divide it equally between two disposable pipettes. Carefully avoiding the pressure port, squirt the contents of one pipette into the syringe. The second pipette is to provide a reference for curing.
2. Start a stopwatch.
3. Push the large syringe plunger (greasing with the same silicone grease used to lubricate the inner tube helps to maintain an effective seal) into the syringe until the rubber tip is entirely within the syringe. This will not increase the pressure as the "top-up" syringe remains open.
4. Push the "top-up" syringe plunger a little way into the syringe, ensuring that the pressure increase is no more than 100 Pa–200 Pa.
5. Pull the relief strip in the direction of the tensometer to approximately the same displacement that it will undergo when the tensometer pulls; this is not difficult, but is easiest done on the basis of experience. It is important that the strip is centred with respect to the syringe, and that it is pulled uniformly across its width; temporarily attaching a "bulldog" clip or similar can assist on the latter point.
6. While still holding the relief strip, lower the upper hinged surface and load it until the pressure inside the chamber reaches the desired level. The strip may now be released; it will recoil.
7. Begin the tensometer programme; when the main strip starts to move, remove the weight from the far end.

   The following steps (to be taken during resin curing) should be taken as and when they are needed; they will be needed multiple times; their order is not important.

8. Record the pressure gauge and balance reading periodically, carefully noting the maximum (stable) balance reading.

[4]The relief of the nonwoven strips beneath the syringe membrane is imprinted on the resin, and causes significant problems in obtaining an acceptable optical surface if it is not amended.

9. The pressure will drop over the period in which the resin is curing; maintain the pressure reading by compressing the "top-up" syringe.

   Move on when the resin is cured.

10. The resin will cure within about 10 min; the remaining resin in the second pipette used for transfer will provide a guide. After this time, stop the tensometer, remove the top plate which holds the syringe, and release the pressure.

It should be noted that even if the pressure is maintained correctly the balance reading *will* fluctuate on a short time scale (corresponding to stick-slip between the main fabric strip and the substrate) and will also vary more slowly as the resin solidifies and expands and contracts slightly due to heating and cooling. This effect is most marked for stiff and thin counter-surfaces. It is concluded that the most appropriate balance reading to take as representative is the largest value attained in the first five minutes or so, corresponding to the equilibrium state when the resin is still fluid, which is essentially that which is captured when it solidifies.

All other steps in the production of the final epoxy anvils are much simpler; the overall process is illustrated in figure C.3. Having obtained the PUR positive, it is secured in a short, squared-off syringe to maintain its orientation and a small piece of the same latex used for the syringe membrane is placed over it, inside facing outwards. This is then pushed up inside a ⌀30 mm casting cup (Seriform, Struers Ltd, Solihull, UK); PUR positives from the larger syringe are snug fits, but those from the smaller syringe require a gasket to produce a liquid-proof seal. For the larger anvils, PUR resin is then poured on top of the latex covered anvil blank and allowed to cure, after which the arrangement is disassembled, ensuring that a mark denoting orientation is faithfully transferred from casting to casting. The counter cast is then ground down a little to remove the casting sprue and make it ready to use as a mould. For smaller anvils wax at 80 °C is used instead of PUR resin to alleviate problems with separating the final anvil from the mould.

Finally, the PUR or wax mould is placed back into a casting cup, and for PUR moulds sprayed liberally with PTFE spray (aerosol PTFE lubricant, RS Components Ltd, Corby, UK) to aid in final separation from the completed anvil. Another (shorter) squared off syringe is placed in the casting cup and shims inserted between syringe and casting pot until the base of the syringe is raised about 2 mm above the mould. Degassed epoxy resin (Epoxy Glosscoat, Vosschemie GmbH, Uetersen, Germany) is then poured into the cup so that the resin level is 2 mm–3 mm above the lowest point of the syringe and then left at room temperature for three to four hours[5]. The cup is then placed in an oven (FED 400, Binder GmbH, Tuttlingen, Germany) at 50 °C for at least a further eight hours for the epoxy resin to cure.

Upon removal from the oven, the contents is removed from the casting cup and separated out; PUR moulds can usually be reused to produce further, identical anvils; wax moulds can sometimes be reused.

It is **very important** that marks indicating the direction in which the tensometer pulled the main strip are made on each casting; without them it is impossible to orient the final anvil correctly.

[5]This reduces or eliminates bubble formation in the epoxy against the mould surface.

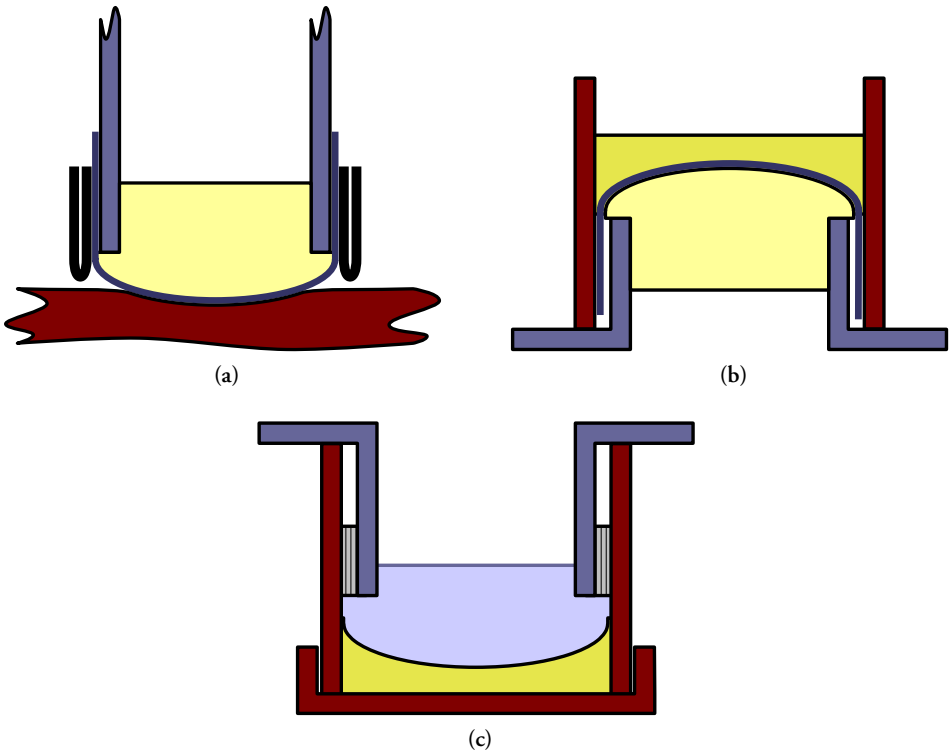

Figure C.3: The processes involved in producing an anvil. (a) PUR resin is introduced to the syringe and pressure and shear stresses applied as described in §C.2. (b) The PUR positive is fixed in a squared off syringe to maintain orientation, and a negative is cast from it, in PUR (large anvils) or wax (small anvils). (c) The negative is placed in a casting cup, a shorter squared off syringe placed to produce the required "step", and slow-curing, transparent epoxy resin is introduced.

The final stage before an anvil is ready for use is polishing. This is done using a Labopol 5 polisher with an MD Dac disc mounted, with DP-stick 3 µm diamond paste and DP-lubricant green (all by Struers Ltd, Solihull, UK). Each sample must be considered individually when polishing. This does not lead to any significant change of shape as the disc and paste are intended for final polishing to optical smoothness: the amount of material removed is very small. The anvil is ready when it is optically transparent over an adequately large region that microscopy can be carried out without difficulty.

C.4 Anvils produced

Though in principle every combination of nonwoven, substrate, pressure, and pulling speed requires a separate anvil this would correspond to an impractically large number of different anvils. Additionally, for a ten minute resin curing time speeds at the faster end of the range covered would require impractically long main strips. As a compromise, anvils have been made for each combination of

nominal substrate material[6] and pressure, with the same anvil used for all nonwovens and pulling speeds. In all cases the main strip used in making the PUR blanks was NW1 and it was pulled at $0.167\,\mathrm{mm}\cdot\mathrm{s}^{-1}$ to minimise the length of nonwoven required.

Partly because of the time taken to make anvils, partly because the relevant equipment is made almost entirely of various woods, but mostly due to no skin being forthcoming for preparatory work, it was not possible to use skin to make the anvils that were to have been used against it. It has thus been necessary to identify a material with a modulus, thickness, and coefficient of friction against nonwoven that are similar to those for skin. Clearly, in view of the large variability of all of these quantities (especially modulus) between subjects and locations approximate agreement is the most that can be hoped for. Coefficients of friction against volar forearm skin have been measured by SCA for each nonwoven (0.38 ± 0.04, 0.36 ± 0.04, and 0.41 ± 0.03 for NW1, NW3, and NW6, respectively), but neither the thickness nor the compression modulus of skin had been measured at the point when the anvils had to be made, so values were estimated from the literature. In §2.2.3 the compression modulus of full thickness skin was estimated to be about 50 kPa, and according to Southwood's measurements [175] the thickness of the skin on the female anterior thorax is about 1.3 mm. All of these are at least fairly approximated by the "4head Quickstrip" pad (DDD Ltd, Watford, UK), a menthol-infusing gel pad with a nonwoven covering designed for non-medicinal migraine relief. Its coefficient of friction against NW1 is about 0.4; its compression behaviour is relatively linear up to about 0.15 nominal strain with a modulus of about 65 kPa (slightly lower at lower strains); and its relaxed thickness is about 2.2 mm. It is thus a fair surrogate in all manners except thickness, where it exceeds Southwood's thickness measurement, but was nonetheless selected as the best available overall match.

A summary of the various anvils produced for use with skin and Lorica Soft experiments is given in table C.1. Various other anvils have been produced, mostly using less developed methods; the only one that need be mentioned is that with designation μ, used for much of the validation work in appendix B. It corresponds to a load of 2.55 N and a pressure of 6.0 kPa.

[6] That is, "skin" and "Lorica Soft" are assumed to be classes within which there is no variation. For Lorica Soft this is not a bad assumption; for skin it is poor, but since it is impractical to produce anvils for each sample it is unavoidable.

Facing material	Designation	Pressure / kPa	Load / N
"Skin" (4head strip)	G	37.1	9.37
	H	5.9	0.74
	I	11.1	1.93
	J	5.3	0.25
	K	27.8	5.02
	L	9.1	1.23
	M	19.6	2.47
Lorica Soft	ρ	32.1	19.0
	σ	1.5	0.73
	τ	5.0	2.65
	ϕ	0.6	0.25
	χ	15.0	8.09
	ψ	6.3	3.14
	ω	2.4	1.23

Table C.1: A summary of anvils produced. Latin majuscule letters refer to "skin" (4head pad—details in the main text); the minuscule Greek letters denote anvils for Lorica Soft. Some letters have not been used to avoid confusion with others; missing blocks of letters were allocated to previous "batches" of anvils that were not eventually used.

Appendix D

Description and validation of "depth of field" technique

In chapter 4 a technique for measuring the contact area between nonwoven and a planar facing surface was described (§4.3). In order to be used "safely" it requires some depth of field measurements to be made; they are reported here. All depth of field (*DoF*) measurements were made using a Leica DMLM microscope and DFC320 camera (Leica Microsystems (UK) Ltd, Milton Keynes, UK), the same combination used in the DoF work reported in the thesis body. Additionally, some aspects of image processing were not described fully; a more complete description is given here. Finally, estimates for the error in the pressures applied during contact measurements are given in §D.6.

D.1 Relationship of microscope divisions to vertical displacement

A prerequisite for measuring the depth of field of anything is the ability to convert between the arbitrary focus units used internally by the microscope and more common distance units. This is simple to establish by measuring the thickness of a transparent object accurately with a micrometer and comparing this with the number of microscope divisions that correspond to moving the focus from one face to the other. Equipment to do this is shown in figure D.1.

As moving the focal plane is fundamentally nothing more than raising or lowering the microscope stage, the lens and lighting conditions that are used do not make any difference to the result: once determined, the conversion factor is valid for all configurations. Because of this, the data were gathered using bright transmission lighting and a $\times 10$ lens[1]. The microscopy data were recorded as when dust motes on one face were in sharpest focus (taking the number to be in the range $[1, 100]$) and when those on the other face were best focused (counting all movement of the focus dial); the data are shown in table D.1. Measurement of the point observed using a micrometre showed the microscope slide to be 1103 mm thick to the nearest micrometre.

Comparing these results, (685 ± 2) div = (1103.0 ± 0.5) µm, which is equivalent to a conversion factor of (1.609 ± 0.005) µm $\cdot$ div^{-1}.

[1] A $\times 20$ lens is in fact available, but the gap between the end of the lens housing and the focal plane is only a few millimetres, which makes it problematic to use.

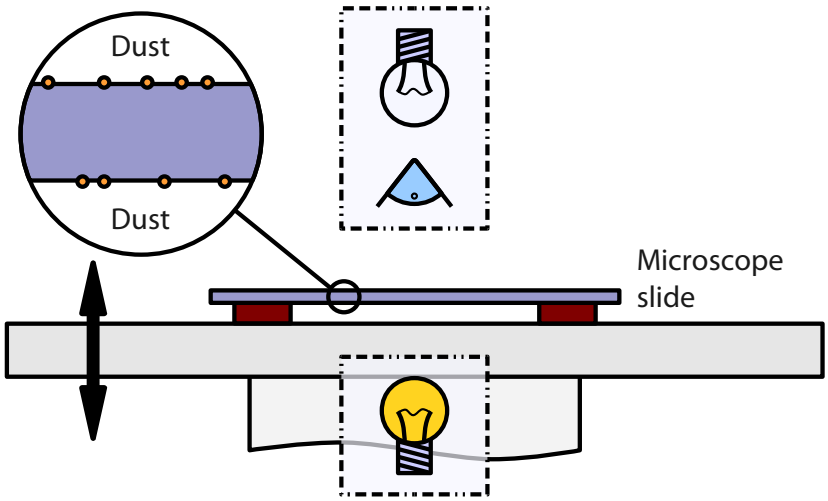

Figure D.1: The apparatus used to measure the thickness of a microscope slide in microscope divisions. It is elevated from the stage so that there is no ambiguity as to what the dust motes used to identify and focus on the surfaces are attached to.

	Observation number				
	1	2	3	4	5
First focus / divs	1	1	0	0	2
Last focus / divs	684	688	683	686	690
Δ / divs	683	687	683	686	688

Table D.1: Data on when dust motes on either side of an elevated microscope slide are in prime focus, measured in arbitrary microscope divisions. The difference is the slide thickness measured in these divisions, and can be compared to the slide thickness measured in more conventional units.

D.2 Measurement of effective depths of field for each nonwoven

Having obtained the conversion factor between microscope divisions and "real" units, it becomes possible to measure effective depth of field for the fibres. Since the assessment of contact is done by capturing an image using the microscope camera it is important that the depth of field is measured here in the same way: eyes are much more accommodating of weak focus than are cameras. In consequence, the method used to determine the effective depth of field of a fibre—that is, the vertical distance over which it appears to remain in focus—is as follows.

1. Place a sample of the chosen nonwoven between two cleaned microscope slides and apply a light load to ensure good contact and the elimination of wrinkles. The exact load is not important: the fibres themselves will not have their cross-sections appreciably altered by any accessible load.

Effective depth of field	**Nonwoven**		
	NW1	NW3	NW6
Mean / µm	24	19	20
Standard deviation / µm	6	5	7
Fibre diameter / µm	16.8 ± 0.2	14.0 ± 0.3	22.5 ± 0.2

Table D.2: Effective depths of field as measured using the technique described in §D.2. Means and standards deviations are taken of a sample of ten points.

2. Open the microscope apertures to their maximum extent (to minimise the depth of field); ensure the microscope is in reflection mode; optimise the camera settings to obtain the clearest possible image of the sample.
3. Focus on a plane approximately half way through the thickness of the nonwoven. Capture an image.
4. Move the stage by 2.5 div (= 4.02 µm) and capture another image.
5. Repeat step 4 until a library of 21 images (20 intervals) has been gathered.
6. Enhance the image library using the differential enhancement routine used in the method described in §4.3.5.
7. Print all of the images out (C203 Digital MFD, Konica Minolta Business Solutions (UK) Ltd, Basildon, UK).
8. Select at random a fibre that goes through all the phases of blurred–focused–blurred through the recorded images. Identify where in the "stack" of images the chosen fibre is first and last in focus, and record both numbers.
9. Repeat step 8 until 10 separate fibres have been considered. Take the difference between the first and last foci for each fibre and find the mean and standard deviation. Finally, multiply both numbers by the distance between adjacent images in the "stack".

This method has been carried out on the three nonwovens chosen for this project; the results at $\times 10$ magnification are shown in table D.2. Data have also been gathered for $\times 5$ magnification for all three nonwovens, but the effective depth of field of fibres at this magnification is so large that no fibres fulfil the criterion stated in step 8 above. It was thus impossible to make measurements, but the effective depth of field was clearly so large that $\times 5$ magnification could not have been used to gather useful data.

The effective depth of field for NW6 deserves special comment: whilst both other nonwovens' fibres have a depth of field a little in excess of their respective diameters, NW6 fibres have an apparent depth of field that is *less* than their diameter. This is surprising; it must be attributed to different optical properties in what is a substantially larger diameter fibre.

```
file_name = input('TIFF file? ', 's');
focus = imread(file_name);
output_file_name = strcat(file_name, '_ngrad.tif');

green = focus(:,:,2);
[greenx, greeny] = gradient( single(green) );
green_grad = sqrt(greenx.^2 + greeny.^2);
green_grad_norm = green_grad ./ max(max(green_grad)) .* 256;

colours = [linspace(1,0.5,64); linspace(1,0,64); linspace(1,0,64)]';
imwrite( green_grad_norm, colours, output_file_name );
```

Code listing D.1: Matlab code used to implement the enhancement of raw DoF images. The code takes a TIFF file (such as produced by Leica's microscope software), selects the green channel, and writes the modulus of the gradient into a new TIFF file.

D.3 Method for enhancing DoF images

The key characteristic of objects that are in focus in a micrograph is that their sharp edges (assuming they are present) *appear* sharp. The task when enhancing raw DoF images in thus to identify and enhance sharp edges and de-emphasise everything else. Following advice from an expert in image enhancement [176] a number of possible methods for achieving this were identified, including squaring the green RGB channel; plotting the gradient image of the green RGB channel; and applying a high-pass frequency filter. All of these methods have been investigated, and the gradient method has proven the most robustly effective at emphasising the focussed fibres.

The routine for implementing the enhancement has been written for Matlab (versions 2007b and 2009b, The Mathworks Ltd, Cambridge, UK); it is very simple, and is shown in code listing D.1.

D.4 Assessment of the repeatability of contact length measurements

All experimental methods for gathering data inevitably introduce error; total elimination of error is impossible, so it is important to quantify it as well as possible. There are three key ways in which variation could originate in the measurement of fibre contact length against a solid substrate: (1) the nonwoven could be different sample-to-sample; (2) the levelling and focusing of the sample could vary, leading to a different image being recorded; and / or (3) the result of manually tracing the enhanced raw images could vary. Of the three, the first is not down to the measurement technique, but the others *are* and thus need to be assessed for repeatability.

The assessment is simple: a piece of NW3 (the most difficult fabric to trace and focus due to the slender fibres) was subjected to a load of 5 kPa using the compression equipment shown in figure 4.8, and was levelled, focused and imaged three times in accordance with the method described in §4.3.4.

Since the nonwoven was trapped in the compression equipment, it did not move significantly during the process of moving and levelling, so if these process were perfectly repeatable then the three images would be identical. Having obtained three enhanced raw images, the first was traced three times and the others once each, thus providing measures of both the repeatability of manual tracing of a given enhanced image and of the combined process of levelling / focussing *and* tracing.

Results are given in figures D.2 (three superimposed tracings of the first image) and D.3 (superimposed tracings of each of the three images) and tables D.3 and D.4. Purely in terms of identified total fibre contact length, the tracing process has a full-range error of $\pm 4\,\%$ of the mean, and the combined levelling / focussing *and* tracing process has a corresponding error of $\pm 5\,\%$ of the mean value. This implies that manual tracing is the principal source of error introduced, and of course provides an overall error estimate.

From figure D.3 is it clear that the fields of view of the three independently levelled and focussed images do not perfectly align. If calculations were performed based on these raw samples then even if neither levelling / focussing nor tracing introduced any errors then the fibre contact lengths would still not agree because they would be based on different samples of fibre. Because of this, the fibre contact segments for each have been cropped to the largest possible rectangle that is covered by all three fields of view (shown in figure D.3), and all quantities in table D.4 and in the text are based upon this reduced sample.

Total fibre contact length is then a respectably reproducible quantity. However, this would be small consolation if the agreement at a fibre-to-fibre level between different tracings and foci were not also good; that is, if there were not a good one-to-one correspondence between fibres identified in one image and those identified in another. Unfortunately, this is a very difficult idea to quantify: for example, the probability of actual coincidence of any of the Bézier control points the describe the fibre contacts even on nominally equivalent curve segments is a floating point zero! Quantities such as the area enclosed between equivalent fibres would be helpful if all fibres were guaranteed to have partners in all images, but become very hard to interpret (or indeed calculate) otherwise. It may be that a useful description could be engineered, but as a brief visual inspection is adequate to show that the agreement is very good, and any descriptive number produced would not be used the questionable return is not worth the significant effort.

D.5 Bitmap tracing script

The process described in this section takes as its input a "clean" bitmap of uniformly coloured curves corresponding to fibre contact segments, and converts it to a set contact lengths and mean curvatures. As noted in §4.3.5, this is accomplished by using an open source bitmap tracer and a custom-written programme to convert the Bézier curves produced by the tracer to lengths and curvatures. These two are both run by a simple BASH script which requires only the file name of the "clean" bitmap; the script is shown in listing D.2.

As a widely available programme, AutoTrace (version 0.31.1, http://autotrace.sourceforge.net) need not be described in detail; it is sufficient that it takes a bitmap, fits Bézier curves to it, and stores the result in the Encapsulated PostScript format (*EPS*, specification available at http://partners.

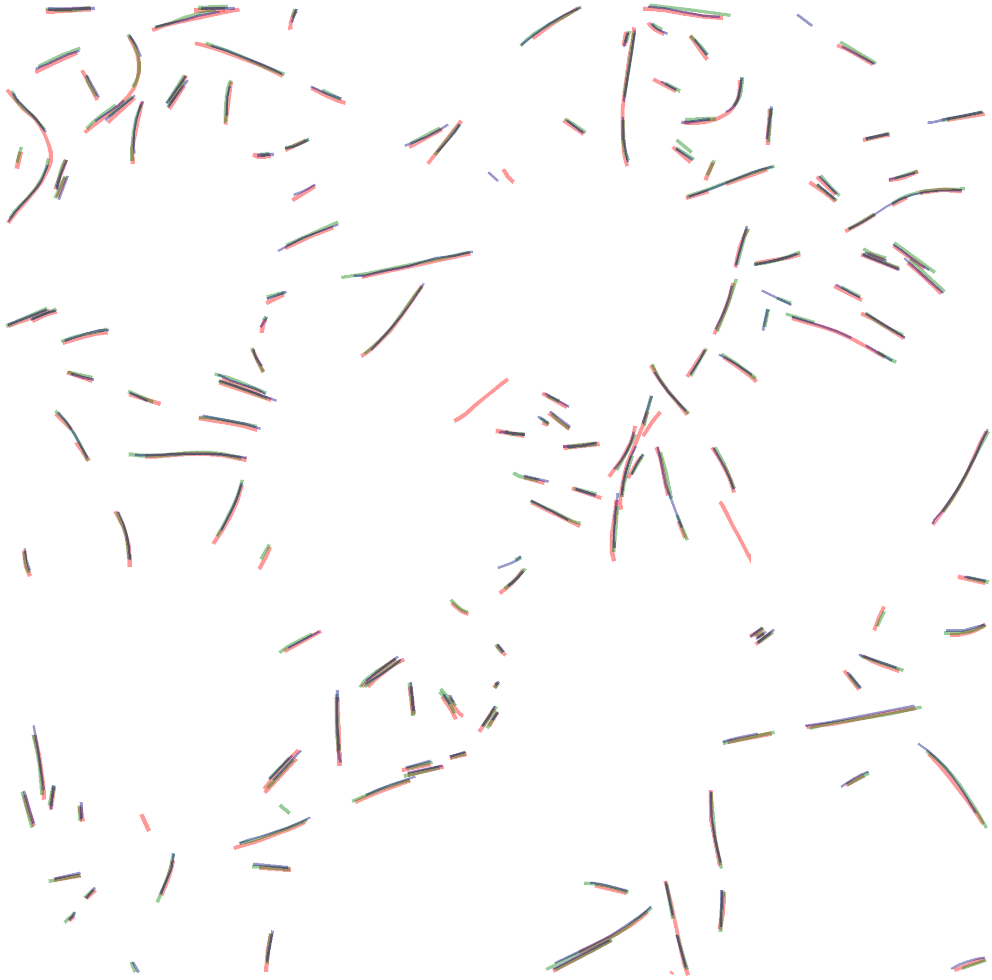

Figure D.2: Three superimposed tracings of a single enhanced image of NW3 under 5 kPa of pressure. The tracings were done in the order red, green, blue. It is immediately obvious that the vast majority of marked contacts are marked similarly in all three tracings. The most common differences are at very short fibre contacts ($< 50\,\mu m$) and where one tracing divides a contact into two parts and others do not. It is clear from this image that the first tracing corresponds to the largest length.

	Tracing repeat			
	1	2	3	Mean
Length / µm	27625	25441	25392	26153
Length / mean length	1.056	0.973	0.971	—

Table D.3: Overall lengths computed from three different tracings of a single enhanced image (figure D.2). Note that this piece of nonwoven has previously been used for pressure testing so has a lower contact length than the corresponding length in §4.3.7, illustrating the "plasticity" described in §4.3.4.

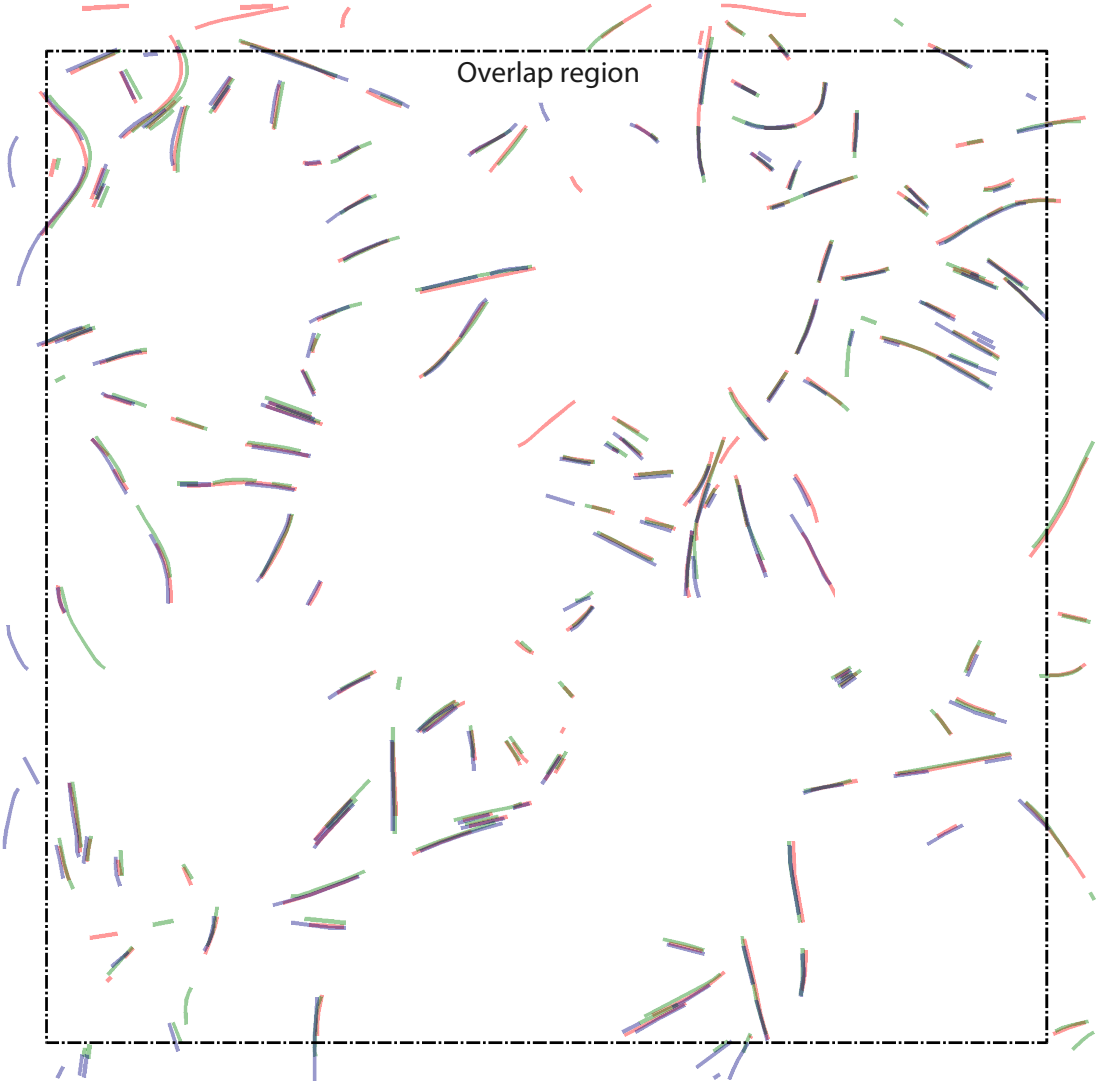

Figure D.3: Superimposed images of a single NW3 sample taken after being independently levelled and focused three times. The images were taken and traced in the order red, green, blue. The majority of the contacts remain in good agreement.

	Levelling / focussing repeat			
	1	2	3	Mean
Length / µm	23344	24257	21830	23144
Length / mean length	1.009	1.048	0.943	—

Table D.4: Overall lengths computed from overlap region shown in figure D.3. The comment on reduced contact length due to "plasticity" (see table D.3) also applies here.

```
#!/bin/bash
echo Autotrace script

if [ -z "$1" ]; then
        echo usage: $0 file_name.bmp
        exit
fi
        input_file=$1

autotrace -report-progress -color-count 2 -background-color FFFFFF -filter-iterations 20 \
        -centerline -tangent-surround 3 -output-file ${input_file%'.bmp'}.eps $input_file

echo Traced to ${input_file%'.bmp'}.eps

epstodist ${input_file%'.bmp'}.eps

echo Line lengths output to ${input_file%'.bmp'}.eps.dist
```

Code listing D.2: The simple BASH script used to convert a "clean" bitmap of the fibre contact segments into first an EPS file (consisting of Bézier curves) and finally to a set of lengths and mean curvatures.

adobe.com/public/developer/en/ps/5002.EPSF_Spec.pdf). The epstodist programme was written for this project, so requires more thorough description.

The epstodist programme is based upon a basic library written by the present author in C++ to handle the stroke primitives in the EPS standard. In essence, the library defines objects to represent curves consisting of contiguous Bézier curves and straight line segments, and containers to interface with and represent EPS files that make use of those parts of the EPS language that are output by the AutoTrace command specified in listing D.2[2]. Although a relatively modest programme, the code for epstodist and the library is far too extensive for verbatim inclusion here, so a simple description is given instead.

epstodist takes as its input any valid output of the AutoTrace command given in listing D.2, which is an EPS file containing a preamble (consisting of various articles of metadata, a setcmykcolor statement, and some command abbreviation definitions) and a number of "strokes", each consisting of a moveto statement (specifying the starting point of the stroke) and one or more lineto or curveto statements (specifying an end point and the nature of the curve). The strokes correspond to the fibre contact segments traced from the enhanced raw micrograph. epstodist reads the EPS file and constructs an "array"[3] of its own stroke objects, each of which consists of straight lines and Bézier

[2]A more comprehensive handling of the EPS format would be a very substantial endeavour, and one which would be of no benefit here.

[3]The data structure is in fact based upon the vector container in the C++ standard library.

curves and can compute both its own length and its mean curvature. These are requested one by one and written to an output text file; each row corresponds to a fibre contact segment, with lengths in the first column and mean curvatures in the second. It is important to note that the scale for both of the characteristics is essentially arbitrary, determined by the print and scan resolutions of the devices used for these processes. The true lengths and curvatures can be recovered by adding in a straight line the full height of the micrograph at the manual tracing stage: its true length is known, so a conversion factor can readily be established.

Limitations of epstodist The epstodist programme handles only a very small subset of the EPS standard. A general EPS file will cause undefined behaviour: it may produce an output (though the output would not be meaningful); or it may crash. In particular, it is dependent upon the command synonyms defined in files produced by AutoTrace: an equivalent bitmap tracer may not use the same conventions, in which case its output would not be correctly processed. However, it is simple to change the commands that epstodist recognises in the EPS files, so most alternative conventions could be fairly readily accommodated.

D.6 Assessment of the error in applied pressure during DoF measurements

In contact measurement experiments a piece of nonwoven is sandwiched between two identical crossed glass microscope slides and a force is applied, either by deadweights alone or by a combination of deadweights and springs. Both the contact area and the applied force have errors associated with them, so the error in the pressure must be estimated. Since

$$p = \frac{F}{A}$$

it follows that

$$\Delta p = \sqrt{\left(\frac{\Delta F}{A}\right)^2 + \left(\frac{F \Delta A}{A^2}\right)^2},$$

where p is pressure, F is applied force, A is contact area, and a prefixed Δ indicates an error.

For deadweight loading the only source of compression is the deadweight itself; the uncertainty is directly measurable, and at around $10^{-5}\,\mathrm{kg} \times 9.8\,\mathrm{N \cdot kg^{-1}} \approx 10^{-4}\,\mathrm{N}$ is negligibly small. For spring loading there are two components of the load:

$$F = F_{\mathrm{dead}} + F_{\mathrm{spring}}$$

so

$$\Delta F = \sqrt{\Delta F_{\mathrm{dead}}^2 + \Delta F_{\mathrm{spring}}^2} \approx |\Delta F_{\mathrm{spring}}|$$

since the deadweight component can be neglected. The spring force can be expressed as

$$F_{\mathrm{spring}} = pk \sum_{i=1}^{4} n_i,$$

where n_i is the number of turns on the nth spring (not necessarily an integer), p is the pitch of the M3 bolt thread, and k is the relevant spring constant. Of these, n is substantially the least well determined, so contributes essentially all of the error:

$$\Delta F_{\text{spring}} \approx \sqrt{4}\Delta n p k$$

where the multiplication by $\sqrt{4}$ is due to the errors on the four spring rotations being independent of each other and thus adding "out of phase".

The area of contact is $w^2/\cos\theta$, where w is the width of a microscope slide (as mass produced precision items they are extremely similar; certainly no difference has been measured) and θ is the angle of deviation from perfect perpendicularity. In consequence

$$\Delta A = \sqrt{\left(\frac{2w\Delta w}{\cos\theta}\right)^2 + \left(\frac{w^2 \sin\theta\Delta\theta}{\cos^2\theta}\right)^2}.$$

However, since $\theta = 0$ for the situation at hand the second term in the square root is zero and the expression simplifies to

$$\Delta A = |2w\Delta w|\,.$$

The typical values of the fundamental errors are $\Delta n = 0.5$ and $\Delta w = 2.5 \times 10^{-4}$ m. Substituting these values into the formulae derived above produces the error estimates shown in table 4.3.

Appendix E

A comprehensive set of graphs for the force against displacement experiment (§4.4)

As noted in the body of the thesis, such a large number of graphs are needed to fully describe and elucidate the results of the friction-displacement experiment that including them in the main text would have been unhelpful. Instead, some example graphs have been included there, whilst all (including the examples, for completeness) have been included here. They are ordered as they are first referred to in §4.4.

All graphs in a given class (for example, illustrating the relationship between friction and load at a fixed sliding speed) have been grouped into the same figure for ease of reference. This means that in many cases a single figure stretches over several pages. For this reason, where part of a figure is a continuation its caption begins "… *Continued*"; when a figure continues past the part at hand its caption finishes "*Continues…*".

In several figures two different fits are shown to the same set of data. In these cases, the two different lines are shown in different line styles (———, ·····) with the equations and coefficients of determination boxed with the same line style.

No more than incidental comments are made in this appendix: substantial comment and analysis can be found in §4.4.

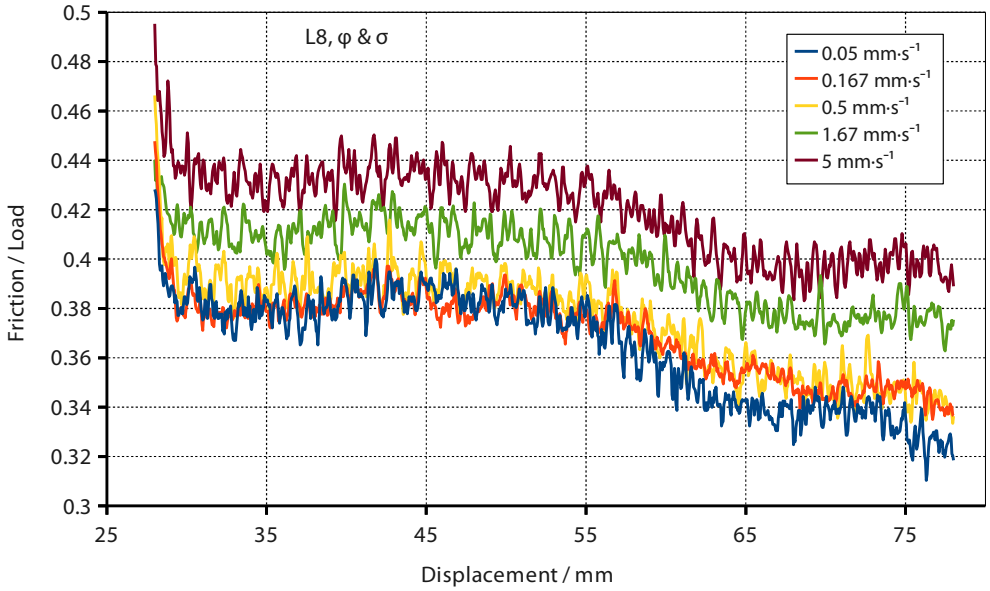

(**a**) NW6, L8, ϕ & σ

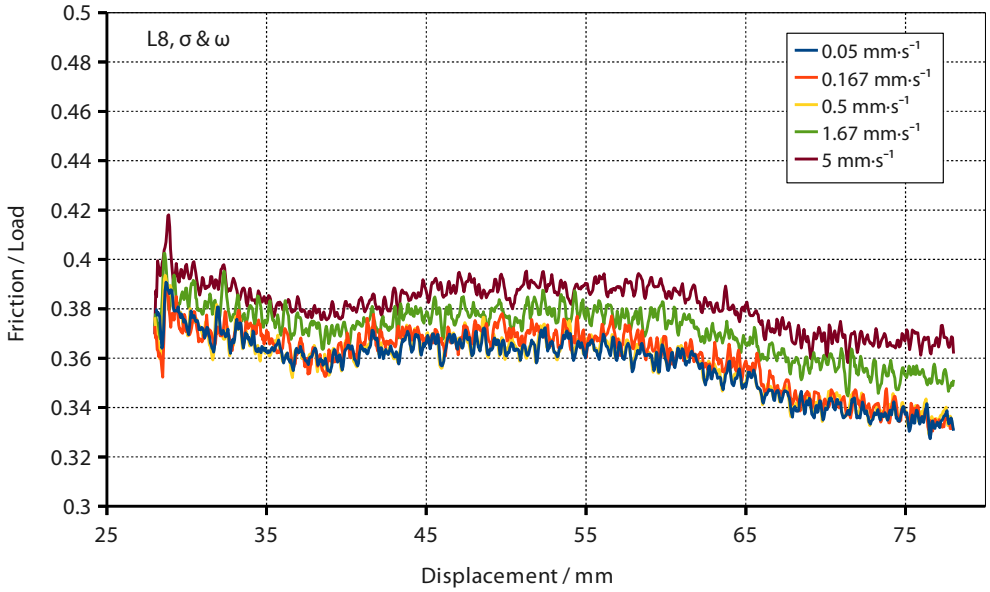

(**b**) NW6, L8, σ & ω

Figure E.1: Comparisons of normalised force-displacement curves at different sliding speeds for the three nonwovens paired with each of the two Lorica Soft sliders at all of the loads tested. *Continues…*

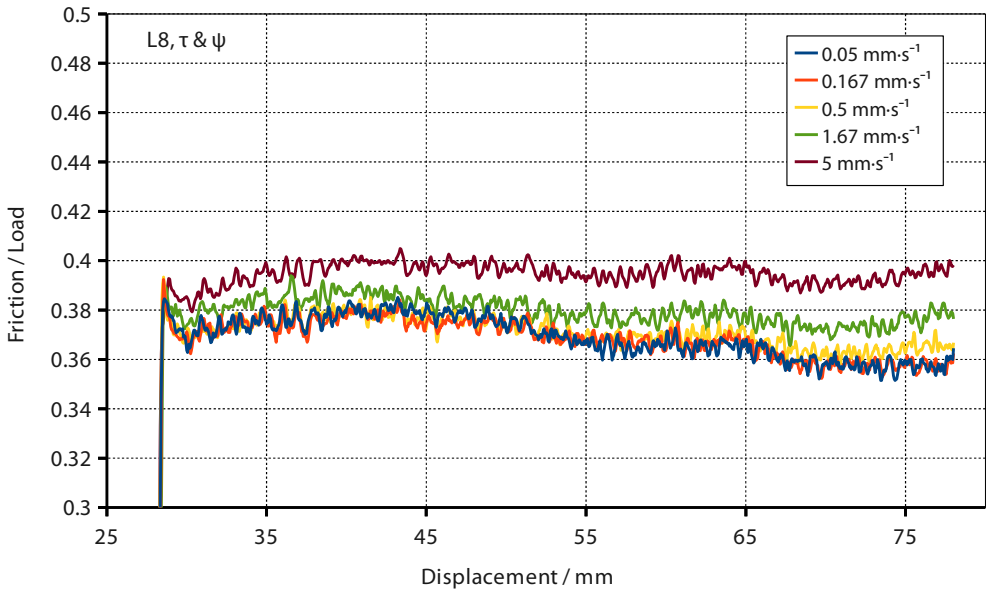

(**c**) NW6, L8, τ & ψ

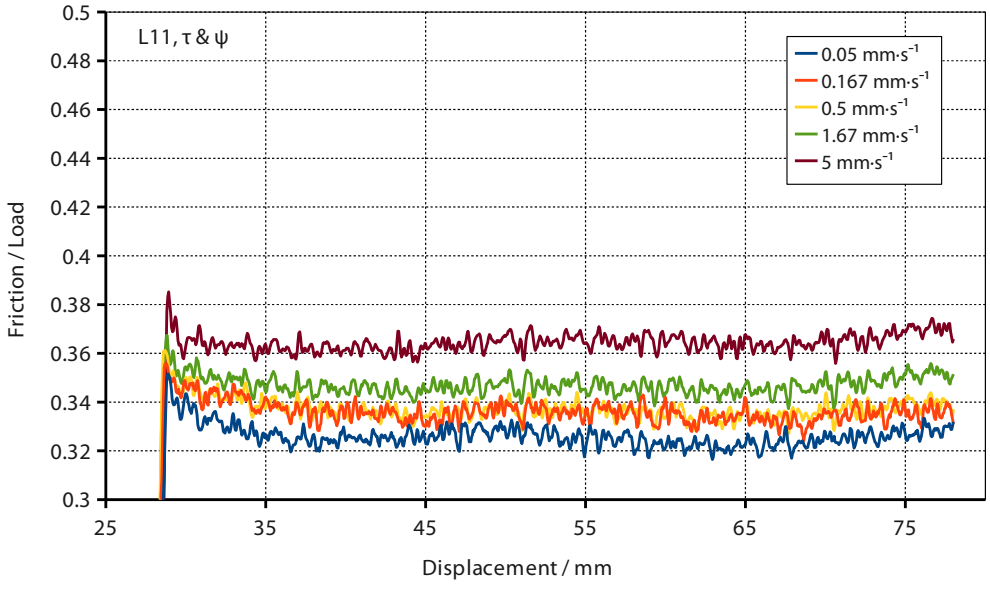

(**d**) NW6, L11, τ & ψ

Figure E.1: … *Continued; Continues…*

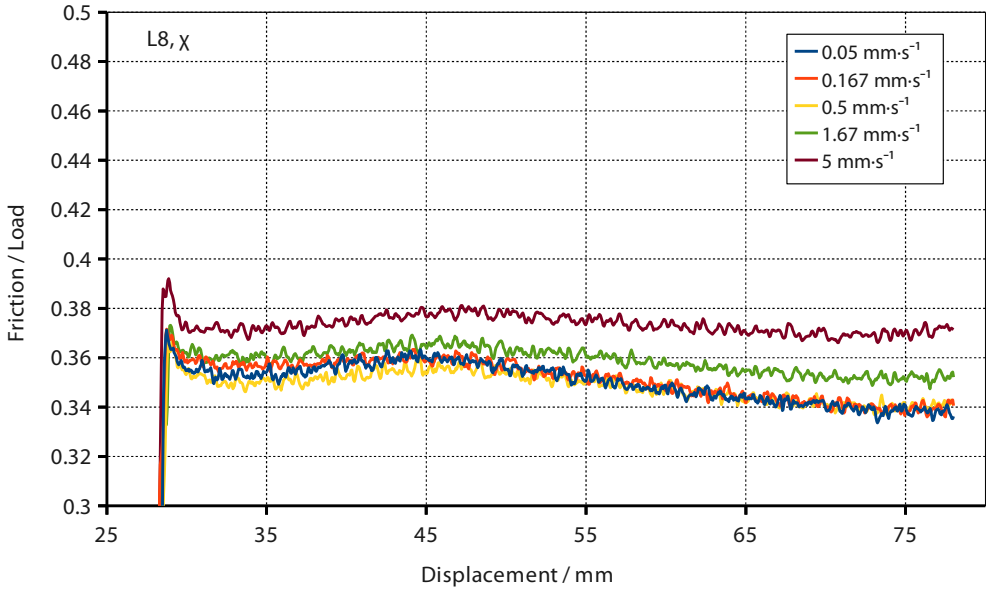

(e) NW6, L8, χ

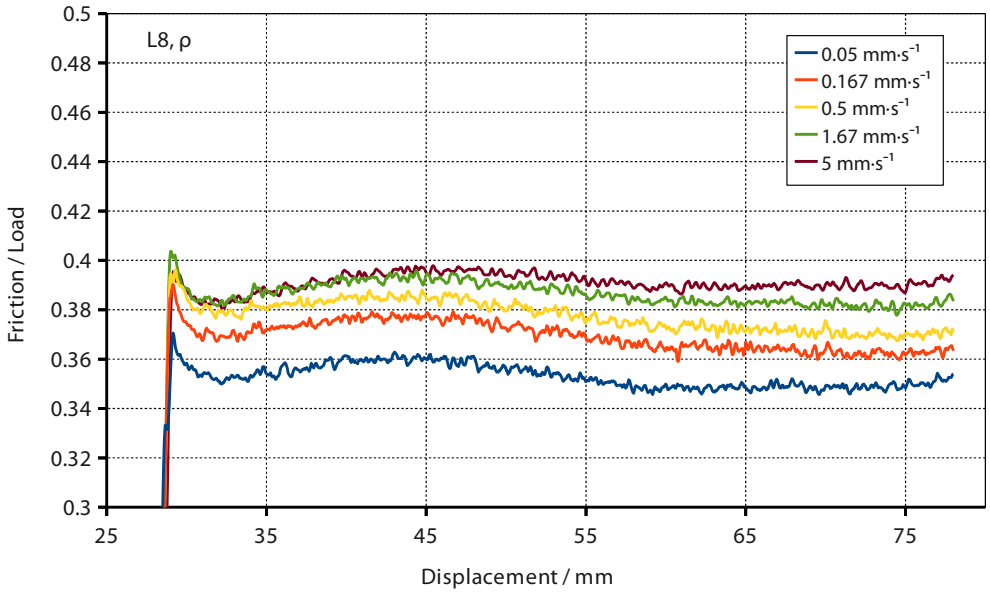

(f) NW6, L8, ρ

Figure E.1: … *Continued; Continues…*

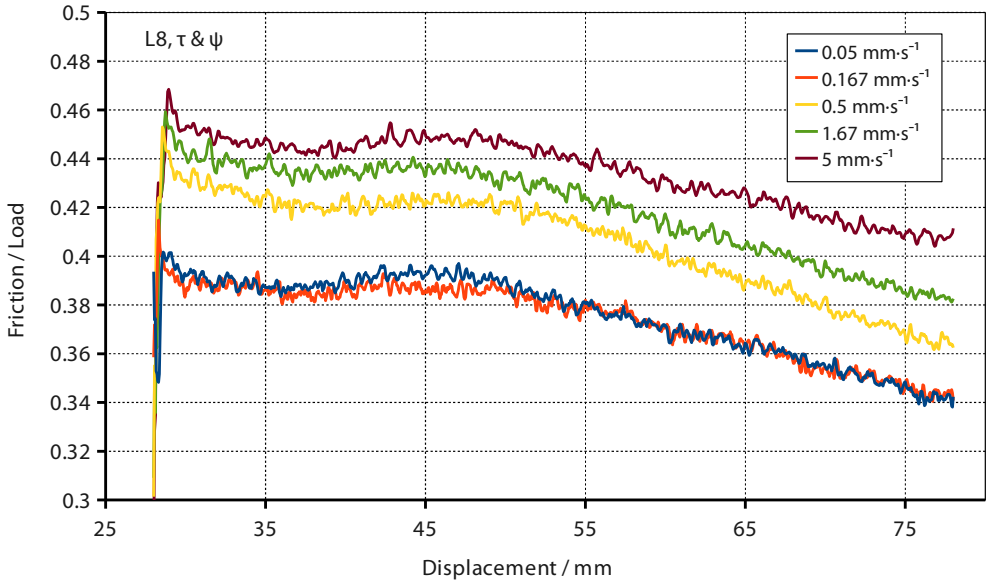

(**g**) NW3, L8, τ & ψ

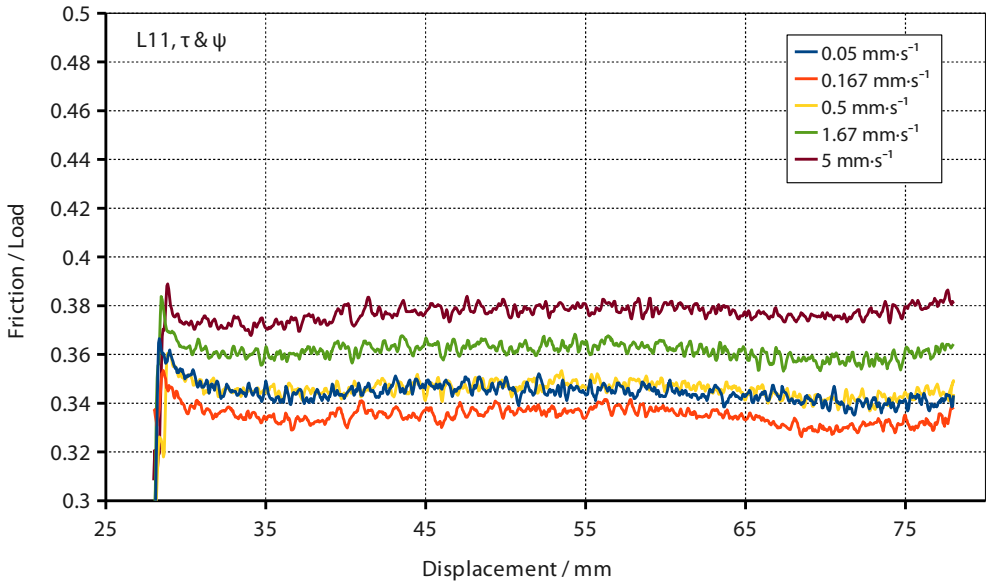

(**h**) NW3, L11, τ & ψ

Figure E.1: … *Continued; Continues…*

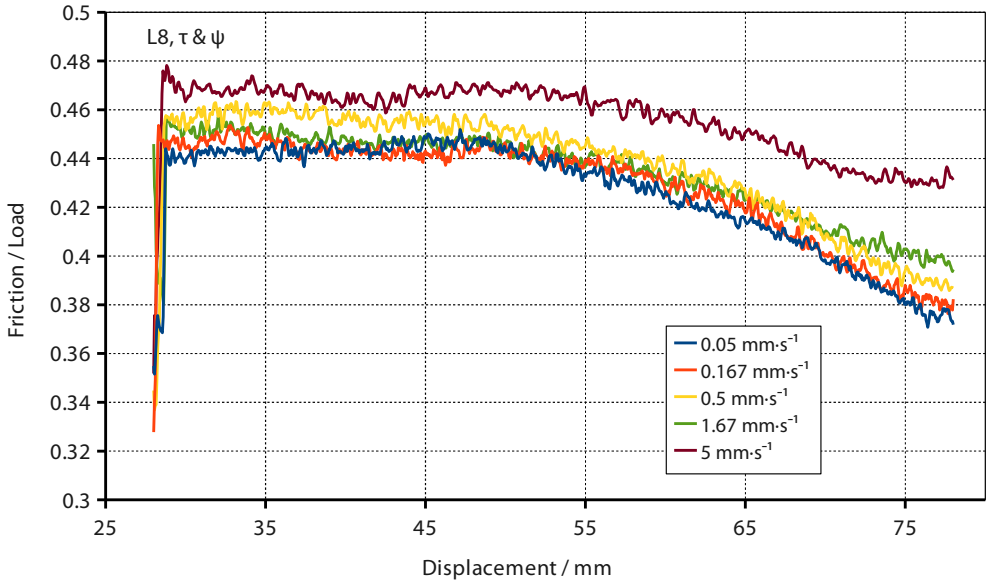

(**i**) NW1, L8, τ & ψ

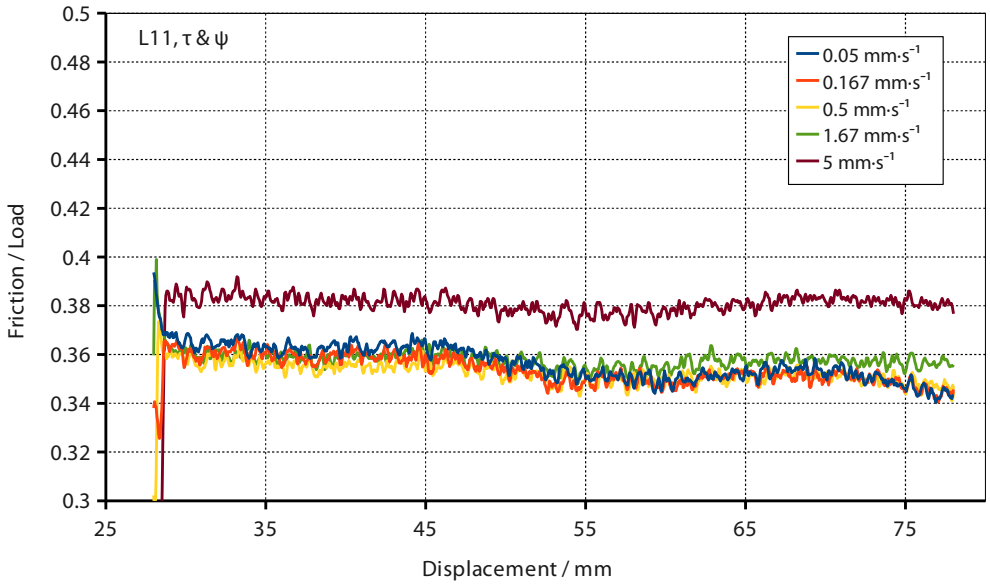

(**j**) NW1, L11, τ & ψ

Figure E.1: … *Continued.*

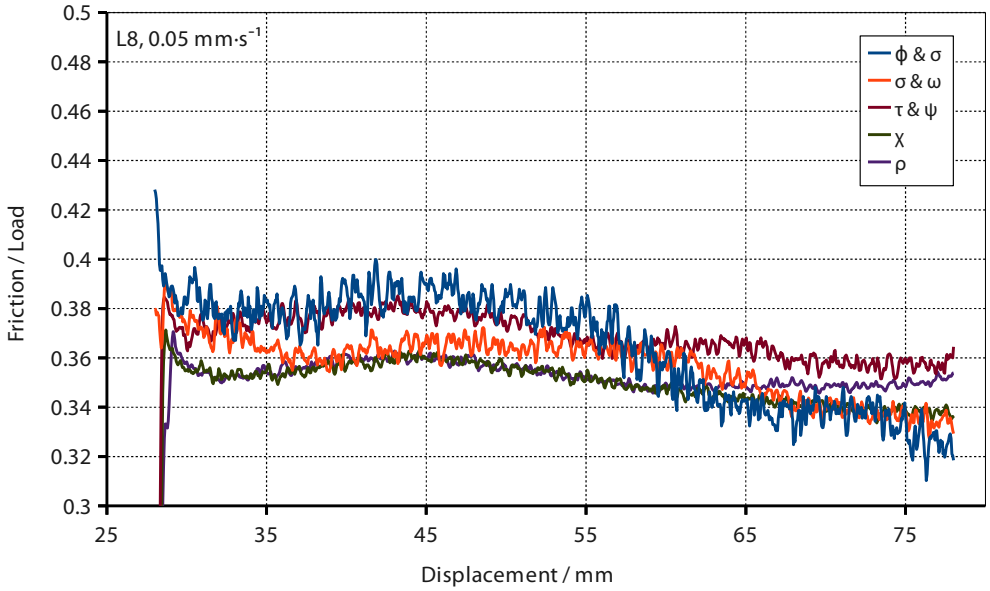

(**a**) NW6, L8, 0.05 mm · s^{-1}

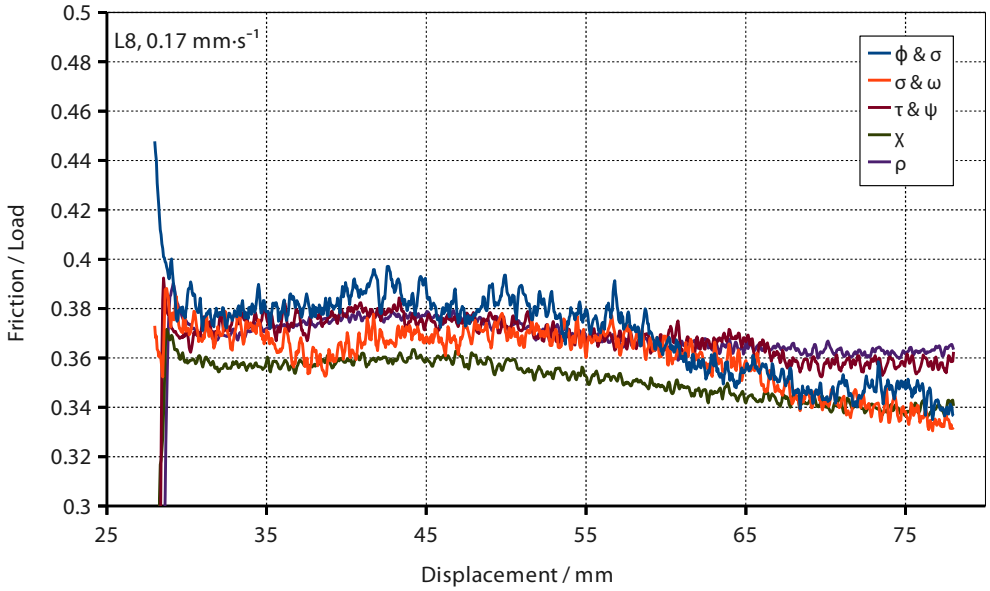

(**b**) NW6, L8, 0.167 mm · s^{-1}

Figure E.2: Comparisons of normalised force-displacement curves at different loads for each nonwoven paired with each of the two Lorica Soft sliders. *Continued…*

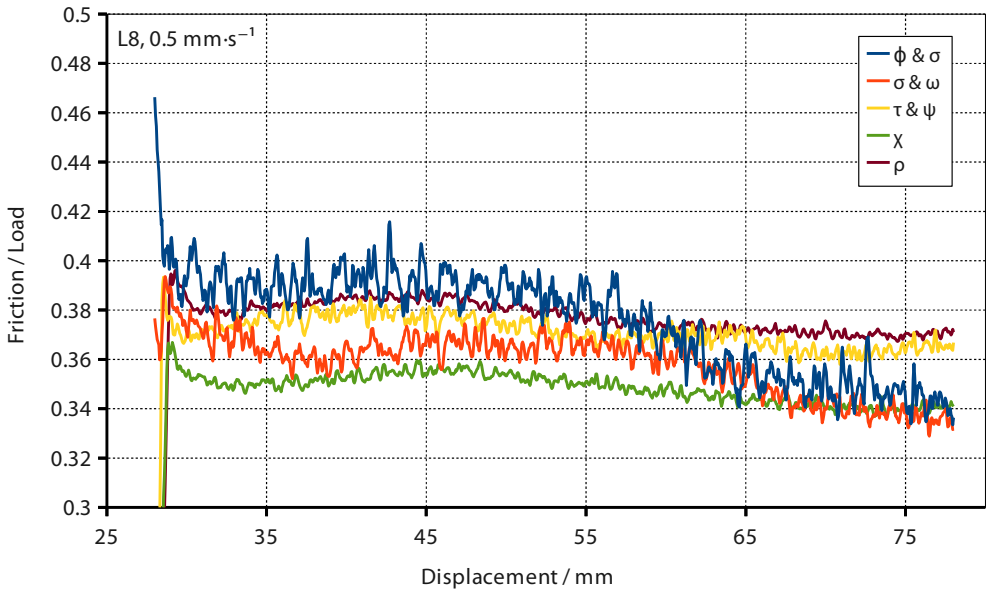

(**c**) NW6, L8, 0.5 mm · s^{-1}

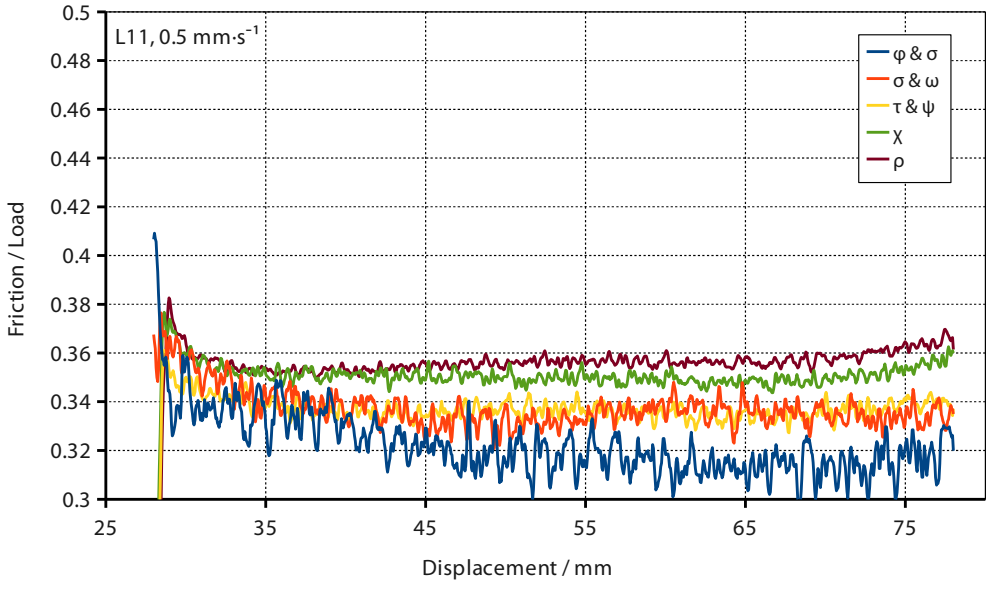

(**d**) NW6, L11, 0.5 mm · s^{-1}

Figure E.2: … *Continued; Continues…*

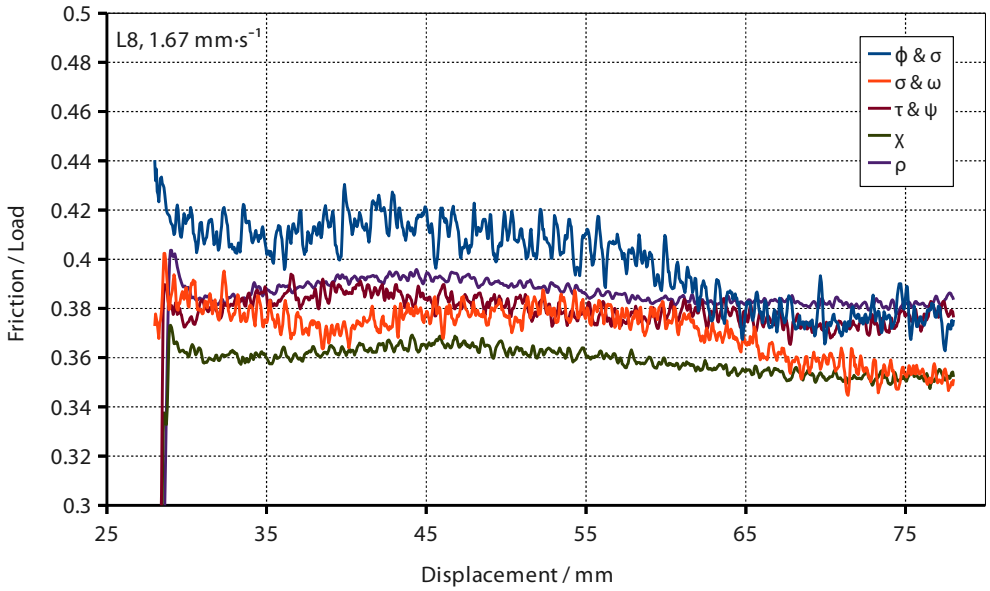

(e) NW6, L8, 1.67 mm · s^{-1}

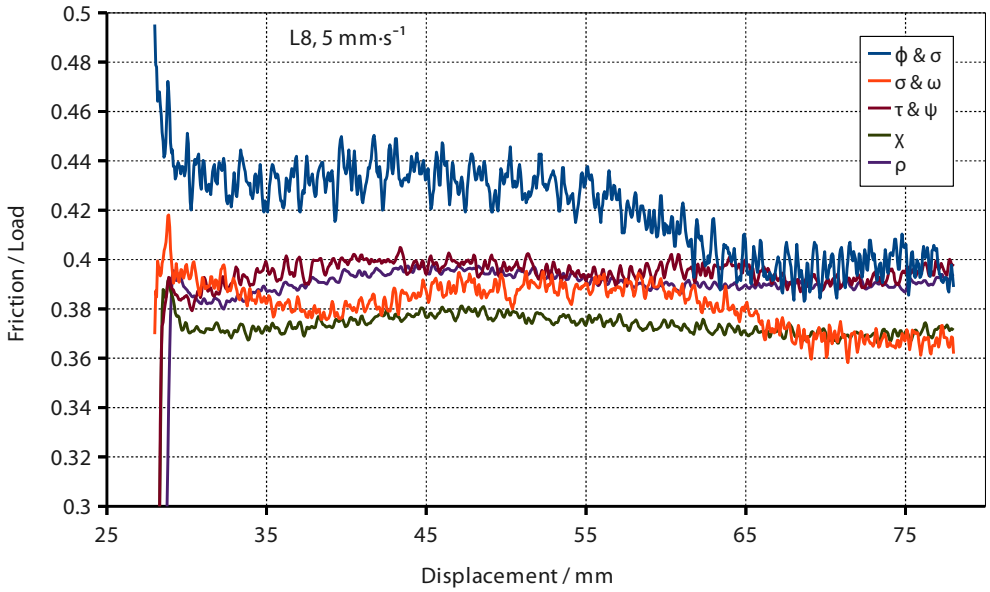

(f) NW6, L8, 5 mm · s^{-1}

Figure E.2: … *Continued; Continues…*

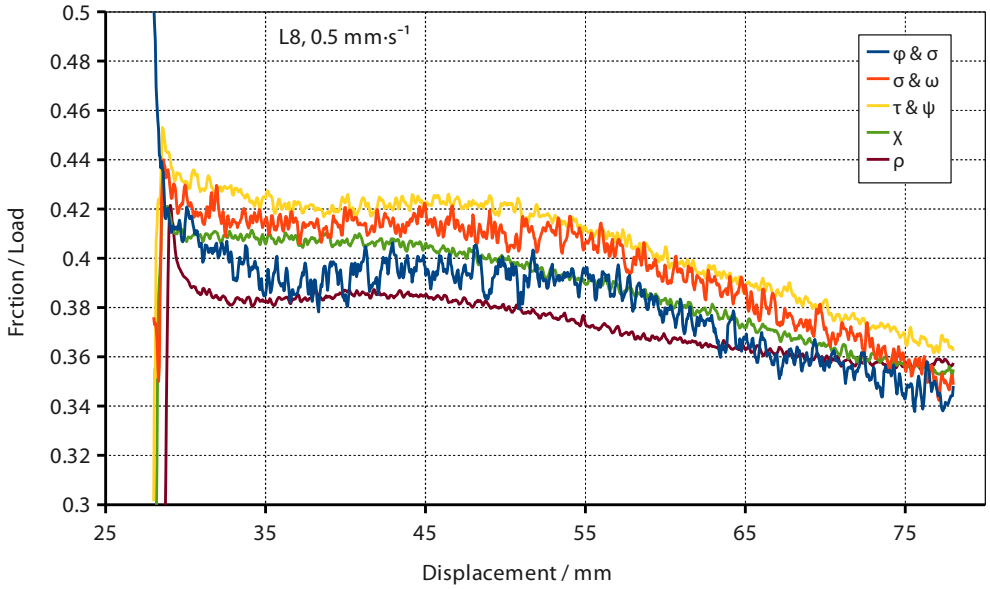

(**g**) NW3, L8, 0.5 mm · s^{-1}

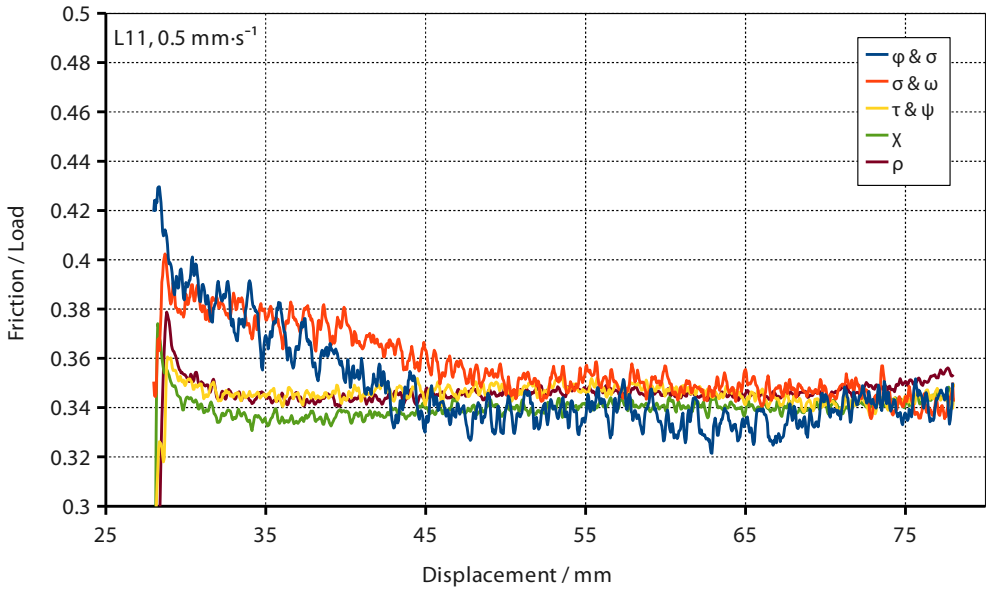

(**h**) NW3, L11, 0.5 mm · s^{-1}

Figure E.2: … *Continued; Continues…*

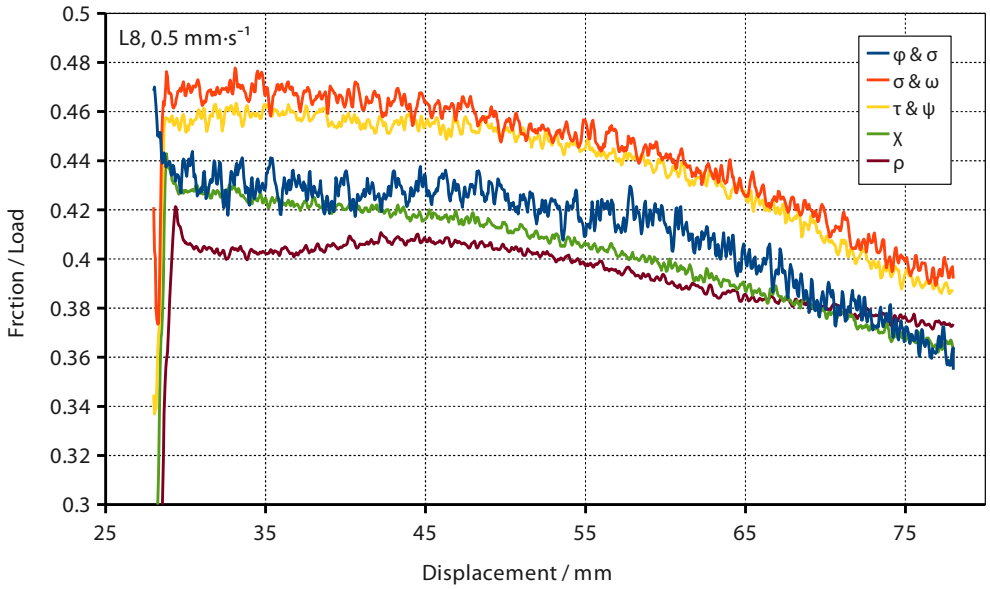

(**i**) NW1, L8, 0.5 mm · s^{-1}

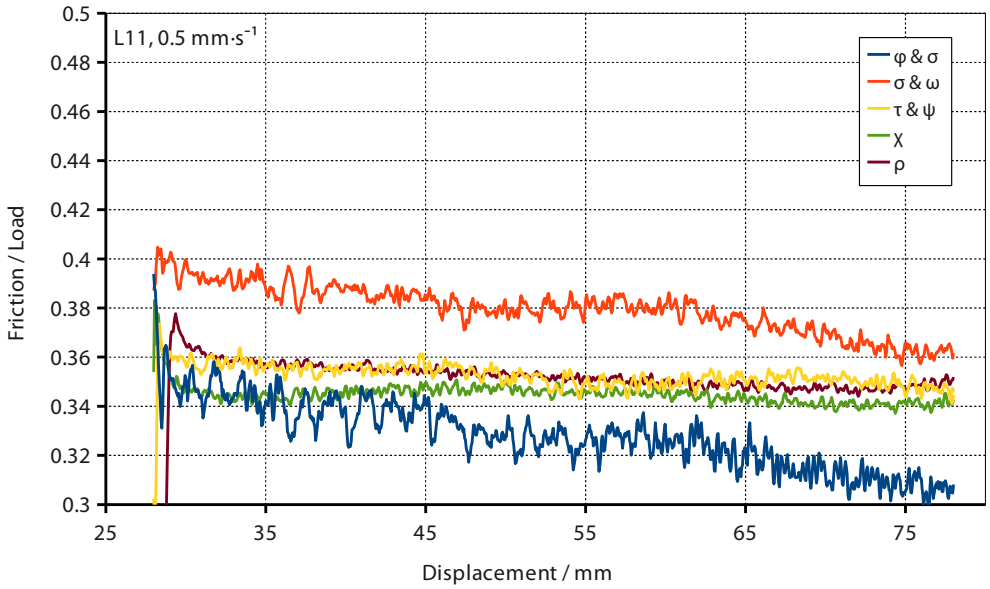

(**j**) NW1, L11, 0.5 mm · s^{-1}

Figure E.2: … *Continued.*

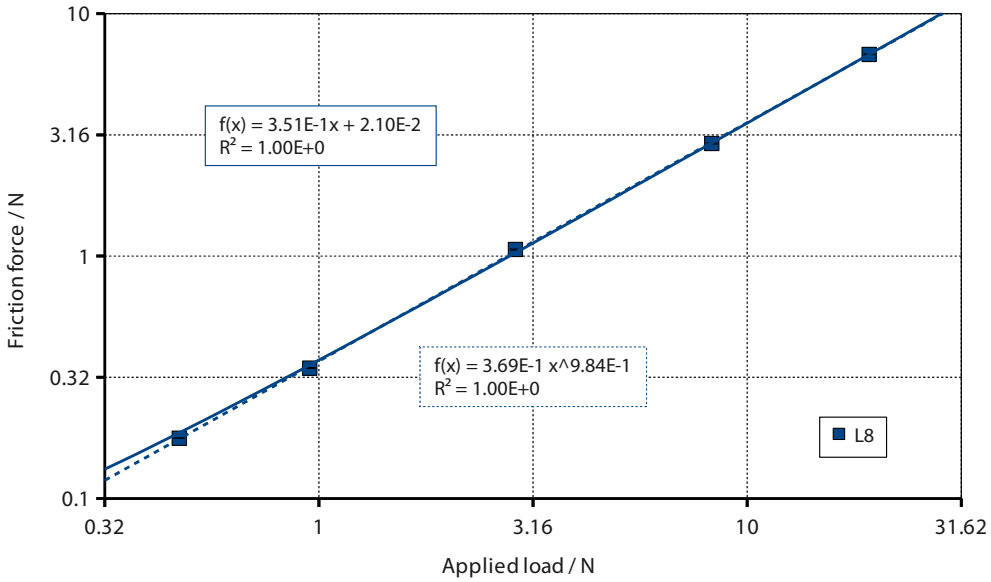

(**a**) NW6, 0.05 mm · s^{-1}

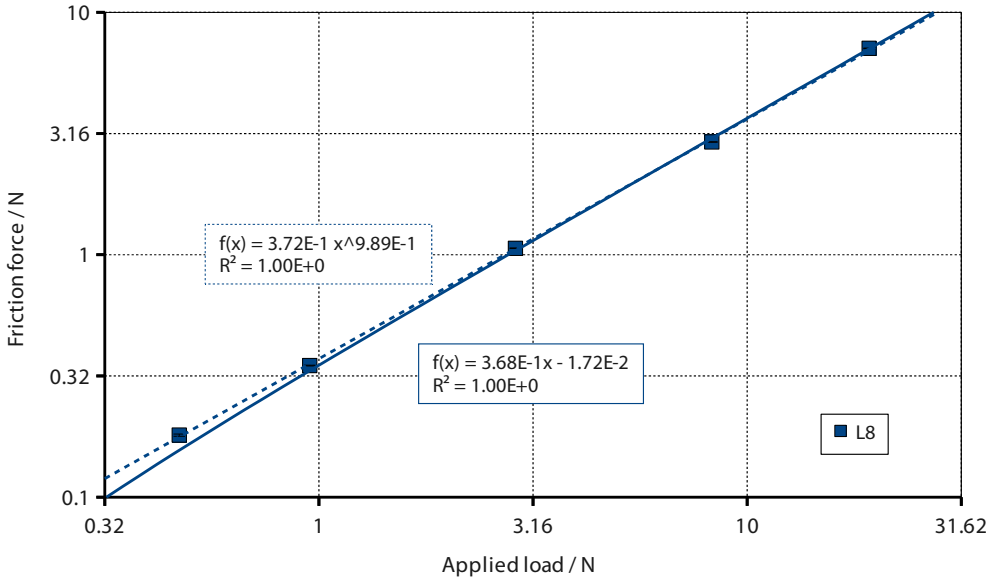

(**b**) NW6, 0.167 mm · s^{-1}

Figure E.3: Summary plots of friction force against load for each of the three nonwovens against each Lorica Soft slider at all sliding speeds considered. Force error bars are present though they are very small. *Continues…*

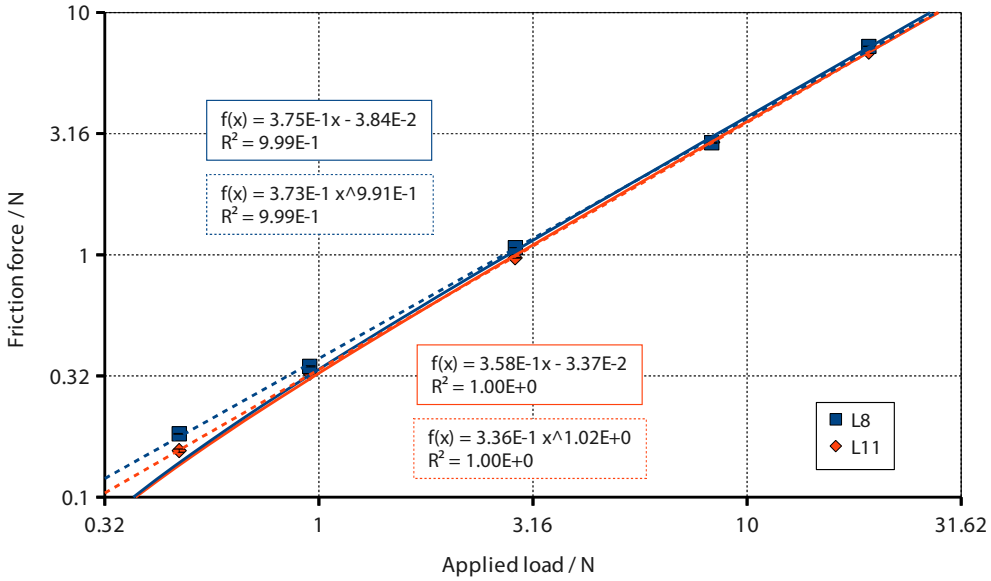

(c) NW6, 0.5 mm · s^{-1}

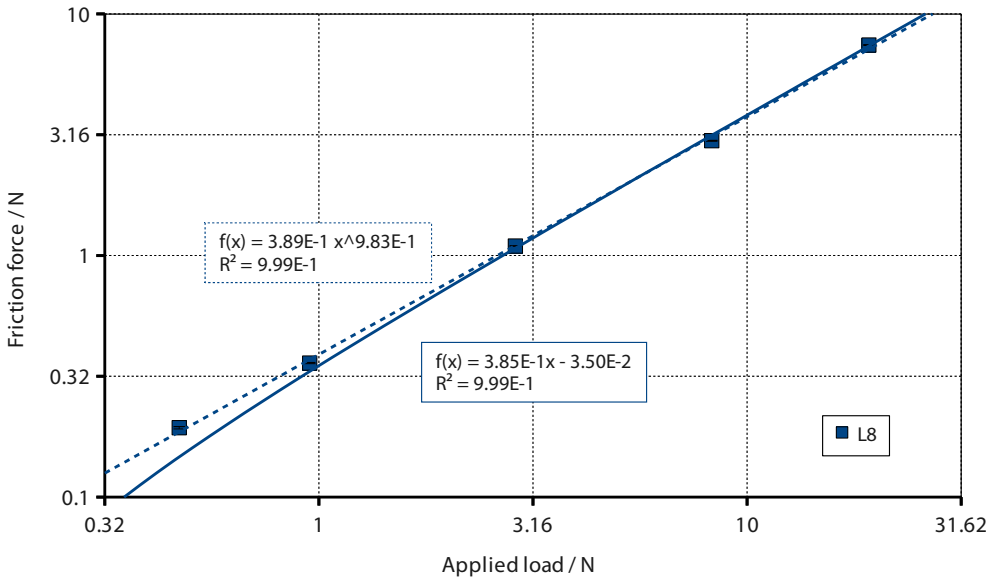

(d) NW6, 1.67 mm · s^{-1}

Figure E.3: … *Continued; Continues…*

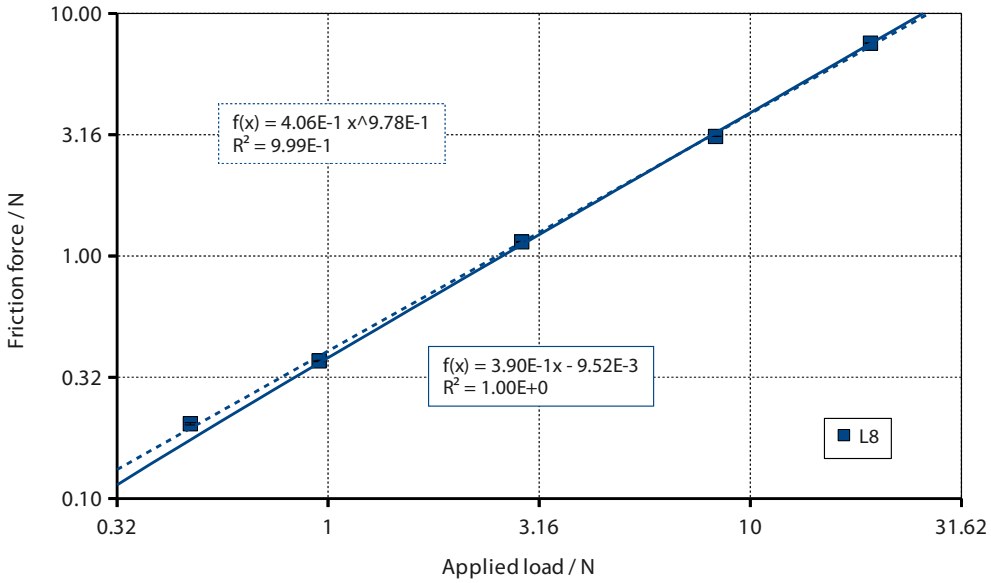

(**e**) NW6, 5 mm · s^{-1}

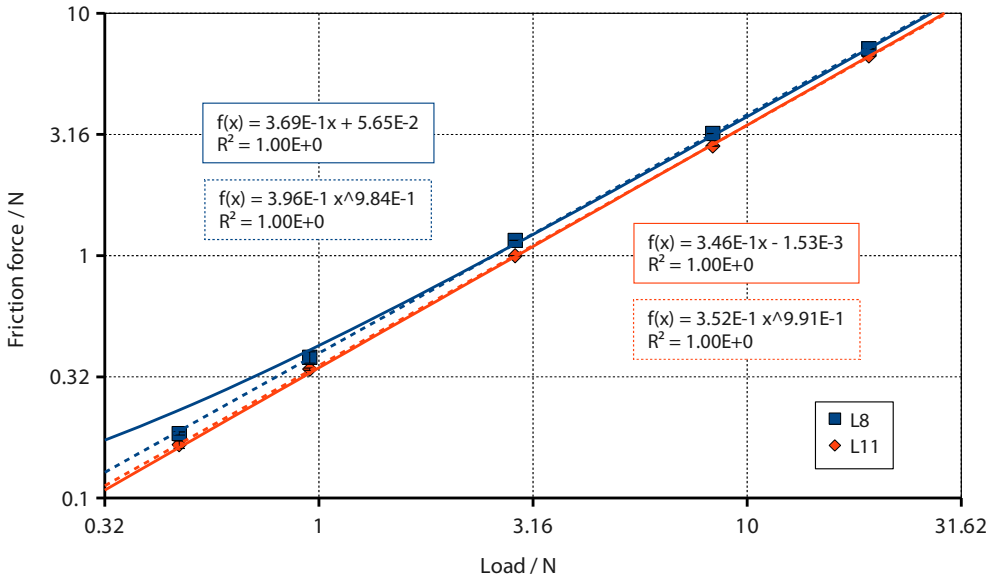

(**f**) NW3, 0.5 mm · s^{-1}

Figure E.3: … *Continued; Continues…*

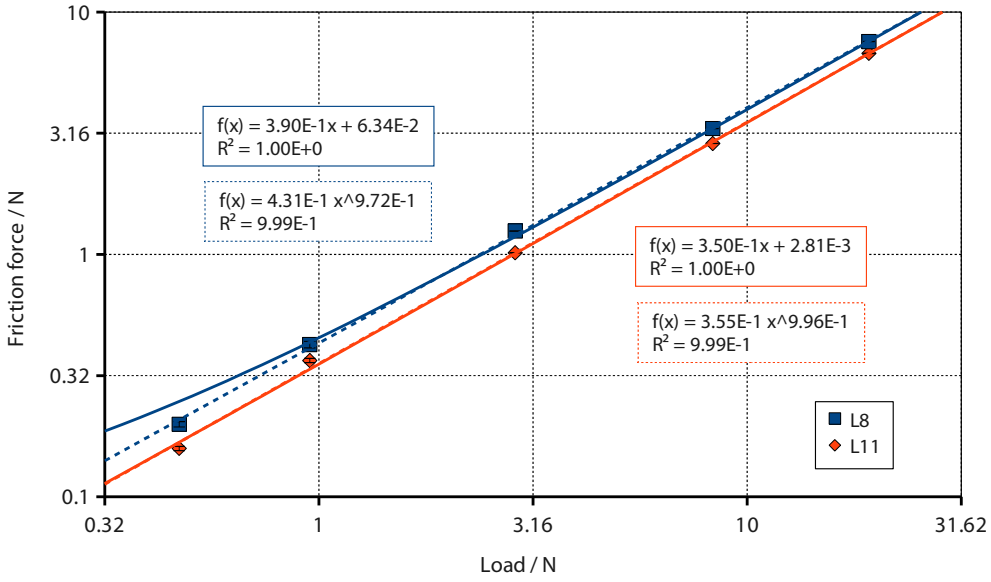

(**g**) NW1, 0.5 mm · s^{-1}

Figure E.3: … *Continued.*

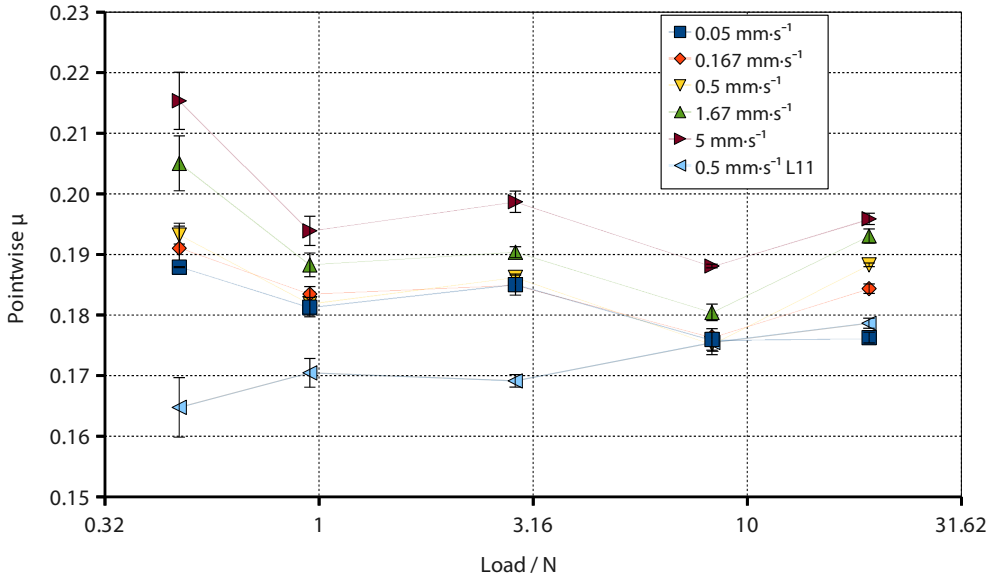

(**a**) NW6; the slider is L8 unless stated otherwise

Figure E.4: Summary plots of pointwise calculated coefficients of friction against load for each of the three nonwovens against each Lorica Soft slider. *Continues…*

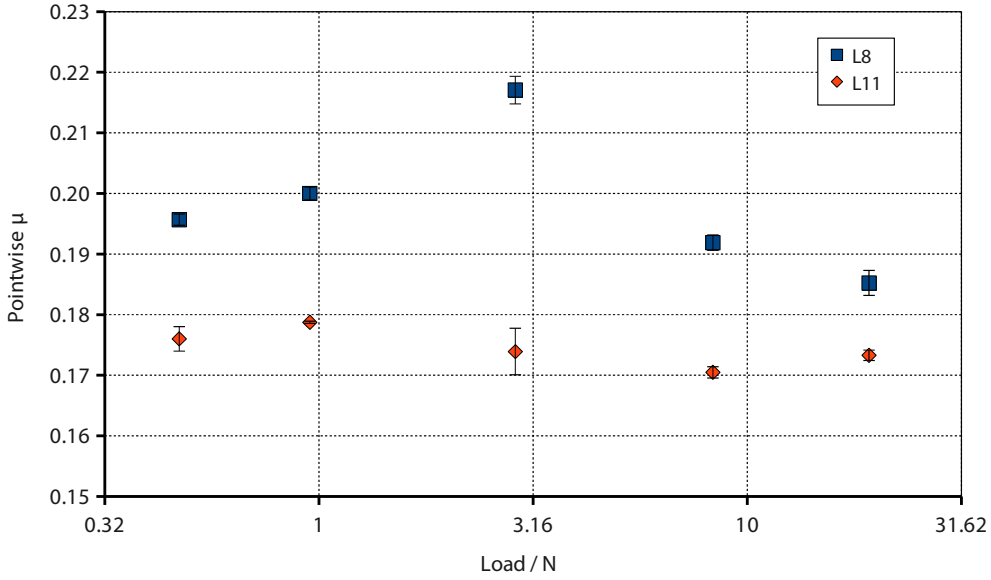

(**b**) NW3

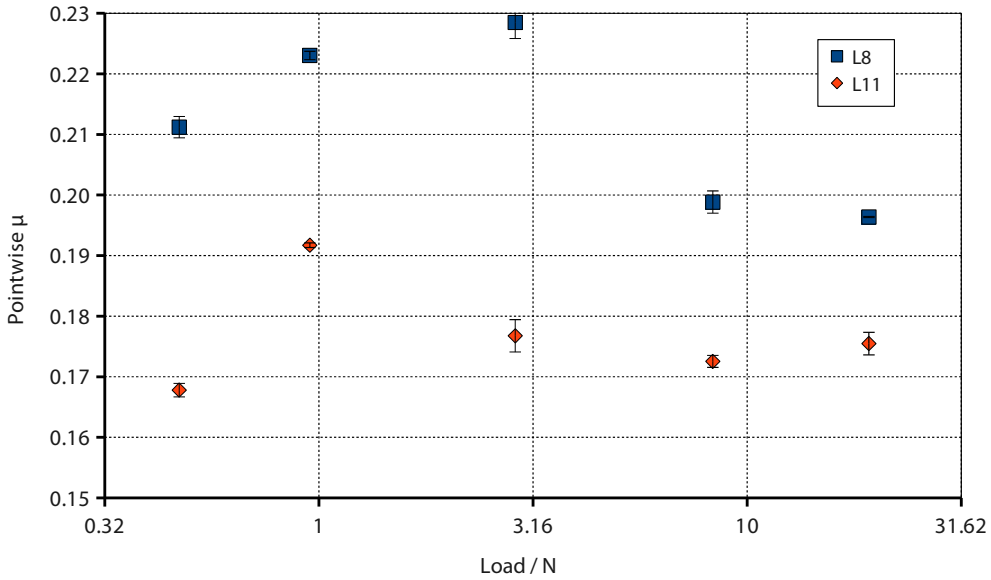

(**c**) NW1

Figure E.4: … *Continued.*

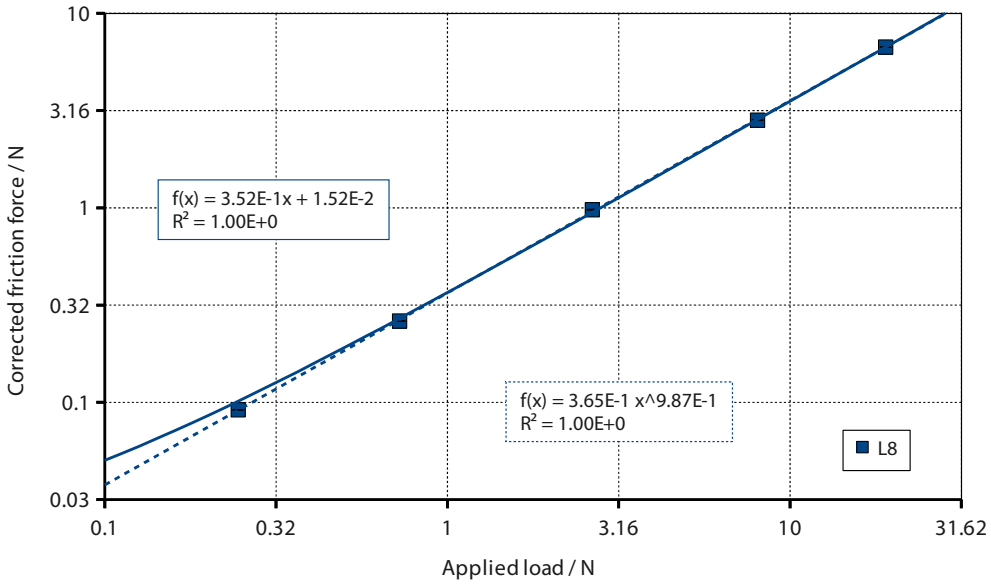

(**a**) NW6, 0.05 mm · s^{-1}

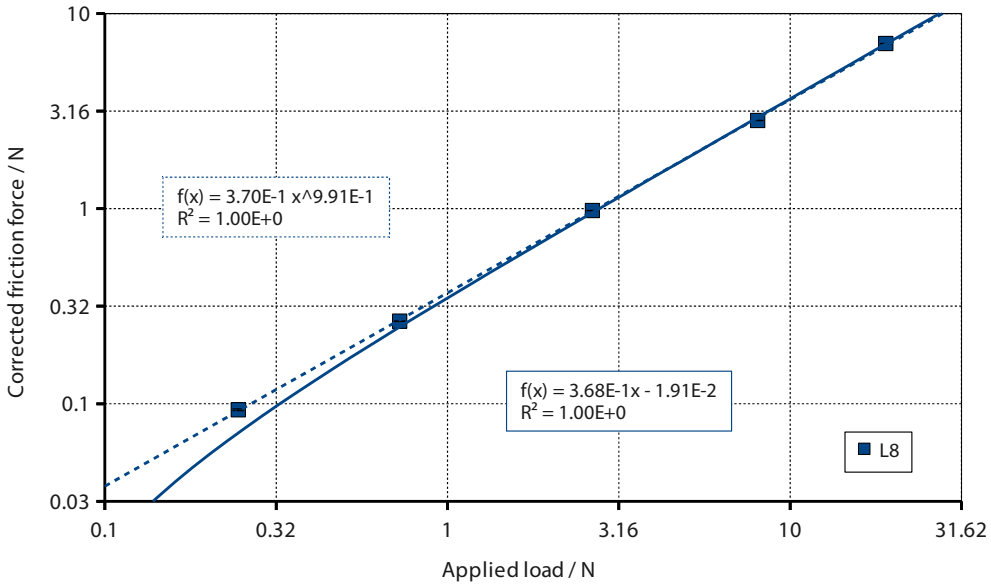

(**b**) NW6, 0.167 mm · s^{-1}

Figure E.5: Summary plots of *corrected* friction force against load for each of the three nonwovens against each Lorica Soft slider at all sliding speeds considered. Force error bars are present though they are very small. *Continues…*

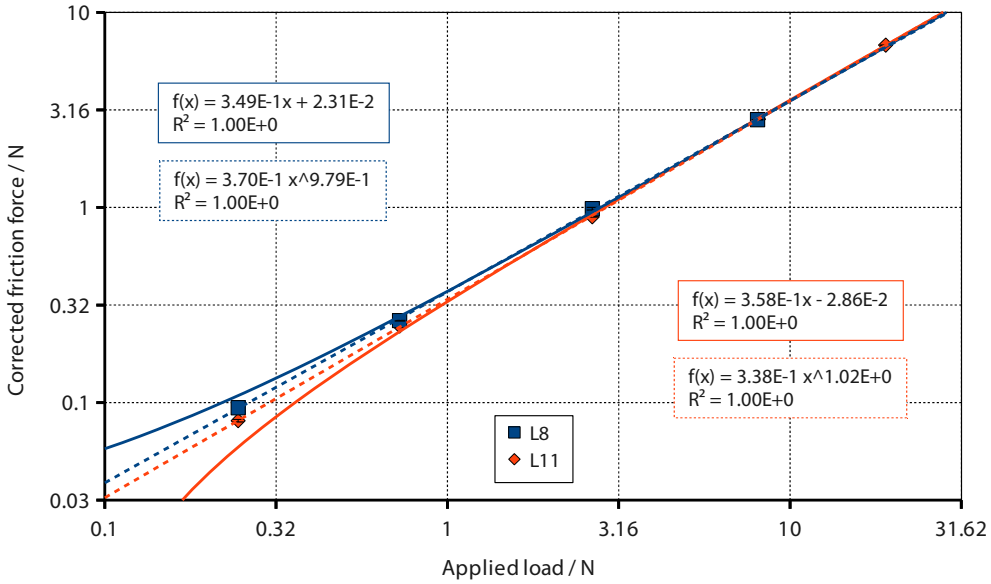

(c) NW6, 0.5 mm · s^{-1}

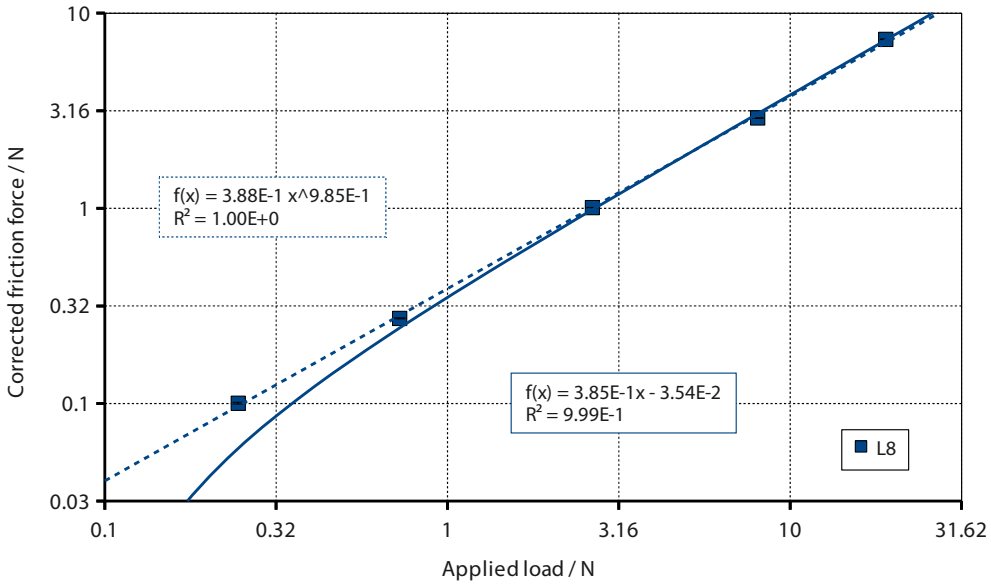

(d) NW6, 1.67 mm · s^{-1}

Figure E.5: … *Continued; Continues…*

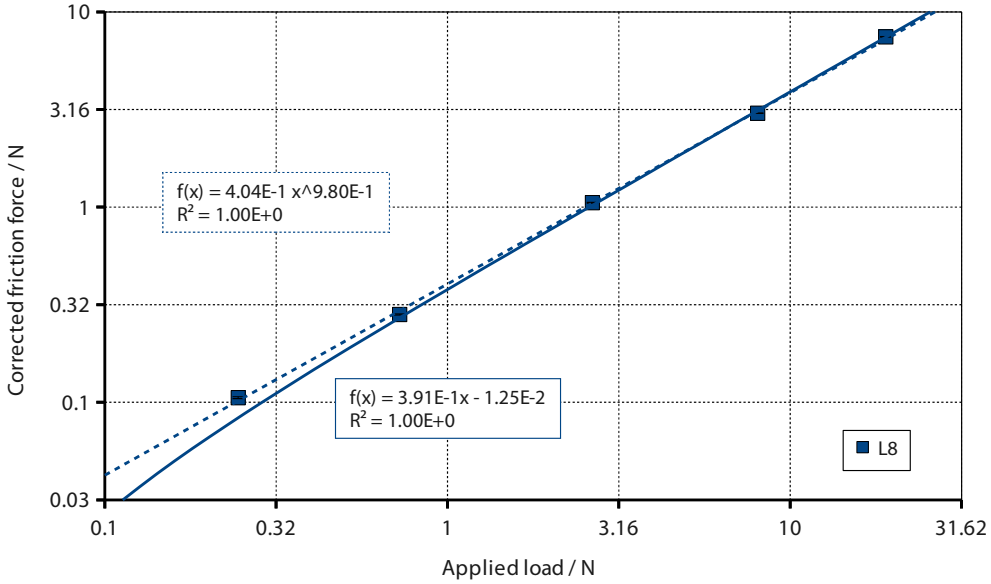

(**e**) NW6, 5 mm · s^{-1}

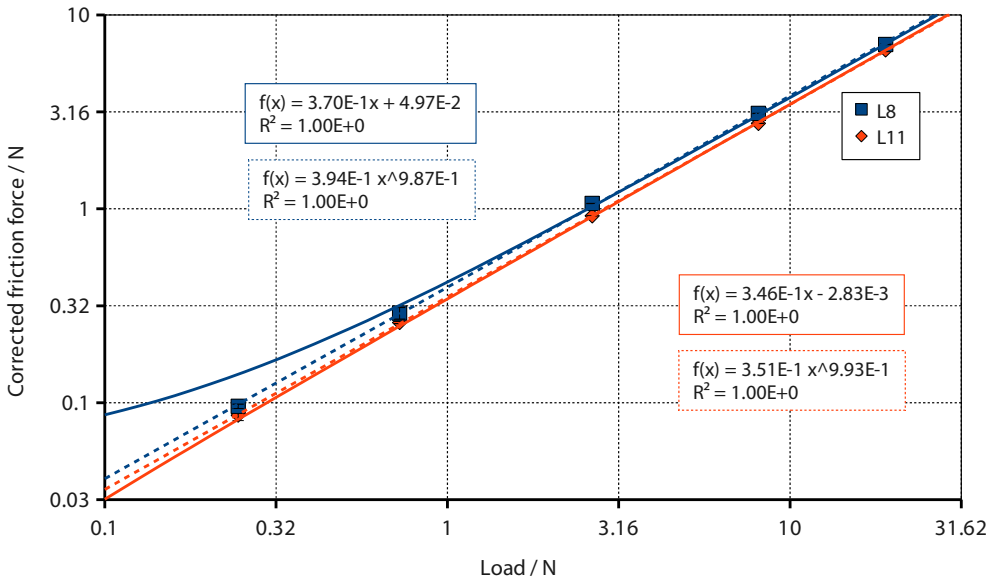

(**f**) NW3, 0.5 mm · s^{-1}

Figure E.5: … *Continued; Continues…*

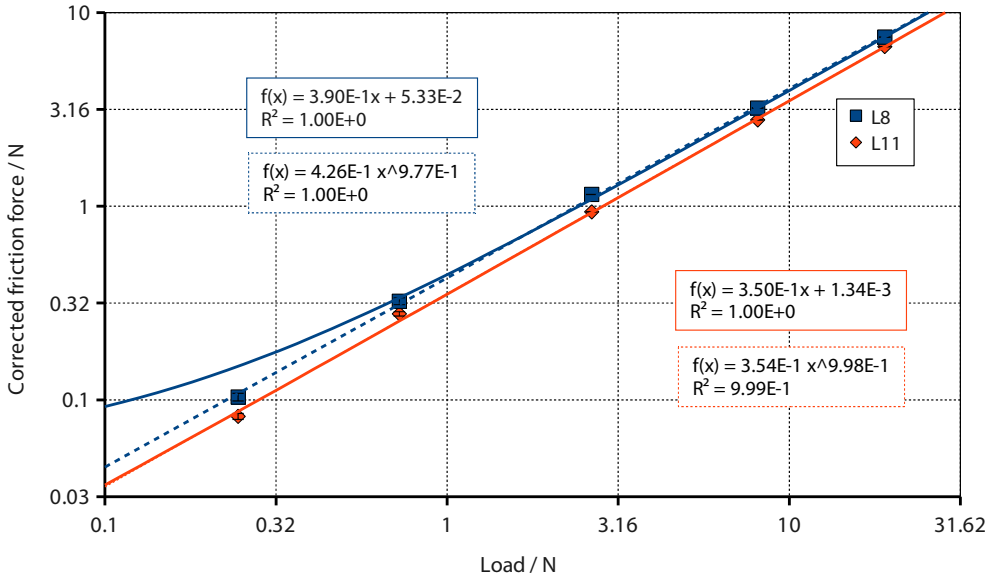

(**g**) NW1, 0.5 mm · s^{-1}

Figure E.5: *…Continued.*

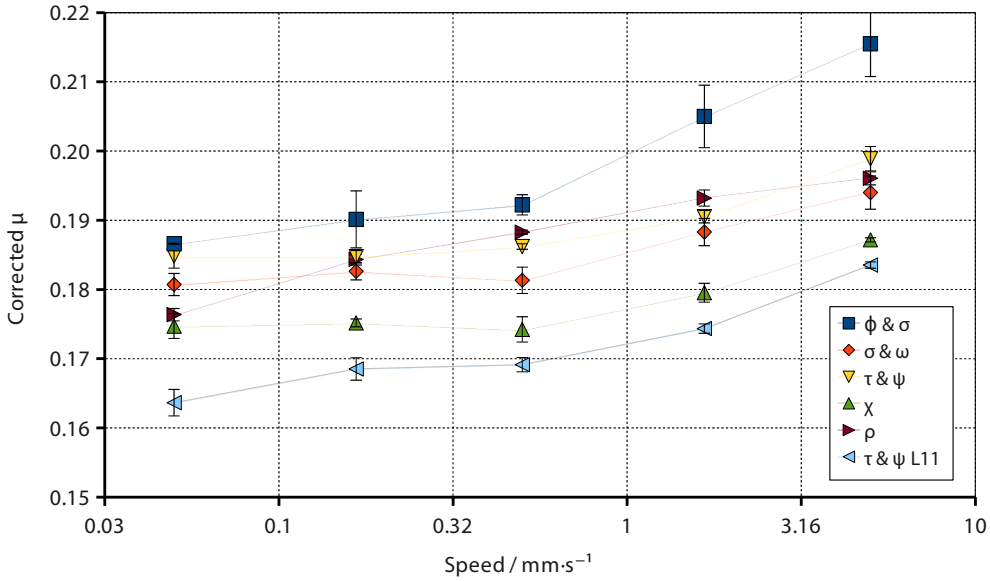

(**a**) NW6; the slider is L8 unless stated otherwise

Figure E.6: Summary plots of pointwise calculated coefficients of friction against velocity for each of the three nonwovens against each Lorica Soft slider at each load considered. *Continues…*

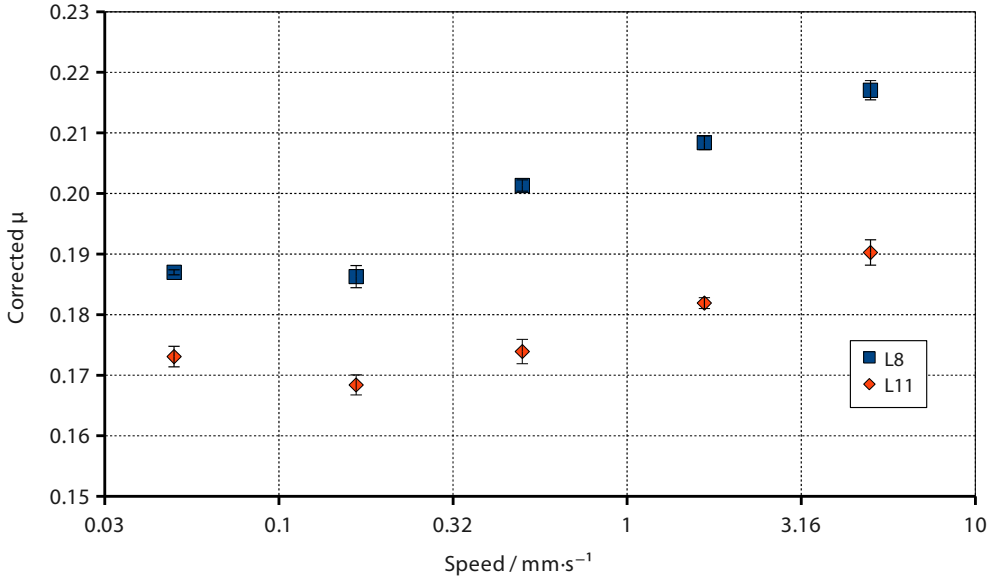

(**b**) NW3

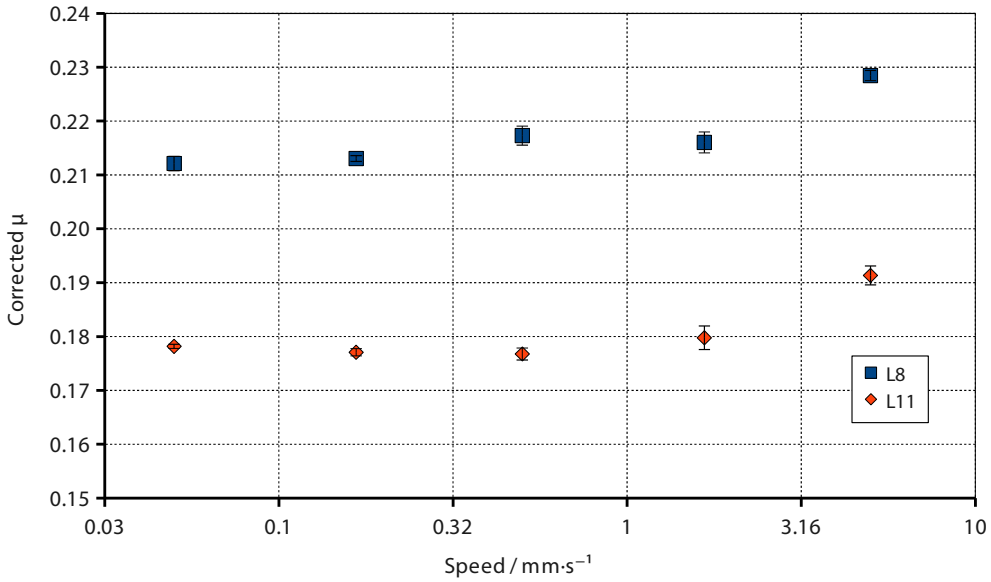

(**c**) NW1

Figure E.6: … *Continued.*

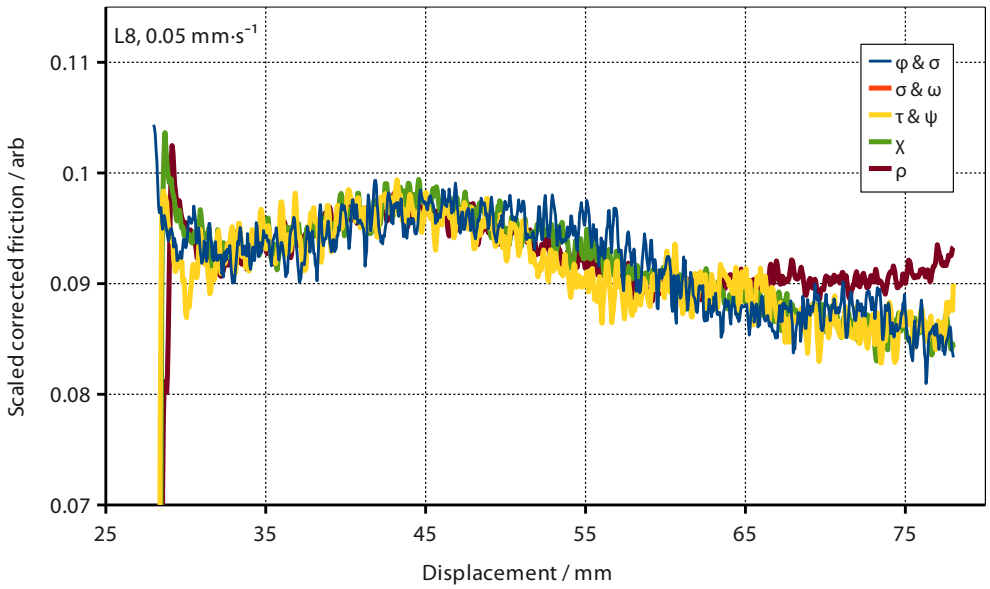

(**a**) NW6, L8, 0.05 mm · s^{-1}

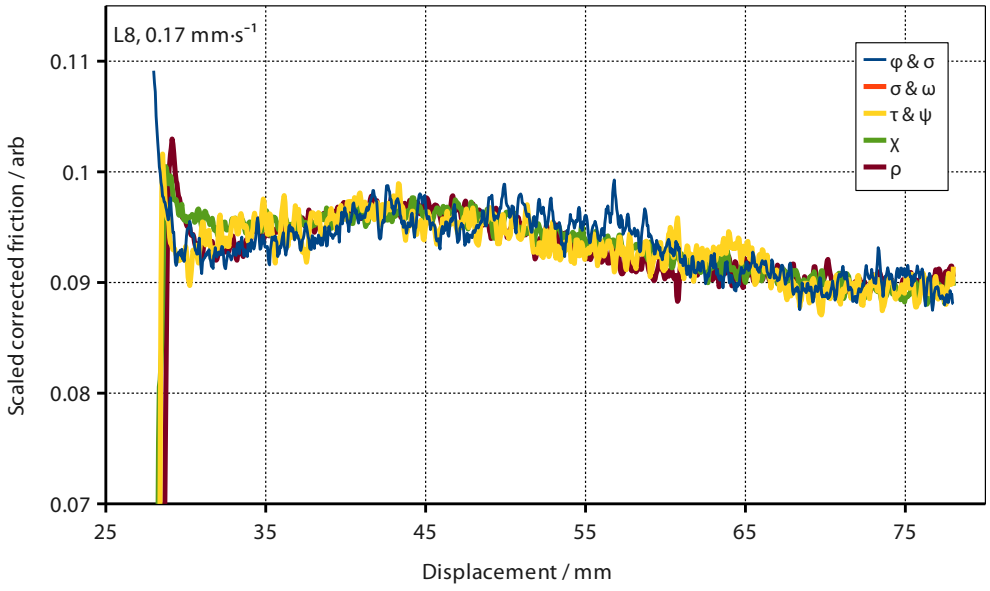

(**b**) NW6, L8, 0.167 mm · s^{-1}

Figure E.7: By application of a linear transform, most of the traces for a given interface at a given sliding speed can be superimposed. Missing traces indicate that this was not possible for that trace. *Continued…*

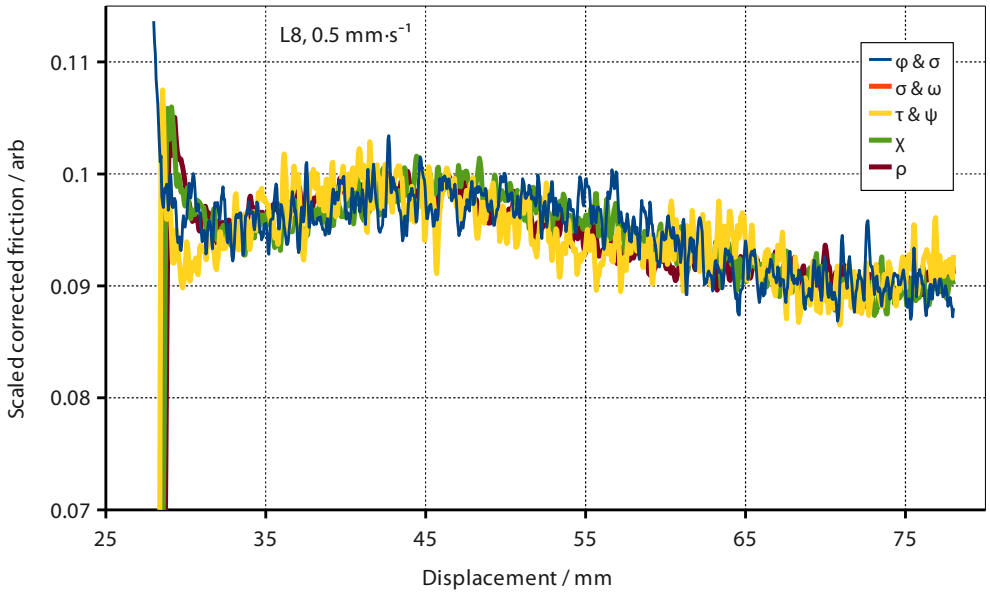

(**c**) NW6, L8, 0.5 mm · s^{-1}

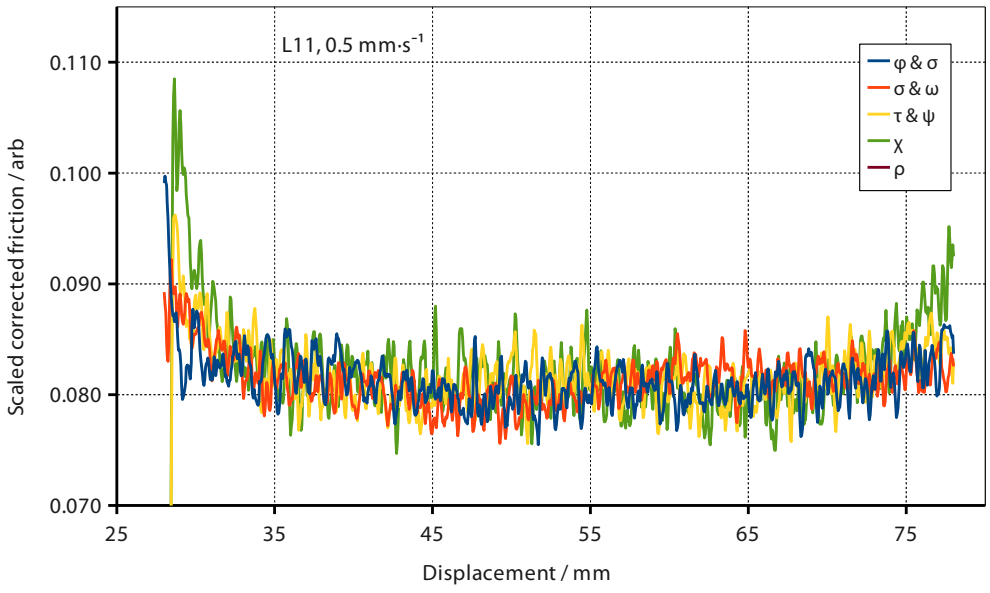

(**d**) NW6, L11, 0.5 mm · s^{-1}

Figure E.7: … *Continued; Continues…*

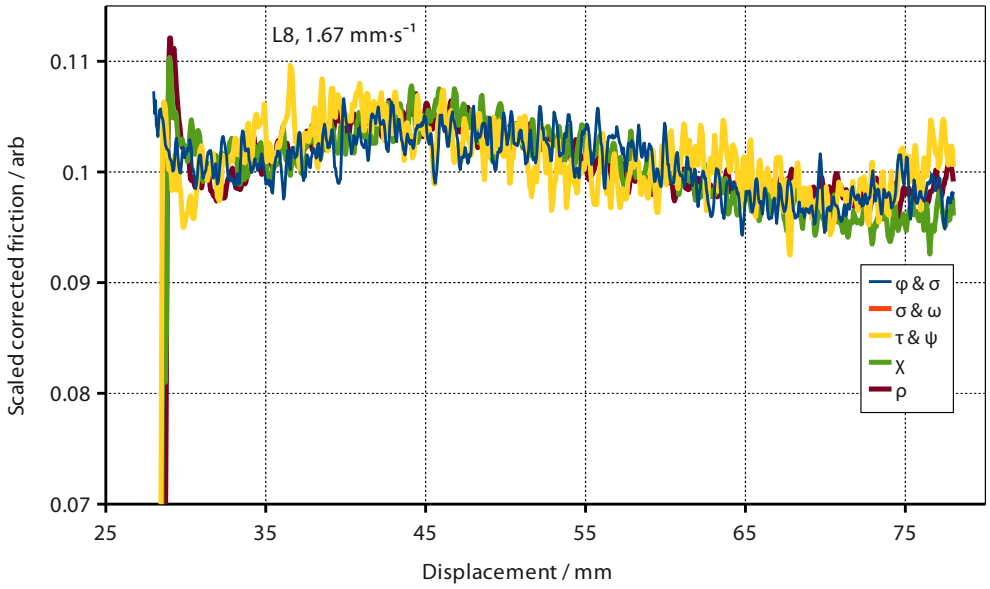

(e) NW6, L8, 1.67 mm · s^{-1}

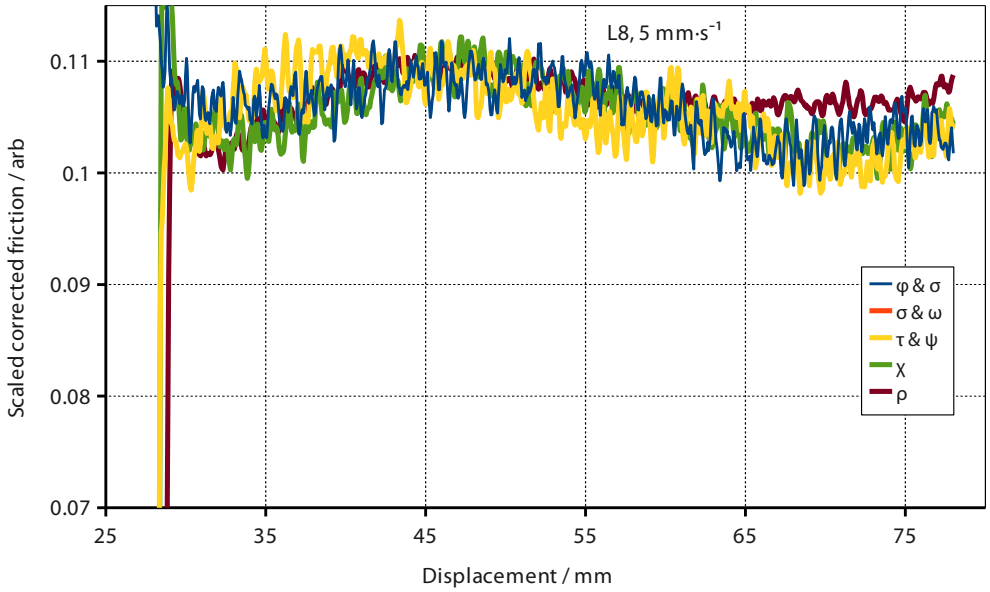

(f) NW6, L8, 5 mm · s^{-1}

Figure E.7: … *Continued; Continues…*

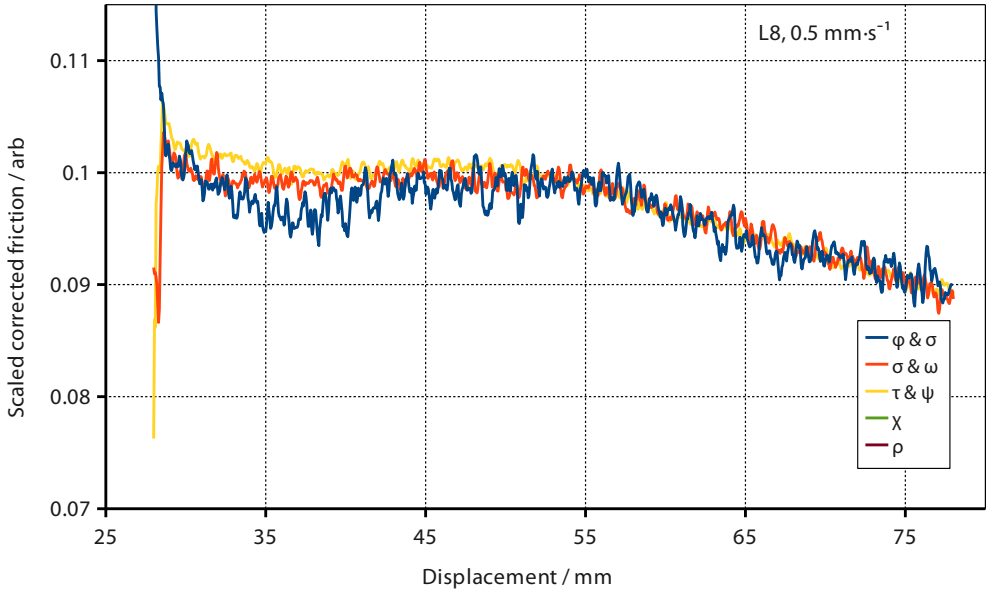

(**g**) NW3, L8, 0.5 mm · s^{-1}

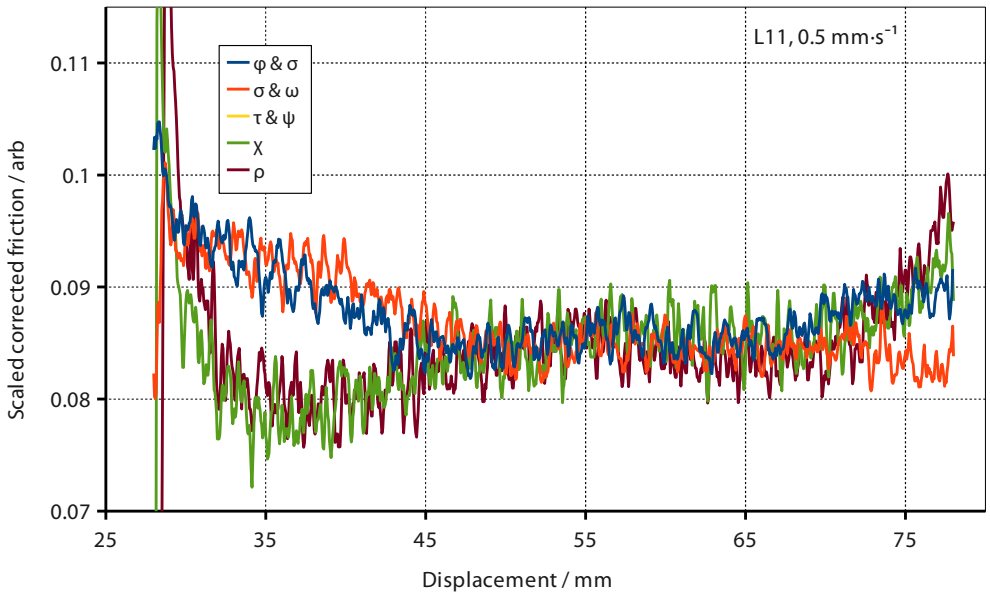

(**h**) NW3, L11, 0.5 mm · s^{-1}

Figure E.7: … *Continued; Continues…*

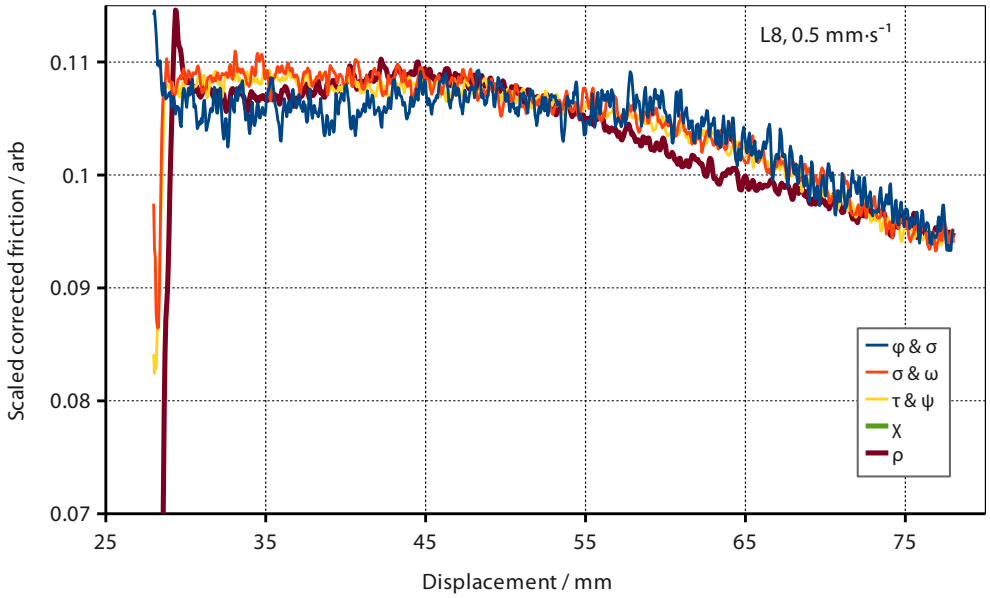

(**i**) NW1, L8, 0.5 mm · s^{-1}

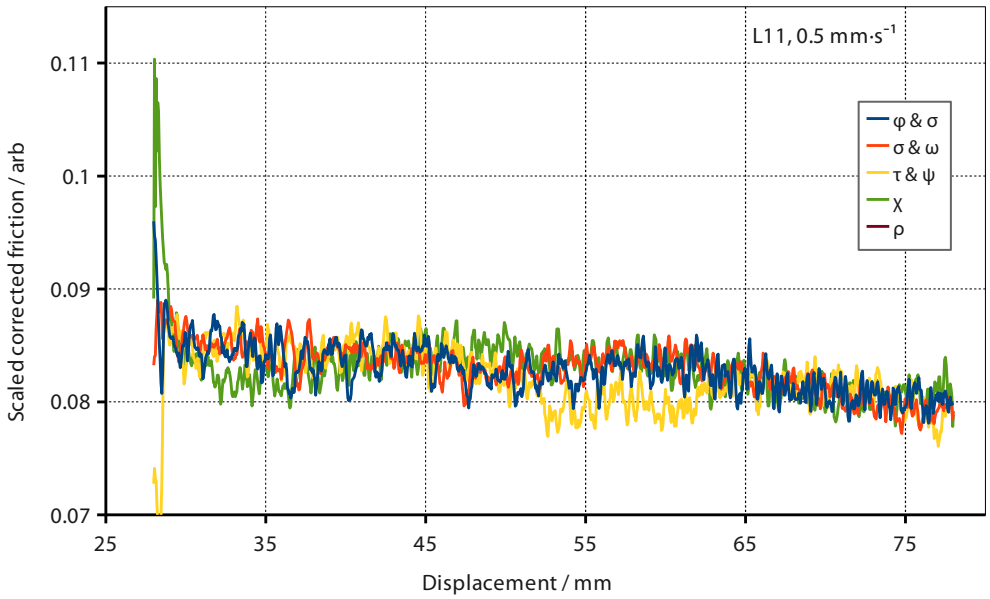

(**j**) NW1, L11, 0.5 mm · s^{-1}

Figure E.7: … *Continued.*

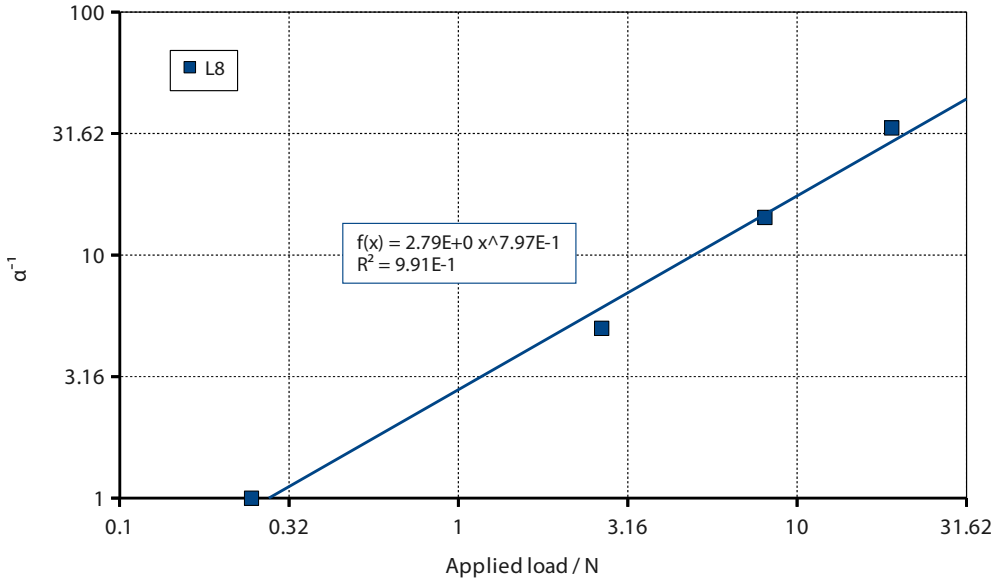

(**a**) NW6, 0.05 mm · s^{-1}

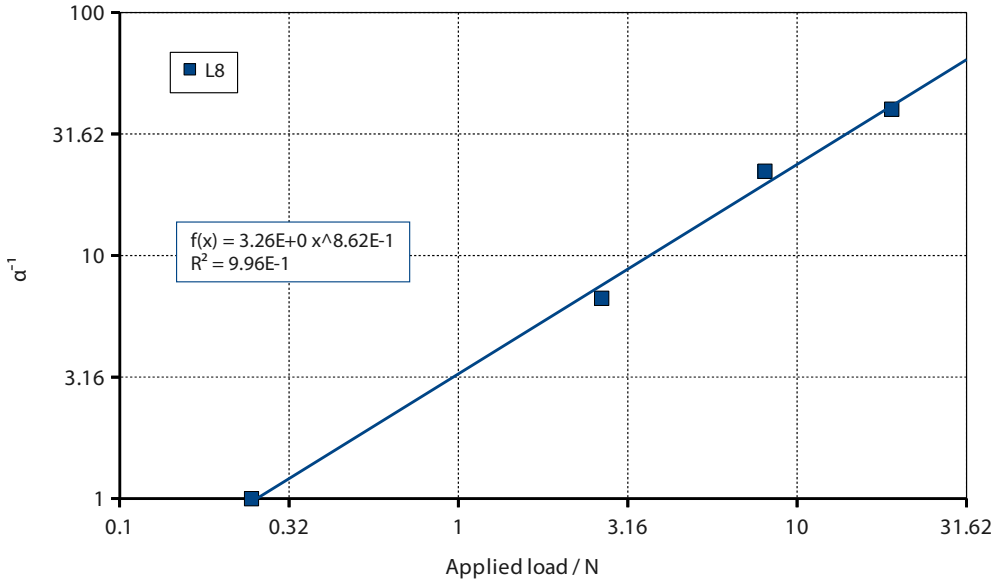

(**b**) NW6, 0.167 mm · s^{-1}

Figure E.8: Plots of α^{-1} against applied load for all examined combinations of nonwoven, Lorica Soft slider, and velocity. *Continued…*

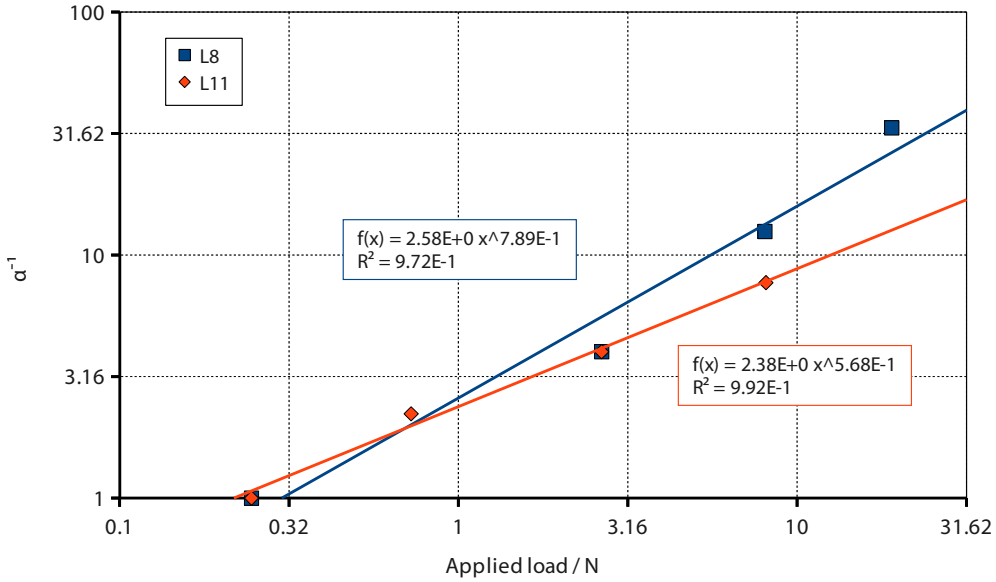

(c) NW6, 0.5 mm · s^{-1}

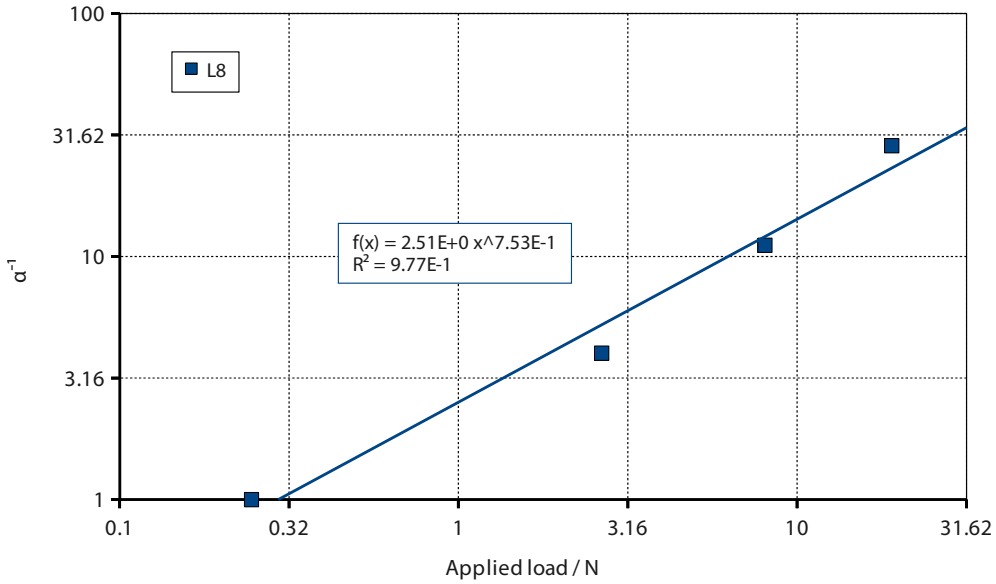

(d) NW6, 1.67 mm · s^{-1}

Figure E.8: … *Continued; Continues…*

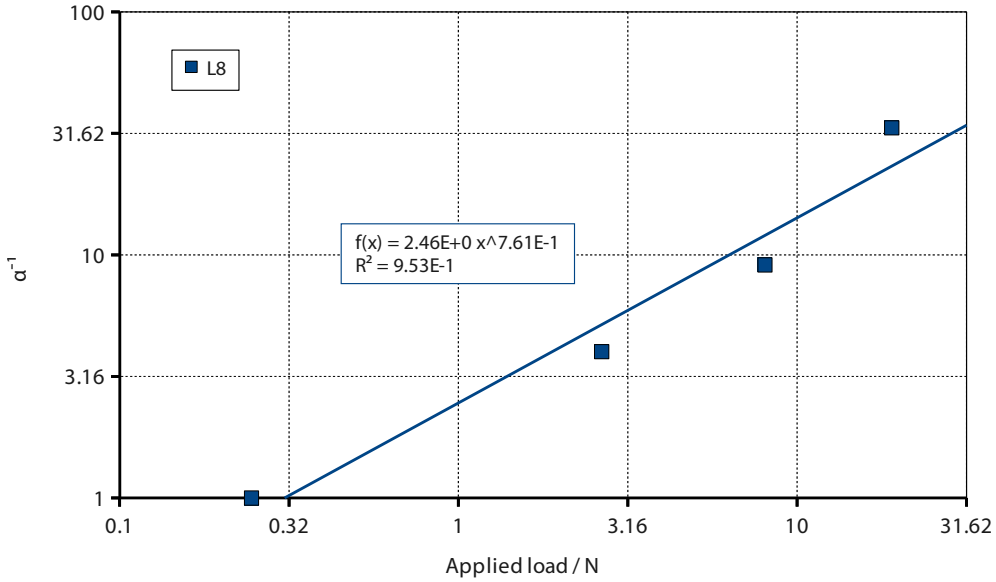

(**e**) NW6, 5 mm · s^{-1}

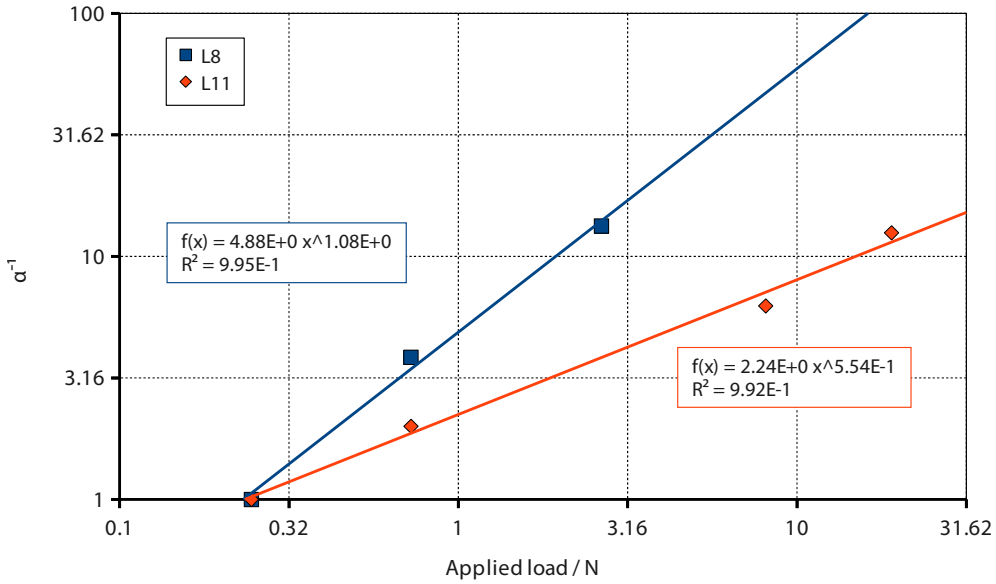

(**f**) NW3, 0.5 mm · s^{-1}

Figure E.8: … *Continued; Continues…*

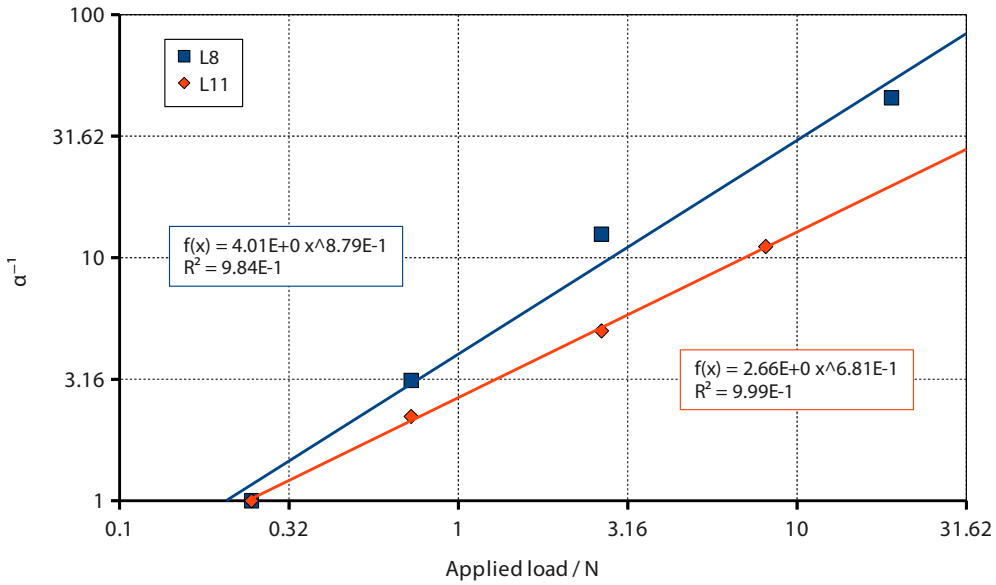

(**g**) NW1, 0.5 mm · s^{-1}

Figure E.8: … *Continued.*

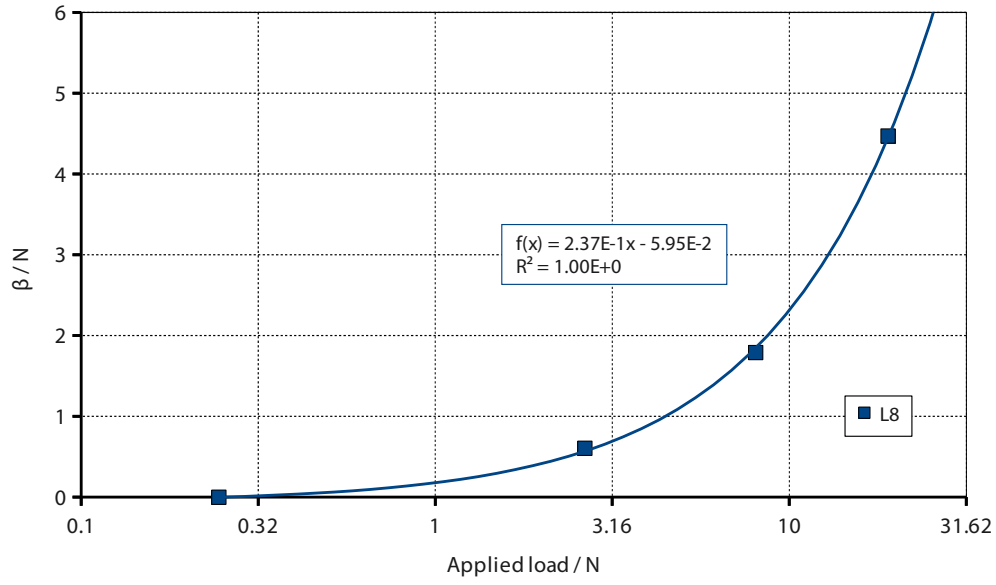

(**a**) NW6, 0.05 mm · s^{-1}

Figure E.9: Plots of β against applied load for all examined combinations of nonwoven, Lorica Soft slider, and velocity. *Continued…*

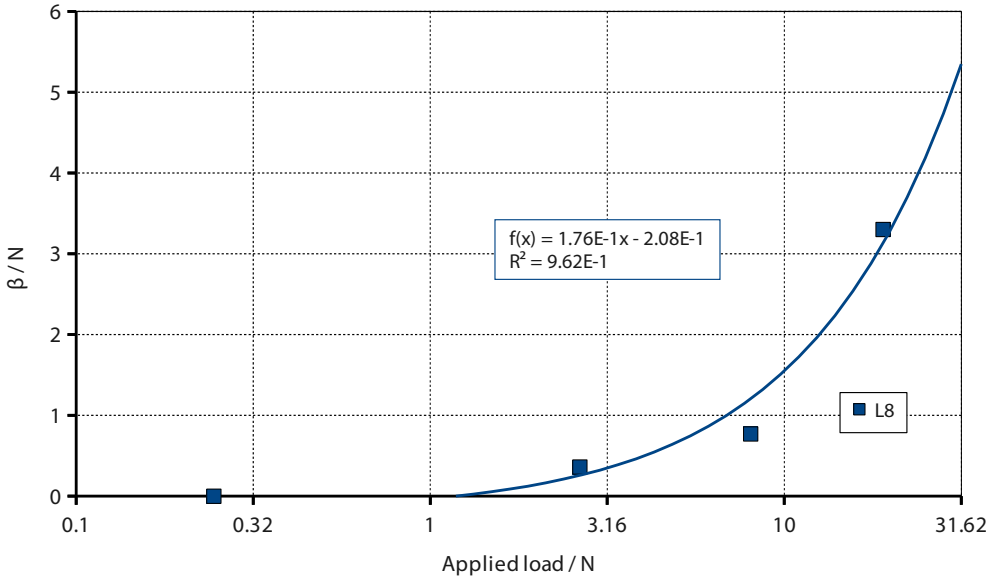

(**b**) NW6, 0.167 mm · s^{-1}

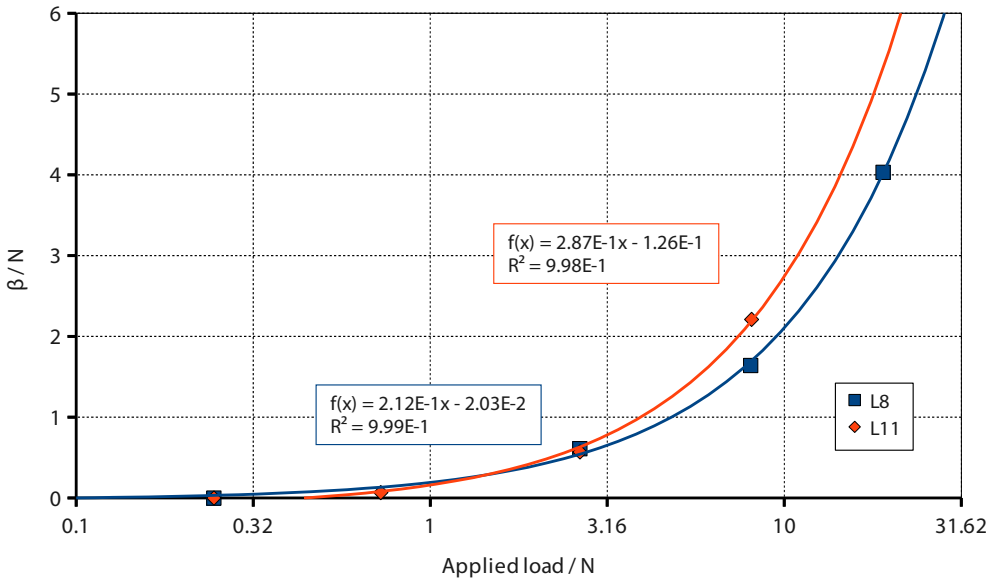

(**c**) NW6, 0.5 mm · s^{-1}

Figure E.9: … *Continued; Continues…*

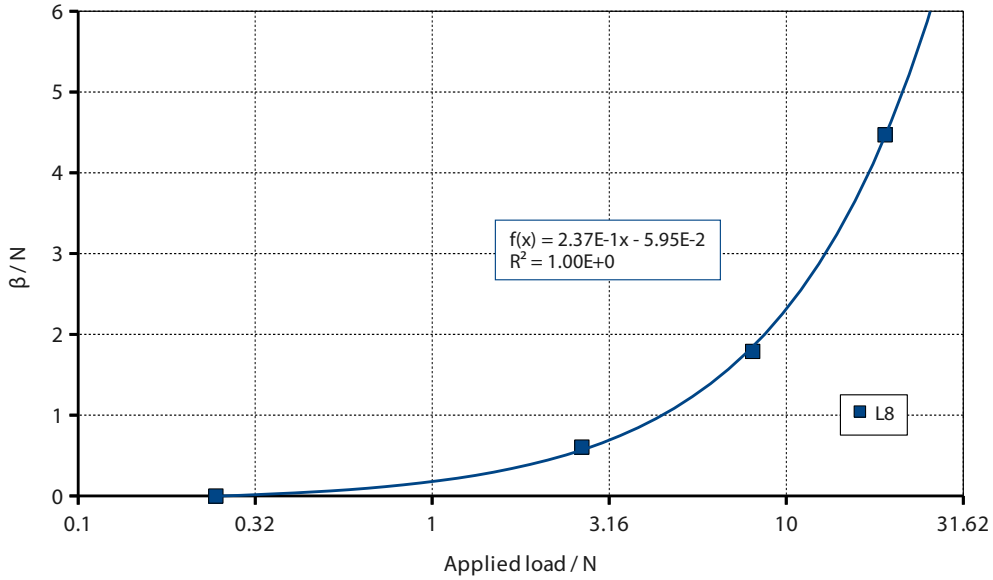

(**d**) NW6, 1.67 mm · s^{-1}

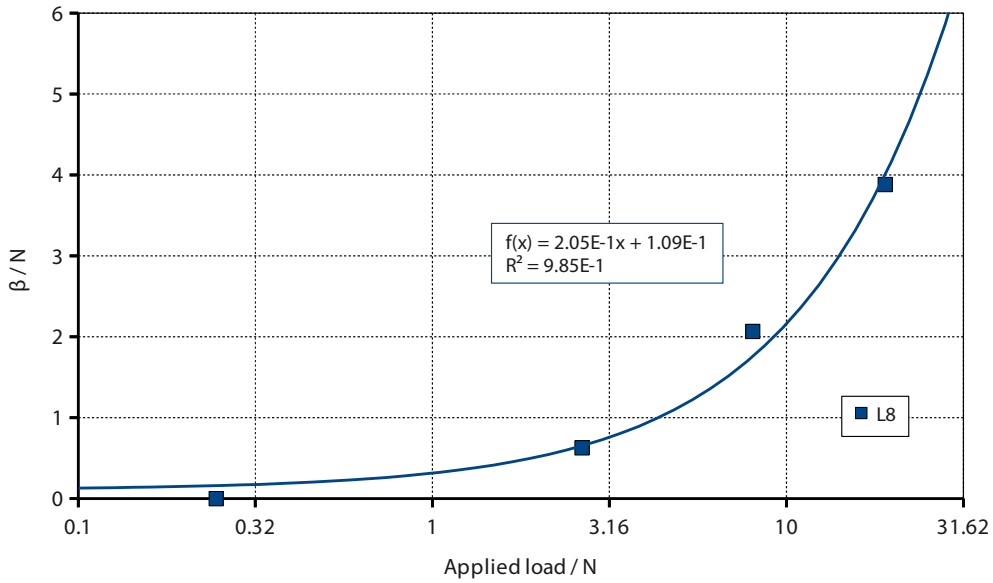

(**e**) NW6, 5 mm · s^{-1}

Figure E.9: … *Continued; Continues…*

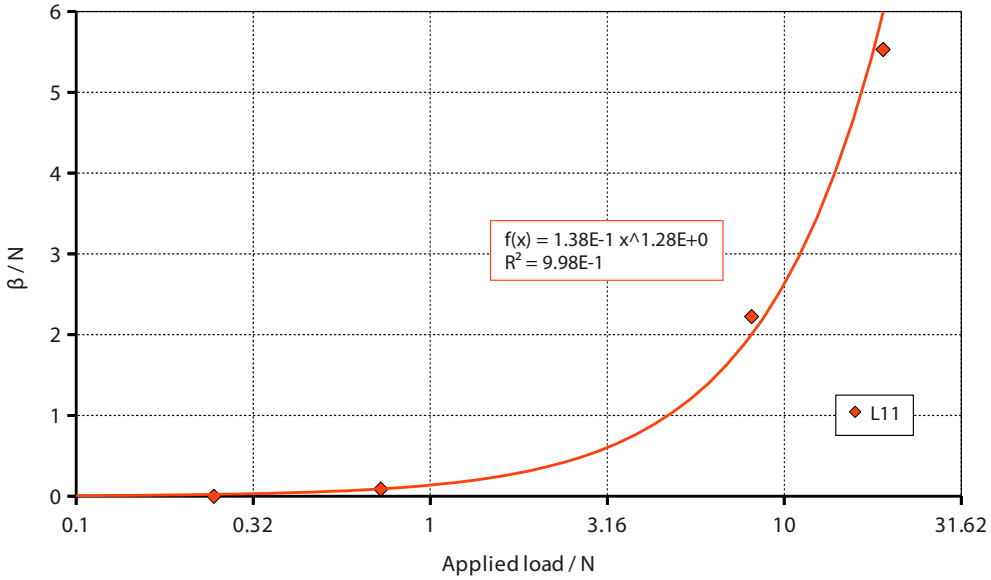

(**f**) NW3, 0.5 mm · s^{-1}

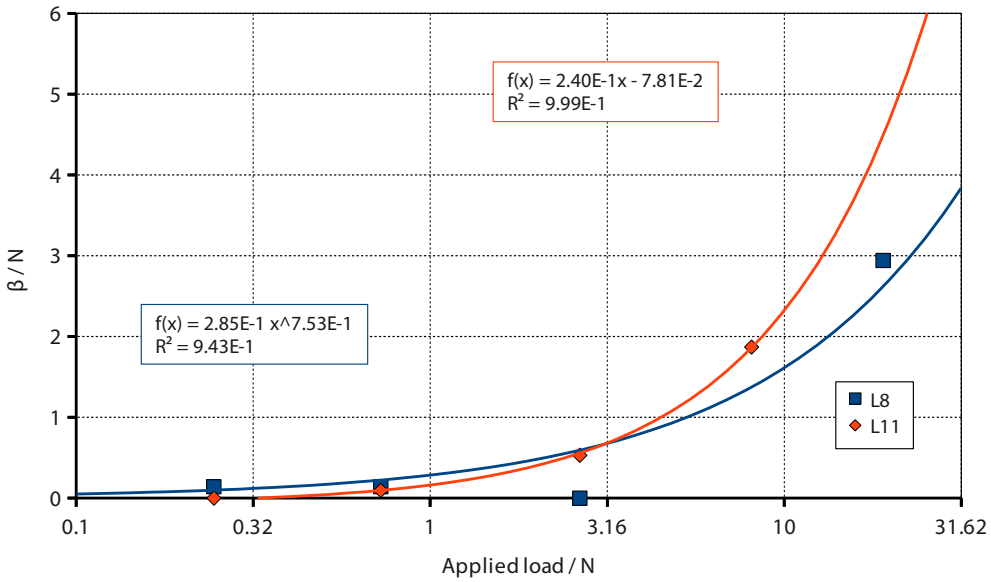

(**g**) NW1, 0.5 mm · s^{-1}

Figure E.9: … *Continued.*

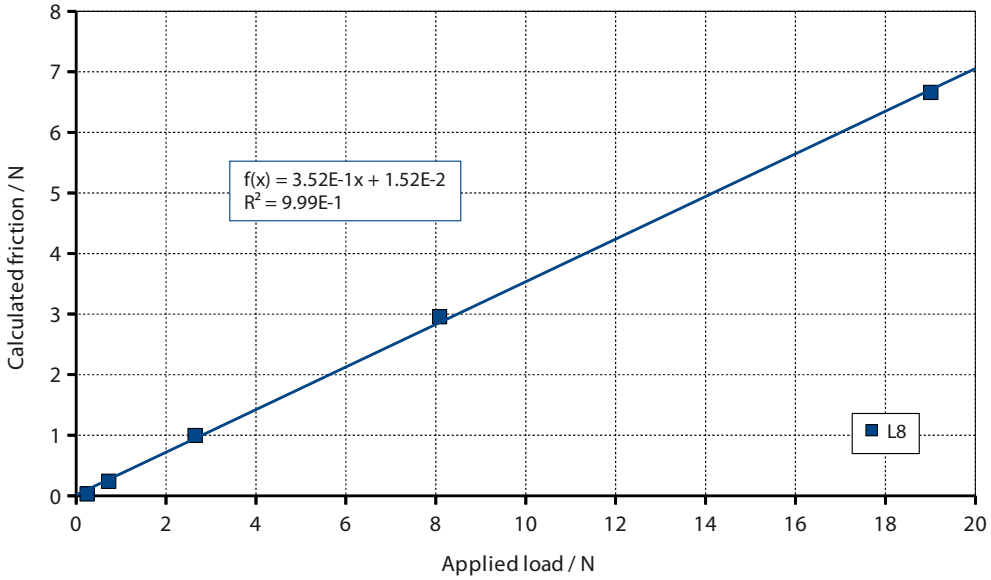

(**a**) NW6, 0.05 mm · s^{-1}

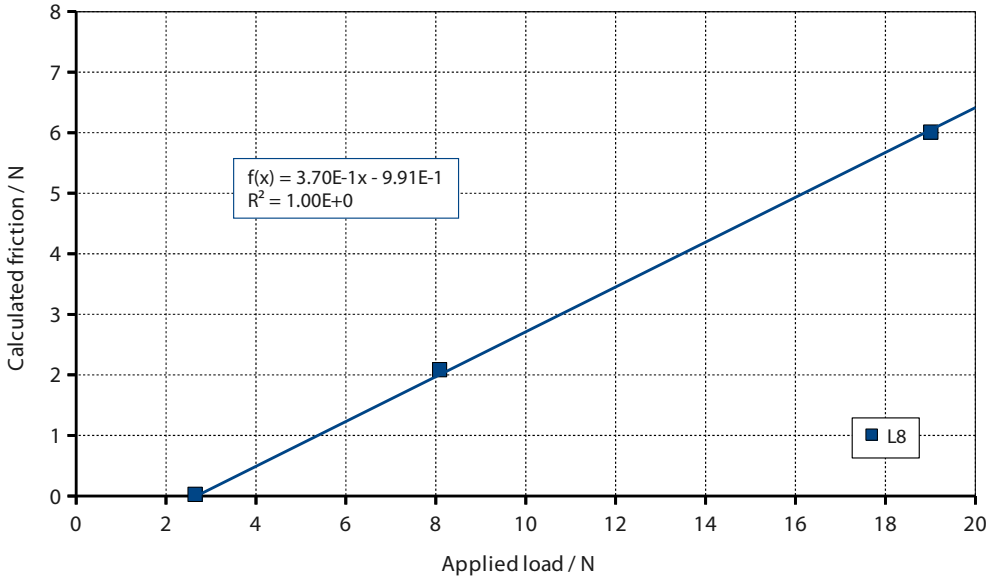

(**b**) NW6, 0.167 mm · s^{-1}

Figure E.10: Graphs of *calculated* friction against load based on the sum of two terms (principal and remainder) where the index of the principal terms with respect to load and the gradient of the remainder term are fixed, and the coefficient of the principal and the offset of the remainder term are free. Both have been manipulated so that the shown least-squares linear best fit matches the *observed* friction-load curve for the interface and sliding speed at hand. *Continued…*

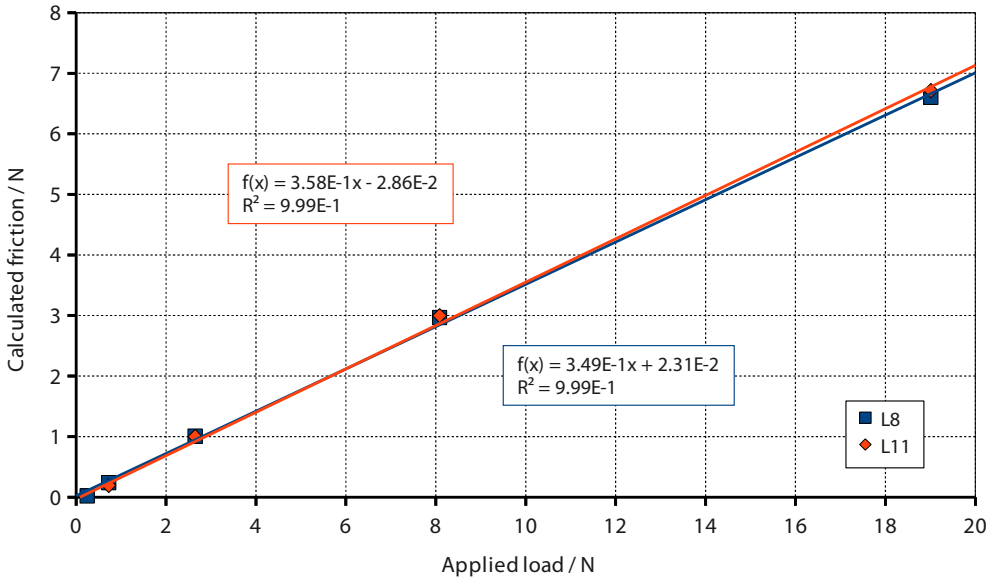

(c) NW6, 0.5 mm · s^{-1}

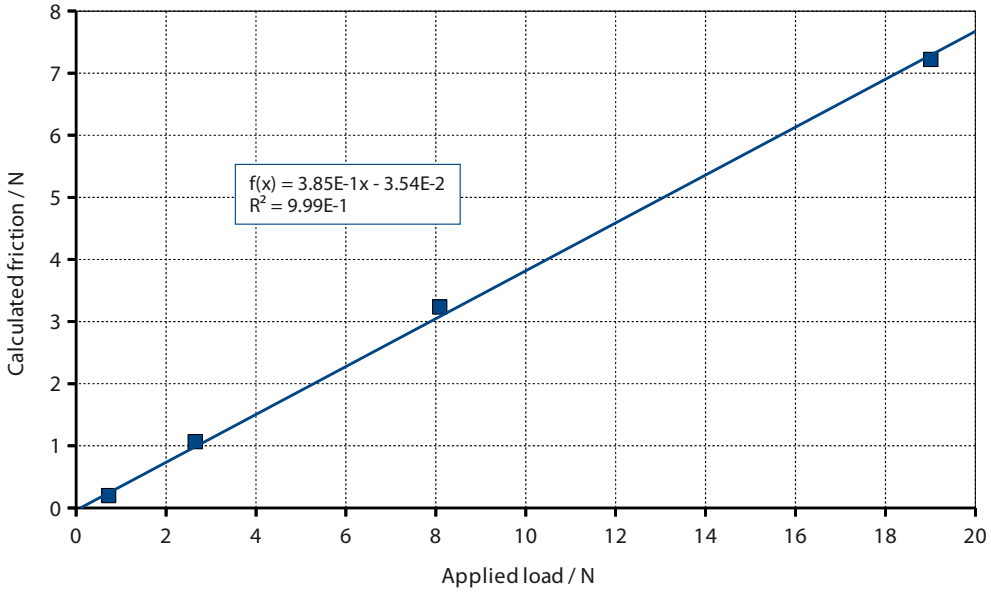

(d) NW6, 1.67 mm · s^{-1}

Figure E.10: … *Continued; Continues…*

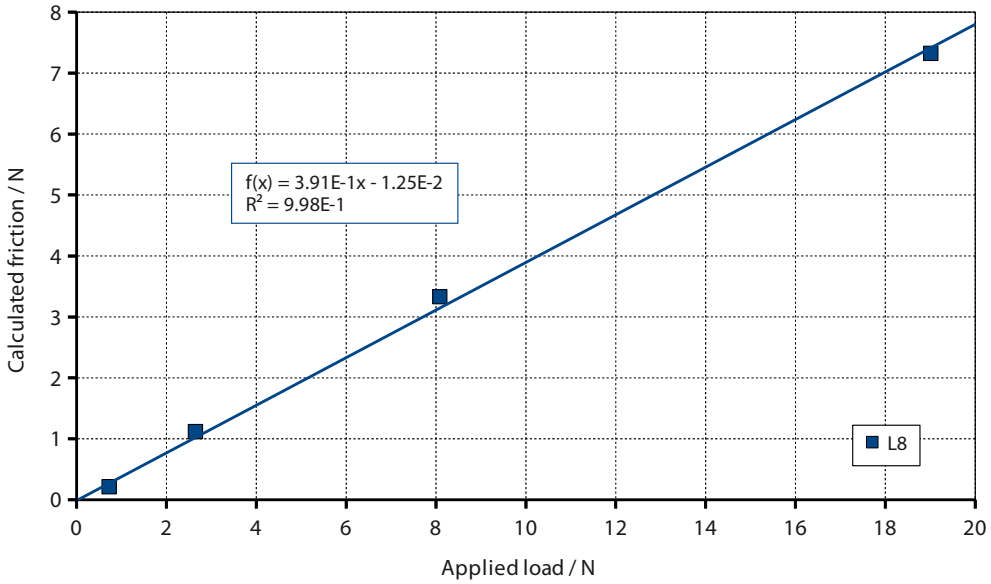

(e) NW6, 5 mm · s^{-1}

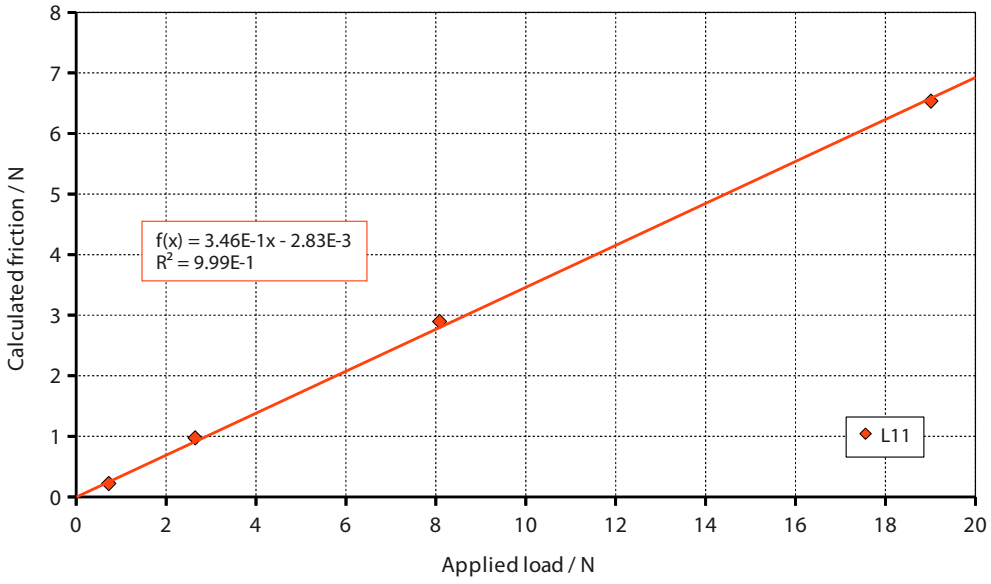

(f) NW3, 0.5 mm · s^{-1}

Figure E.10: … *Continued; Continues…*

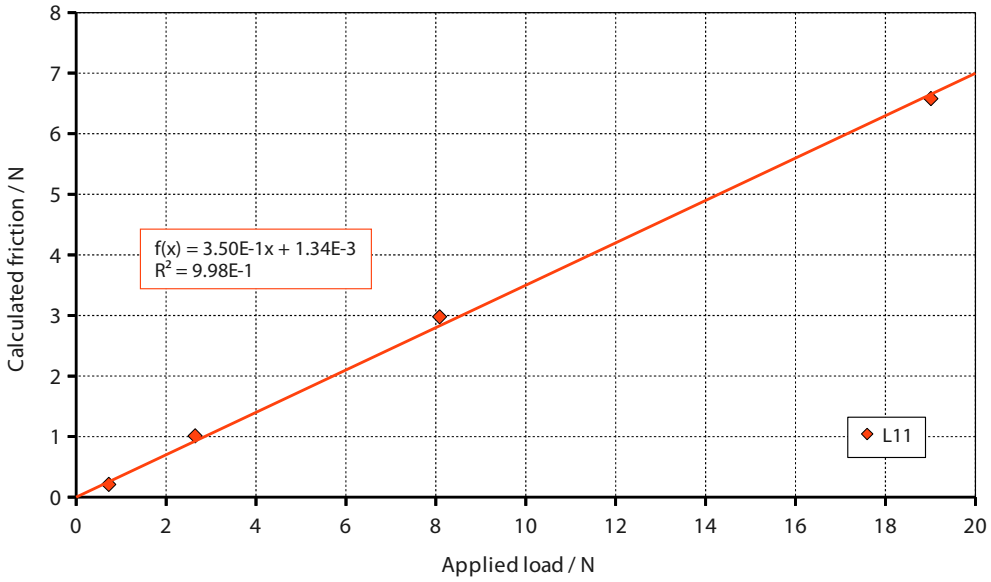

(g) NW1, $0.5\,\mathrm{mm}\cdot\mathrm{s}^{-1}$

Figure E.10: … *Continued.*

Appendix F

Normal velocity and acceleration at interfaces

In §5.3.2 the relationship between stress and contact forces at an accelerating contact was established, subject to the assumption that the two surfaces remained in contact throughout. It was stated there that this required that the normal components of both acceleration and velocity for the two surfaces were the same,

$$\dot{\chi}_n \cdot \hat{N} = \dot{\chi}_s \cdot \hat{N} \quad , \quad \ddot{\chi}_n \cdot \hat{N} = \ddot{\chi}_s \cdot \hat{N}. \tag{F.1}$$

No explanation of the apparent contradiction was offered in §5.3.2: it is given here.

F.1 Elucidation of the apparent contradiction

At first sight, the equations F.1 appear to force rather stringent constraints on the evolution of the unit normal, but do not provide or describe a mechanism for enforcing them: a naïve differentiation of the velocity conditions would appear to produce

$$\text{“}\ddot{\chi}_n \cdot \hat{N} + \dot{\chi}_n \cdot \dot{\hat{N}} = \ddot{\chi}_s \cdot \hat{N} + \dot{\chi}_s \cdot \dot{\hat{N}}\text{”}, \tag{F.2}$$

apparently requiring “$\dot{\chi}_n \cdot \dot{\hat{N}} = \dot{\chi}_s \cdot \dot{\hat{N}}$”. However, this equation does not mean what it at first appears to. Recall that the superposed dot represents a material picture derivative (§2.1.1), and consider the changes in

$$\dot{\chi}_n(X_n, t) \cdot \hat{N}_n(X_n, t) = \dot{\chi}_s(X_s, t) \cdot \hat{N}_s(X_s, t)$$

over a time increment dt. In this increment, the changes on either side are

$$\begin{aligned} \dot{\chi}_n(X_n, t+dt) \cdot \hat{N}_n(X_n, t+dt) - \dot{\chi}_n(X_n, t) \cdot \hat{N}_n(X_n, t) \\ = \dot{\chi}_s(X_s, t+dt) \cdot \hat{N}_s(X_s, t+dt) - \dot{\chi}_s(X_s, t) \cdot \hat{N}_s(X_s, t), \end{aligned} \tag{F.3}$$

but in this time the spatial location of the particles with reference position X_n and X_s have also changed:

$$\chi_n(X_n, t) \to \chi_n(X_n, t+dt) = \chi_n(X_n, t) + \dot{\chi}_n(X_n, t)dt,$$

$$\chi_s(\mathbf{X}_s, t) \to \chi_s(\mathbf{X}_s, t + dt) = \chi_s(\mathbf{X}_s, t) + \dot{\chi}_s(\mathbf{X}_s, t)dt.$$

There is certainly no requirement that the velocity components orthogonal to the normal are equal, so the spatial locations described by either side of equation F.3 are generally not the same. The equation F.2 is *not* incorrect, but it does not mean what it might be supposed to: it relates to the behaviour of particles on their own respective flowlines which were coincident at time t, not to the behaviour of material at a fixed location at time t.

Now that it is clear why there is no obvious contradiction in §5.3.2, the reasons why equations F.1 hold can be considered.

F.2 Demonstration of the mutual necessity of equations F.1

Consider material particles N and S at positions $\mathbf{x}_N$ and $\mathbf{x}_S$ in the nonwoven and substrate, respectively, at time $t - dt$. Require that $(\mathbf{x}_N - \mathbf{x}_S) \cdot \hat{\mathbf{N}} = 0$—that is that the two particles are both at the interface—and consider the requirements on the local velocity fields such that the particles coincide at time t.

$$\mathbf{x}_N \to \mathbf{x}_N + \dot{\chi}_n(\mathbf{x}_N, t - dt)dt \quad , \quad \mathbf{x}_S \to \mathbf{x}_S + \dot{\chi}_s(\mathbf{x}_S, t - dt)dt$$

so

$$\mathbf{x}_N + \dot{\chi}_n(\mathbf{x}_N, t - dt)dt = \mathbf{x}_S + \dot{\chi}_s(\mathbf{x}_S, t - dt)dt = \mathbf{x} \tag{F.4}$$

Now take the dot product of equation F.4 with $\hat{\mathbf{N}}$:

$$\{\mathbf{x}_N + \dot{\chi}_n(\mathbf{x}_N, t - dt)dt\} \cdot \hat{\mathbf{N}} = \{\mathbf{x}_S + \dot{\chi}_s(\mathbf{x}_S, t - dt)dt\} \cdot \hat{\mathbf{N}}$$

hence

$$\dot{\chi}_n(\mathbf{x}_N, t - dt) \cdot \hat{\mathbf{N}} = \dot{\chi}_s(\mathbf{x}_S, t - dt) \cdot \hat{\mathbf{N}}. \tag{F.5}$$

since $(\mathbf{x}_N - \mathbf{x}_S) \cdot \hat{\mathbf{N}} = 0$. In order to avoid the pitfall exposed in §F.1 the flux vectors must be expressed in terms of the location $\mathbf{x}$. Consider for the moment the left hand side of equation F.5. Recalling that $\mathbf{x}_N = \mathbf{x} - \dot{\chi}_n(\mathbf{x}_N, t - dt)dt$,

$$\begin{aligned}
\dot{\chi}_n(\mathbf{x}_N, t - dt) \cdot \hat{\mathbf{N}} &= \dot{\chi}_n(\mathbf{x} - \dot{\chi}_n(\mathbf{x} - \dot{\chi}_n(\cdots)dt, t - dt)dt, t - dt) \cdot \hat{\mathbf{N}} \\
&= \{\dot{\chi}_n(\mathbf{x}, t) - \dot{\chi}_n(\mathbf{x}, t) \cdot \nabla\dot{\chi}_n(\mathbf{x}, t)dt - dt\dot{\chi}_n(\mathbf{x}, t) \\
&\qquad - dt\partial_t\dot{\chi}_n(\mathbf{x}, t) + \mathcal{O}(dt^2)\} \cdot \hat{\mathbf{N}} \\
&= \{\dot{\chi}_n(\mathbf{x}, t) - dt\ddot{\chi}_n(\mathbf{x}, t) + \mathcal{O}(dt^2)\} \cdot \hat{\mathbf{N}}.
\end{aligned}$$

Substituting this back into equation F.5, it follows that

$$\{\dot{\chi}_n(\mathbf{x}, t) - dt\ddot{\chi}_n(\mathbf{x}, t) + \mathcal{O}(dt^2)\} \cdot \hat{\mathbf{N}} = \{\dot{\chi}_s(\mathbf{x}, t) - dt\ddot{\chi}_s(\mathbf{x}, t) + \mathcal{O}(dt^2)\} \cdot \hat{\mathbf{N}} \tag{F.6}$$

Equation F.6 makes it clear that for particles on the mutual boundary to remain on the mutual boundary the condition of matched normal velocity does *not* contradict but rather *implies* matched normal acceleration.

Bibliography

[1] Cottenden, A. M., Wong, W. K. R., Cottenden, D. J. & Farbrot, A. Development and validation of a new method for measuring friction between skin and nonwoven materials. *J. Eng. Med.* **222**, 791–803 (2008).

[2] Keller, B. P. J. A., Wille, J., van Ramshorst, B. & van den Werken, C. Pressure ulcers in intensive care patients: a review of risks and prevention. *Intensive Care Med.* **28**, 1379–1388 (2002).

[3] Runeman, B. Skin interaction with absorbent hygiene products. *Clinics in Dermatology* **26**, 45–51 (2008).

[4] Good practice in continence services. Tech. Rep., Department of Health, UK, London (2000).

[5] Schallamach, A. The load dependence of rubber friction. *Proc. Phys. Soc. B* **65**, 657–661 (1952).

[6] Bowden, F. & Tabor, D. *The friction and lubrication of solids*, chap. 1 (OUP, Oxford, UK, 1986).

[7] Greenwood, J. & Tabor, D. The friction of hard sliders on lubricated rubber: the importance of deformation losses. *Proc. Phys. Soc.* **71**, 989–1001 (1958).

[8] Gent, A. Friction and wear of highly-elastic solids. *Wear* **29**, 111–116 (1974).

[9] Barquins, M. & Roberts, A. Rubber friction variation with rate and temperature: some new observations. *J. Phys. D: Appl. Phys.* **19**, 547–563 (1986).

[10] Truesdell, C. & Noll, W. *The non-linear field theories of mechanics* (Springer, 1965).

[11] Pressley, A. *Elementary differential geometry* (Springer-Verlag, London, UK, 2001).

[12] Weisstein, E. W. Convective derivative. URL http://mathworld.wolfram.com/ConvectiveDerivative.html. From "Mathworld"–A Wolfram web resource, Accessed 26/09/2010.

[13] Timoshenko, S. & Goodier, J. *Theory of elasticity*, chap. 8 (McGraw-Hill, 1970).

[14] Johnson, K. *Contact Mechanics* (CUP, Cambridge, UK, 1985).

[15] Lee, Y. An alternative derivation of the polar decomposition. *Mech. Res. Commun.* **26**, 525–528 (1999).

[16] Acharya, A. On compatibility conditions for the left Cauchy-Green deformation field in three dimensions. *J. Elasticity* **56**, 95–105 (1999).

[17] Blume, J. Compatibility conditions for a left Cauchy-Green strain field. *J. Elasticity* **21**, 271–308 (1989).

[18] Shield, R. T. The rotation associated with large strains. *SIAM J. Appl. Math.* **25**, 483–491 (1973).

[19] Hertz, H. Über die Berührung fester elastischer Körper (on the contact of elastic solids). *J. reine und angewandte Mathematik* **92**, 156–171 (1882).

[20] Johnson, K., Kendall, K. & Roberts, A. Surface energy and the contact of elastic solids. *Proc. R. Soc. Lond. A* **324**, 301–313 (1971).

[21] Derjaguin, B. V., Muller, V. M. & Toporov, Y. P. Effect of contact deformation on the adhesion of particles. *J. Colloid Interface Sci.* **53**, 314–326 (1975).

[22] Maugis, D. Adhesion of spheres: the JKR-DMT transition using a Dugdale model. *J. Colloid Interface Sci.* **150**, 243–269 (1992).

[23] Tabor, D. Surface forces and surface interactions. *J. Colloid Interface Sci.* **58**, 2–13 (1977).

[24] Phillips, J. & Johnson, K. Tactile spacial resolution. iii. a continuum mechanics model of skin predicting mechanoreceptor responses to bars, edges, and gratings. *J. Neurophys.* **46**, 1204–1225 (1981).

[25] Vega-Bermudez, F. & Johnson, K. Fingertip skin conformance accounts, in part, for differences in tactile spatial acuity in young subjects, but not for the decline in spatial acuity with aging. *Perception and Psychophysics* **66**, 60–67 (2004).

[26] Wolfram, L. Friction of skin. *J. Soc. Cosmet.* **34**, 465–476 (1983).

[27] Zahouani, H., Asserin, J. & Humbert, P. *Bioengineering of the skin: skin biomechanics*, chap. Mechanical properties of the skin during friction assesment (CRC, 2002).

[28] Barquins, M. & Courtel, R. Rubber friction and the rheology of viscoelastic contact. *Wear* **32**, 133–150 (1975).

[29] Silver, F., Siperko, L. & Seehra, G. Mechanobiology of force transduction in dermal tissue. *Skin Res. Technol.* **9**, 3–23 (2003).

[30] Asserin, J. *et al.* Measurement of the friction coefficient of the human skin in vivo: quantification of the cutaneous smoothness. *Colloids and surfaces B* **19**, 1–12 (2000).

[31] Marks, R. *Physiology, biochemistry, and molecular biology of the skin*, chap. 21 (OUP, Oxford, UK, 1991).

[32] Barel, A. O., Courage, W. & Clarys, P. *Handbook of non-invasive methods and the skin*, chap. 14.3 (CRC, Boca Raton, 1995).

[33] Smalls, L. K., Wickett, R. R. & Visscher, M. O. Effect of dermal thickness, tissue composition, and body site on skin biomechanical properties. *Skin Res. Technol.* **12**, 43–49 (2006).

[34] Delalleau, A., Josse, G., Lagarde, J.-M., Zahouani, H. & Bergheau, J.-M. A nonlinear elastic behaviour to identify the mechanical parameters of human skin *in vivo*. *Skin Res. Technol.* **14**, 152–164 (2008).

[35] Gerhardt, L.-C., Strässle, V., Lenz, A., Spencer, N. D. & Derler, S. Influence of epidermal hydration on the friction of human skin against textiles. *J. R. Soc. Interface* **5**, 1317–1328 (2008).

[36] Gerhardt, L.-C., Lenz, A., Spencer, N. D., Münzer, T. & Derler, S. Skin-textile friction and skin elasticity in young and aged persons. *Skin Res. Technol.* **15**, 288–298 (2009).

[37] Kwiatkowska, M., Franklin, S. E., Hendriks, C. P. & Kwiatkowski, K. Friction and deformation behaviour of human skin. *Wear* **267**, 1264–1273 (2009).

[38] Hendriks, F. *et al.* A numerical-experimental method to characterise the non-linear mechanical behaviour of human skin. *Skin Res. Technol.* **9**, 274–283 (2003).

[39] Hendriks, F., Brokken, D., Oomens, C. & Baaijens, F. Influence of hydration and experimental length scale on the mechanical respone of human skin *in vivo*, using optical coherence tomography. *Skin Res. Technol.* **10**, 231–241 (2004).

[40] Hendriks, F. M., Brokken, D., Oomens, C. W. J., Bader, D. L. & Baaijens, F. P. T. The relative contributions of different skin layers to the mechanical behaviour of human skin *in vivo* using suction experiments. *Medical Eng. & Phys.* **28**, 259–266 (2006).

[41] Pailler-Mattéi, C. *et al.* Contribution of stratum corneum in determining bio-tribological properties of the human skin. *Wear* **263**, 1038–1043 (2007).

[42] Pailler-Mattéi, C., Bec, S. & Zahouani, H. *In vivo* measurements of the elastic mechanical properties of human skin by indentation tests. *Med. Eng. & Phys.* **30**, 599–606 (2008).

[43] Jachowicz, J., McMullen, R. & Prettypaul, D. Indentometric analysis of *in vivo* skin and comparison with artificial skin models. *Skin Res. Technol.* **13**, 299–309 (2007).

[44] Agache, P. G., Monneur, C., Leveque, J. L. & De Rigal, J. Mechanical properties and young's modulus of human skin in vivo. *Arch. Dermatol. Res.* **269**, 221–232 (1980).

[45] Leveque, J. L., de Rigal, J., Agache, P. G. & Monneur, C. Influence of aging on the in vivo extensibility of human skin at a low stress. *Arch. Dermatol. Res.* **269**, 127–135 (1980).

[46] Christensen, M. S., Hargens III, C. W., Nacht, S. & Gans, E. H. Viscoelastic properties of intact human skin: instrumentation, hydration effects, and the contribution of the stratum corneum. *J. Invest. Dermat.* **69**, 282–286 (1977).

[47] Khatyr, F. *et al.* Model of the viscoelastic behaviour of skin *in vivo* and study of anisotropy. *Skin Res. Technol.* **10**, 96–103 (2004).

[48] Evans, S. L. & Holt, C. A. Measuring the mechanical properties of human skin *in vivo* using digital image correlation and finite element modelling. *J. Strain Analysis* **44**, 337–345 (2009).

[49] Dawes-Higgs, E. K., Swain, M. V., Higgs, R. J. E. D., Appleyard, R. & Kossard, S. Accuracy and reliability of a dynamics biomechanical skin measurement probe for the analysis of stiffness and viscoelasticity. *Physiol. Meas.* **25**, 97–105 (2004).

[50] Gennisson, J.-L. *et al.* Assessment of elastic parameters of human skin using dynamic elastography. *IEEE Trans. Ultrason., Ferroelect., Freq. Contr.* **51**, 980–989 (2004).

[51] Park, A. C. & Baddiel, C. B. Rheology of stratum corneum—i: a molecular interpretation of the stress—strain curve. *J. Soc. Cosmet. Chem.* **23**, 3–12 (1972).

[52] Dunn, M. & Silver, F. Viscoelastic beahviour of human connective tissues: relative contribution of viscous and elastic components. *Connective tissue research* **12**, 59–70 (1983).

[53] Oxlund, H., Manschot, J. & Viidik, A. The role of elastin in the mechanical properties of skin. *J. Biomech.* **21**, 213–218 (1988).

[54] Silver, F. H., Seehra, G. P., Freeman, J. W. & DeVore, D. Viscoelastic properties of young and old human dermis: a proposed molecular mechanism for elastic energy storage in collagen and elastin. *J. Appl Polymer Sci.* **86**, 1978–1985 (2002).

[55] Wu, J. Z. & Cutlip, R. G. Evaluation of nonlinear elastic behaviours of skin. *Skin Res. Technol.* **11**, 287–288 (2005).

[56] Scheuplein, R. J. & Blank, I. H. Permeability of the skin. *Physiol. Rev.* **51**, 702–747 (1971).

[57] Timoshenko, S. & Woinowsky-Krieger, S. *Theory of Plates and Shells*, 82 (McGraw-Hill, New York, USA, 1959).

[58] Ingalls, D. Personal communication (2008). (Sales & Marketing manager, MatTek Corportation).

[59] Gerhardt, L.-C., Mattle, N., Schrade, G., Spencer, N. & Derler, S. Study of skin-fabric interaction of relevance to decubitus: friction and contact-pressure measurements. *Skin Res. Technol.* **14**, 77–88 (2007).

[60] Derler, S., Schrade, U. & Gerhardt, L.-C. Tribology of human skin and mechanical skin equivalents in contact with textiles. *Wear* **263**, 1112–1116 (2007).

[61] Silver, F. H., Freeman, J. W. & DeVore, D. Viscoelastic properties of human skin and processed dermis. *Skin Res. Technol.* 7, 18–23 (2001).

[62] EDANA. What are nonwovens. URL http://www.edana.org/content/default.asp?PageID=33. Accessed 14/06/2010.

[63] EDANA. How they [nonwovens] are made. URL http://www.edana.org/content/default.asp?PageID=36. Accessed 15/06/2010.

[64] Berland, C. Personal communication (2010). (Senior Scientist, SCA Hygiene Products AB).

[65] EDANA. Web formation - spunlaid. URL http://www.edana.org/content/Default.asp?PageID=41#spunlaid. Accessed 15/06/2010.

[66] EDANA. Web bonding - thermal bonding. URL http://www.edana.org/content/Default.asp?PageID=42#thermalbonding. Accessed 15/06/2010.

[67] Bhat, G. S. & Malkan, S. R. *Handbook of Nonwovens*, chap. 4, 143–200 (Woodhouse Publishing Ltd., Cambridge, UK, 2007).

[68] Russell, S. Personal Communication (2010). (Professor of Textile Materials and Technology, University of Leeds).

[69] van Wyck, C. M. Note on the compressibility of wool. *J. Textile Institute* **37**, T285–T292 (1946).

[70] Stearn, A. E. The effect of anisotropy in the randomness of the fibre orientation on fibre-to-fibre contacts. *J. Textile Institute* **62**, 353–360 (1971).

[71] Komori, T. & Makishima, K. Numbers of fibre-to-fibre contacts in general fibre assemblies. *Textile Research Journal* **47**, 13–17 (1977).

[72] Komori, T. & Makishima, K. Estimation of fibre orientation and length in fibre assemblies. *Textile Research Journal* **48**, 309–314 (1978).

[73] Lee, D. H. & Lee, J. K. Initial compressional behaviour of fibre assembly. In Kawabata, S., Postle, R. & Niwa, M. (eds.) *Objective measurements: application to product design and process control*, 613–622 (1986).

[74] Carnaby, G. & Pan, N. Theory of the compression hysteresis of fibrous assemblies. *Textile Research Journal* **59**, 275–284 (1989).

[75] Pan, N. & Carnaby, G. Theory of the shear deformation of fibrous assemblies. *Textile Research Journal* **59**, 285–292 (1989).

[76] Komori, T. & Itoh, M. A new approach to the theory of the compression of fibre assemblies. *Textile Research Journal* **61**, 420–428 (1991).

[77] Komori, T. & Itoh, M. Theory of the general deformation of fibre assemblies. *Textile Research Journal* **61**, 588–594 (1991).

[78] Pan, N. A modified analysis of the microstructural characteristics of general fibre assemblies. *Textile Research Journal* **63**, 336–345 (1993).

[79] Toll, S. Note: on the tube model for fibre suspensions. *J. Rheology* **37**, 123–125 (1993).

[80] Komori, T. & Itoh, M. A modified theory of fibre contact in general fibre assemblies. *Textile Research Journal* **64**, 519–528 (1994).

[81] Toll, S. Packing mechanisms of fibre reinforcements. *Polymer Engineering and Science* **38**, 1337–1350 (1998).

[82] Kabla, A. & Mahadevan, L. Nonlinear mechanics of soft fibrous networks. *J. R. Soc. Interface* **4**, 99–106 (2007).

[83] Head, D. A., Levine, A. J. & MacKintosh, F. C. Deformation of cross-linked semiflexible polymer networks. *Phys. Rev. Lett.* **91**, 108102–1–102102–4 (2003).

[84] Storm, C., Pastore, J. J., MacKintosh, F. C., Lubensky, T. C. & Janmey, P. A. Nonlinear elasticity in biological gels. *Nature* **435**, 191–194 (2005).

[85] Chandran, P. L. & Barocas, V. H. Affine versus non-affine fibril kinematics in collagen networks: theoretical studies of network behaviour. *J. Biomech. Eng.* **128**, 259–270 (2006).

[86] Amontons, G. *Les Mémoires de Mathématique et de Physique*, chap. De la resistance causée dans les machines, 206 (l'Academie Royale des Sciences, Paris, 1699).

[87] Bhushan, B. *Principles and applications of tribology*, chap. 6 (Wiley, 1999).

[88] Bowden, F. & Tabor, D. *The friction and lubrication of solids*, chap. 4 (OUP, Oxford, UK, 1986).

[89] Bowden, F. & Tabor, D. *The friction and lubrication of solids*, chap. 5 (OUP, Oxford, UK, 1986).

[90] Quinn, T. *Physical analysis for tribology*, chap. 1 (CUP, Cambridge, UK, 1991).

[91] Stachowiak, G. & Batchelor, A. *Engineering Tribology (Second Edition)*, chap. 10 (Butterworth-Heinemann, 2001).

[92] Archard, J. F. Elastic deformation and the laws of friction. *Proc. R. Soc. Lond. A* **243**, 190–205 (1957).

[93] Johnson, K. A note on the adhesion of elastic solids. *Brit. J. appl. Phys.* **9**, 199–200 (1958).

[94] Archard, J. F. Contact and rubbing of flat surfaces. *J. Appl. Phys.* **24**, 981–988 (1953).

[95] Greenwood, J. & Williamson, J. Contact of nominally flat surfaces. *Proc. R. Soc. Lond. A* **295**, 300–319 (1966).

[96] Whitehouse, D. J. & Archard, J. F. The properties of random surfaces of significance in their contact. *Proc. R. Soc. Lond. A* **316**, 97–121 (1970).

[97] Greenwood, J. A. & Wu, J. J. Surface roughness and contact: an apology. *Meccanica* **36**, 617–630 (2001).

[98] Tabor, D. A simplified account of surface topography and the contact between solids. *Wear* **32**, 269–271 (1975).

[99] Wong, W. K. R. *A study of evaporation and friction on hydrated forearm skin*. Ph.D. thesis, Dept. Medical Physics & Bioengineering, University College London (2008).

[100] Gwosdow, A. R., Stevens, J. C., Berglund, L. G. & Stolwijk, J. A. J. Skin friction and fabric sensation in neutral and warm environments. *Textile Res. J.* **56**, 574–580 (1986).

[101] Kenins, P. Influence of fiber type and moisture on measured fabric-to-skin friction. *Textile Res. J.* **64**, 722–728 (1994).

[102] Hong, K. H., Kim, S. C., Kang, T. J. & Oh, K. W. Effect of abrasion and absorbed water on the handle of nonwovens. *Textile Res. J.* **75**, 544–550 (2005).

[103] Comaish, S. & Bottoms, E. The skin and friction: deviations from Amontons' laws, and the effects of hydration and lubrication. *Br. J. Derm.* **84**, 37–43 (1971).

[104] Zhang, M. & Mak, A. F. T. *In vivo* friction properties of human skin. *Prosthetics and Orthotics Int.* **23**, 135–141 (1999).

[105] Shames, I. H. *Engineering mechanics: statics and dynamics* (Prentice Hall, New Jersey, USA, 1996). P. 301.

[106] Howell, H. G. The general case of friction of a string round a cylinder. *J. Textile Institute* **44**, T359–T362 (1953).

[107] Cottenden, A. M., Cottenden, D. J., Karavokiros, S. & Wong, W. K. R. Development and experimental validation of a mathematical model for friction between fabrics and a volar forearm phantom. *J. Eng. Med.* **222**, 1097–1106 (2008).

[108] Johnson, S., Gorman, D., Admans, M. & Briscoe, B. *Thin films in Tribology*, chap. The friction and lubrication of human stratum corneum (Elsevier Science Publishers, 1993).

[109] El-Shimi, A. In vivo skin friction measurements. *J. Soc. Cosmet. Chem.* **28**, 37–51 (1977).

[110] Nakajima, K. & Narasaka, H. Evaluation of skin surface associated with morphology and coefficient of friction. *Int. J. Cosmet. Sci.* **15**, 135–151 (1993).

[111] Bobjer, O. *et al.* Friction between hand and handle. Effects of oil and lard on textured and non-textured surfaces; perception of discomfort. *Appl. Ergonomics* **24**, 190–202 (1993).

[112] Koudine, A. A., Barquins, M., Anthoine, P., Aubert, L. & Lévêque, J.-L. Frictional properties of skin: proposal of a new approach. *Int. J. Cosmet. Sci.* **22**, 11–20 (2000).

[113] Sivamani, R., Goodman, J., Gitis, N. & Maibach, H. Friction coefficient of skin in real-time. *Skin Res. Technol.* **9**, 235–239 (2003).

[114] Adams, M., Briscoe, B. & Johnson, S. Friction and lubrication of human skin. *Trib. Lett.* **26**, 239–253 (2007).

[115] Tang, W., Ge, S., Zhu, H., Cao, X. & Li, N. The influence of normal load and sliding speed on frictional properties of skin. *J. Bionic Eng.* **5**, 33–38 (2008).

[116] Hendriks, C. P. & Franklin, S. E. Influence of surface roughness, material and climate conditions on the friction of human skin. *Tribol. Lett.* **37**, 361–373 (2010).

[117] Tomlinson, S. E., Lewis, R. & Carré, M. J. Review of the frctional properties of finger-object contact when gripping. *J. Eng. Trib.* **221**, 842–850 (2007).

[118] Wilson, D. A study of fabric-on-fabric dynamic frction. *J. Textile Institute* **54**, T143–T155 (1963).

[119] Carr, W., Posey, J. & Tincher, W. Frictional characteristics of apparel fabrics. *Textile Res. J.* 129–136 (1988).

[120] Ajayi, J. O. Fabrics smoothness, friction, and handle. *Textile Res. J.* **62**, 52–59 (1992).

[121] Ajayi, J. O. Effects of fabric structure on frictional properties. *Textile Res. J.* **62**, 87–93 (1992).

[122] Hosseini Ravandi, S. A., Toriumi, K. & Matsumoto, Y. Spectral analysis of the stick-slip motion of dynamic friction in the fabric surface. *Textile Res. J.* **64**, 224–229 (1994).

[123] Virto, L. & Naik, A. Frictional behavior of textile fabrics part 1: sliding phenomenon of fabrics on metallic and polymeric solid surfaces. *Textile Res. J.* **67**, 793–802 (1997).

[124] Jeddi, A. A. A., Shams, S., Nosraty, H. & Sarsharzadeh, A. Relations between fabric structure and friction. Part I: woven fabrics. *J. Textile Institute* **94**, 223–234 (2003).

[125] Ramkumar, S. S. *et al.* Experimental verification of the failure of Amontons' law in polymeric textiles. *J. Appl. Polymer. Sci.* **91**, 3879–3885 (2004).

[126] Ramkumar, S. S. & Roedel, C. Study of needle penetration speeds on frictional properties of nonwoven webs: a new approach. *J. Appl. Polymer. Sci.* **89**, 3626–3631 (2003).

[127] Ramkumar, S. S. *et al.* Study of the effects of sliding velocity on the frictional properties of nonwoven fabric substrates. *Wear* **256**, 221–225 (2004).

[128] Wang, X. Y., Gong, R. H., Dong, Z. & Porat, I. Frictional properties of thermally bonded 3d nonwoven fabrics prepared from polypropylene/polyester bicomponent staple fibre. *Polymer. Eng. Sci.* **46**, 853–863 (2006).

[129] Hermann, D., Ramkumar, S., Seshaiyer, P. & Parameswaran, S. Frictional study of woven fabrics: the relationship between the friction and velocity of testing. *J. Appl. Polymer. Sci.* **92**, 2420–2424 (2004).

[130] Bhushan, B. *Principles and applications of tribology*, chap. 2 (Wiley, 1999).

[131] Moore, D. & Geyer, W. A review of hysteresis theories for elastomers. *Wear* **30**, 1–34 (1974).

[132] Flom, D. G. & Bueche, A. M. Theory of rolling friction for spheres. *J. Appl. Phys.* **30**, 1725–1730 (1959).

[133] Norman, R. H. The rolling friction of cylinders on planes. *Brit. J. Appl. Phys.* **13**, 358–361 (1962).

[134] Reiger, H. Ph.D. thesis, Institut für Verbrennungskraftmaschinen und Kraftfahrzeuge, Technische Universität, München (1968).

[135] Persson, B. N. J. Theory of rubber friction and contact mechanics. *J. Chem. Phys.* **115**, 3840–3861 (2001).

[136] Müser, M. H. Rigorous field-theoretical approach to the contact mechanics of rough elastic solids. *Phys. Rev. Lett.* **100**, 055504–1–055504–4 (2008).

[137] Moore, D. & Geyer, W. A review of adhesion theories for elastomers. *Wear* **22**, 113–141 (1972).

[138] Schallamach, A. The velocity and temperature dependence of rubber friction. *Proc. Phys. Soc. B* **66**, 386–392 (1953).

[139] Schallamach, A. A theory of dynamic rubber friction. *Wear* **6**, 375–382 (1963).

[140] Heslot, F., Baumberger, T., Perrin, B., Caroli, B. & Caroli, C. Creep, stick-slip, and dry friction dynamics: experiments and a heuristic model. *Phys. Rev. E* **49**, 4973–4988 (1994).

[141] Caroli, C. & Velicky, B. Dry friction as an elasto-plastic response: effect of compressive plasticity. *J. de Physique I* 7, 1391–1416 (1997).

[142] Caroli, C. & Nozières, P. Hysteresis and elastic interaction of microasperities in dry friction. *Euro. Phys. J. B* **4**, 233–246 (1998).

[143] Baumberger, T. & Caroli, C. Solid friction from stick-slip down to pinning and aging. *Adv. Phys.* **55**, 279–348 (2006).

[144] Rice, J. & Ruina, A. Stability of steady frictional slipping. *J. Appl. Mech.* **50**, 343–349 (1983).

[145] Baumberger, T., Berthoud, P. & Caroli, C. Physical analysis of the state- and rate-dependent friction law. II. Dynamic friction. *Phys. Rev. B* **60**, 3928–3939 (1999).

[146] Vollmer, A. & Nattermann, T. Towards a statistical theory of solid dry friction. *Z. für Physik B* **104**, 363–371 (1997).

[147] Tanguy, A., Gounelle, M. & Roux, S. From individual to collective pinning: effect of long-range elastic interactions. *Phys. Rev. E* **58**, 1577–1590 (1998).

[148] Tanguy, A. & Vettorel, T. From weak to strong pinning I: a finite size study. *Euro. Phys. J. B* **38**, 71–82 (2004).

[149] Larkin, A. I. & Ovchinnikov, Y. N. Pinning in type II superconductors. *J. Low. Temp. Phys.* **34**, 409–428 (1979).

[150] Sokoloff, J. B. Static friction between elastic solids due to random asperities. *Phys. Rev. Lett.* **86**, 3312–3315 (2001).

[151] Marone, C. Laborartory-derived friction laws and their application to seismic faulting. *Annu. Rev. Earth Planet Sci.* **26**, 643–696 (1998).

[152] Ruina, A. L. Slip instability and state variable friction laws. *J. Geophys. Res.* **88**, 10359–10370 (1983).

[153] Dieterich, J. H. Modelling of rock friction 1. Experimental results and constitutive equations. *J. Geophys. Res.* **84**, 2161–2168 (1979).

[154] Schallamach, A. How does rubber slide? *Wear* **17**, 301–312 (1971).

[155] Roberts, A. & Jackson, S. Sliding friction of rubber. *Nature* **257**, 118–120 (1975).

[156] Kaye, G. W. C. & Laby, T. H. Tables of physical and chemical constants (2004). URL http://www.kayelaby.npl.co.uk/. Web edition, Accessed 16/04/2010.

[157] Fader, M. *et al.* Absorbant products for urinary/faecal incontinence: a comparative evaluation of key product designs. *Health Tech. Assessment* **12** (2008).

[158] Sufi, P. Personal communication (2008). (Consultant surgeon, Whittington Hospital, London).

[159] Johnson, K. *Contact Mechanics*, 17 (CUP, Cambridge, UK, 1985).

[160] Johnson, K. *Contact Mechanics*, 49 (CUP, Cambridge, UK, 1985).

[161] Johnson, K. *Contact Mechanics*, 65 (CUP, Cambridge, UK, 1985).

[162] Johnson, K. *Contact Mechanics*, 101 (CUP, Cambridge, UK, 1985).

[163] Riley, K., Hobson, M. & Bence, S. *Mathematical methods for physics and engineering* (CUP, Cambridge, UK, 1998).

[164] Hild, P. Non-unique slipping in the Coulomb friction model in two dimensional linear elasticity. *Quart. J. Mech. Appl. Math.* **57**, 225–235 (2004).

[165] Hild, P. Multiple solution of stick and separation type in the signorini model with coulomb friction. *Z. Angew. Math. Mech.* **85**, 673–680 (2005).

[166] Hassani, R., Hild, P. & Ionescu, I. Analysis of eigenvalue problems modelling friction: sufficient conditions of non-uniqueness for the elastic equilibrium. In Martins, J. & Marques, M. D. M. (eds.) *Proceedings of the third contact mechanics symposium (CMIS 2001), Peniche, Portugal, June 18–21, 2001*, 133–140 (Kluwer Academic Publishers, 2002).

[167] Hassani, R., Hild, P. & Ionescu, I. Sufficient conditions of non-uniqueness for the coulomb friction problem. *Math. Meth. Appl. Sci.* **27**, 47–67 (2004).

[168] Lünenschloss, J. & Albrecht, W. *Non-woven bonded fabrics* (Ellis Horwood, Chichester, UK, 1985).

[169] Karavokyros, S. *Skin friction: validating a mathematical model with a simple laboratory model*. Master's thesis, University College London (2007).

[170] Asimakopoulos, V. Personal communication (2010). (Ph.D student, Dept. Medical Physics, UCL).

[171] Cottenden, D. J. & Cottenden, A. M. An analytical model of the motion of a conformable sheet over a general convex surface in the presence of frictional coupling. *Quart. J. Mech. Appl. Math.* **62**, 345–364 (2009).

[172] Cottenden, A. M. *et al. Textiles for hygiene and infection control*, chap. Incontinence products (Woodhead Publishing, Cambridge, UK, 2010 (In press)).

[173] Johnson, K. *Contact Mechanics*, 59 (CUP, Cambridge, UK, 1985).

[174] Johnson, K. *Contact Mechanics*, 47 (CUP, Cambridge, UK, 1985).

[175] Southwood, W. F. W. The thickness of the skin. *Plastic and Reconstructive Surgery* **15**, 432–429 (1955).

[176] Atkinson, D. Personal communication (2009). (Lecturer, Dept. Medical Physics, UCL).